UNIVERSITY OF SOUTHAMPTON

Institute of Sound and Vibration Research

THE SURFACE PROPAGATION OF GROUND VIBRATION

by

David Vaughan Jones

Submitted for the degree of

Doctor of Philosophy

August 1987

ACKNOWLEDGEMENTS

I thank my supervisor, Dr. Maurice Petyt, for his regular help and guidance during this work. I also thank British Rail for aiding this work with a CASE Award, and Mr. Charles Frederick, Mr. Colin Stanworth and Mr. Tom Dawn for many useful suggestions.

I am grateful to Mrs. Maureen Strickland for her accurate typing of this thesis.

CONTENTS

LIST OF FIGURES

LIST OF TABLES

LIST OF SYMBOLS

Note (i) A "$_1$" is used to denote a quantity applying to the half-space below the layer.

Note (ii) A "$^-$" is used to denote a Fourier transformed quantity.

Note (iii) Further expressions in Chapter 6 are represented by the symbols: E, F, G, H, O, P, Q, R, D, Y, U, V, W and X.

Roman Symbol	Description
a	Strip-load half-width
$[A]$	Matrix comprising part of linear dynamic stiffness matrix (Chapter 4)
$\{A\} = [A_1, A_2, B_1, B_2]^T$	Integration constants (Chapter 3)
A, B, C, D	Integration constants (Chapter 9)
$[B]$	Matrix, as for [A]
b, c	Dimensions of rectangle
$[C]$	Matrix used in Chapter 5
c_1, c_2, c_R	Compression, shear and Rayleigh wavespeeds respectively
c_1^*, c_2^*	As for c_1 and c_2, for zero damping
C_1, C_2, D_1, D_2	Integration constants (Chapter 6)
d	Depth of layer (Chapter 6)
D	Determinant used in Chapter 5
$[D_m]$	Matrix of displacements at top & bottom of a sub-layer
e_{xx}, e_{yy}, e_{zz}	Components of strain
E	Young's modulus
f	Frequency (Hz)
F_1, F_2, F_3	Forces used in receptance work of Chapter 8
$F(\beta,\gamma)$	The Rayleigh equation, defined in Chapter 9
g	$= e^{-\alpha z}$
G	Potential function used in Chapter 6
$[G]$	Matrix, as for [A]
h	Compression wavenumber (Chapter 9)
h	Layer depth
h_m	Sub-layer depth
H	Potential function
i	$\sqrt{(-1)}$
$[I]$	The identity matrix
$J(\omega^*)$	The number of natural frequencies in a layer, which exist below the frequency ω^* (see Chapter 6)
$J_o(\omega^*)$	As for $J(\omega^*)$, except that the edges of the layer are fixed
k	Shear wavenumber (Chapter 9)
k_1, k_2, k_R	Compression, shear and Rayleigh wavenumbers respectively
$[M]$	Matrix, as for [A]
$\|M\|$	Determinant identical to the period equation for the elastic foundation model
m	Mass, used in Chapter 8

P	Total load (Newtons)
q	$= e^{-\beta z}$
$[R]$	Dynamic stiffness matrix for a half-space
$[S]$	Matrix used in Chapter 5
$s[T]$	The "sign count" of matrix [T] (see Chapter 6)
t	Time (seconds)
$[T]$	Dynamic stiffness matrix (see Chapter 6)
T^{Δ}	Upper triangular form of [T]
u	Horizontal displacement in x-direction
$\tilde{u}(x_1)$	Result of first integration of double Fourier transformed horizontal motion, evaluated at $x = x_1$ (Chapter 9)
$u_{i,j}$	$= \frac{\partial u_i}{\partial x_j}$
$[U]$	Matrix of displacements
v	Transverse displacement in y-direction
$\underline{v}$	= (u,w), displacement vector (Chapter 6)
w	Vertical displacement in z-direction
w_1, w_2, w_3	Displacements used in receptance work of Chapter 8
$\tilde{w}(x_1)$	As for $\tilde{u}$, but for the vertical motion
$[\bar{w}]$	Matrix of Fourier transformed displacements
x	Horizontal co-ordinate
$[X]$	Matrix used in Chapter 3
$[X_{11}]$, $[X_{21}]$	Two components of [X]
y	Transverse co-ordinate
Y	$= \alpha\beta + \zeta^2$ (Chapter 6)
z	Vertical co-ordinate
Z	$= \alpha\beta - \zeta^2$ (Chapter 6)
W	Energy absorbed during a cycle (Chapter 2)
ΔW	Maximum stored energy during a cycle (Chapter 2)

Greek Symbol	Description
α	$= \sqrt{(\zeta^2 - k_1^2)}$
α_1	$= \sqrt{(\beta^2 + \gamma^2 - h^2)}$ (Chapter 9)
α_2	$= \sqrt{(\beta^2 + \gamma^2 - k^2)}$ (Chapter 9)
α_{ij}	Receptance of a mass
β	$= \sqrt{(\alpha^2 - k_2^2)}$
β	Wavenumber (Chapter 9)
β_C	Maximum value of β for integration (Chapter 9)
β_{ij}	Receptance of ground
γ	Wavenumber (Chapter 9)
γ_C	Maximum value of γ for integration (Chapter 9)
δ_{ij}	Kronecker Delta
Δ	Dilatation, $= \frac{\partial u}{\partial x} + \frac{\partial v}{\partial y} + \frac{\partial w}{\partial z}$

ε_{ij}	Components of strain (Chapter 9)
ζ	Wavenumber
η	Loss factor
η_s, η_c	Loss factors associated with shear and compression respectively
θ	Potential function (Chapter 6)
θ	= tan μ (Chapter 2)
κ	Bulk modulus
λ'	Eigenvalue (Chapter 4)
λ_1, λ_2, λ_R	Wavelengths of compression, shear and Rayleigh waves respectively
μ	Shear modulus
υ	Poisson's ratio
π	= 3.1415296...
ρ	Density ($Kg.m^{-3}$)
σ_{ij}	Stress component (Chapter 9)
τ_{ij}	Stress component
$[\tau]$	Matrix of Fourier transformed stress components
ϕ	Potential function
ϕ_L	Loss angle (Chapter 2)
ω	Radial frequency
ω^*	Chosen fixed frequency (Chapter 6)
ω_n	Natural frequency of order n
Ω	Non-dimensional frequency ($= \omega a \sqrt{\left[\frac{\rho}{E}\right]}$)

The following operators are used:

∇f Gradient $= i \frac{\partial f}{\partial x} + j \frac{\partial f}{\partial y} + k \frac{\partial f}{\partial z}$

where i, j, k are unit vectors in the x, y, z directions, and f is a scalar

$\nabla . \underline{v}$ Divergence $= \frac{\partial u}{\partial x} + \frac{\partial v}{\partial y} + \frac{\partial w}{\partial z}$

where u, v, w are components in the x, y, z directions of a vector

$\nabla^2 f$ Laplacian $= \frac{\partial^2 f}{\partial x^2} + \frac{\partial^2 f}{\partial y^2} + \frac{\partial^2 f}{\partial z^2}$

UNIVERSITY OF SOUTHAMPTON

ABSTRACT

FACULTY OF ENGINEERING AND APPLIED SCIENCE
INSTITUTE OF SOUND AND VIBRATION RESEARCH

Doctor of Philosophy

THE SURFACE PROPAGATION OF GROUND VIBRATION

by David Vaughan Jones

This work involves the numerical solution of a mathematical model, which idealises the source of the ground vibration as a strip of pressure varying harmonically in time. The ground below the strip is modelled as homogeneous, isotropic and elastic, with hysteretic internal damping characterised by a loss factor. For an infinite strip load, which reduces the problem to two dimensions, three ground structures have been considered: a half-space, a layer over an inflexible half-space, and a layer over a flexible half-space of different material properties to the layer. For a finite (rectangular) strip load, only the half-space ground structure has been analysed.

The formulation of the problem involves partial differential equations, which are Fourier transformed and solved in the transform domain. The inverse transformation to the space domain is calculated numerically, to yield the surface displacements.

For the layered ground structures, the natural modes of free propagation have been studied, and used to interpret the forced response results.

The forced response problem has been extended to include masses either at the load, at the response point or between the load and response point, to study the value of isolation masses.

CHAPTER 1

INTRODUCTION

1.1 The Railway Vibration Problem

Vibration caused in the vicinity of a moving train becomes a problem if people are disturbed. Only in exceptional circumstances are the vibrations great enough to damage buildings. The vibrations propagating away from a moving train are due in part to the changing stress pattern produced in the supporting ground. In addition, rail level defects and imperfections in the running gear of the train can cause stress waves in the ground, and periodic defects due to joints, wheel-flats and welds are also significant.

The total railway vibration problem can be broken into four components:

(i) vehicle-track system dynamics,
(ii) the ground vibration,
(iii) the response of buildings,
(iv) the subjective response of occupants.

An attempt at modelling the first component has been made by the O.R.E. [28], and British Rail have obtained experimental data relating to components (ii) to (iv) [13]. The aim of this work is to study the second component, and produce a mathematical model of the ground vibration, which will give theoretical predictions of the surface vibration at the wayside of the train.

1.2 Previous Work on Ground Vibration Propagation

This section briefly reviews previous work in this field, which is discussed in more detail in the relevant chapters. Some previous work which is applicable to the railway problem, but does not relate to the mathematical models used in this work, is also mentioned here.

In 1885, Rayleigh [67] discovered the 'surface wave' named after him, which can propagate on the surface of an elastic space, by seeking a solution to the defining elastodynamic equations (see equations (3.1) and (3.2)), in the form of a wave whose amplitude decays exponentially with depth. This approach was suggested by experimental seismograms, which could not be explained simply by considering the 'compression' and 'shear' waves, the two 'body' waves which were already known to exist in the ground. Subsequently, Lamb [44, 45] laid the theoretical foundation for all later work, in his treatment of plane and cylindrically symmetric problems. His assumptions that the ground is homogeneous, isotropic, elastic and flat have been adhered to by most workers who followed him. Lamb's solution for the surface displacements due to impulse loads is in the form of asymptotic expressions, valid in the 'far-field'.

During the 1920's, Stoneley [73] generalised the Rayleigh wave to include a 'surface' wave propagating at the interface of two solids, and Love [49] studied the stress distribution under a vibrating rectangle, strip or circle. This work was a fore-runner of later work concerned with the effects of a vibrating machine on its foundation, and in fact most work since the 1930's has examined the displacements and stresses immediately below the surface loading. Reissner [81] and later Miller and Pursey [56] used simplified boundary conditions to study, theoretically, a vibrating disc on a half-space. Their solutions do not require the disc to be rigid, a condition which introduces awkward mixed boundary conditions of constant displacement under the disc, and zero surface stress outside the disc. However, this rigidity is an important factor in machine foundation vibration. Bycroft [9] tried to approximate the rigidity while avoiding these mixed boundary conditions, by basing his assumed stress distribution under the disc on the exact static solution. This gave a good approximation at low frequency.

About ten years after Bycroft's work, Awojobi and Grootenhuis [4] and Robertson [70] tackled the genuine problem of a vibrating rigid disc, by using different sophisticated techniques which lead to series expansions for the stress and displacement under the disc.

Kobori and Thompson [40] studied the problem of a rectangular load on a half-space. Their analysis involves a double Fourier transform, and to

avoid excessive complications, they used a uniform stress distribution over the rectangle. Kobori *et al* [39] later extended this work, to a vibrating rectangular load on the surface of a layer over a rigid half-space.

Richardson [68] was among the first workers interested in the surface displacements near to the disc. He used Bycroft's stress distribution under the disc to find a numerical solution for the near-field displacements. Kuhlemeyer [43] and Waas [79] used the Finite Element Method to study the surface vibrations, due to a disc load, of a layer over a rigid half-space. Waas showed this method to be particularly useful for modelling awkward surface geometries, such as trenches.

With the advent of powerful computers, workers since the mid-1970's have used numerical techniques. Among others, Gazetas and Roesset [22,23] have done further work on machine foundation vibration, and Kausel and Roesset [36] introduced a dynamic stiffness matrix for a layer in the ground. Gaul [19] has extended the work of Kobori and Thompson [40], and looked at the surface vibrations in the vicinity of a square load. The developments of the last fifteen years are considered in greater detail in later Chapters.

In this work, the load always acts on the surface of the ground, but Hushmand [33] and Novak and Beredugo [59] have studied the effect of embedding the load in the surface. They have used both theoretical and experimental models, and have found that embedment increases any resonant frequencies. A technique for reducing the propagation of vibration which has been considered, is to dig a trench either near the source or near the area to be isolated. Barkan [5] was not encouraged by the results of trench experiments, and ECOM [14] found that existing surface irregularities had little isolation value. However, Waas [79], in his Finite Element solution, found that low frequency propagation could be considerably reduced by a trench. Woods [7], in a thorough experimental investigation of trenches dug around either the source or the response point, also met with qualified success.

Much previous work is concerned with the propagation of Love waves. These are horizontally polarised waves which can exist in a surface

layer, provided the material beneath is less elastic (see [5], for example). However, such waves can only be excited if horizontal stresses exist on the surface, which is not the case in the models presented in this work.

Further work specific to railway vibration has been performed recently. Grassie [76] has used both experimental and mathematical models to study the dynamic response of railway track with unsupported sleepers, and the ORE [28] have attempted to model a moving load.

1.3 The Mathematical Models used in this Work

In this work, three distinct models of the ground are used: (i) a half-space, (ii) a single layer of constant depth over an inflexible half-space, (iii) a single layer of constant depth over a flexible half-space. The second two models are referred to as the "bedrock model" and the "elastic foundation model" respectively. In all cases, the ground is considered homogeneous, elastic, isotropic and flat. In the elastic foundation model, the half-space has different material properties to the layer. When a forced response is studied, hysteretic damping is incorporated throughout the ground. For the free vibration, no damping is present, to allow the full development of natural modes. The theoretical formulation of the problem is based on the theory of linear elasticity. This is justified because of the small strains produced in the ground. Further, Richart and Whitman [82] have found from footing experiments that provided the acceleration of the footing does not exceed (g/2), then the linear approximation gives good estimates of true vibration amplitudes.

The maximum frequency of the harmonic load used in this work is 64 Hz. This is in accordance with the frequency range of the dominant vibrations produced by passing trains, as measured in adjacent houses. The hysteretic damping is characterised by the "loss factor" η (see Chapter 2), and for this frequency range, the ORE [28] have found that η does not vary significantly. Therefore, a constant loss factor is used for a given model, for the whole half-space and all frequencies.

Most of the forced response work is with an infinite strip load; Chapter 9 deals with a rectangular load. In each case, the load acts uniformly over the load area, and so displacement under the load is not constant. This simplification is considered justified, because it is not expected to greatly affect the near-field displacements, which are of more interest in this context than the displacements under the load.

The ORE [28] maintain that a theoretical approach to the ground vibration problem must incorporate (a) the distance to the source, (b) the ground dissipation, (c) the depth, (d) the stratification. The models developed here all involve (a) and (b), and the bedrock and elastic foundation models introduce (d). The depth within the layer is of less interest here, as the load and response point are both on the surface.

In Chapter 2, the material properties of interest, in particular the damping, are discussed. In Chapter 3, the forced response of an infinite strip on a half-space is analysed. The harmonic load acts vertically, and the boundary conditions are 'smooth' - no shear stresses exist. This is always the case in this work. The method of solution involves solving Navier's elastodynamic equations of motion, by first transforming the equations to the transform domain, and then solving the resulting ordinary differential equations. The surface displacements are obtained by numerically inverse transforming these transformed solutions, using a method described in Appendix A. Some comparison of the results obtained with the receptance graphs of previous workers is possible. However, no work on the near-field displacements due to an infinite strip load acting on a half-space appears to have been done previously.

In Chapter 4, the free vibration of the bedrock model is considered. The problem is formulated using a dynamic stiffness matrix for the layer, and to aid solution a linear approximation to this matrix is used. This follows the work of Waas [79]; the problem is solved as an eigenvalue problem to give the dispersion curves and modeshapes of the propagating waves. In Chapter 5, the forced response of an infinite strip load acting on the bedrock model is analysed. The exact dynamic stiffness matrix for the layer is derived in the transform domain. This leads to the solution for the transformed components of motion at discrete values

of wavenumber, which allows numerical integration as before to obtain the surface displacements. As with the half-space forced response results, comparison is only possible with the receptance graphs of previous workers.

Chapter 6 deals with the free vibration of the elastic foundation model. A method developed by Wittrick and Williams [89] is used to solve the non-linear dynamic stiffness matrix for the layer, as an eigenvalue problem. This gives the dispersion curves. The "period equation" is derived, and with the knowledge of the "eigenfrequencies" from the dispersion curves, this is solved to give the modeshapes in the layer. It is found that the dispersion curves agree closely with an approximate expression due to Newlands [54], which is valid for large (ζd), where ζ is the wavenumber and d the depth of the layer, provided (ζd) > 25.

In Chapter 7, the forced response of an infinite strip load on the elastic foundation model is studied. The approach used is similar to that of Chapter 5, and involves solution of the dynamic stiffness matrix in the transformed domain. As before, the only previous results which afford comparison with those here are receptance graphs. A comparison is made in Chapter 7 between the results of the three ground structure models.

In Chapter 8, masses are introduced into the three models. The purpose of this study is principally to predict the effectiveness of isolation masses. Various masses are placed at the load, or at the response point, or between the load and response point, and the effect on direct and transfer receptance is studied for all three models. In some cases, masses at two locations are used. Several previous workers have produced results which can be compared with some results in Chapter 8.

Chapter 9 is concerned with the forced response of a rectangular patch of uniform pressure on a half-space. An analytical approach based on the work of Kobori and Thompson [40] is used, involving a double Fourier transform to find the transformed displacements. The inverse transformation is then accomplished using the method described in Appendix A, and also an application of Simpson's Rule. The effect of

masses placed on the surface is also investigated, and direct and transfer receptance graphs produced with and without the masses. These can be compared with results from earlier workers. Additionally, the method can be adapted to study the case of a square patch of uniform pressure on a half-space, as treated by Gaul [19], and a close correspondence of results is found.

CHAPTER 2

MATERIAL PROPERTIES AND THEIR MEASUREMENT

2.1 Some Definitions

Certain quantities which define the material properties of a solid are required in this work, and are defined in this section. Young's modulus, denoted by the symbol E, can be described as [41] "the ratio between the applied stress and the fractional extension, when a cylindrical or prismatic specimen is subjected to a uniform stress over its plane ends and its lateral surfaces are free from constraint". The shear or rigidity modulus, denoted by μ, is the ratio between the shear stress and the shear strain of a similar specimen. Poisson's ratio, denoted by ν, is the ratio between the lateral contraction and the longitudinal extension of the specimen, the lateral surfaces being free. The bulk modulus, κ, is "the ratio between the applied pressure and the fractional change in volume, when the solid is subjected to uniform hydrostatic compression".

The shear modulus, μ, is also known as one of the two Lame constants; the other is denoted by λ. For an isotropic homogeneous elastic solid (that is, one which has no preferred direction of strain, has identical properties throughout its body, and obeys the linear elastic stress-strain relations which are valid for small strains), μ and λ are the only two constants required in the governing stress-strain relations.

To define the quantities E, ν and κ mathematically, it is convenient to choose coordinate axes such that the x-axis is parallel to the axis of the cylindrical specimen. Then the only non-zero stress component is σ_{xx}, and the stress-strain relations are (see [26] for example):

$$\begin{aligned} \sigma_{xx} &= (\lambda + 2\mu)e_{xx} + \lambda(e_{yy} + e_{zz}) \\ 0 &= (\lambda + 2\mu)e_{yy} + \lambda(e_{xx} + e_{zz}) \\ 0 &= (\lambda + 2\mu)e_{zz} + \lambda(e_{xx} + e_{yy}) \end{aligned} \qquad (2.1)$$

where $e_{xx} = \partial u/\partial x$, etc., and u is the displacement component in the x-direction.

Then solving for e_{xx}, e_{yy} and e_{zz} gives:

$$e_{xx} = \frac{(\lambda + \mu)}{\mu(3\lambda + 2\mu)}\sigma_{xx}; \quad e_{yy} = e_{zz} = -\frac{\lambda\sigma_{xx}}{2\mu(3\lambda + 2\mu)} \tag{2.2}$$

and therefore

$$E = \frac{\sigma_{xx}}{e_{xx}} = \frac{\mu(3\lambda + 2\mu)}{\lambda + \mu} \tag{2.3}$$

and

$$\nu = -\frac{e_{yy}}{e_{xx}} = \frac{\lambda}{2(\lambda + \mu)} \tag{2.4}$$

In the case of uniform hydrostatic pressure $\sigma_{xx} = \sigma_{yy} = \sigma_{zz} = -P$ (say)
and $\sigma_{yz} = \sigma_{zx} = \sigma_{xy} = 0.$ (2.5)

Solving the stress-strain relations for this case gives

$$e_{xx} = e_{yy} = e_{zz} = -\frac{P}{3\lambda + 2\mu} \tag{2.6}$$

The fractional change in volume $= -\Delta = -(e_{xx} + e_{yy} + e_{zz})$

Therefore

$$k = \frac{P}{\Delta} = \lambda + \frac{2\mu}{3} \tag{2.7}$$

The conditions for stability of the solid are that the bulk and shear moduli are positive, as these represent the resistance to compression and shearing respectively. The extreme case of a body which resists shear but does not resist compression, is described by $\lambda + 2\mu/3 = 0$. The other extreme case of a body which resists

compression but not shear, is described by $\mu = 0$. These two cases in conjunction with equation (2.4) lead to theoretical limits on the value of ν, such that $-1 \leqslant \nu \leqslant \frac{1}{2}$. However, no materials with a negative Poisson's ratio are known, and so a more practical statement of the range of ν is

$$0 \leqslant \nu \leqslant \frac{1}{2} \tag{2.8}$$

2.2 Material Damping

The mathematical model of the ground used in this thesis includes dissipation due to internal damping. This makes the model more realistic, and has the additional advantage of removing integrand singularities which exist in the zero-damping case.

For harmonic motion, as applies in this work, the damping can be represented by making the elastic moduli complex. Taking E as an example, we then have:

$$E = (E_1 + iE_2)e^{i\omega t} \tag{2.9}$$

which is a vector rotating with angular velocity ω. E_1 is in phase with the stress and is related to the recoverable elastic energy, and E_2 is 90° out of phase with the stress, and is related to the unrecoverable energy lost in damping. The strain vector lags behind the stress vector (both rotate at frequency ω) by the "loss angle" ϕ_L, where

$$\tan \phi_L = \text{the "loss tangent"} = E_2/E_1 \tag{2.10}$$

The actual stresses and strains at a given moment are the projections of the vectors on to the real axis.

Several models have been used in the past to describe the behaviour of the damping term E_2. In the Voigt model of viscoelasticity, the term E (which for the purposes of this discussion can represent any of the elastic moduli) is replaced by one of the form:

$$E \rightarrow (E + iE' \frac{\partial}{\partial t}) \qquad (2.11)$$

where E' determines the magnitude of the damping. This model assumes a viscous-type damping, proportional to velocity. This introduces a frequency dependence in the damping term, so that from equation (2.9), $E_2 = \omega E'$. For this reason, many authors ([5], [22], [41], [52], [79] and [20]) reject the Voigt model as inappropriate for soils, on the grounds that experiments have shown the elastic moduli and damping in soils to be almost unaffected by frequency, at least in the range of interest (in this work this is below 64 Hz; see for example [5] or [79] for descriptions of experimental work). Warburton [80] has suggested removing the frequency dependence, by modifying equation (2.11) to

$$E \rightarrow (E + \frac{iE'}{\omega} \frac{\partial}{\partial t}) \qquad (2.12)$$

Kolsky [41] analyses combinations of the Voigt and Maxwell damping models, where the Maxwell model introduces a damping term which is inversely proportional to frequency.

However, most authors choose a "constant hysteresis" model of damping, which is independent of frequency. This model is used in this work. Of course, it should be realised that in reality, the behaviour of soil is anelastic and its damping mechanism complex, so all the models mentioned are strongly idealised. To explain the constant hysteresis model, the usual diagram of a stress-strain hysteresis loop, shown in Fig. 2.1, is useful:

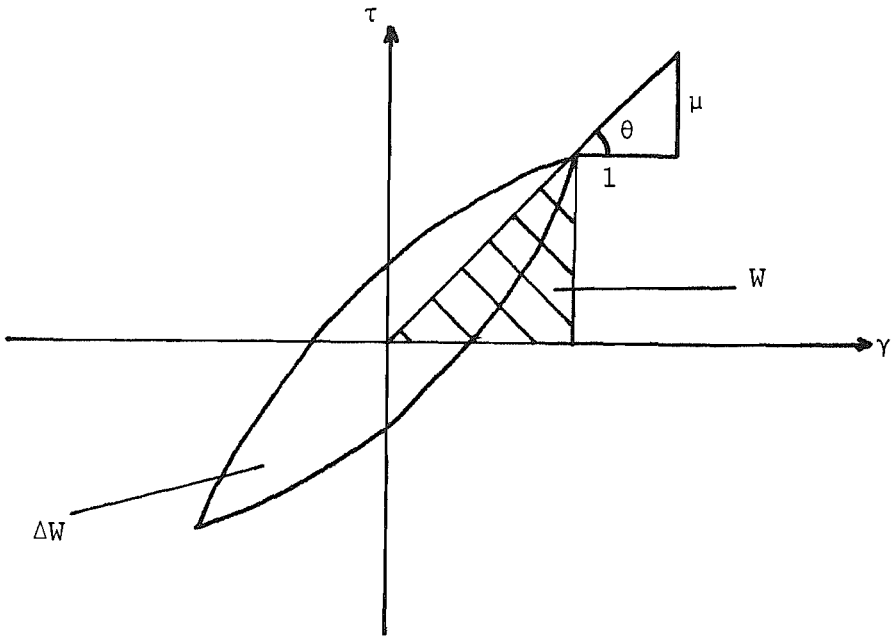

Fig. 2.1: Hysteresis loop

The loop shows the variation of stress with strain during one cycle of the motion. The total work done during the cycle, ΔW, is given by the area enclosed by the loop. The maximum energy stored during the cycle, W, is given by the shaded area. As shown in Figure 2.1, and from its definition, μ is given by

$$\mu = \arctan \theta \tag{2.13}$$

where θ is the angle subtended with the γ-axis by a line drawn through the origin and the tips of the loop. A measure of the damping in the system is given by $\Delta W/W$. This ratio leads naturally to the introduction of the "loss factor" used in structural mechanics, which results from energy considerations in a simple mass-spring-damper system [55]:

$$m\ddot{x} + c\dot{x} + kx = F_o e^{i\omega t} \tag{2.14}$$

The forcing function has been included for generality. If the hysteresis condition

$$c(\omega) = \frac{h}{\omega}, \qquad h = \text{constant} \tag{2.15}$$

is introduced, then for harmonic motion equation (2.14) becomes

$$m\ddot{x} + (ih + k)x = F_o e^{i\omega t} \tag{2.16}$$

This can be rewritten:

$$m\ddot{x} + k(1 + i\eta)x = F_o e^{i\omega t} \tag{2.17}$$

where the "loss factor" $\eta = h/k$ (2.18)

To relate the loss factor to the ratio $\Delta W/W$, consider the energy dissipated per cycle:

$$\text{E.D./cycle} = \Delta W = \int_o^{2\pi/\omega} c\dot{x}^2 dt \tag{2.19}$$

For a harmonic response

$$x = |X| \cos(\omega t - \beta) \tag{2.20}$$

where $|X|$ is the amplitude of the response. Hence from equations (2.15), (2.19) and (2.20)

$$\Delta W = \pi h \omega |X|^2 \tag{2.21}$$

Similarly, the maximum strain energy stored during a cycle is

$$W = \tfrac{1}{2} k |X|^2 \tag{2.22}$$

So from equations (2.21) and (2.22)

$$\frac{\Delta W}{W} = \frac{\pi h |X|^2}{\tfrac{1}{2} k |X|^2} = \frac{2\pi h}{k} = 2\pi\eta \tag{2.23a}$$

or

$$\eta = \frac{1}{2\pi} \frac{\Delta W}{W} \tag{2.23}$$

Kolsky [41] gives alternative definitions of the loss factor, based on the rate of decay of motion in the soil during free vibration, or on the width of a resonance peak in a receptance diagram.

In general, shear and compression in soil have different associated loss factors, which can be denoted η_S and η_C respectively. However, as explained in Section 2.4, there is a lack of consensus among experimental workers about the relative magnitudes of η_S and η_C. For simplicity, in this work a single loss factor η is used, so that

$$\eta = \eta_S = \eta_C \tag{2.24}$$

The O.R.E. [28] have noted that dissipation in soils "causes a pronounced weakening" of the high frequency vibration. To see why this is, consider the general expression for radial variation of amplitude with distance from a source of vibration

$$U = \frac{A(\omega,z)}{r^n} e^{i(\omega t - kr)} \tag{2.25}$$

The values of A, k and n are different for the Rayleigh, shear and compression waves. From consideration of asymptotic solutions [5], it is known that in the far-field, $n = 2$ for the body waves, and $n = \frac{1}{2}$ for the Rayleigh waves.

With internal damping characterised by loss factor η,

$$\text{wavenumber } k = \frac{\omega}{c(1 + i\eta)^{\frac{1}{2}}} \tag{2.26}$$

where c is the relevant characteristic wavespeed (shear, compression or Rayleigh) in a perfectly elastic (undamped) soil, and the square root is due to the definitions of the characteristic wavespeeds (see equation (3.7)).

Equation (2.26) is equivalent to

$$k = \frac{\omega(1 - i\eta)^{1/2}}{c(1 + \eta^2)^{1/2}} \qquad (2.27)$$

But

$$(1 - i\eta) = (1 + \eta^2)^{1/2} e^{-i \arctan\eta} \qquad (2.28a)$$

Therefore

$$(1 - i\eta)^{1/2} = (1 + \eta^2)^{1/4} e^{-\frac{1}{2}i \arctan\eta} \qquad (2.28)$$

Putting $\epsilon = \frac{1}{2} \arctan \eta$ (2.29)

this gives

$$k = k_R - i\alpha = \frac{\omega}{c(1 + \eta^2)^{1/4}} (\cos \epsilon - i \sin \epsilon) \qquad (2.30)$$

Hence equation (2.25) can be rewritten:

$$U = \frac{A(\omega, z)}{r^{n}} e^{i(\omega t - k_R r)} e^{-\alpha r} \qquad (2.31)$$

From equation (2.30), α is proportional to ω, and so the term $(e^{-\alpha r})$ in equation (2.31) is smaller for higher frequency, and the greater weakening of high frequency vibration with distance is predicted.

2.3 Experimental Methods of Determining Soil Parameters

Several methods have been used by many workers to estimate soil parameters. They fall into one of two classes, either laboratory or "in-situ" experiments. Seed and Idriss [71] have found that tests on a specimen of soil in a laboratory, are appropriate for moderate to high induced strains. Triaxial compression, simple shear and torsional shear tests can all be accomplished, which with cyclic loads can yield experimental hysteresis loops. Forced vibration tests can find resonant frequencies, and free vibration tests (conducted by observing

the decay of motion after a cyclic load is removed) give the "logarithmic decrement" δ. This is defined as the natural logarithm of the ratio of successive amplitudes of the decay, and is related to the loss factor, η (for small η) by [79]:

$$\delta = \log_e\left(\frac{A_1}{A_2}\right) = \pi\eta \qquad (2.32)$$

In-situ tests have not generally proved a suitable means of estimating damping, although the O.R.E. [28] mention a method described by Alvarez and Clement [78], based on the degree to which an impulse signal is widened by the distance travelled. They also point out that if the Rayleigh wave is known to dominate the response at some distance, the measurement of the vertical amplitude at distances r_1 and r_2 leads to the following relation involving α:

$$\frac{U_Z(r_1)}{U_Z(r_2)} = \left(\frac{r_2}{r_1}\right) e^{-\alpha_R(r_1 - r_2)} \qquad (2.33)$$

where α is as given in equation (2.30), and in the case of equation (2.33) gives the Rayleigh wave dissipation.

More usually, in-situ experiments have given the wave velocities, which in turn can give the elastic moduli. The O.R.E. use a "cross-hole" procedure, which allows the variation of compression wavespeed with depth to be measured. Bore-holes are dug, and a pulse is generated at a certain depth. The travel-time to a point at the same depth in another bore-hole is recorded. Because the compression wave is the fastest, it corresponds to the first arrival. The Rayleigh wavespeed can be determined by measuring the phase change with a sinusoidal excitation between points r_1 and r_2, which is given by $\frac{2\pi}{c_R}(r_2 - r_1)$, where c_R is the Rayleigh wavespeed.

British Rail [32] have developed their own method of determining the shear wavespeed, which does not involve drilling. A shear wave is generated by impacting a bar held on the ground by the rear wheels of a Land-Rover. The difficulty in recognising the arrival of the shear wave

at some distant point, is reduced by using a geophone sensitive to horizontal vibrations. They also use a seismic technique to find the compression wavespeeds of each layer of the ground. A pulse is generated by striking a metal plate, and the first arrival at a geophone is timed. If the plate is moved away from the geophone, Fig. 2.2 shows the form of the resulting time-distance graph:

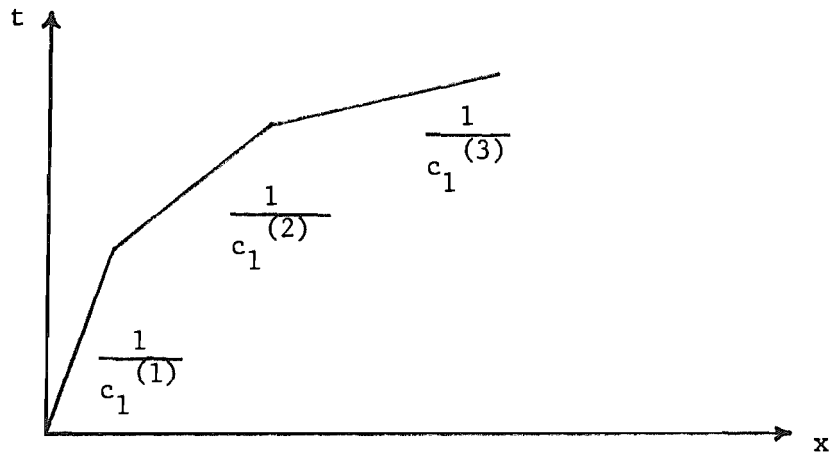

Fig. 2.2 Time/distance graph resulting from seismic tests

The different slopes of the graph give the compression wavespeeds in each layer.

British Rail estimate the density of the ground, ρ, from an empirical relation between the compression wavespeed c_1 and ρ. Then by the definition of the shear wavespeed (see equation (3.7)):

$$\mu = \rho c_2^2 \tag{2.34}$$

where c_2 is the shear wavespeed. From the results of Section 2.1, it can be shown that

$$\nu = \frac{(c_1/c_2)^2 - 2}{2(c_1/c_2)^2 - 2} \tag{2.35}$$

Hence, the other required parameters can be calculated.

Grootenhuis and Awojobi [27] have suggested that in-situ tests are best performed with an electromagnetic exciter, rather than a vibrator using rotating out-of-balance forces. This is because the soil's elastic moduli are known to vary according to the amplitude of the motion (see Section 2.4), and as the force of this latter vibrator is a function of the frequency, as will therefore be the induced amplitude, any receptance curves produced with it will be of limited value. Grootenhuis and Awojobi prefer to keep the amplitude constant and vary the force of their exciter. Resonant frequencies can then be determined by varying the frequency to give the same amplitude for minimum force. By finding the resonant frequencies with two different masses at the load, Awojobi's previous work [3] allows ν and μ to be found. Provided the masses are not too different, it can be assumed μ will not be significantly affected by the difference in the two resonant frequencies. Young's modulus can then be found from:

$$E = \frac{2\mu}{1 + \nu} \qquad (2.36)$$

This technique also allows non-linear effects to be studied, by repeating tests with different amplitudes.

2.4 A Review of Published Data on Material Properties

Seed and Idriss [71] have found that the main factors affecting the elastic moduli and damping of soils are: (i) the strain amplitude, γ; (ii) the effective mean principal stress, σ_m'; (iii) the "void ratio" (or relative density) e; (iv) the number of cycles of loading, N; (v) the degree of saturation in cohesive soils. All workers agree that the shear modulus and damping are proportional to the strain; hence the hysteresis curve for higher strains will have a larger area. However, there is some disagreement among workers on the influence of other factors. Seed and Idriss have found that the grain size of sandy soils is not important, although the void ratio is. Barkan [5] found exactly the reverse. Whereas Seed and Idriss were unable to draw conclusions from their test results on clay soils, Barkan found that damping in clay is proportional to moisture content.

Such contradictions as these reflect the difficulties in soil testing, and also in some cases the danger of comparing laboratory results with those obtained in-situ. Chae [11] found that only the "confining pressure" tests in the laboratory give consistent results with those obtained in-situ. Using sandy soil of void ratio 0.52, four different techniques - the "resonant column", "seismic", "amplitude ratio", and Chae's own semi-analytical "half-space" technique, all gave close results for the proportional variation of shear modulus with confining pressure.

Choosing a realistic loss factor is complicated by the great range of results for various soils, as shown in Table 2.1, which is a condensation of results from previous authors.

Ref. No.	Material	μ (Nm^{-2})	ν	Loss Factors η_s	Loss Factors η_c	Confining pressure or strain, if given
[75]	Saturated clay	6.9×10^{7}	0.5	0.3	0.125	7891 Nm^{-2}
[75]	Partially saturated clay	5.6×10^{7}	0.4	>0.05	-	"
[75]	Sandy gravel	1.12×10^{8}	0.3	>0.05	-	"
[75]	Beach sand	8.5×10^{7}	0.3	>0.05	-	"
[28]	Saturated clay	4.09×10^{8}	0.45	$\eta = 1.0$		-
[28]	Sand	5.0×10^{8}	0.25	$\eta = 0.1$		-
[28]	Granite	2.25×10^{8}	0.25	$\eta = 0.1$		-
[28]	Deep geological formations	-	-	$\eta < 0.01$		-
[19]	Clay	-	0.4	0.05	0.1	-
[79]	No specific material			≥ 0.04 ≤ 0.1	$<\eta_s$	A large range of strains
[52]	No specific material			$0.04 \leq \eta \leq 0.4$		"
[33]	No specific material			$\eta < 0.1$		Maximum strain $\gamma = 10^{-3}$
[71]	No specific material			$\eta < 0.3$		Maximum strain $\gamma = 10^{-2}$
[29]	Sand	-	-	$\eta = 0.1$		-
[29]	Clay	-	-	$\eta = 0.5$		-
[88]	Crustal rocks	-	-	$\eta = 0.01$		(Seismic wave generated by explosive blast)

Table 2.1. Previous experimental results

No experiments were performed in the course of this work. Although most of the results presented here are in a non-dimensional form, they are designed to be easily interpreted for a particular British Rail test-site, called Clarborough. The material properties which have been measured at Clarborough, using the British Rail technique described in Section 2.3, are tabulated below.

Property	Above 7 m	Below 7 m
Density, ρ ($kg.m^{-3}$)	1550	2450
Young's modulus, E (Nm^{-2})	2.69×10^8	204.26×10^8
Shear modulus, μ (Nm^{-2})	1.07×10^8	87.36×10^8
Poisson's ratio, ν	0.257	0.179

Table 2.2: Clarborough material properties.

Three ground structure models are used in this work. For the "half-space" (Chapters 3 and 9) and "bedrock" (Chapters 4 and 5) models, only the material properties shown for the top layer (above 7 m) are necessary. For the "elastic foundation" model (Chapters 6 and 7), a half-space, having the material properties below 7 m is assumed to support the layer.

No data are available for the damping at Clarborough and so a constant value of

$$\eta = \eta_S = \eta_C = 0.1 \qquad (2.37)$$

has been used, although strictly the loss factor should vary with distance from the load, because η is strain dependent. However, in

the absence of the necessary data it is difficult to predict this variation with distance. Also, there is no reason why η_S should equal η_C, but the results in Table 2.1 do not indicate which loss factor should be the greater. The material properties of the top layer at Clarborough (Table 2.2) seem to correspond most closely to Sutherland's sandy gravel ([75] in Table 2.1). Accordingly, $\eta = 0.1$ has been taken as a rough average of the sandy soils tabulated.

Note: The O.R.E. results for sand in Table 2.1 ([28]) show a similar Poisson's ratio to Clarborough, and also a loss factor $\eta = 0.1$. The large difference in shear modulus, however, may be because the O.R.E.'s modulus has been calculated from an experimentally found compression wavespeed and Poisson's ratio, and the wavespeed was calculated as an average through depth. It is likely that the wavespeed will increase with depth of soil, due to the greater pressure, and so increase the average value.

CHAPTER 3

INFINITE STRIP LOAD ACTING ON A HALF-SPACE

3.1 Introduction

In this Chapter, the railway vibration source is mathematically idealised as a single, infinite strip of uniform, harmonically varying pressure, acting on the surface of an homogeneous, isotropic, elastic half-space. The half-space exhibits "constant hysteretic" damping, as described in Section 2.2. There is no mass at the vibrating strip - this complication is considered in Chapter 8. The contact between the strip and the half-space surface is "smooth" - no shear stresses act at the surface. The method of analysis involves expressing the problem in terms of Navier's elastodynamic partial differential equations, which are Fourier transformed to produce ordinary differential equations. The boundary conditions are also Fourier transformed, and solution expressions are found in the transform domain. These expressions are then numerically inverse transformed to give the approximate surface displacements, using a method explained in Appendix A.

As discussed in Chapter 1, much of the work on ground vibration has been concerned with displacements directly underneath the foundations of vibrating machines. Where the load has been modelled as an infinite strip acting on a half-space, the more complicated case of a rigid strip has been modelled [2,4,22,51,60,16]. In this case the boundary conditions are mixed (constant displacement under the load, and zero surface stresses elsewhere) leading to dual integral equations. Both "smooth" and "welded" contacts have been considered. The results produced are mostly in the form of direct receptance graphs, and are discussed in Chapter 8.

Very little previous work exists on the near-field surface effects of a strip load on a half-space. Miller and Pursey [56] have used the same boundary conditions, and similar analysis to here, but they seek asymptotic solutions of the inverse transform integrals using complex

contour integration, which are only valid in the far-field. Gopalacharyulu and Rebbeck [25], expanding on the work of Barkan [5] (who, in turn, gives Lamb's [45] results), give asymptotic solutions for a line-load. However, their results for displacements near the source are inaccurate: the asymptotic expression given in their equation (11.2) can only be reduced to one term if the products (hx) and (kx) are very large, where h and k are respectively the compression and shear wavenumbers. Lamb gives the asymptotic series in full ([45], equation (89)), and if a ratio test is performed on the first and second terms, with realistic values of h and k, the second, neglected term can be shown to dominate the first, for considerably more than the 100 m distance considered. Gopalacharyulu and Rebbeck also consider a strip loading, and produce an asymptotic expression for the Rayleigh wave contribution to surface vibration. However, their method only allows solution under the load, and so does not afford comparison with the near-field results given here.

The method of analysis used here is described in Section 3.2. The non-dimensionalisation of the results is explained in Section 3.3, and the results are presented in Section 3.4. These are discussed in Section 3.5.

3.2 Analysis of Infinite Strip Load acting on a Half-Space

The half-space is assumed homogeneous, isotropic and elastic (the last assumption requires small strains). Following Sections 2.1 and 2.2, the elastic moduli E, μ and λ have their previous definitions, and throughout are complex parameters depending on the loss factor η.

The boundary conditions and ground structure model, together with the coordinate system, are shown in Fig. 3.1.

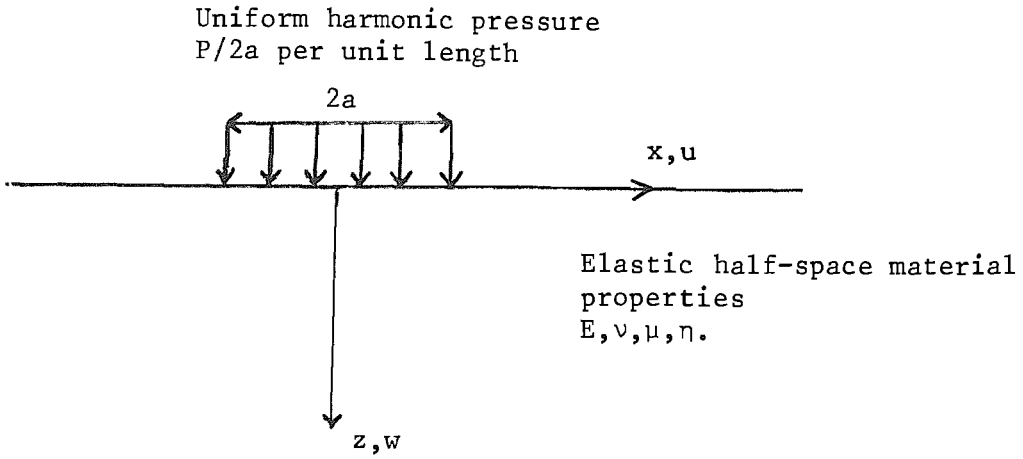

Fig. 3.1 Diagram of strip-load acting on half-space

The harmonic uniform pressure P/2a (P is the force per unit length in the y-direction) acts on a strip of the surface which is (2a) wide. u and w are the displacements in the x and z directions, respectively. Navier's Equations of Motion can be expressed in the following form (see [26], for example):

$$\rho \frac{\partial^2 u}{\partial t^2} = (\lambda+\mu) \frac{\partial \Delta}{\partial x} + \mu \nabla^2 u \qquad (3.1)$$

$$\rho \frac{\partial^2 w}{\partial t^2} = (\lambda+\mu) \frac{\partial \Delta}{\partial z} + \mu \nabla^2 w \qquad (3.2)$$

where ρ= density of medium, λ and μ are the Lamé constants, Δ is the dilatation = $\frac{\partial u}{\partial x} + \frac{\partial w}{\partial z}$; body forces have been assumed zero, and only the two equations relevant to the two-dimensional model have been given.

Introduce potentials ϕ and H such that

$$u = \frac{\partial \phi}{\partial x} - \frac{\partial H}{\partial z} \qquad (3.3)$$

$$w = \frac{\partial \phi}{\partial z} + \frac{\partial H}{\partial x} \tag{3.4}$$

Inserting eqs.(3.3) and (3.4) into eqs. (3.1) and (3.2) gives:

$$\nabla^2 \phi - \frac{1}{c_1^2} \ddot{\phi} = 0 \tag{3.5}$$

$$\nabla^2 H - \frac{1}{c_2^2} \ddot{H} = 0 \tag{3.6}$$

where $\ddot{}$ denotes double differentiation w.r.t. time, and

$c_1^2 = \frac{\lambda+2\mu}{\rho}$ = compression wave speed, $c_2^2 = \frac{\mu}{\rho}$ = shear wave speed. (3.7)

We assume harmonic solutions to result from an harmonic input:

$$\phi = \phi(x,z)e^{i\omega t}; \quad H = H(x,z)e^{i\omega t} \tag{3.8}$$

Equation (3.8) into eqs. (3.5) and (3.6):

$$\nabla^2 \phi + k_1^2 \phi = 0 \tag{3.9}$$

$$\nabla^2 H + k_2^2 H = 0 \tag{3.10}$$

where

$$k_1 = \frac{\omega}{c_1}; \qquad k_2 = \frac{\omega}{c_2} \tag{3.11}$$

Define the Fourier Transform pair as [35]:

$$\bar{f}(\zeta) = \frac{1}{2\pi} \int_{-\infty}^{\infty} f(x)e^{-\zeta x i} dx; \quad f(x) = \int_{-\infty}^{\infty} \bar{f}(\zeta)e^{i\zeta x} d\zeta \tag{3.12}$$

Use eq. (3.12) to transform eqs. (3.9) and (3.10) to the ζ plane:

$$\frac{d^2\bar{\phi}}{dz^2} + \frac{1}{2\pi} \int_{-\infty}^{\infty} \frac{d^2\phi}{dx^2} e^{-\zeta x i} dx + k_1^2 \bar{\phi} = 0$$

Integrating by parts gives:

$$\frac{d^2\bar{\phi}}{dz^2} - (\zeta^2 - k_1^2) \bar{\phi} = 0 \tag{3.13}$$

and likewise:

$$\frac{d^2\bar{H}}{dz^2} - (\zeta^2 - k_2^2)\,\bar{H} = 0 \qquad (3.14)$$

Putting $\alpha^2 = \zeta^2 - k_1^2$; $\beta^2 = \zeta^2 - k_2^2$ (3.15)

gives:

$$\frac{d^2\bar{\phi}}{dz^2} - \alpha^2\bar{\phi} = 0 \qquad (3.16)$$

$$\frac{d^2\bar{H}}{dz^2} - \beta^2\bar{H} = 0 \qquad (3.17)$$

Equations (3.16) and (3.17) have solutions:

$$\bar{\phi} = A_1 e^{-\alpha z} + A_2 e^{\alpha z} \qquad (3.18)$$

$$\bar{H} = B_1 e^{-\beta z} + B_2 e^{\beta z} \qquad (3.19)$$

Transforming equations (3.3) and (3.4):

$$\bar{u} = i\zeta\bar{\phi} - \frac{d\bar{H}}{dz} \qquad (3.20)$$

$$\bar{w} = \frac{d\bar{\phi}}{dz} + i\zeta\bar{H} \qquad (3.21)$$

Equations (3.18) and (3.19) into equations (3.20) and (3.21):

$$\bar{u} = i\zeta\{A_1 e^{-\alpha z} + A_2 e^{\alpha z}\} + \beta\{B_1 e^{-\beta z} - B_2 e^{\beta z}\} \qquad (3.22)$$

$$\bar{w} = -\alpha\{A_1 e^{-\alpha z} - A_2 e^{\alpha z}\} + i\zeta\{B_1 e^{-\beta z} + B_2 e^{\beta z}\} \qquad (3.23)$$

The relevant stresses are defined as [26]:

$$\tau_{zz} = \lambda \frac{\partial u}{\partial x} + (\lambda+2\mu) \frac{\partial w}{\partial z} \qquad (3.24)$$

$$\tau_{zx} = \mu \left(\frac{\partial u}{\partial z} + \frac{\partial w}{\partial x}\right) \qquad (3.25)$$

Transforming equations (3.24) and (3.25) gives:

$$\bar{\tau}_{zz} = \lambda i \zeta \bar{u} + (\lambda+2\mu) \frac{d\bar{w}}{dz} \qquad (3.26)$$

$$\bar{\tau}_{zx} = \mu \left(\frac{d\bar{u}}{dz} + i\zeta\bar{\omega}\right) \qquad (3.27)$$

Substituting eqs. (3.22) and (3.23) into eqs. (3.26) and (3.27) gives:

$$\bar{\tau}_{zz} = [2\mu\zeta^2-(\lambda+2\mu)k_1^2] \{A_1e^{-\alpha z}+ A_2e^{\alpha z}\}$$

$$-2\mu i\beta\zeta\{B_1e^{-\beta z}-B_2e^{\beta z}\} \qquad (3.28)$$

Also

$$\bar{\tau}_{zx} = -2\mu\alpha i\zeta \{A_1e^{-\alpha z}-A_2e^{\alpha z}\}$$

$$-\mu(2\zeta^2 - k_2^2)\{B_1e^{-\beta z}+ B_2e^{\beta z}\} \qquad (3.29)$$

Equations (3.22), (3.23), (3.28) and (3.29) can be combined in matrix form as:

where $$\{\bar{U}\} = [X] \{A\} \qquad (3.30)$$

$$\{\bar{U}\}^T = \lfloor \bar{u} \quad \bar{w} \quad \bar{\tau}_{zz} \quad \bar{\tau}_{zx} \rfloor$$

$$\{A\}^T = \lfloor A_1 \quad B_1 \quad A_2 \quad B_2 \rfloor \qquad (3.31)$$

and $[X] =$

$$\begin{bmatrix} i\zeta g & \beta q & i\zeta g^{-1} & -\beta q^{-1} \\ -\alpha g & i\zeta q & \alpha g^{-1} & i\zeta q^{-1} \\ \{2\mu\zeta-(\lambda+2\mu)k_1^2\}g & -2\mu i\zeta\beta q & \{2\mu\zeta^2-(\lambda+2\mu)k_1^2\}g^{-1} & 2\mu i\zeta\beta q^{-1} \\ -2\mu\alpha i\zeta g & -\mu(2\zeta^2-k_2^2)q & 2\mu i\alpha\zeta g^{-1} & -\mu(2\zeta^2-k_2^2)q^{-1} \end{bmatrix} \qquad (3.32)$$

where $g = e^{-\alpha z}$, $q = e^{-\beta z}$ (3.33)

We now introduce the surface stress boundary conditions. The "smooth" contact means that the surface shear stress $\tau_{zx} = 0$. The uniform harmonic stress acting on the strip $= (P/2a)e^{i\omega t}$, and for convenience the $e^{i\omega t}$ term will be assumed but not written.

Clearly $$\tau_{zz} = \begin{cases} -P/2a & |x| < a \\ 0 & |x| > a \end{cases} \qquad (3.34)$$

Equation (3.34) transforms to:

$$\left.\begin{aligned} \bar{\tau}_{zz} &= -\frac{P}{2\pi}\,\frac{\sin\zeta a}{\zeta a} \\ \text{also}\quad \bar{\tau}_{zx} &= 0 \end{aligned}\right\} \qquad (3.35)$$

Now, for the half-space ground structure, only waves travelling in the positive z direction are permissible, so

$$A_2 = B_2 = 0$$

Evaluating eq. (3.30) at z=0 and applying the boundary condition eq. (3.35)

$$\{\bar{U}\}_{z=0} = [X]_{z=0} \begin{bmatrix} A_1 \\ B_1 \\ 0 \\ 0 \end{bmatrix} \qquad (3.36)$$

Therefore

$$\begin{bmatrix} \bar{u} \\ \bar{w} \end{bmatrix}_{z=0} = \begin{bmatrix} i\zeta & \beta \\ -\alpha & i\zeta \end{bmatrix} \begin{bmatrix} A_1 \\ B_1 \end{bmatrix} \qquad (3.37)$$

and

$$\begin{bmatrix} \bar{\tau}_{zz} \\ \bar{\tau}_{zx} \end{bmatrix}_{z=0} = \begin{bmatrix} 2\mu\zeta-(\lambda+2\mu)k_1^2 & -2\mu i\zeta\beta \\ -2\mu\alpha i\zeta & -\mu(2\zeta^2-k_2^2) \end{bmatrix} \begin{bmatrix} A_1 \\ B_1 \end{bmatrix}$$

$$= \begin{bmatrix} \frac{-P}{2\pi} \cdot \frac{\sin\zeta a}{\zeta a} \\ 0 \end{bmatrix} \qquad (3.38)$$

Using eq. (3.38) to replace $\begin{bmatrix} A_1 \\ B_1 \end{bmatrix}$ in eq. (3.37):

$$\begin{bmatrix} \bar{u} \\ \bar{w} \end{bmatrix} = \begin{bmatrix} i\zeta & \beta \\ -\alpha & i\zeta \end{bmatrix} \begin{bmatrix} 2\mu\zeta-(\lambda+2\mu)k_1^2 & -2\mu i\zeta\beta \\ -2\mu\alpha i\zeta & -\mu(2\zeta^2-k_2^2) \end{bmatrix}^{-1} \begin{bmatrix} \frac{-P\sin\zeta a}{2\pi\zeta a} \\ 0 \end{bmatrix} \qquad (3.39)$$

Equation (3.39) can be written as:

$$\begin{bmatrix} \bar{u} \\ \bar{w} \end{bmatrix}_{z=0} = [X_{11}]\ [X_{21}]^{-1} \begin{bmatrix} -\frac{P\sin\zeta a}{2\pi\zeta a} \\ 0 \end{bmatrix} \qquad (3.40)$$

This expression for $\bar{u}$ and $\bar{w}$ must be inverse-transformed, to give the surface displacements u and w.

3.3 The non-dimensionalising of parameters

Nearly all the results in this work are designed to be easily interpreted for the "Clarborough" test site (see Section 2.4), but many are in fact non-dimensionalised. The method of non-dimensionalising the results is explained here.

The solution $w(x,z)$ (or $u(x,z)$) is a function of nine variables, and so we have

$$g(w,x,z,a,\rho,E,P,\omega,\eta,\nu) = 0 \qquad (3.41)$$

where all the parameters are as defined previously. Dimensionally,

$$[w] = [x] = [z] = [a] = [L]; \quad [\rho] = [M][L]^{-3}$$
$$[E] = [M][L]^{-1}[T]^{-2}; \quad [\omega] = [T]^{-1}; \quad [P] = [M][T]^{-2} \qquad (3.42)$$

The force P has the dimensions given because it is a force per unit length along the strip. For the three-dimensional model used in Chapter 9, $[P] = [M][L][T]^{-2}$. For the "bedrock" and "elastic foundation" models discussed later, a layer depth 'h' is required and $[h] = [L]$. η and ν are dimensionless. With a few exceptions, ν will have the value 0.257.

If E, a and ρ are used to non-dimensionalise the other parameters, we find

$$g\left[\frac{w}{a}, \frac{x}{a}, \frac{z}{a}, \frac{P}{Ea}, \frac{\omega^2\rho a^2}{E}, \eta, \nu\right] = 0 \qquad (3.43)$$

The term $\frac{\omega^2\rho a^2}{E} = \Omega^2$ can be considered the non-dimensionalised (frequency)^2. In the wavenumber domain, parameters will non-dimensionalise by multiplying by 'a', e.g. (ak_1), $(a\zeta)$, $(a\bar{u})$.

The wavespeed c_2, for example, is non-dimensionalised by dividing by $(a\omega)$, so that

$$\frac{c_2^2}{a^2\omega^2} = \frac{E}{2(1+\nu)\rho a^2\omega^2} \qquad (3.44)$$

3.4 Results

The numerical quadrature routine used to inverse transform equation (3.40) is described in Appendix A. An example of the computer programs used, written in Fortran and called HSWM4F, is listed in Appendix B. A note explaining the program, and the programming alterations necessary to produce all the results given, precedes the listing.

The material properties measured at Clarborough and given in Table 2.2 have been used, with an imaginary part added to each elastic modulus dependent on η, for example $E(1 + i\eta)$, as explained in Section 2.2. With a few exceptions, the loss factor used is $\eta = 0.1$. The load P has magnitude 2π, in this and all subsequent Chapters except Chapters 8 and 9. For some of the results in these Chapters P has magnitude either π or 1.

The compression and shear wavespeeds are given in terms of the complex elastic moduli by equation (3.7). If c_1^* and c_2^* are the compression and shear wavespeeds in an undamped medium, then the relationships between c_1, c_2, c_1^*, c_2^* and η are:

$$c_1 = c_1^*(1 + i\eta)^{1/2}, \quad c_2 = c_2^*(1 + i\eta)^{1/2} \qquad (3.45)$$

c_1 and c_2 will always be used to denote the complex wavespeeds.

Figures 3.4, 3.5, 3.6, 3.7 and 3.10 are non-dimensionalised as explained in Section 3.3. Figures 3.2 and 3.3 show the variation of $|\bar{w}|$ and $|\bar{u}|$ in the wavenumber (ζ) domain, for the five frequencies 4, 8, 16, 32 and 64 Hz. To exaggerate the features of these curves, a low loss factor, $\eta = 0.002$, and a log scale for the amplitude of $\bar{w}$ and $\bar{u}$ have been used.

Figures 3.4 and 3.5 show the non-dimensionalised vertical and horizontal amplitude components of motion respectively, plotted against non-dimensionalised distance, for the six non-dimensionalised

frequencies $\Omega^2 = \omega^2\rho a^2/E = 0.002$, 0.008, 0.033, 0.131, 0.295 and 0.524. These values, with $a = 0.75$ m, correspond to the following frequencies at Clarborough: 4, 8, 16, 32, 48 and 64 Hz respectively. This value of the strip half-width, a, means that the $x/a = 33^1/_3$ range plotted is equivalent to 25 m at Clarborough.

Figures 3.6 and 3.7 show the phase change with non-dimensionalised distance for vertical and horizontal motion respectively, for the non-dimensionalised frequencies $\Omega^2 = 0.002$, 0.033 and 0.524. Consideration of more frequencies in these figures would have resulted in a confusing number of lines, and would not have provided any significant extra information. The apparent discontinuity in phase at $\pm\pi$ is a plotting convenience, to restrict the graphs to convenient bounds. In reality, the phase change is continuous. Failure of the curves to touch lines through $\pm\pi$ is because of an inadequate number of data points.

Figures 3.8 and 3.9 show the attenuation of the amplitude of vertical motion, on a dB log scale, over the first 75 m at Clarborough (equivalent to $x/a = 100$), for the six frequencies considered previously, and for the loss factors $\eta = 0.1$ and $\eta = 0.02$ respectively.

Figure 3.10 shows the effect on the amplitude of vertical motion at the centre of the load, of varying the strip width, with a constant force/unit width. Four non-dimensionalised frequencies are considered: $\Omega^2 = 3.2 \times 10^{-5}$, 0.131, 0.524 and 1.279, which are equivalent to 0.5, 32, 64 and 100 Hz at Clarborough.

3.5 Discussion

Figures 3.2 and 3.3 show the variation of $\bar{w}$ and $\bar{u}$ in the wavenumber domain, for various frequencies and a loss factor $\eta = 0.002$. The main features of all six graphs shown are a major and a minor peak in otherwise smooth curves. The log scale also reveals an inflection on the 'left side' of the major peak. Calculation of the wavenumber of the Rayleigh, shear and compression waves in the

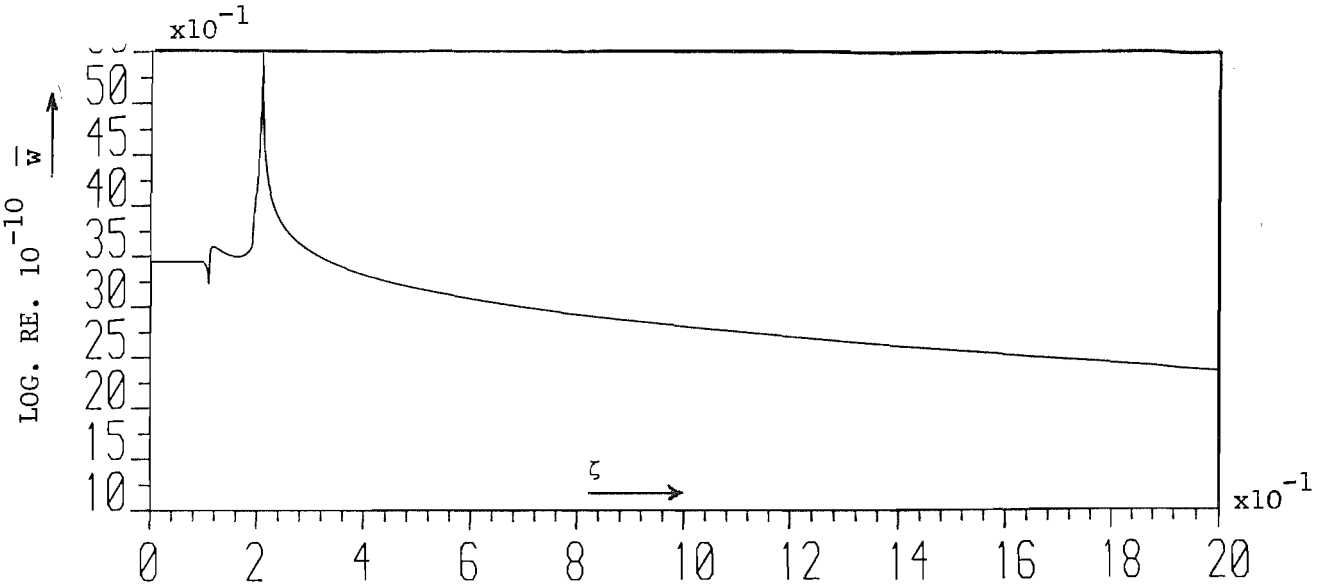

Fig 3.2(a): Frequency = 8 Hz

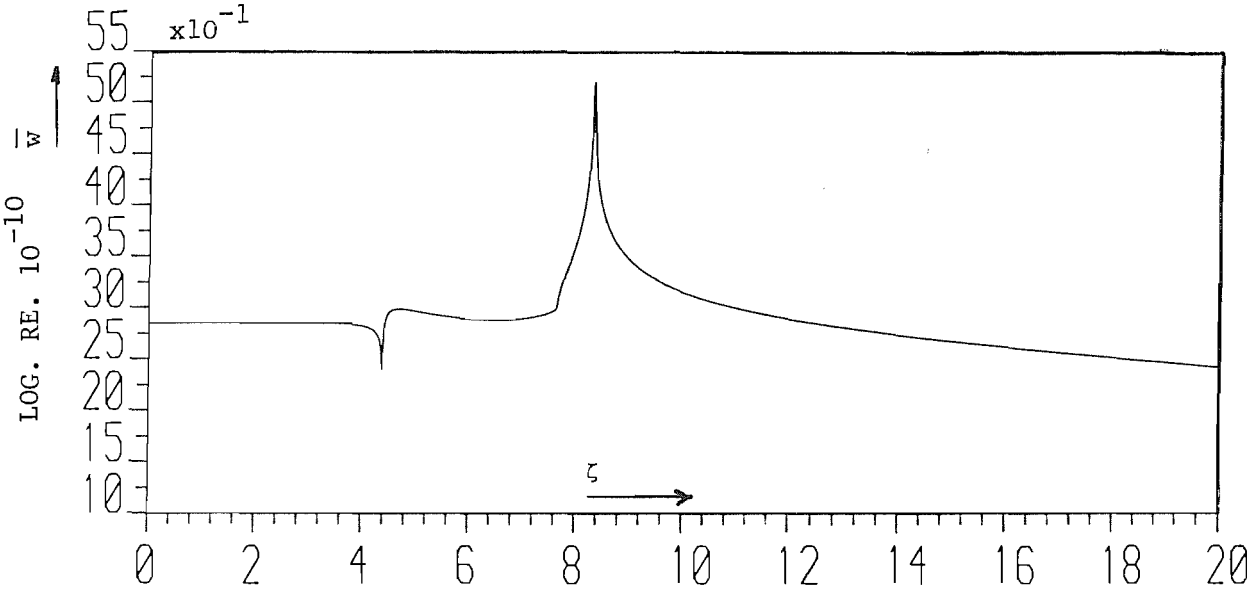

Fig 3.2(b): Frequency = 32 Hz

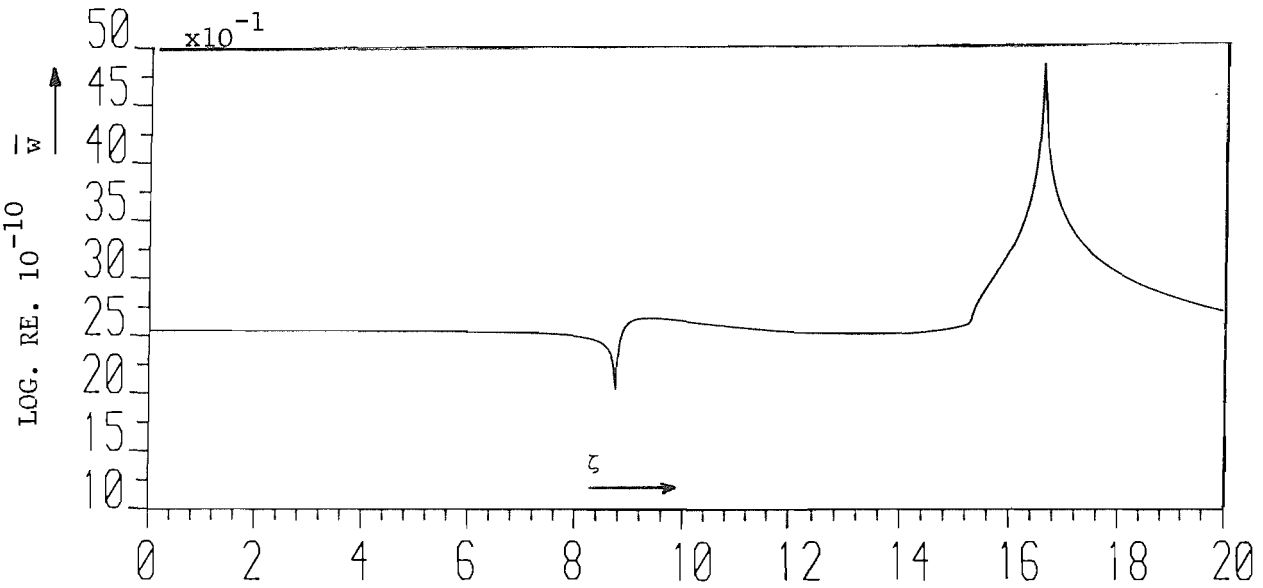

Fig 3.2(c): Frequency = 64 Hz

Fig 3.2 Transformed Vertical Motion, Half-Space Model, $\eta = 0.002$

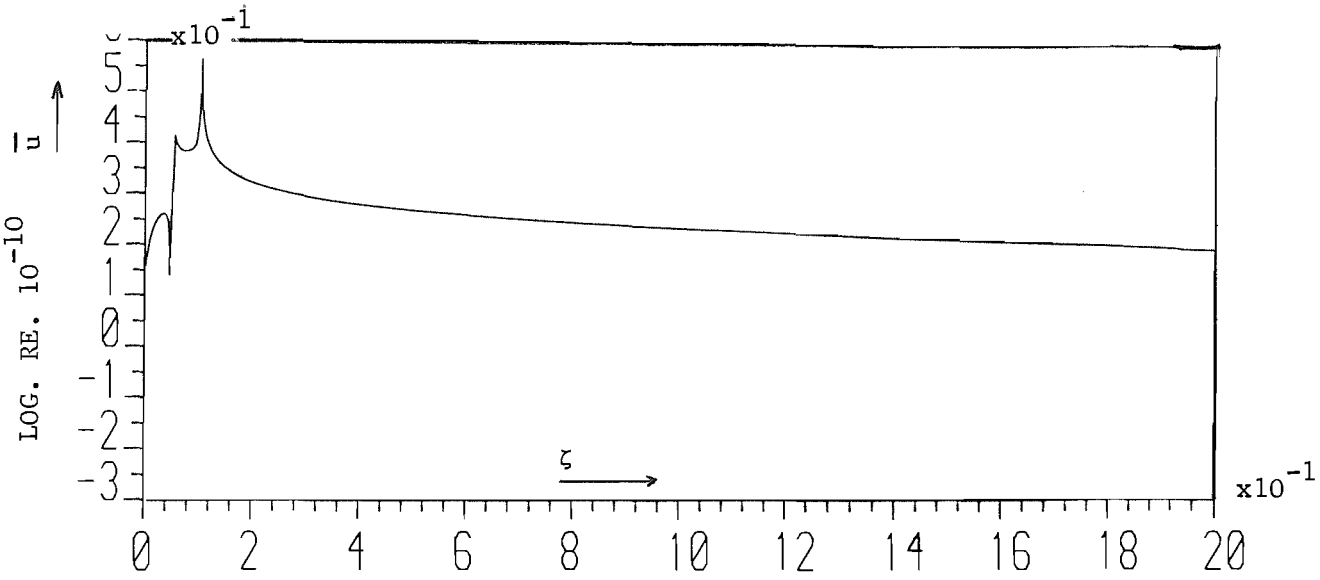

Fig 3.3(a): Frequency = 4 Hz

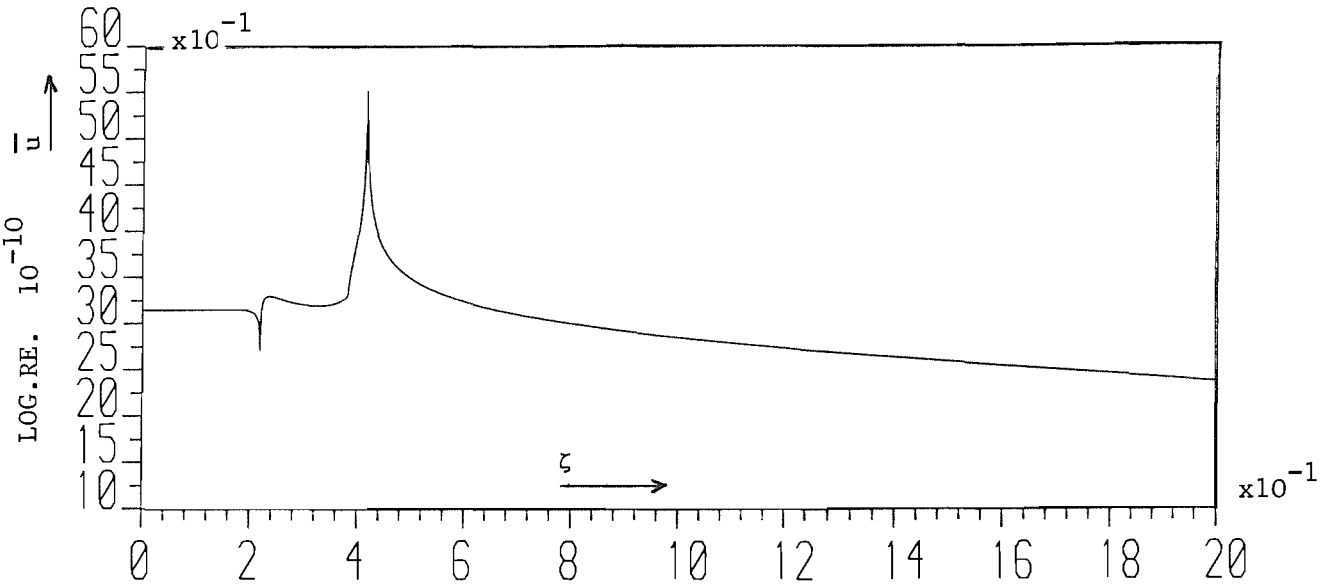

Fig 3.3(b): Frequency = 16 Hz

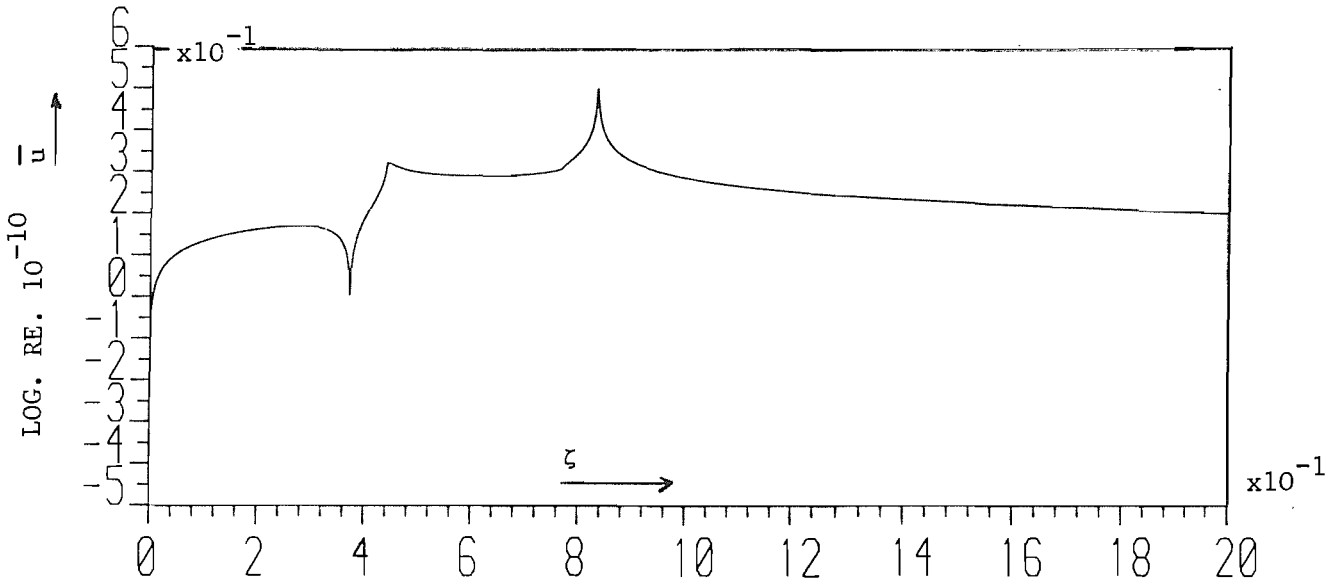

Fig 3.3(c): Frequency = 32 Hz

Fig 3.3: Transformed Horizontal Motion, Half-Space Model, $\eta = 0.002$

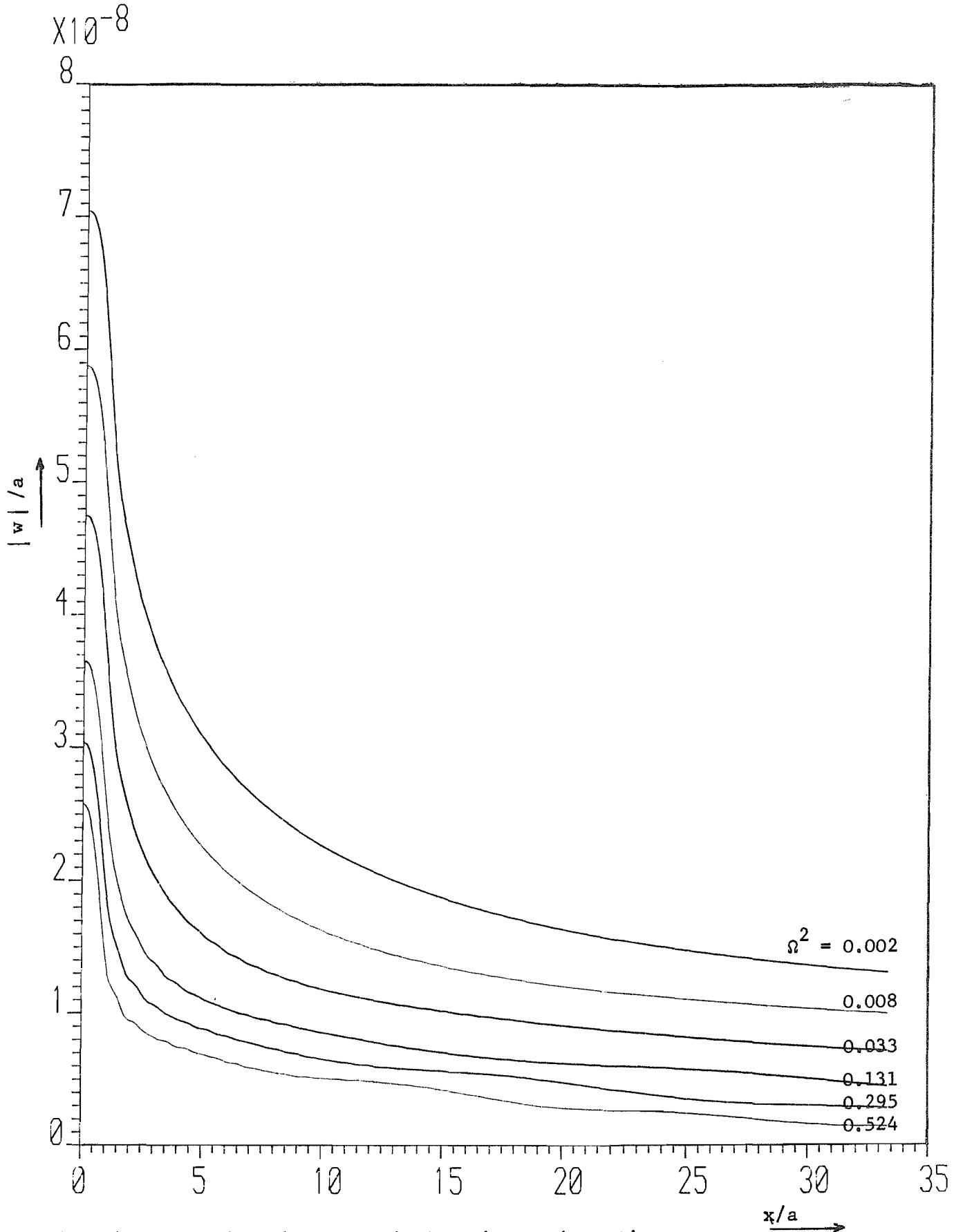

Fig 3.4: Non- Dimensional Vertical Motion Against Distance For Ω^2 = 0.002, 0.008, 0.033, 0.131, 0.295 and 0.524

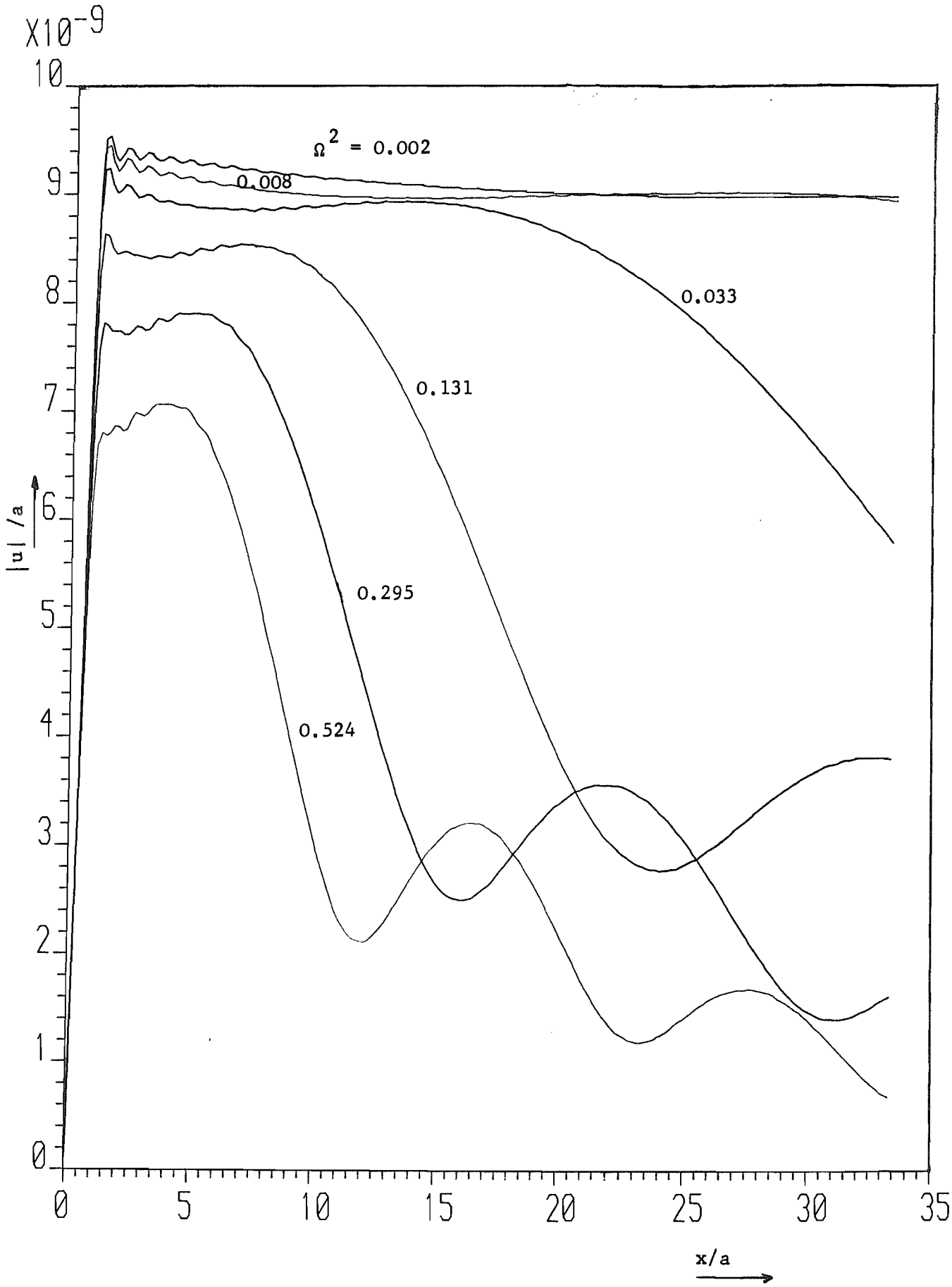

Fig 3.5: Non-Dimensional Horizontal Motion Against Distance For Ω^2 = 0.002, 0.008, 0.033, 0.131, 0.295 and 0.524

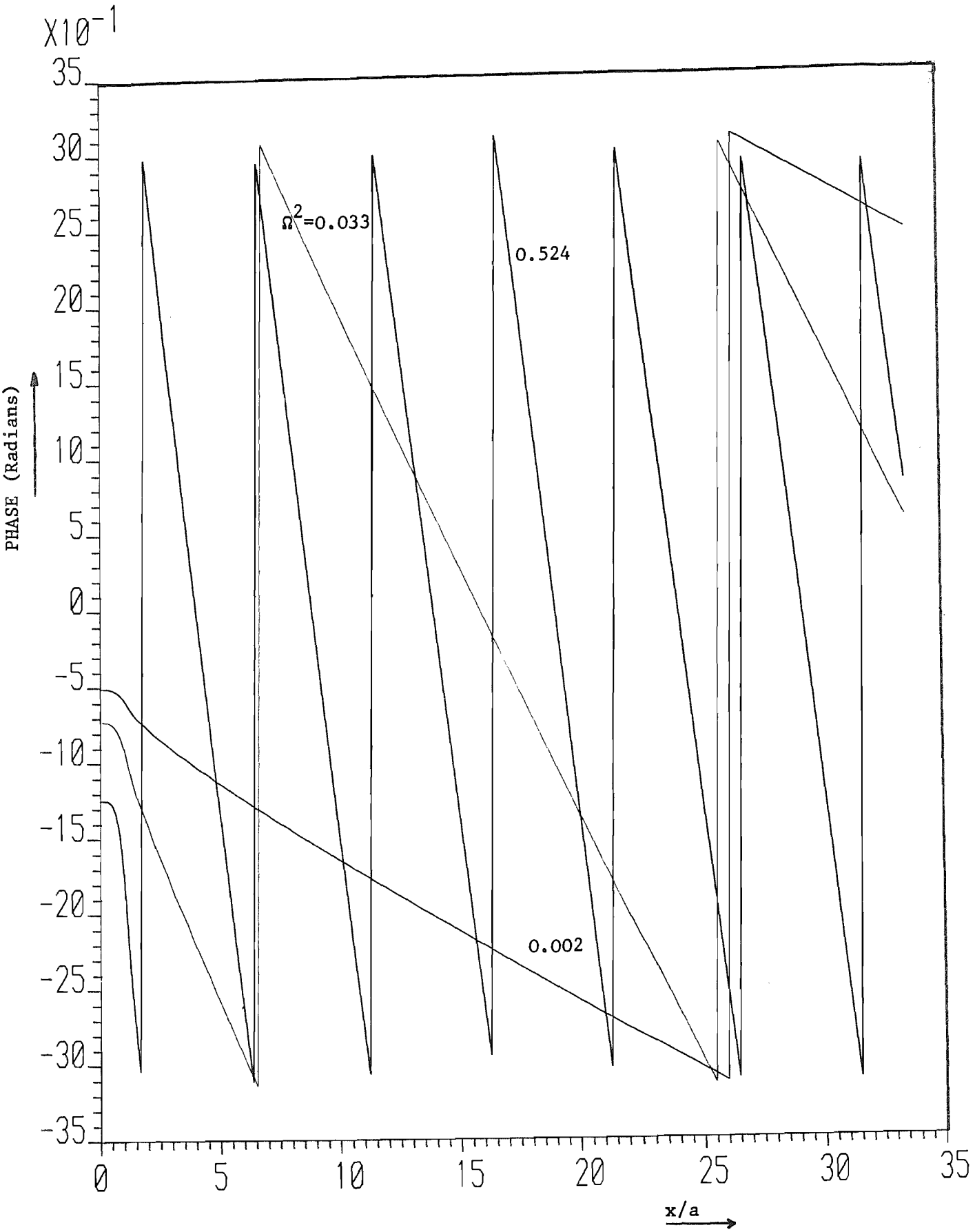

Fig 3.6: Phase Change Against Distance, Vertical Motion For Ω^2 = 0.002, 0.033 and 0.524

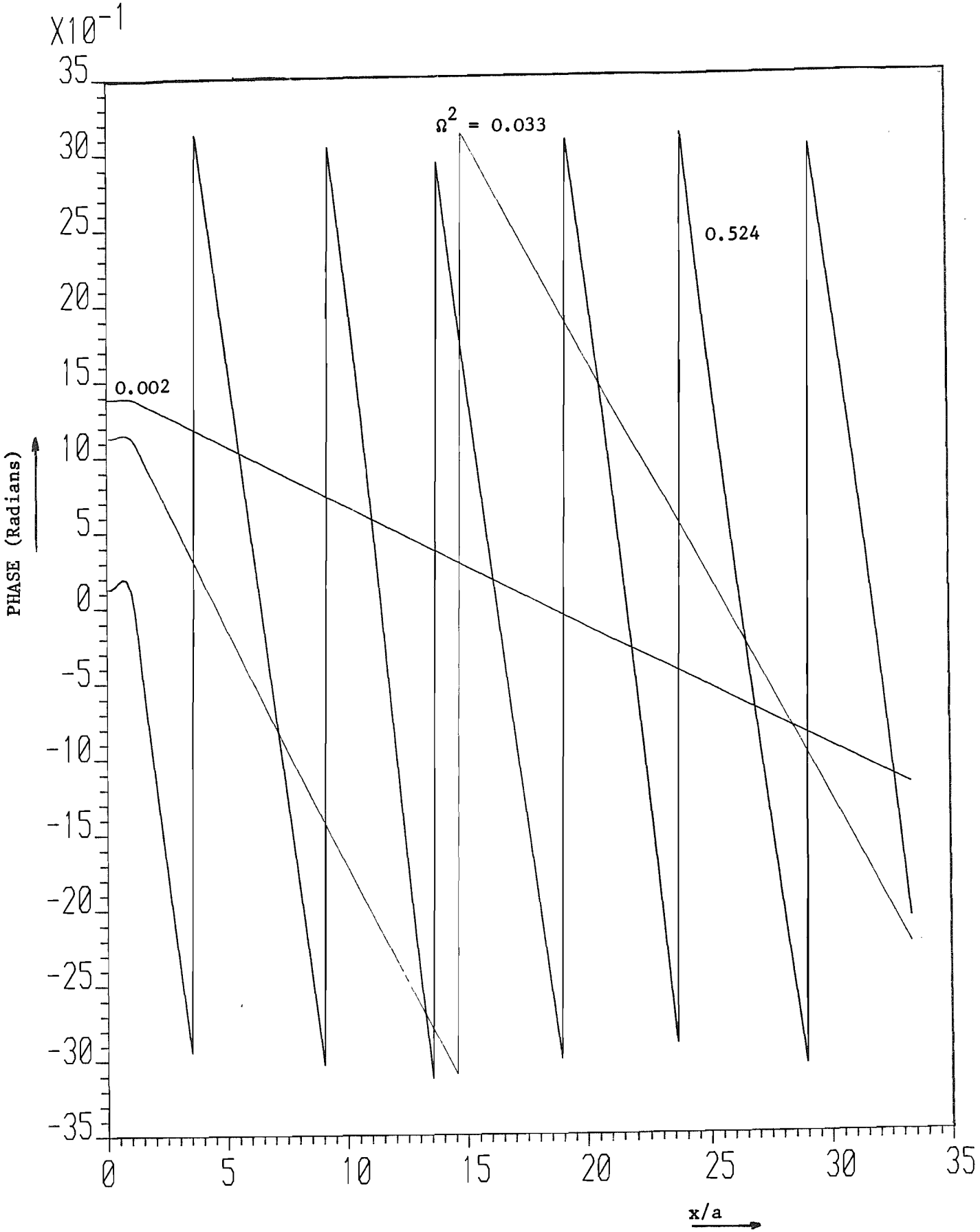

Fig 3.7: Phase Change Against Distance, Horizontal Motion, For Ω^2 = 0.002, 0.033 and 0.524

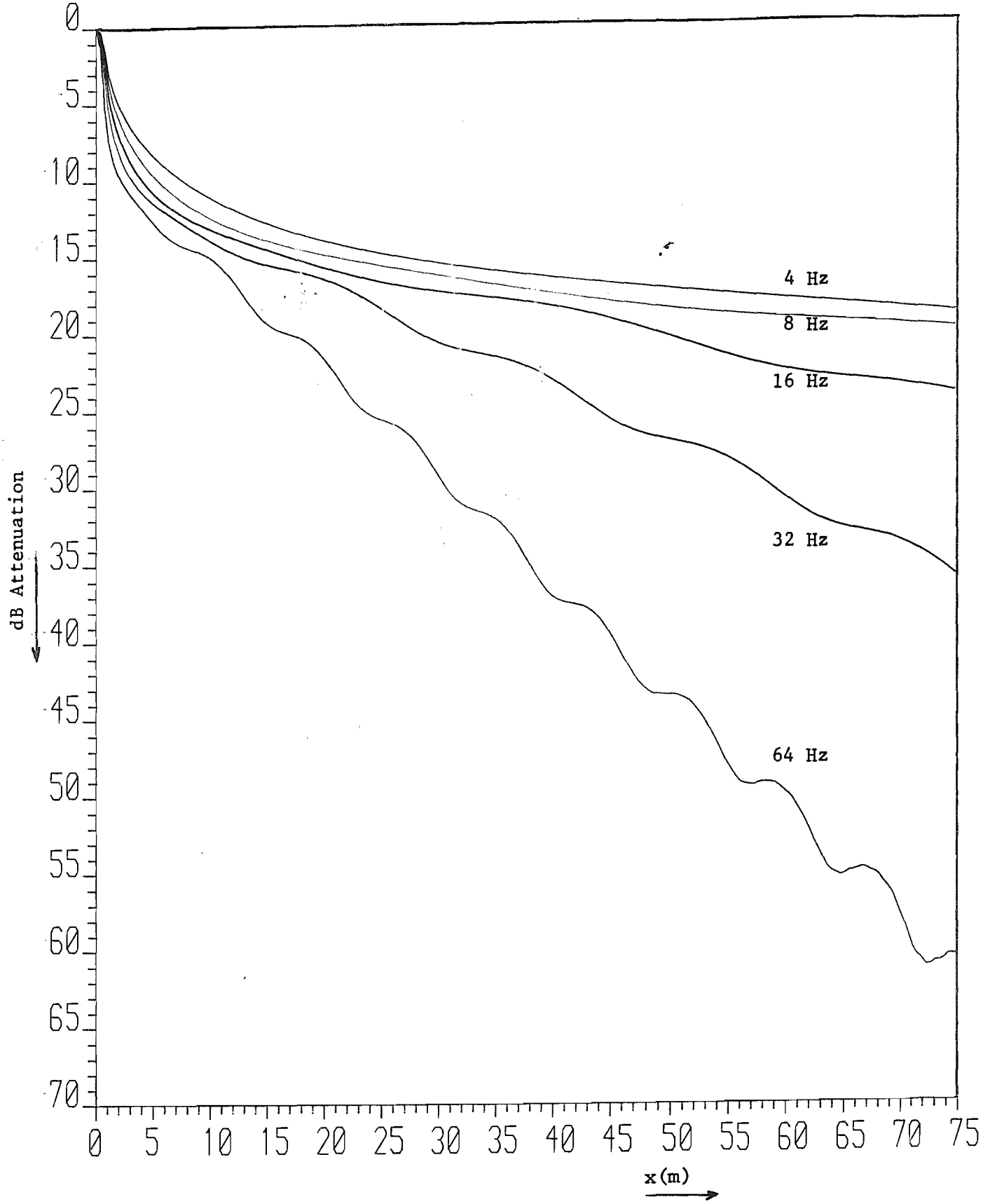

Fig 3.8: Attenuation of Vertical Motion For x < 75m And $\eta = 0.1$, For Five Frequencies.

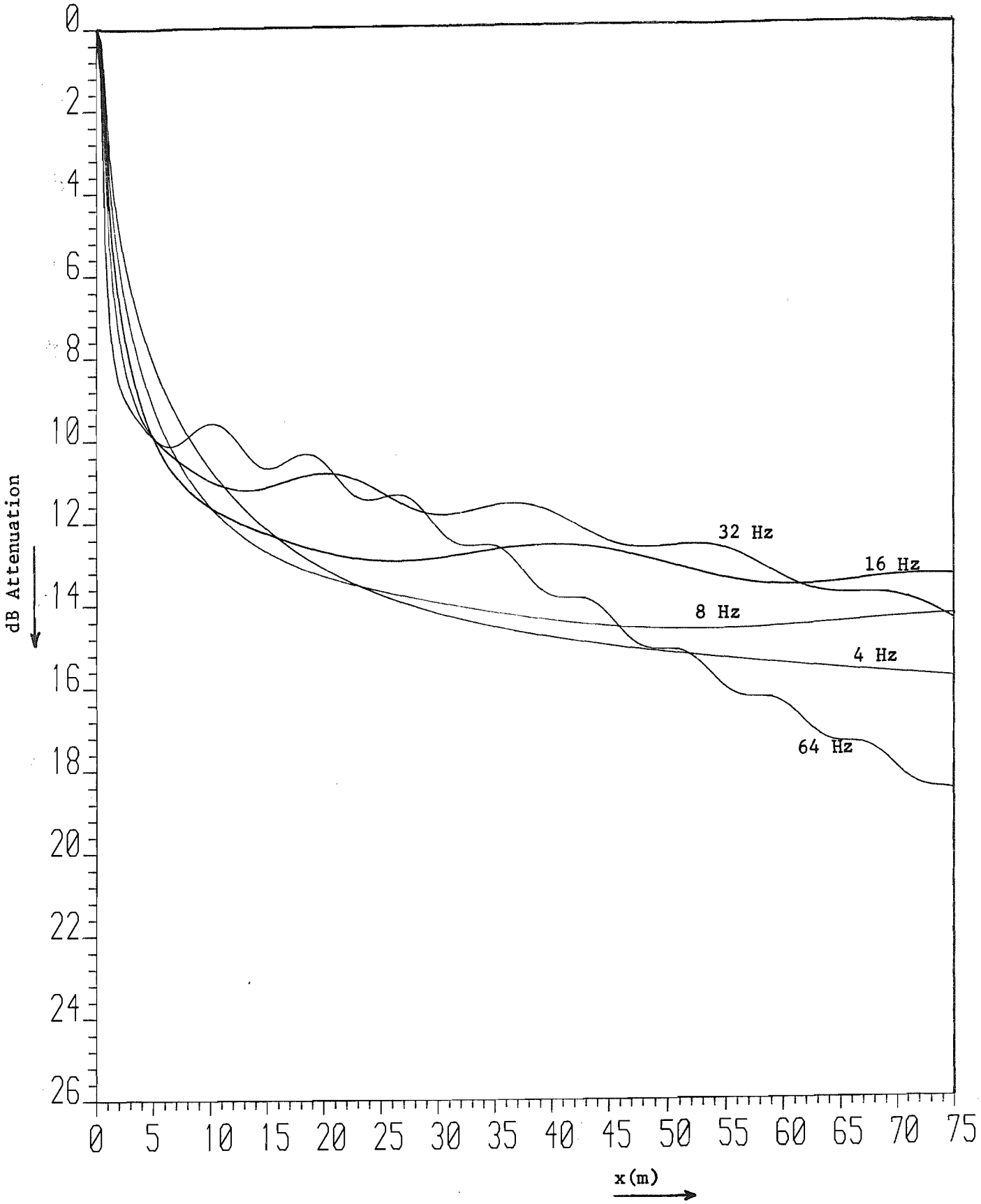

Fig 3.9: Attenuation Of Vertical Motion For x < 75m And η = 0.02, For Five Frequencies.

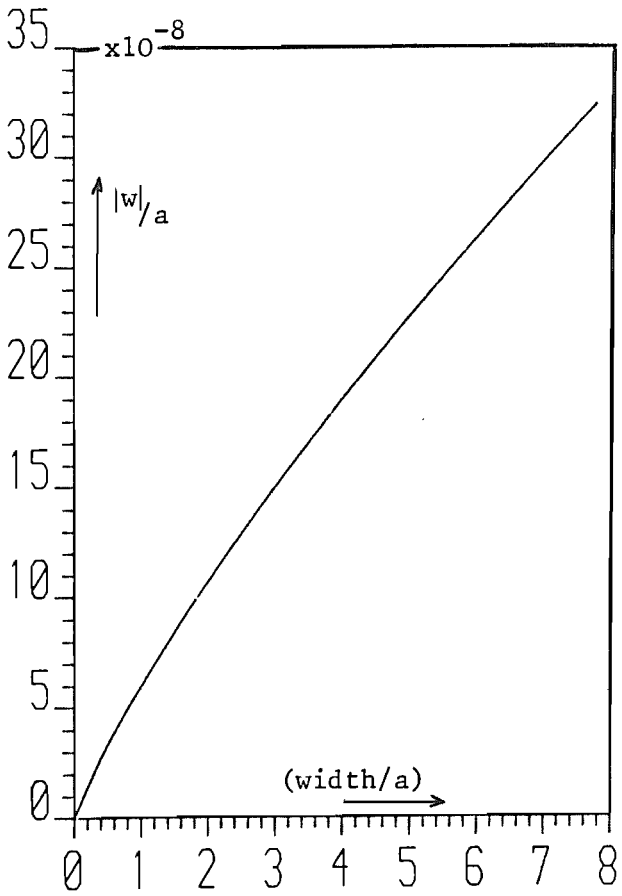

Fig 3.10(a): Frequency = 0.5Hz

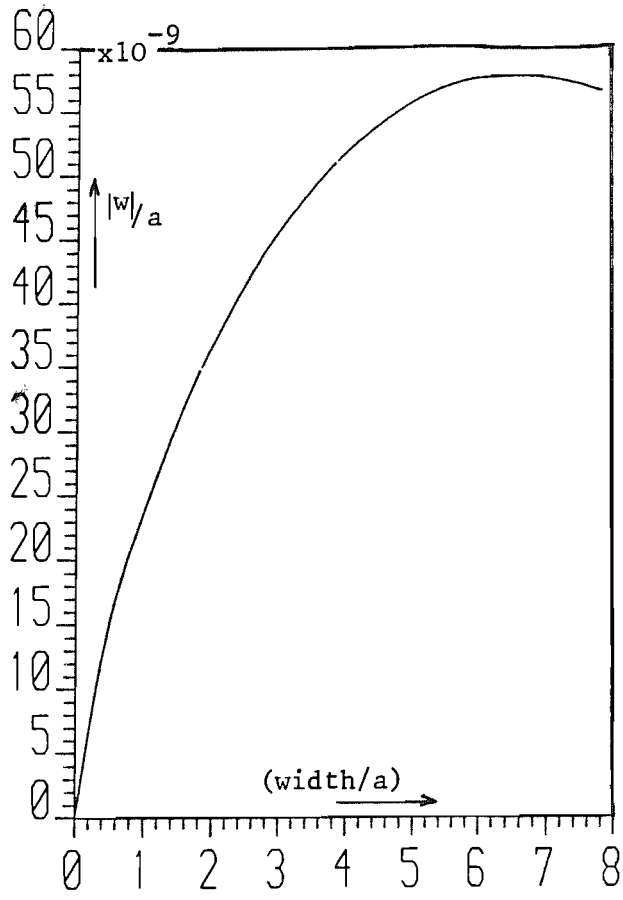

Fig 3.10(b): Frequency = 32Hz

Fig 3.10: Effect On Displacement At The Centre Of The Load Of Varying Load Width, With Constant Load / Unit Width; η = 0.02

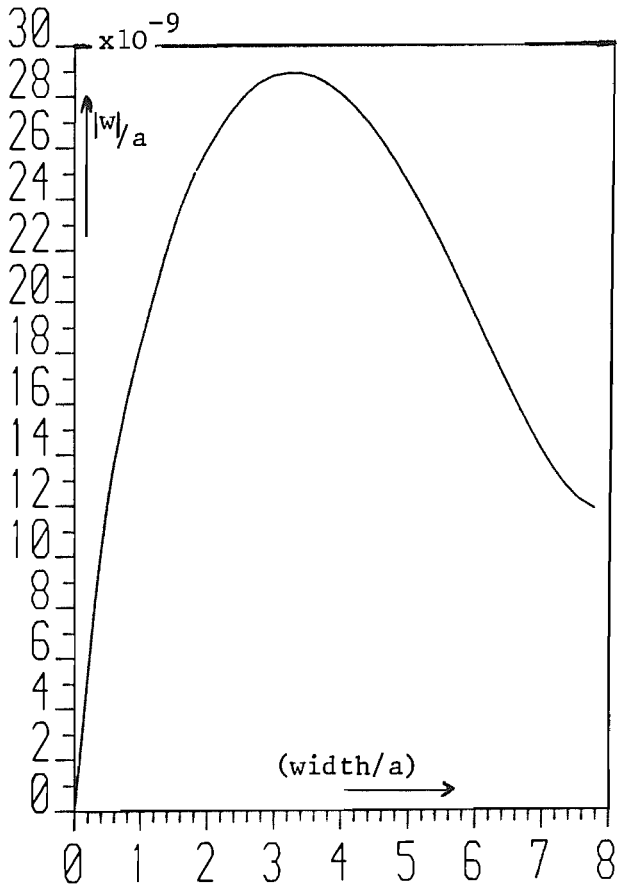

Fig 3.10(c): Frequency = 64 Hz

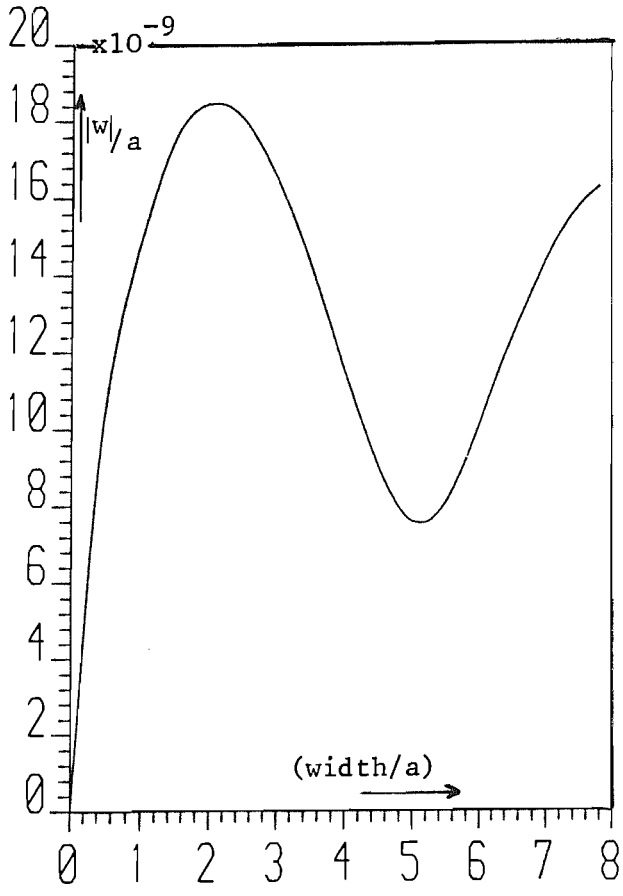

Fig 3.10(d): Frequency = 100Hz

equivalent perfectly elastic (no damping) solid, reveals that at each frequency shown, these wavenumbers match respectively the major peak, inflection and minor peak. Table 3.1 clarifies this for the vertical component $\bar{w}$, by giving the wavenumbers of the two peaks. k_1, k_2 and k_R are the wavenumbers of the compression, shear and Rayleigh waves respectively, with no damping.

Freq. (Hz)	k_1 (η=0)	k_2 (η=0)	k_R (η=0)	Wavenumber domain location of $\bar{w}$ peaks (η = 0.1)		
				Minor peak (modulus)	Major peak (Real part)	(Imag. part)
4	0.055	0.096	0.104	0.057	0.110	0.105
8	0.109	0.191	0.208	0.115	0.220	0.209
16	0.219	0.383	0.416	0.227	0.437	0.416
32	0.437	0.765	0.831	0.455	0.873	0.831
48	0.657	1.148	1.247	-	-	-
64	0.876	1.531	1.662	0.907	1.742	1.660

Table 3.1: Relevant wavenumbers with and without damping

The 48 Hz information is included in Table 3.1 for later reference. The k_1, k_2 and k_R values were found using:

$$k_i = \omega/c_i \qquad (3.46)$$

where the Rayleigh wavespeed was calculated as described by equation (4.14). The locations of the wavenumber domain peaks have been found from turning points in discrete data, and so the very close but not exact agreement between the imaginary part of the major peak wavenumber and the Rayleigh wavenumber k_R, is to be expected. The real and imaginary parts of this peak have been tabulated, to show the effect of damping, which for the Table is larger than for Figs. 3.2 and 3.3 to emphasise the effect. In fact, $\eta = 0.1$ is the value used for most subsequent figures. Allowing for the damping effect, the wavenumber of $|\bar{w}|$ at the minor peak is very close to k_1, and comparing the k_2 values with Figure 3.2, these values are clearly close to the inflections in each major peak.

The locations of the $\bar{u}$ major peaks are very similar to those of $\bar{w}$, except that the real and imaginary parts are reversed. This is because of the 90^{o} phase difference between the vertical and horizontal motion, which can be seen in Figures 3.6 and 3.7, and is a consequence of the form of equation (3.39). For zero damping, the peaks are at the same wavenumbers.

Figures 3.4 to 3.7 give the amplitude and phase change with distance of vertical and horizontal motion. It can be shown with this information, that the motion of a particle on the surface is anti-clockwise, and elliptical, becoming more circular with distance from the load (with local exceptions to this rule, particularly at higher frequencies, because of the "wavyness" of the variation of amplitude, as shown in Figures 3.4 and 3.5). The greater propagation of the lower frequencies is very clear, and is partly caused by the tendency towards an infinite static solution (see Chapter 8 for a consideration of this feature of the infinite strip solution). The oscillation in the graphs of Figures 3.4 and particularly 3.5, is connected to the "extraneous" roots of the Rayleigh equation, and is discussed in Chapter 9.

The horizontal motion is zero at the centre of the load (Fig. 3.5), as required by symmetry, and so the effect of the load edge at $x/a = 1$ is more pronounced than for the vertical motion. The reason for the 'crinkles' in each curve of Figure 3.5 near the load edge is not known; because it is not frequency dependent it is probably not due to interference between the Rayleigh and body waves.

The changes of phase shown in Figures 3.6 and 3.7 show the domination of the Rayleigh wave, which is clarified in the following table, in which λ_1, λ_2 and λ_R refer to the compression, shear and Rayleigh waves respectively, calculated from

$$\lambda_i = \frac{2\pi}{k_i} \qquad (3.47)$$

Non-dimensional Frequency Ω^2	Non-dimensionalised Wavelengths		
	λ_1/a	λ_2/a	λ_R/a
0.002	152.3	87.2	80.5
0.008	76.2	43.6	40.3
0.033	38.1	21.8	20.1
0.131	19.0	10.9	10.1
0.295	12.7	8.1	7.6
0.524	9.5	5.5	5.0
1.279	6.1	3.5	3.2

Table 3.2: Relevant non-dimensionalised wavelengths

Information for $\Omega^2 = 0.295$ and 1.279 (equivalent to 48 and 100 Hz at Clarborough) is included in Table 3.2 for later reference. Each frequency component in Figures 3.6 and 3.7 changes phase by 360° in slightly less distance than $x/a = \lambda_R/a$, due to the damping present.

Figures 3.8 and 3.9 show the attenuation of vertical motion over a greater distance, for different loss factors, and log scales have been used for the displacement amplitudes. In comparing these two figures, it should be noted that each scale has been chosen to fit the data, and so they are not equal. Also, because each frequency curve shows attenuation relative to the deflection under the load for the same frequency, it does not necessarily follow in Figure 3.9 that the displacements due to higher frequencies will exceed those of lower frequencies - rather, it can only be concluded that the higher frequency components are less attenuated for part of the frequency range. The greater attenuation of higher frequencies due to damping, as discussed in Section 2.2, is clear in Figure 3.8. The change in loss factor from $\eta = 0.1$ to $\eta = 0.02$ has a great effect, and shows that the heavier damping inhibits certain phenomena. The regular wavyness in each curve, the 'wavelength' of which is proportional to frequency, can be seen in every curve of Figure 3.9, where $\eta = 0.02$. This low damping also allows another quite separate interference phenomenon to become evident, due to the different speeds of the three propagating waves. This effect is also discussed in Chapter 9, and is the reason why, for example, the 64 Hz component is the least attenuated in the range $10 \text{ m} < x < 20 \text{ m}$. The form of these attenuation results, with regular ripples and a continuous phase

change, is very similar to the experimental results of the U.S. Army ECOM [14]. However, in Figure 3.8, the extra crinkles in the 64 Hz curve for $x > 55$ m, are due not to interference effects, but lack of accuracy in the numerical integration, as the displacements concerned are very small.

These results suggest that in ground with low damping, the low frequency components cannot necessarily be expected to dominate the response in the near-field.

Figure 3.10 shows that the displacement of the strip load, for a given frequency, is sensitive to the strip width. Apart from Figure 3.10(a), in which the frequency is too low (or alternatively the width variation too small) to reveal a pattern, each curve has a peak at a particular width. Figure 3.10(d) suggests a regular series of peaks and troughs. The change in these peak-displacement widths is inversely proportional to frequency, or proportional to wavelength. It seems logical that a maximum displacement can be expected when the strip half-width equals a quarter wavelength of the propagating wave. On this basis, and consulting Table 3.2, in each case a wavelength about 20% larger than the shear wavelength is predicted. Now, although in the far-field the Rayleigh wave dominates the surface response, because unlike the body waves it does not lose energy into the half-space, this is not true under the load, and so a wavelength greater than the Rayleigh wavelength must be expected. A tentative estimate of the effects of the body and Rayleigh waves can be made with the energy distribution among the waves calculated by Miller and Pursey [57]. Their load acted on a disc, and so the distribution can only approximately apply to the strip. They calculated that the Rayleigh wave carries 67% of the energy from the load, the compression wave 7% and the shear wave 26%. Considering the case $\Omega^2 = 0.524$ listed in Table 3.2 (the other frequencies and wavelengths are directly proportional), the resultant non-dimensional wavelength, λ_m, with no damping, can thus be estimated:

$$\frac{\lambda_m}{a} = \frac{(67 \times 5.0) + (26 \times 5.5) + (7 \times 9.5)}{100} \qquad (3.48)$$

$$\therefore \quad \frac{\lambda_m}{a} = 5.45. \qquad (3.49)$$

The peak in Figure 3.10(c) predicts a wavelength near $\lambda/a = 6.4$, somewhat longer than 5.45. However, apart from the approximate nature of the calculation above, an alternative solution for the division of energy among the propagating waves, mentioned by the O.R.E. [28], gives less prominence to the Rayleigh waves. This would clearly result in a predicted wavelength longer than $\lambda_m/a = 5.45$.

CHAPTER 4

FREE VIBRATION IN AN ELASTIC LAYER OVER A RIGID BEDROCK

4.1 Introduction

In this and the next Chapter, the ground is modelled as an homogeneous, isotropic elastic layer over an inflexible half-space. This will for convenience be described as the "bedrock model". In Chapter 5, the forced response in a damped layer is studied, with the load as an infinite strip. The problem is therefore plane. In this Chapter, the free vibration in an undamped layer is considered. Because the purpose of the work in this Chapter is to explain certain features of the forced response results, a plane formulation will be used here too.

Some previous workers have studied free vibration for the bedrock model. The formulation of the problem used by Waas [79] is used here. He provides, along with most other workers, a simple method of predicting the natural frequencies of the layer for zero wavenumber (see Section 4.4). Waas also shows that the axisymmetric problem has an identical solution to the plane problem. Tolstoy and Usdin [77] use the "interference principle" of ray theory, to derive the period equations (which give the wavenumbers of the natural frequencies) for several ground structures. The "interference principle" is based on the equality of amplitude at a given depth of each of the compression and shear waves, which is the requirement for unattenuated propagation; zero internal damping is clearly a prerequisite. Their treatment of an elastic layer over a flexible half-space is considered in Chapter 6. They show that the bedrock model period equation tends to the well-known Rayleigh equation (equation (9.53)), as the layer depth tends to infinity. Like Kuhlemeyer [43], who also uses the interference principle, they give dispersion curves (that is, the variation of wavenumber or wavespeed with frequency) of the first two propagation modes in the layer. The relevance of their solutions to this work is discussed in Section 4.4.

Kobori *et al* [39] study the bedrock model free vibration as part of their work on the forced response with a rectangular load. They give dispersion curves, and note interesting features which are in common with

the results presented here. These are discussed in Section 4.4. Also working in three dimensions, Kausel and Roesset [36] give the three dimensional dynamic stiffness matrix for the layer (which relates the displacements in the layer to the stresses), while Girardi [24] has calculated the dispersion curves for the torsional motion of a disc.

* * * * * * *

In Chapter 5, the exact dynamic stiffness matrix for the bedrock model is derived. The dynamic stiffness matrix for several sub-layers is assembled in the usual way, with overlapping matrices for each layer, so that the stresses at the sub-layer interfaces other than the top and bottom of the layer cancel (see equation (5.26)). Because of the zero displacement boundary condition at the bottom of the layer, which allows the bottom two rows of the stiffness matrix to be neglected, and so excludes the unknown interface stresses, the free vibration (which requires zero surface stresses) natural frequencies are determined by equating the determinant of the assembled dynamic stiffness matrix to zero. However, this multi-layered determinant contains transcendental terms, which make the eigenvalue solution very difficult. This problem is overcome by following the work of Waas, who obtains a discrete solution. If the bedrock layer is divided into sufficient sub-layers, the variation of the displacements $u(x,z)$ and $w(x,z)$ in the z-direction can be approximated as linear. Waas performs the necessary "virtual work" analysis to derive the resulting approximate linear dynamic stiffness matrix. This can be expressed as a quadratic equation in wavenumber ζ (see equation (4.1)), in which the coefficients of the equation, for a single sub-layer, are 4×4 symmetric matrices. In the absence of damping, these are real matrices. In this form, the matrix is amenable to solution, and the method used is described in Section 4.2.

The solution "eigenfrequencies" of the matrix are the natural frequencies of free plane waves, which propagate along the layer. The eigenvectors give the variation of displacement, as a function of z, of each natural plane wave. This is analogous to stiffness matrix solutions of structural problems, and so the natural plane waves, which

can propagate at different discrete natural frequencies, are the natural "modes" of the system. The eigenvectors therefore give the "mode shapes".

The results obtained from this linear solution are described in Section 4.3, and discussed in Section 4.4.

4.2 Eigenvalue Solution of the Linear Dynamic Stiffness Matrix

The linearised dynamic stiffness matrix was introduced in the last section. For this approximation to be accurate, the height of the sub-layers must be small compared to the wavelengths of interest. For a single sub-layer, Waas [79] gives the linearised free vibration problem in the following form:

$$\{A\zeta^2 + B\zeta + G - \omega^2 M\}[D_m] = 0 \qquad (4.1)$$

where $[D_m]$ is the vector of displacements at the top and bottom of the m'th layer, so that

$$[D_m] = [U_m,\ W_m,\ U_{m+1},\ W_{m+1}]^T \qquad (4.2)$$

and

$$A = \frac{h_m}{6}\begin{bmatrix} 2(\lambda+2\mu) & 0 & (\lambda+2\mu) & 0 \\ 0 & 2\mu & 0 & \mu \\ (\lambda+2\mu) & 0 & 2(\lambda+2\mu) & 0 \\ 0 & \mu & 0 & 2\mu \end{bmatrix} \qquad (4.3)$$

$$B = \frac{1}{2}\begin{bmatrix} 0 & (\lambda-\mu) & 0 & -(\lambda+\mu) \\ (\lambda-\mu) & 0 & (\lambda+\mu) & 0 \\ 0 & (\lambda+\mu) & 0 & -(\lambda-\mu) \\ -(\lambda+\mu) & 0 & -(\lambda-\mu) & 0 \end{bmatrix} \qquad (4.4)$$

$$G = \frac{1}{h_m}\begin{bmatrix} \mu & 0 & -\mu & 0 \\ 0 & (\lambda + 2\mu) & 0 & -(\lambda + 2\mu) \\ -\mu & 0 & \mu & 0 \\ 0 & -(\lambda + 2\mu) & 0 & (\lambda + 2\mu) \end{bmatrix} \qquad (4.5)$$

$$M = \frac{\rho h_m}{6}\begin{bmatrix} 2 & 0 & 1 & 0 \\ 0 & 2 & 0 & 1 \\ 1 & 0 & 2 & 0 \\ 0 & 1 & 0 & 2 \end{bmatrix} \qquad (4.6)$$

where h_m is the height of the sub-layer; in this work, all the sub-layers will have equal height, so that h_m will equal the layer depth divided by the total number of sub-layers. The other parameters in equations (4.1) to (4.6) are as before.

Equation (4.1) can be regarded as a linear equation for ω^2, by solving for chosen real values of ζ. This will be called the "linear eigenvalue solution", and because ζ is chosen real, will only give solution modes which propagate unattenuated. This is clear from the form of the displacement functions:

$$u = u(z)e^{i(\omega t - \zeta x)}; \qquad w = w(z)e^{i(\omega t - \zeta x)} \qquad (4.7)$$

More generally, a frequency can be chosen, and a "quadratic eigenvalue solution" sought, which will allow ζ to be real, imaginary or complex.

The linear eigenvalue solution is straightforward, and is achieved with a computer program described briefly in Section 4.3, which uses a NAG library routine. The quadratic eigenvalue solution involves some manipulation of equation (4.1), using a method described by Wilkinson and Reinsch [85]. This involves reducing equation (4.1) to a linear form, given by:

$$\{[C] - \zeta[I]\}\{y\} = 0 \qquad (4.8)$$

where

$$[C] = \begin{bmatrix} 0 & I \\ B_0 & B_1 \end{bmatrix}, \quad B_0 = -A^{-1}(G - \omega^2 m), \quad B_1 = -A^{-1}B \qquad (4.9)$$

and

$$\{y\} = \begin{Bmatrix} D_m \\ \zeta D_m \end{Bmatrix} \qquad (4.10)$$

[I] is the identity matrix, and the matrices A,B, G and M are the same as in equation (4.1). Equation (4.8) can be solved using standard techniques. This is peformed by another computer program, which is briefly described in Section 4.3, and uses more NAG library routines.

Of course, the linear approximation requires many sub-layers, and for N layers a dynamic stiffness matrix of order 2N is assembled from the (4 × 4) matrices A, B, G and M, such that the component matrices overlap (equation (5.26) shows the matrix structure). This means that matrix [C] in equation (4.9) will be of order 4N. Apart from the accuracy requirement, using many layers has the added advantage of giving smooth mode shapes, as these are given by the solution eigenvectors.

4.3 Results

The solution of the linear eigenvalue problem mentioned in Section 4.2, was found with a Fortran program using the NAG library routine F02ADF, which uses Householder Reduction and the QL algorithm to solve an equation of the form

$$Ax = \lambda' Bx \qquad (4.11)$$

where A and B are real symmetric matrices, and λ' is the eigenvalue.

The quadratic eigenvalue solution is found with the Fortran program ZFINDW, which is listed with notes in Appendix B. This program uses the NAG library routines F04ACF and F02AGF. The former finds the inverse of a real, square, symmetric, banded matrix. The latter finds the eigenvectors and eigenvalues of a matrix. Program ZFINDW could be

adapted to also give the linear eigenvalue solution, which is a subset of the quadratic solution.

For the frequency range of interest, below 64 Hz, a linear dynamic stiffness matrix composed from 25 sub-layers (giving a matrix of order 50), was found to give adequate accuracy. Because the accuracy is dependent on the sub-layer height being much less than the wavelengths of interest, a fixed number of layers will result in a progressively less accurate approximation as the frequency increases. The wavelength of a wave, λ_i, is related to its wavespeed c_i by:

$$\lambda_i = c_i/f \qquad (4.12)$$

where f is the frequency in Hz.

In general the accuracy can be checked by comparing with solutions obtained using more layers, but for the case $\zeta = 0$, the exact solution is known. The discrete frequencies at which $\zeta = 0$ for the propagating modes are given by the natural frequencies of a one-dimensional rod, which has the same height as the layer, and the same "fixed-free" boundary conditions. This is explained in Section 4.4, but the numerical results for $\zeta = 0$ are tabulated here in Table 4.1, with the exact values given for a comparison. Only the six solutions which exist for frequencies less than 70 Hz are given. The material properties of Clarborough (see Table 2.2) have been used. All the results in this Chapter are dimensionalised for Clarborough, which gives the following undamped wavespeeds:

$$c_1 = 459.43 \text{ ms}^{-1}; \quad c_2 = 262.74 \text{ ms}^{-1}; \quad c_R = 241.98 \text{ ms}^{-1} \qquad (4.13)$$

c_1 and c_2 are defined algebraically in equation (3.7), and c_R is given by the approximate relation (see [26])

$$c_R/c_2 = (0.87 + 1.12\nu)/(1 + \nu) \qquad (4.14)$$

WFIND50 Results using 25 sub-layers for $\zeta = 0$ Frequency (Hz)	$f_m = \frac{(2m-1)}{4}\frac{c_2}{h}$ (Hz)	$f_n = \frac{(2n-1)}{4}\frac{c_1}{h}$ (Hz)
9.385	9.384 (m = 1)	
16.411		16.408 (n = 1)
28.192	28.151 (m = 2)	
47.111	46.918 (m = 3)	
49.298		49.225 (n = 2)
66.216	65.685 (m = 4)	

Table 4.1: Natural frequencies for zero wavenumber for the bedrock model.

The numerical data in Table 4.1 was calculated with a program called WFIND50. This program used 200 points per curve to plot Figures 4.1 and 4.2. These give exactly the same information, but in different forms. Figure 4.1 is in a form amenable to later analysis in Chapter 5, and shows the variation of wavenumber with frequency of the first ten modes. Additionally three lines have been superimposed on Figure 4.1, to show the variation of wavenumber with frequency of the Rayleigh, shear and compression waves (calculated with equation (3.46)). Figure 4.2 is the more usual dispersion curve for the ten modes, showing variation of speed with frequency. For reference, the Rayleigh and body wavespeeds have been marked on the speed axis. The zero wavenumber information is not included in Figure 4.1 as a programming convenience, because this information corresponds to infinite wavespeeds in Figure 4.2. A frequency range much larger than 64 Hz has been used, to show the asymptotic behaviour of the dispersion curves at high frequency.

Features of these Figures are discussed in Section 4.4. It should be noted that although the first and second mode curves in both Figures 4.1 and 4.2 are shown not crossing, this is in fact due to inadequate resolution in the graph-plotting, and these curves should cross, like all the other pairs of curves. This has been confirmed by studying the mode shapes of the type shown in Figures 4.3 and 4.4 at frequencies just above and below the intersection frequency. The continuity of mode shape shows that the dispersion curves do cross.

It can be seen that the fourth mode dispersion curve is double-valued for a small range of frequency. (Note that the "first mode" is considered to be the one which propagates at the lowest wavespeed and so on for the higher order modes.) Its stationary frequency, or 'turning point' is at 44.839 Hz, as calculated numerically. The mode is single-valued above 47.111 Hz (as shown in Table 4.1, this is the numerical solution - the exact value is 46.918 Hz).

The general behaviour of these dispersion curves is dictated by the bedrock model boundary conditions, not by the material properties. Other material properties were used to produce results identical in form; for example, the Checkerhouse test-site material properties were used, which are given in Table 4.2. This produced similar results, but with a lowest frequency for the first mode of 7.09 Hz.

Young's modulus, E ($MN.m^{-2}$)	132.4
Density, ρ ($kg.m^{-3}$)	1780
Poisson's ratio, ν	0.158
Layer depth, h (m)	20

Table 4.2: Checkerhouse test-site material properties

Figure 4.3 was produced with program ZFINDW, and shows the vertical motion component of the mode shapes. Figure 4.4 was produced by a version of the program slightly adapted to give the horizontal motion components. In fact, Figure 4.3 shows the variation of (iw), as the problem was formulated as in Chapter 5 (see equation (5.24)). There is a 90^{o} phase difference between the vertical and horizontal motion.

Four different frequencies have been chosen at which to plot these two figures, which show the general appearance of several modes, and in particular the behaviour of the fourth mode in the range

44.839 Hz ≤ frequency ≤ 47.111 Hz, where it is double-valued. The vertical scales show the depth of the layer. The Clarborough layer is 7 m deep, and so there is no motion at (or beyond) z = 7 m. The horizontal scales are of arbitrary magnitude, since the eigenvalue solutions can only be found to within an arbitrary multiplicative constant.

As mentioned in Section 4.3, the linear eigenvalue solution wavenumbers are a subset of the quadratic eigenvalue solution, which provides a useful check on the results of programs WFIND50 and ZFINDW. The other eigenvectors in the quadratic eigenvalue solution are the wavenumbers of non-propagating modes. These range from large wavenumbers which are purely imaginary, resulting in a rapid decay of amplitude of the modes with distance (this is clear from equation (4.7)), to complex wavenumbers with large real parts and small imaginary parts, which cause the modes to decay slowly with distance. The eigenvectors come in complex conjugate pairs, representing positive- and negative-travelling modes.

4.4 Discussion

When the wavenumber $\zeta = 0$, the solution of equation (4.1) is expressed by

$$|[G] - \omega^2[M]| = 0 \qquad (4.15)$$

From equation (4.7), the displacements in the layer for zero wavenumber are independent of x, and so effectively a one-dimensional standing wave results. Waas [79] hs shown that if the vector of displacement [D] for the whole layer is re-ordered, so that the horizontal and vertical motion components are separate, i.e.,

$$[D] = [U_1, U_2, \ldots, U_m, \ldots, U_n; \; W_1, W_2, \ldots, W_m, \ldots, W_n]^T \qquad (4.16)$$

and if the equivalent changes are made to the dynamic stiffness matrix, the horizontal and vertical motion components for zero wavenumber uncouple:

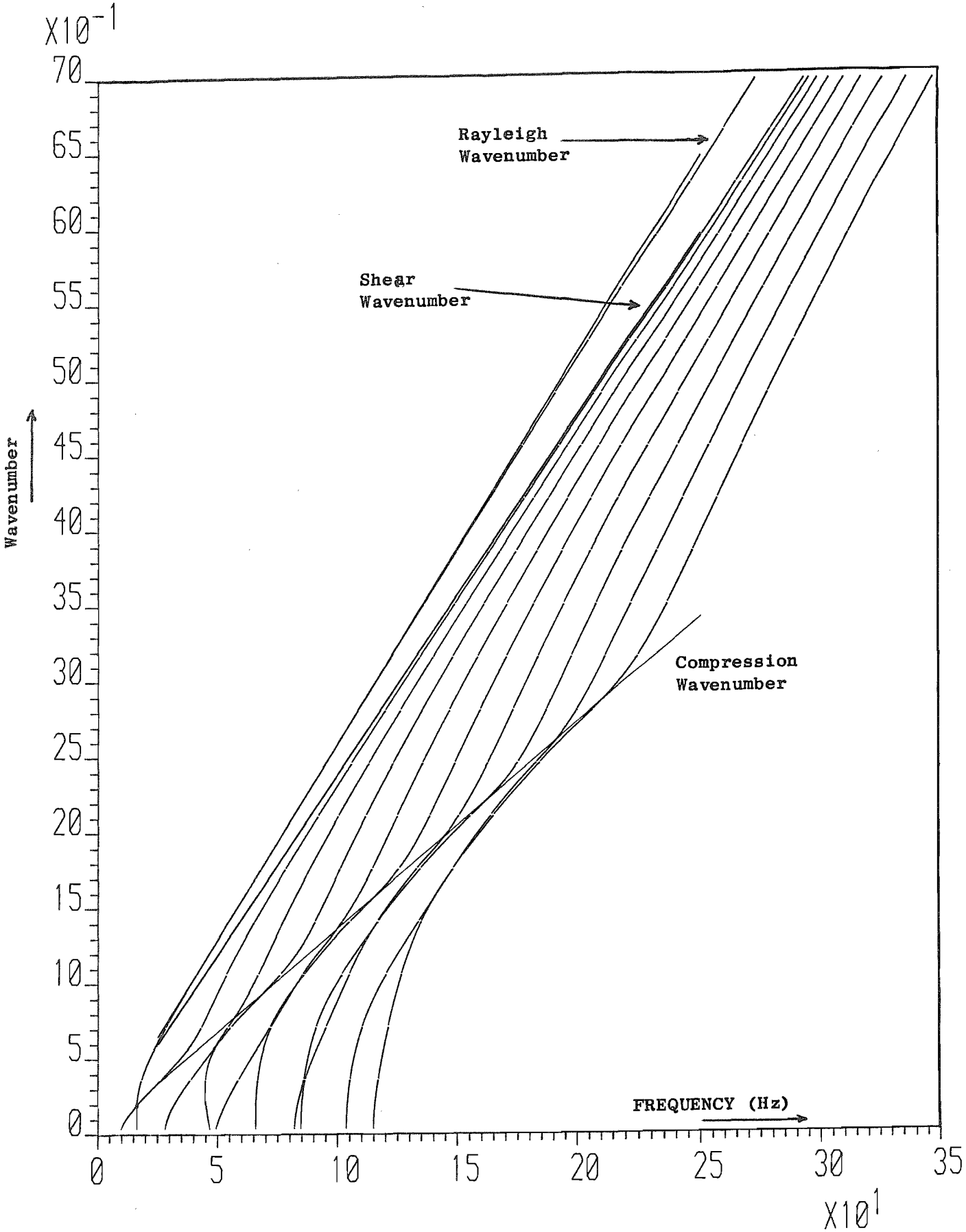

Fig 4.1: Variation Of Wavenumber With Frequency Of First Ten Natural Propagating Modes, Bedrock Model.

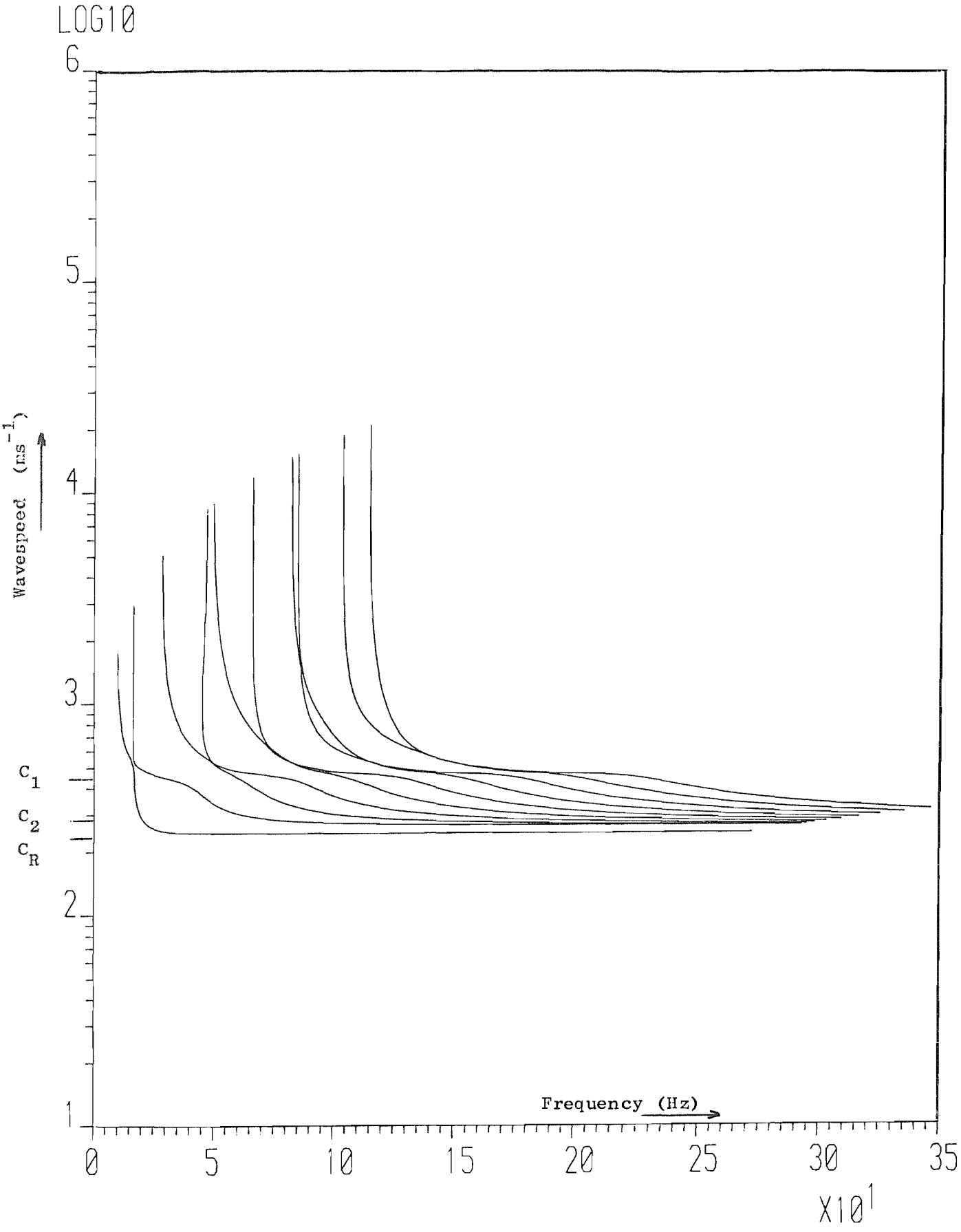

Fig 4.2: Variation Of Wavespeed With Frequency Of First Ten Propagating Modes, Bedrock Model

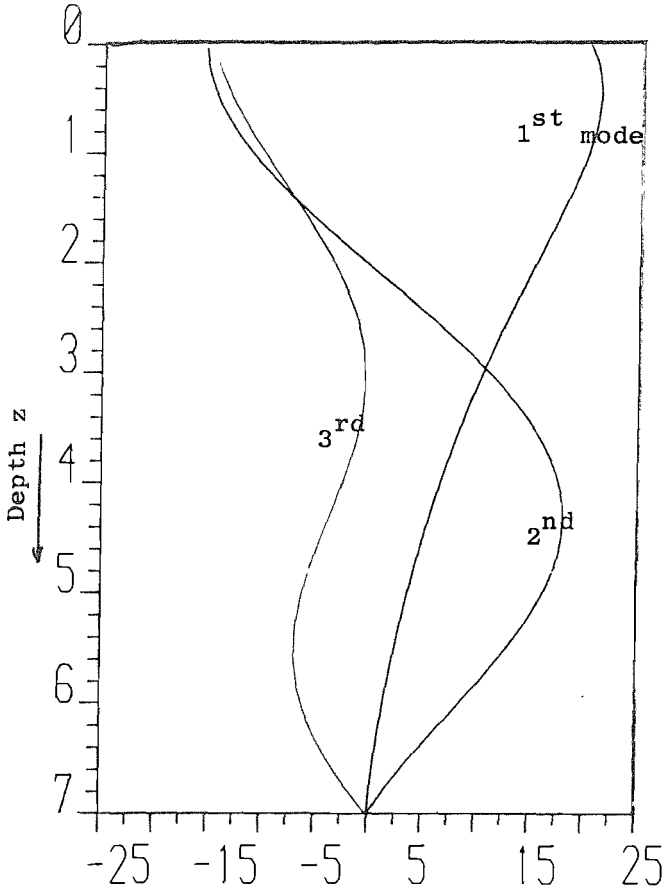

Fig 4.3(a): Frequency = 44.82 Hz

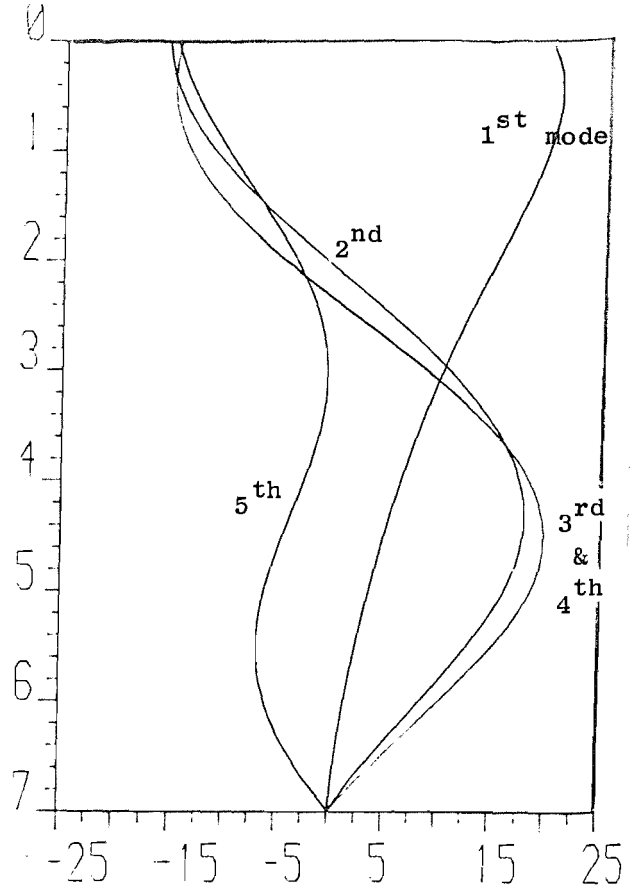

Fig4.3(b): Frequency = 44.839Hz

Fig 4.3: Bedrock Model Natural Mode Shapes, Vertical Motion Components

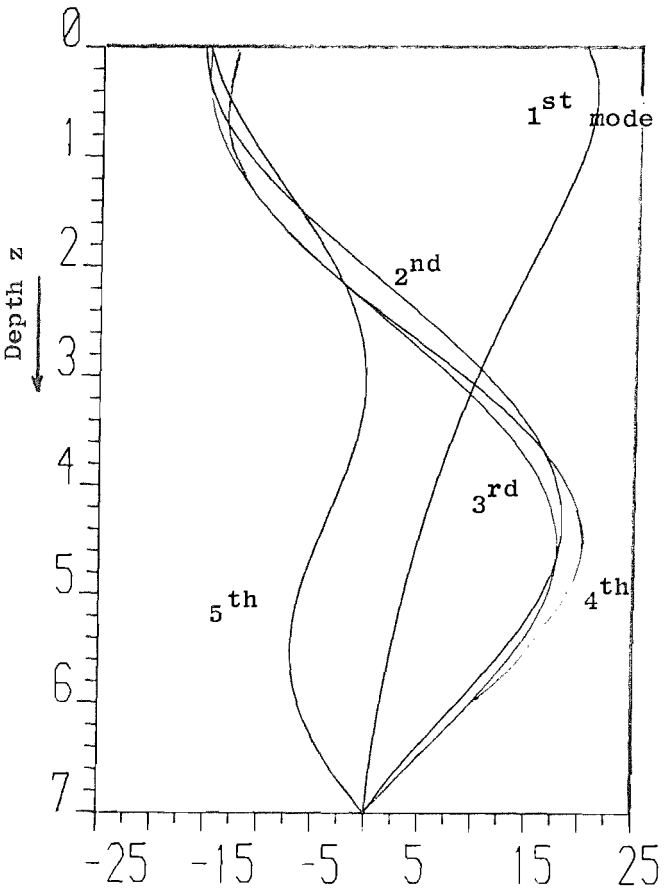

Fig 4.3(c): Frequency = 45.5 Hz

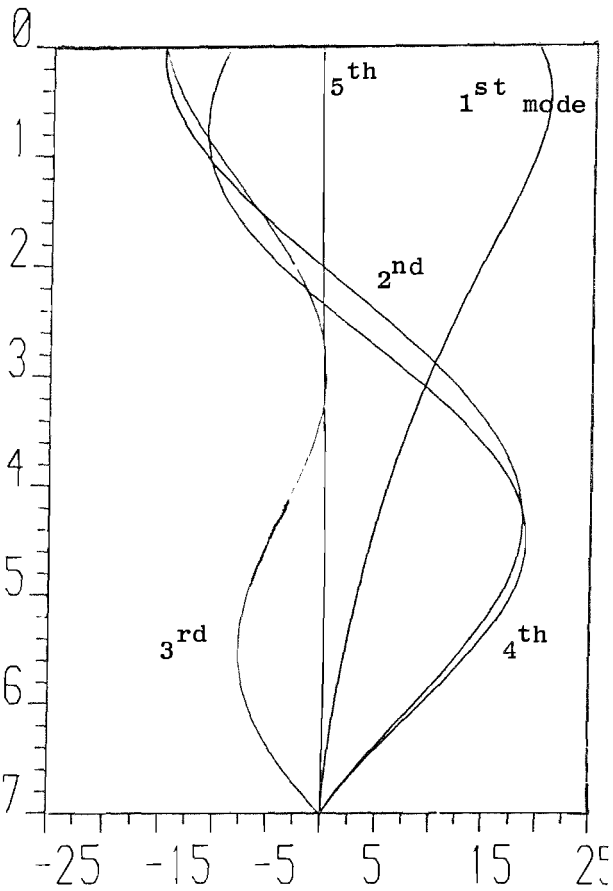

Fig 4.3(d): Frequency = 47.111Hz

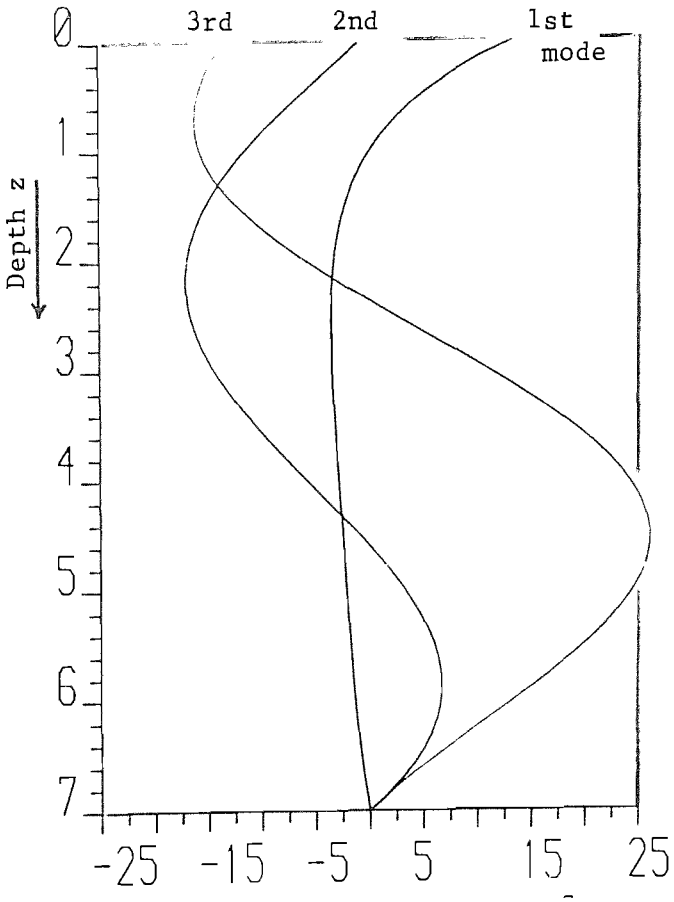

Fig. 4.4(a) Freq. = 44.82 Hz

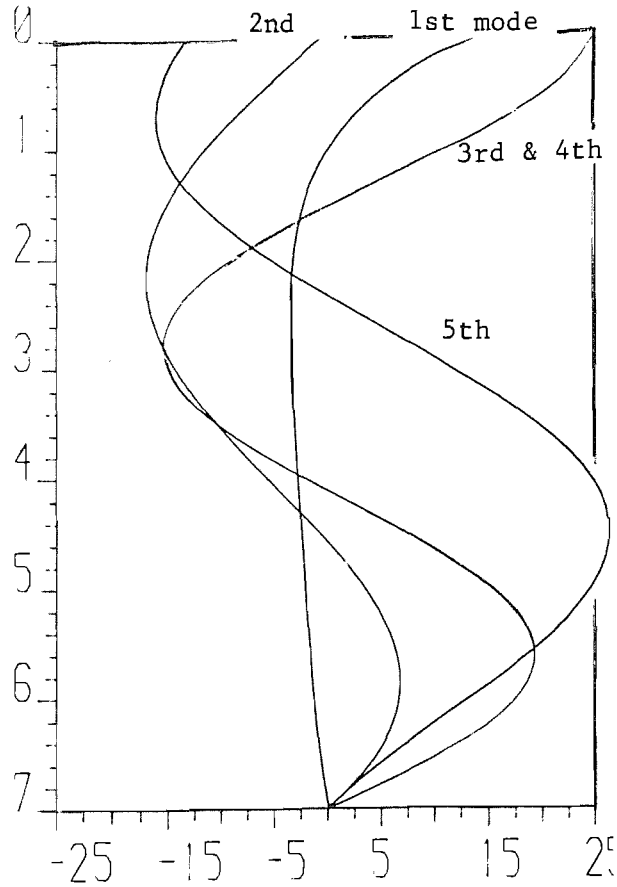

Fig. 4.4(b) Freq. = 44.839 Hz

Fig. 4.4 Bedrock model natural modeshapes, horizontal motion components

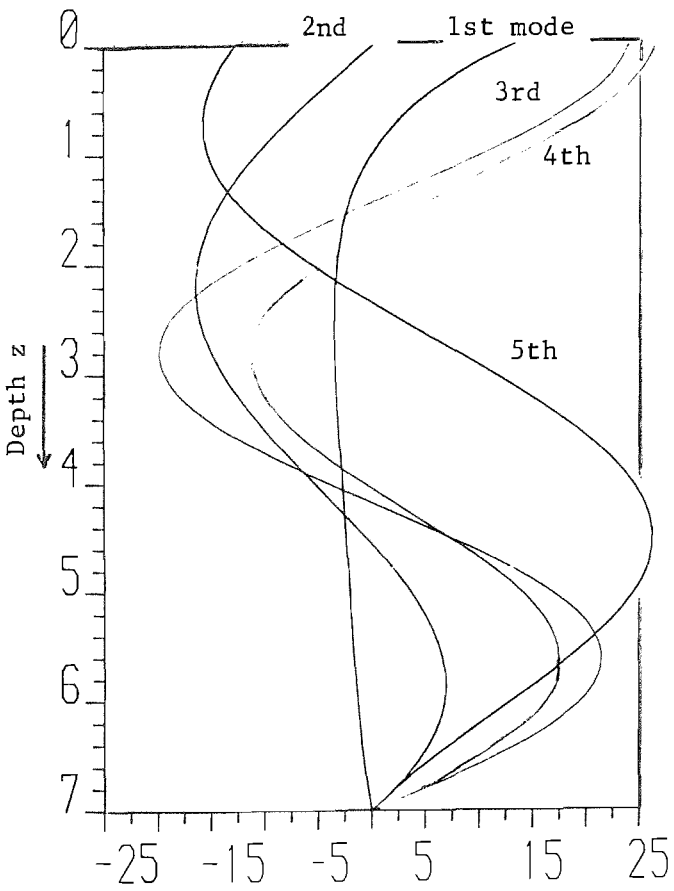

Fig. 4.4(c) Freq. = 45.5 Hz

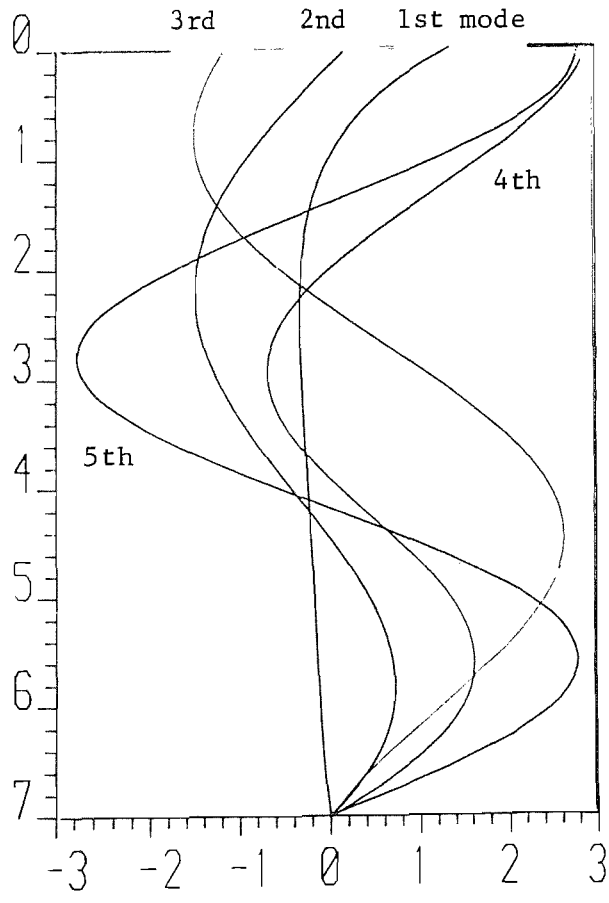

Fig. 4.4(d) Freq. = 47.111 Hz

$$\left[\begin{array}{c|c} C_K & 0 \\ \hline 0 & C_Z \end{array}\right] \left[\begin{array}{c} U_1 \\ \vdots \\ U_n \\ \hline W_1 \\ \vdots \\ W_n \end{array}\right] = 0 \qquad (4.17)$$

Therefore, the $\zeta = 0$ condition results in standing waves which have either just horizontal motion (pure shear waves), or just vertical motion (pure compression waves). The natural frequencies are given by the related one-dimensional "fixed-free" rod natural frequencies, which in terms of the body wavespeeds and height of layer 'h' are:

$$f_n = \frac{(2n-1)}{4} \frac{c_i}{h} , \qquad c_i = c_1 \text{ or } c_2 \qquad (4.18)$$

Equation (4.18) has been used to construct Table 4.1. After those given in the table, the next six frequencies given by equation (4.18) are 82.04, 84.45, 103.22, 114.86, 121.99 and 147.67 Hz. These can be seen to be very close to the $\zeta = 0$ 'roots' of the dispersion curves in Figure 4.1. The slight disparity, which increases with frequency, is due to the lack of accuracy in the numerical solution.

Kobori *et al* [39] have noticed an extra significance of these frequencies. The crossing of two dispersion curves always occurs at one of these frequencies, as can be clearly seen by comparing the twelve frequencies given with either Figure 4.1 or Figure 4.2. Kobori *et al* also mention that for $\nu = 0.25$ the first two modes intersect when their wavespeeds are exactly twice the shear wavespeed. Tolstoy and Usdin [77] also mention this in their earlier work. In this work, $\nu = 0.257$, which is very close to their value, and it is found that the first two modes' dispersion curves intersect very near $2c_2$ (see Figure 4.2). This was checked by finding the wavenumber of the first mode corresponding to the frequency of intersection, 16.41 Hz, and then calculating the wavespeed.

In Chapter 5, it is shown that the intersection of the first two modes, produces a resonance in the forced response at that frequency.

Because this frequency can be easily predicted with equation (4.18), a simple estimate is possible for the resonant frequency of any ground with a layer over a much stiffer bedrock.

Another feature noted by Kobori *et al* is the exceptional behaviour of the fourth mode, in being double-valued for a small range of frequency. The development of this mode through this frequency range is shown in Figures 4.3 and 4.4. At 44.82 Hz, only the first three modes exist (Figures 4.3/4(a)). At 44.839 Hz (Figures 4.3/4(b)), two almost equal modes exist - these are the two manifestations of the 4th mode, called the 4th and '5th' modes in the figures, and the frequency is just above the turning frequency. At 45.5 Hz (Figures 4.3/4(c)), the 4th and 5th modes are quite distinct. Figures 4.3/4(d) show the five modes present at a frequency just below where the fourth mode becomes single-valued. The so-called fifth mode shape in Fig. 4.3/4(d) shows how the mode behaves like a pure shear wave at $\zeta = 0$. The vertical motion component is almost non-existent, and the horizontal motion component is larger than that of any other mode.

Although the various features noted above have been observed and relationships discovered, their causes are not fully understood. These natural modes are the result of a complicated interaction between the shear and compression waves, interfering constructively to produce propagating waves. The compression wavenumber line superimposed on Figure 4.1 shows the effects described all occur for modes travelling faster than the compression wave. The dispersion curves seem to inflect along this line, and then once they represent speeds less than the compression wavespeed, they all asymptote towards the shear wavespeed with increasing frequency. These effects are also clear in Figure 4.2. It seems that although each mode is the result of an interaction between the body waves, at certain frequencies one body wave dominates the other.

The intersections of dispersion curves, and the double-valued behaviour of the fourth mode, are the result of the severe "bedrock model" boundary condition, zero motion at the bottom of the layer. The more realistic "elastic foundation" dispersion curves given in Chapter 6 do not possess these peculiarities. Another effect of the boundary condition is the lack of propagation below 9.38 Hz. The rigid base

inhibits the modes from developing. As a result, the dispersion curves of Figure 4.2 each go to infinity at their minimum frequency. In Figures 4.1 and 4.2, the appearance of the curves for negative wavenumber (representing waves travelling in the opposite direction) will be the reflection in the frequency axis of the curves presented.

Figures 4.1 and 4.2 show that the first mode is distinct from all the others, in that above 30 Hz its wavespeed equals that of the Rayleigh surface wave for the medium. In fact, at sufficiently high frequency, the first mode is indistinguishable from the Rayleigh wave. In Figure 4.1, the deviation of the first mode dispersion curve from the Rayleigh wavenumber line at high frequency is an indication of the degree of inaccuracy in the high frequency results. Figures 4.2 and 4.4 confirm that the vertical and horizontal motion components of the first mode, have the well-known shape of the Rayleigh wave. The vertical component has a maximum at about $2/27\ \lambda_R$ below the surface (this is discussed in relation to the elastic foundation model in Section 6.5.1). Below about 30 Hz, the layer is too shallow to allow a true Rayleigh wave to develop.

CHAPTER 5

INFINITE STRIP LOAD ACTING ON AN ELASTIC LAYER OVER RIGID BEDROCK

5.1 Introduction

The 'bedrock model' was introduced in the last Chapter and its ground structure is shown in Figure 5.1. In this Chapter, the surface vibrations of this model, caused by an infinite strip of harmonically varying pressure are studied. The model has been investigated by a number of previous workers. Warburton [80] looked at the direct receptance of a rigid disc load. He approximated the stress distribution under the load by the static solution. He did not incorporate internal damping, and found the resonant frequencies for which the response is infinite. These frequencies are related to this work in Section 5.4. Waas [79] has used the Finite Element Method to study the direct receptance of a forced rigid strip or disc. He also gives the surface displacement with distance, caused by a rigid disc embedded in an inhomogeneous layer.

Gazetas and Roesset [22] have studied the swaying and rocking direct receptances of an infinite strip, using the Fast Fourier Transform. Kausel and Roesset [36] followed this work by calculating the three-dimensional dynamic stiffness matrix for the layer. Kausel and Peek [38] later applied this matrix to find the vertical direct receptance for a disc load.

Kobori *et al* [39] have produced direct receptance graphs for a rectangular load, and they show how the resonance peaks in these are greatly reduced in amplitude by increased damping. Small and Booker [72] have found the stress distribution through the layer using a flexibility matrix approach, which has the advantage over a stiffness matrix of not becoming infinite for incompressible materials.

Some of the results mentioned above can be compared with the receptance figures given in Chapter 8. However, none of these workers have considered the variation of surface displacement with distance for the bedrock model. The closest results are Waas' for a disc embedded in an inhomogeneous layer. Therefore, no direct comparison is possible with most of the results in this Chapter, which are predominantly for

surface displacements in the 'near-field'. The results are non-dimensionalised as described in Section 3.3, to aid comparison with the results of other Chapters. Additional figures show (i) the Fourier transforms of the displacements plotted in the wavenumber domain; (ii) the effect varying the strip width has on the strip displacement; and (iii) the maximum deformations through the layer under the strip.

The necessary analysis of the problem is given in Section 5.2. The results are described and presented in Section 5.3, and then discussed in Section 5.4.

5.2 Analysis of the Elastic Layer over Bedrock Model

A layer of finite depth, of homogeneous and isotropic material, over lies a half-space of inelastic material, or "bedrock". The model is two-dimensional, and the following diagram details the coordinate system and relevant parameters used.

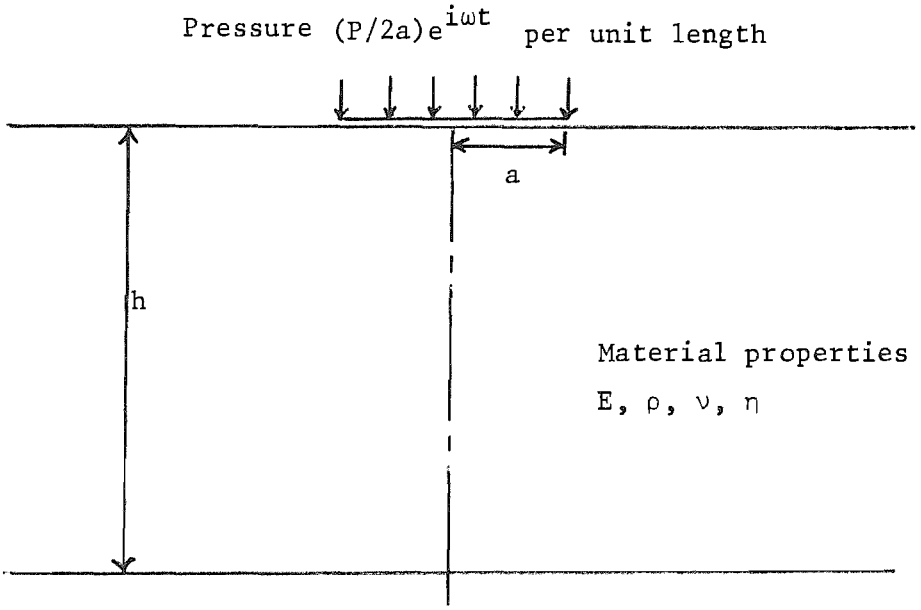

Figure 5.1: The bedrock ground structure and infinite strip load

"h" is the depth of the layer, and "a" the half-width of the load. As shown, the boundary condition is a force not a displacement.

Much of the analysis is included in Chapter 3. Essentially it is a treatment of the "Navier-Stokes" equations, involving the Fourier Transform to produce ordinary differential equations which can be solved. The analysis of Chapter 3 can be followed until equation (3.29). After this a new formulation is required, as to follow a similar method merely with changed boundary conditions would encounter problems over the terms $e^{\pm\alpha z}$ and $e^{\pm\beta z}$. This is because with a layer these terms must now be calculated down to the maximum depth of the layer, and as α and β are of a similar magnitude to wavenumber ζ, overflow would quickly result, for any realistic layer depth. Dividing the layer into several layers all with exactly the same ground parameters, E, ρ, ν and η did not prove an adequate solution, because in the subsequent cross-multiplications of the matrix algebra, the overflow occurs again, even though the order of the ultimate answer would be quite acceptable. An attempt to scale parameters is not appropriate, because within each matrix are very large and very small elements, since the exponents (αz) and (βz) occur with both signs. The alternative is to reject the formulation of the problem represented by equation (3.30), and instead consider a dynamic stiffness matrix approach which has been successfully used for structural vibration problems. From equations (3.22) and (3.23)

$$[\bar{u}(o),\ \bar{w}(o),\ \bar{u}(h),\bar{w}(h)]^T = [C]\ [A_1\ A_2\ B_1\ B_2]^T$$

or

$$\{\bar{U}\} = [C]\ A \qquad (5.1)$$

The matrix [C] is:

$$[C] = \begin{bmatrix} i\zeta & i\zeta & \beta & -\beta \\ -\alpha & \alpha & i\zeta & i\zeta \\ i\zeta e^{-\alpha h} & i\zeta e^{\alpha h} & \beta e^{-\beta h} & -\beta e^{\beta h} \\ -\alpha e^{-\alpha h} & \alpha e^{\alpha h} & i\zeta e^{-\beta h} & i\zeta e^{\beta h} \end{bmatrix} \qquad (5.2)$$

Hence $\{A\} = [C]^{-1} \{\bar{U}\}$ (5.3)

From the equations (3.28) and (3.29) we also have

$$[-\bar{\tau}_{zz}(o), -\bar{\tau}_{zx}(o), \bar{\tau}_{zz}(h), \bar{\tau}_{zx}(h)]^T = [S] \{A\}$$

or

$$\{\bar{\tau}\} = [S] \{A\} \quad (5.4)$$

where $\bar{\tau}_{zz}$ is the transform of the stress component τ_{zz}, etc. The negative signs are for later convenience.

The matrix [S] is given by:

$$[S] = \begin{bmatrix} -2\mu\zeta^2+(\lambda+2\mu)k_1^2 & -2\mu\zeta^2+(\lambda+2\mu)k_1^2 & 2\mu\zeta\beta i & -2\mu\zeta\beta i \\ 2\mu\zeta\alpha i & -2\mu\zeta\alpha i & 2\mu\zeta^2-\mu k_2^2 & 2\mu\zeta^2-\mu k_2^2 \\ \{2\mu\zeta^2-(\lambda+2\mu)k_1^2\}g & \{2\mu\zeta^2-(\lambda+2\mu)k_1^2\}g^{-1} & -2\mu\zeta\beta iq & 2\mu\zeta\beta iq^{-1} \\ -2\mu\zeta\alpha ig & 2\mu\zeta\alpha ig^{-1} & \{-2\mu\zeta^2+\mu k_2^2\}q & \{-2\mu\zeta^2+\mu k_2^2\}q^{-1} \end{bmatrix}$$

(5.5)

where g and q are defined by equation (3.33).

Combining equations (5.3) and (5.4) gives

$$\{\bar{\tau}\} = [S][C]^{-1}\{\bar{U}\} \quad (5.6)$$

To ease the inversion of [C], as required by equation (5.6) write

$$\begin{bmatrix} C_{11} & C_{12} \\ C_{21} & C_{22} \end{bmatrix} \begin{bmatrix} x_1 \\ x_2 \end{bmatrix} = \begin{bmatrix} I & 0 \\ 0 & I \end{bmatrix} \quad (5.7)$$

where [I] is the 2x2 identity matrix.

Hence $$C_{11}x_1 + C_{12}x_2 = [I \quad 0] \tag{5.8}$$

and $$C_{21}x_1 + C_{22}x_2 = [0 \quad I] \tag{5.9}$$

and therefore from equation (5.8)

$$x_1 = C_{11}^{-1}[[I \quad 0] - C_{12}x_2] \tag{5.10}$$

therefore equation (5.9) gives

$$x_2 = [C_{22} - C_{21}C_{11}^{-1}C_{12}]^{-1}\,[[0 \quad I] - C_{21}C_{11}^{-1}[I \quad 0]] \tag{5.11}$$

The algebraic steps involved in the process described by equations (5.8) to (5.11) are tedious, and will be condensed. We have, from equation (5.2)

$$C_{11} = \begin{bmatrix} i\zeta & i\zeta \\ -\alpha & \alpha \end{bmatrix}\ ; \qquad C_{12} = \begin{bmatrix} \beta & -\beta \\ i\zeta & i\zeta \end{bmatrix} \tag{5.12}$$

$$C_{21} = \begin{bmatrix} i\zeta g & i\zeta g^{-1} \\ -\alpha g & \alpha g^{-1} \end{bmatrix}; \qquad C_{22} = \begin{bmatrix} \beta q & -\beta q^{-1} \\ i\zeta q & i\zeta q^{-1} \end{bmatrix} \tag{5.13}$$

Therefore, from equation (5.12):

$$C_{11}^{-1} = \frac{1}{2i\zeta\alpha}\begin{bmatrix} \alpha & -i\zeta \\ \alpha & i\zeta \end{bmatrix} \tag{5.14}$$

It therefore follows from equations (5.12), (5.13) and (5.14) that

$$C_{21}C_{11}^{-1}C_{12} = \frac{1}{2i\zeta\alpha}\begin{bmatrix} i\zeta\{g(\alpha\beta+\zeta^2)+g^{-1}(\alpha\beta-\zeta^2)\}, & i\zeta\{g(\zeta^2-\alpha\beta)-g^{-1}(\alpha\beta+\zeta^2)\} \\ -\alpha\{g(\alpha\beta+\zeta^2)-g^{-1}(\alpha\beta-\zeta^2)\}, & -\alpha\{g(\zeta^2-\alpha\beta)+g^{-1}(\alpha\beta+\zeta^2)\} \end{bmatrix} \tag{5.15}$$

Putting $Y = \alpha\beta + \zeta^2$ and $Z = \alpha\beta - \zeta^2$ (5.16)

and introducing C_{22} gives

$$C_{22} - C_{21}C_{11}^{-1}C_{12} = \begin{bmatrix} \beta q - \frac{1}{2\alpha}(gY+g^{-1}Z), & \frac{1}{2\alpha}(g^{-1}Y + gZ) - \beta q^{-1} \\ i\zeta q - \frac{i}{2\zeta}(gY-g^{-1}Z), & i\zeta q^{-1} - \frac{i}{2\zeta}(g^{-1}Y-gZ) \end{bmatrix} \quad (5.17)$$

After some algebra and a little manipulation, the determinant of equation (5.17) can be expressed:

$$|C_{22} - C_{21}C_{11}^{-1}C_{12}| = D =$$

$$4i\beta\zeta(1 - \cosh\alpha z\cosh\beta z) + 2i\left(\frac{\alpha\beta^2}{\zeta} + \frac{\zeta^3}{\alpha}\right)\sinh\alpha z\sinh\beta z \quad (5.18)$$

Therefore we can write:

$$[C_{22} - C_{21}C_{11}C_{12}]^{-1} = \frac{1}{D}\begin{bmatrix} i\zeta q^{-1} - \frac{i}{2\zeta}(g^{-1}Y-gZ), & \beta q^{-1} - \frac{1}{2\alpha}(g^{-1}Y + gZ) \\ -i\zeta q + \frac{i}{2\zeta}(gY-g^{-1}Z), & \beta q - \frac{1}{2\alpha}(gY + g^{-1}Z) \end{bmatrix} \quad (5.19)$$

Also, from equations (5.13) and (5.14)

$$C_{21}C_{11}^{-1} = \begin{bmatrix} \cosh\alpha z & \frac{i\zeta}{\alpha}\sinh\alpha z \\ -\frac{i\alpha}{\zeta}\sinh\alpha z & \cosh\alpha z \end{bmatrix} \quad (5.20)$$

Equation (5.20) yields

$$[0 \quad I] - C_{21}C_{11}^{-1}[I \quad 0] = \begin{bmatrix} -\cosh\alpha z, & \frac{i\zeta}{\alpha}\sinh\alpha z, & 1, & 0 \\ \frac{i\alpha}{\zeta}\sinh\alpha z, & -\cosh\alpha z, & 0, & 1 \end{bmatrix} \quad (5.21)$$

The (2×4) matrix x_2 can now be evaluated from equation (5.11), by multiplying together equations (5.19) and (5.21). The algebraically complicated result is given by the bottom half of matrix $[C]^{-1}$ in equation (5.22).

Combining equations (5.12), (5.14) and (5.21), equation (5.10) gives x_1, the top half of matrix $[C]^{-1}$.

$$[C]^{-1}=\frac{1}{D}\begin{bmatrix}
\begin{bmatrix}\beta(1-\cosh\alpha z\cosh\beta z-\sinh\alpha z\cosh\beta z)\\ +\frac{\zeta^2}{\alpha}(\sinh\alpha z\sinh\beta z+\cosh\alpha z\sinh\beta z)\end{bmatrix}, & \begin{bmatrix}\frac{\beta^2}{i\zeta}\sinh\beta z(\sinh\alpha z+\cosh\alpha z)\\ +\frac{\beta\zeta}{i\alpha}(1-\cosh\alpha z\cosh\beta z-\sinh\alpha z\cosh\beta z)\end{bmatrix}, & -\frac{1}{\zeta^2\alpha}\begin{bmatrix}\alpha\beta\zeta^2\cosh\beta z\\ -\alpha\beta\zeta^2\sinh\alpha z\\ +\zeta^4\sinh\beta z\\ -\alpha\beta\zeta^2\cosh\alpha z\end{bmatrix}, & \frac{\beta}{i\zeta\alpha}\begin{bmatrix}\zeta^2\sinh\alpha z\\ +\zeta^2\cosh\alpha z\\ -\zeta^2\cosh\beta z\\ -\alpha\beta\sinh\beta z\end{bmatrix}\\
\begin{bmatrix}\beta(1-\cosh\alpha z\cosh\beta z+\sinh\alpha z\cosh\beta z)\\ +\frac{\zeta^2}{\alpha}(\sinh\alpha z\sinh\beta z-\cosh\alpha z\sinh\beta z)\end{bmatrix}, & \begin{bmatrix}\frac{\beta^2}{i\zeta}\sinh\beta z(\cosh\alpha z-\sinh\alpha z)\\ -\frac{\beta\zeta}{i\alpha}(1-\cosh\alpha z\cosh\beta z+\sinh\alpha z\cosh\beta z)\end{bmatrix}, & \frac{1}{\zeta^2\alpha}\begin{bmatrix}\zeta^4\sinh\beta z+\\ \alpha\beta\zeta^2\cosh\alpha z\\ \alpha\beta\zeta^2\cosh\beta z\\ -\alpha\beta\zeta^2\sinh\alpha z\end{bmatrix}, & \frac{\beta}{i\zeta\alpha}\begin{bmatrix}\zeta^2\cosh\beta z\\ +\zeta^2\sinh\alpha z\\ -\zeta^2\cosh\alpha z\\ -\alpha\beta\sinh\beta z\end{bmatrix}\\
i\zeta+\frac{iq^{-1}}{\zeta}(\alpha\beta\sinh\alpha z-\zeta^2\cosh\alpha z), & \beta+\frac{q^{-1}}{\alpha}(\zeta^2\sinh\alpha z-\alpha\beta\cosh\alpha z), & i\zeta q^{-1}-\frac{i}{\zeta}\begin{bmatrix}\alpha\beta\sinh\alpha z\\ +\zeta^2\cosh\alpha z\end{bmatrix}, & \begin{bmatrix}\beta q^{-1}-\frac{1}{\alpha}(\alpha\beta\cosh\alpha z\\ +\zeta^2\sinh\alpha z)\end{bmatrix}\\
\frac{iq}{\zeta}(\zeta^2\cosh\alpha z+\alpha\beta\sinh\alpha z)-\zeta i\ , & \beta-\frac{q}{\alpha}(\zeta^2\sinh\alpha z+\alpha\beta\cosh\alpha z), & -i\zeta q+\frac{i}{\zeta}\begin{bmatrix}-\alpha\beta\sinh\alpha z\\ +\zeta^2\cosh\alpha z\end{bmatrix}, & \begin{bmatrix}\beta q^{-1}-\frac{1}{\alpha}(\alpha\beta\cosh\alpha z\\ -\zeta^2\sinh\alpha z)\end{bmatrix}
\end{bmatrix}$$

(5.22)

where $D = 4i\beta\zeta\,(1-\cosh\alpha z\cosh\beta z) + 2i\,(\frac{\alpha\beta^2}{\zeta} + \frac{\zeta^3}{\alpha})\sinh\alpha z\sinh\beta z$ and $q = e^{-\beta h}$, $g = e^{-\alpha h}$.

The product $[S]\,[C]^{-1}$ will give a symmetrical stiffness matrix, provided the matrices in equation (5.4) are manipulated so that

$$\{\bar{\tau}\} = [-i\,\bar{\tau}_{zz}(o),\ -\bar{\tau}_{zx}(o),\ i\bar{\tau}_{zz}(h),\ \bar{\tau}_{zx}(h)]^{T} \qquad (5.23)$$

and

$$\{\bar{U}\} = [i\bar{w}(o),\ \bar{u}(o),\ i\bar{w}(h),\ \bar{u}(h)]^{T} \qquad (5.24)$$

This transformation is after Kausel and Roesset [36].

The matrix $[T] = [S]\,[C]^{-1}$ is then: (only the top half of the symmetrical matrix is shown)

$$\frac{1}{D}\begin{bmatrix} \frac{2\beta i}{\alpha\zeta}(\lambda+2\mu)k_1^2\begin{bmatrix}\zeta^2\sinh\alpha z\cosh\beta z\\ -\alpha\beta\sinh\beta z\cosh\alpha z\end{bmatrix}, & \begin{bmatrix}2i\beta(1-\cosh\alpha z\cosh\beta z)\begin{bmatrix}(\lambda+2\mu)k_1^2\\ -4\mu\zeta^2\end{bmatrix}\\ +2i\zeta\sinh\alpha z\sinh\beta z \times ((\lambda+2\mu)k_1^2\frac{\zeta}{\alpha}\\ -2\mu(\frac{\alpha\beta^2}{\zeta}+\frac{\zeta^3}{\alpha}))\end{bmatrix}, & \frac{2\beta i}{\alpha\zeta}(\lambda+2\mu)k_1^2(\alpha\beta\sinh\beta z-\zeta^2\sinh\alpha z), & -2\mu i\beta k_2(\cosh\beta z-\cosh\alpha z) \\ " , & \frac{2\mu ik_2^2}{\zeta}\begin{bmatrix}\zeta^2\cosh\alpha z\sinh\beta z\\ -\alpha\beta\sinh\alpha z\cosh\beta z\end{bmatrix}, & 2\mu i\beta k_2^2(\cosh\beta z-\cosh\alpha z), & \frac{2\mu ik_2^2}{\zeta}\begin{bmatrix}\alpha\beta\sinh\alpha z\\ -\\ \zeta^2\sinh\beta z\end{bmatrix} \\ " , " , & \begin{bmatrix}\frac{2\beta i}{\alpha\zeta}(\lambda+2\mu)k_1^2(\zeta^2\sinh\alpha z\cosh\beta z\\ -\alpha\beta\sinh\beta z\cosh\alpha z)\end{bmatrix}, & \begin{bmatrix}-2i\beta(1-\cosh\alpha z\cosh\beta z)\times\\ \{(\lambda+2\mu)k_1^2-4\mu\zeta^2\}-\\ 2i\zeta\sinh\alpha z\sinh\beta z\times\\ \{(\lambda+2\mu)k_1^2\frac{\zeta}{\alpha}-2\mu(\frac{\alpha\beta^2}{\zeta}+\frac{\zeta^3}{\alpha})\}\end{bmatrix} \\ " , " , " , & \frac{2\mu ik_2^2}{\zeta}\times\begin{bmatrix}\zeta^2\cosh\alpha z\sinh\beta z\\ -\alpha\beta\sinh\alpha z\cosh\beta z\end{bmatrix} \end{bmatrix}$$

(5.25)

where D has the same definition as before.

With this analytically derived stiffness matrix, the matrix corresponding to a problem with several layers of depth "h" can be assembled; for example, for three layers:

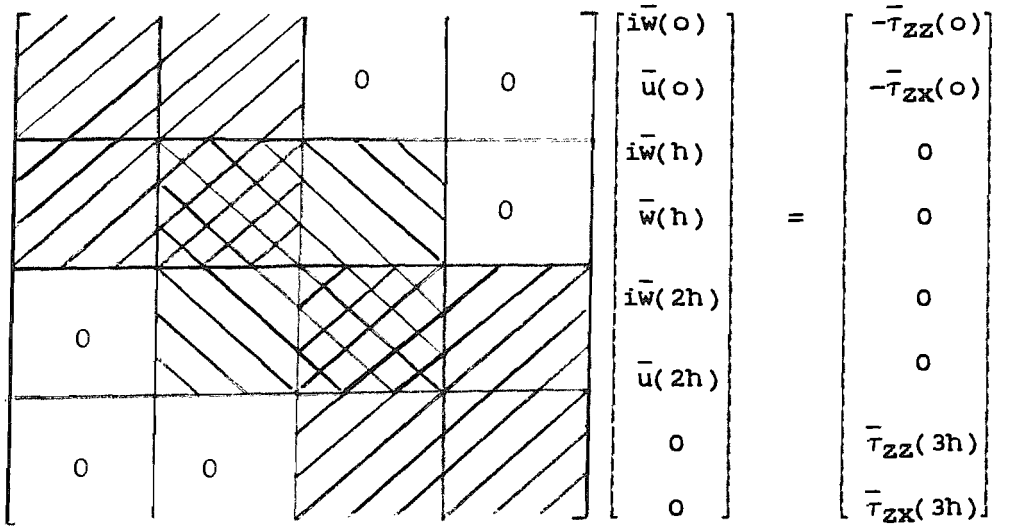

(5.26)

where each 4x4 square marked within the 8x8 stiffness matrix corresponds to [T], with the relevant additions of elements at the intersections. If a single layer is being divided into 3 layers of identical material properties, and the total layer height is H, then the "h" in equation (5.26) will be such that H=3h. Because the stresses at the surface are already known, since the boundary conditions are imposed, equation (5.26) reduces to six equations in just six unknowns. From equations (3.34) and (3.35) we have

$$\left.\begin{aligned} \bar{\tau}_{zz}(o) &= -\frac{P}{2\pi}\,\frac{\sin\zeta a}{\zeta a} \\ \bar{\tau}_{zx}(o) &= 0 \end{aligned}\right\} \qquad (5.27)$$

Hence expressions for $\bar{u}(\zeta,o)$ and $\bar{w}(\zeta,o)$ can be found, and these can be inverse-transformed to give u(x,o) and w(x,o) using the quadrature routine described in Appendix A. This routine is an efficient way of exploiting the symmetry and generally good behaviour of $\bar{u}$ and $\bar{w}$.

Note 1: In the limiting case ζ=0, the dynamic stiffness matrix has been taken from Ref [36].

Note 2: Clearly, if the displacements at depths below the surface are required, these can be found directly by inverse transforming $\bar{u}(h)$, $\bar{w}(h)$ at the necessary depths.

5.3 Results

Of the results which follow, Figures 5.2, 5.3 and 5.11 are specifically for the Clarborough test-site, the material properties of which are given in Table 2.2. The other figures are non-dimensionalised, but whereas most are designed for easy interpretation as Clarborough, with $\nu = 0.257$, Figure 5.9 is an exception. Figure 5.9 is most easily interpreted as the Checkerhouse test-site, the material properties of which are given in Table 4.2. Therefore a Poisson's ratio $\nu = 0.158$ has been used. The non-dimensionalisation of the results is described in Section 3.3. In order to re-dimensionalise to find the Checkerhouse information, the Checkerhouse material properties with $a = 3$ m must be used. This large value of a (for Clarborough, $a = 0.75$ m) is because the Checkerhouse layer depth, which must be non-dimensionalised, is also large, and must be reduced in this way to avoid computer overflow. An alternative would have been to use the layer height as the non-dimensionalising parameter. This, of course, is not possible with the half-space model of Chapters 3 and 9.

The Figures were all produced with versions of a Fortran program, which can be easily derived from the program EF64H2, listed in Appendix B. Figures 5.2 and 5.3 show the variation of $|\bar{w}|$ and $|\bar{u}|$ respectively with wavenumber, for several frequencies, and $\eta = 0.002$. A log scale has been used, to reveal smaller peaks which are dwarfed on a linear scale. Figures 5.2(a) and 5.3(a) show, by their lack of peaks and small amplitudes, that no propagation of motion occurs at either 4 or 8 Hz. The peaks in the other diagrams indicate the wavenumbers of the propagating waves, and are analysed in Section 5.4. To this end, Table 5.1 lists the wavenumbers of the peaks.

Figure 5.4 shows the vertical motion amplitude against distance, for six frequencies. To avoid dwarfing the other curves, the

($\Omega^2 = 0.033$) curve has only been plotted for $x/a > 8$. The whole curve is given in Figure 7.16. Figure 5.5 is like Figure 5.4, except that it shows the variation of horizontal motion amplitude, and here the ($\Omega^2 = 0.033$) curve is shown complete.

Frequency Hz	(Ω^2)	Wavenumber location of peaks of $\lvert\bar{w}\rvert$, $\lvert\bar{u}\rvert$: $\eta = 0.002$ 1st	2nd	3rd	4th	5th
4	(0.002)	-	-	-	-	-
8	(0.008)	-	-	-	-	-
16	(0.033)	0.19	-	-	-	-
32	(0.131)	0.88	0.46	0.20	-	-
48	(0.295)	1.25	0.88	0.57	0.55	-
64	(0.524)	1.66	1.38	0.98	0.86	0.51

Table 5.1: Wavenumbers of peaks of $\lvert\bar{w}\rvert$ and $\lvert\bar{u}\rvert$, bedrock model.

Figures 5.6, 5.7 and 5.9 all show the attenuation of vertical motion on a dB log scale, over a greater distance than the previous two figures covered, and for just four frequencies. The reference amplitude for the attenuation is the displacement at $x/a = 0$, for each frequency. Figures 5.6 and 5.9 are for $\eta = 0.1$, and Figure 5.7 for $\eta = 0.02$. Figure 5.8 shows the phase change with distance corresponding to two of the frequency components shown in Figure 5.6. If curves for more frequencies were shown in Figure 5.8, the result would be a confusing number of lines, and little extra information would be included.

Figure 5.10 shows the effect varying the strip width has on the vertical displacement at the centre of the strip, with constant force per unit width, and for four frequencies. Figure 5.11 is a representation of the way the ground deforms under the strip. The displacements have been made discernible by scaling the vertical and horizontal motion differently, and multiplying the movements' magnitudes by 10^6.

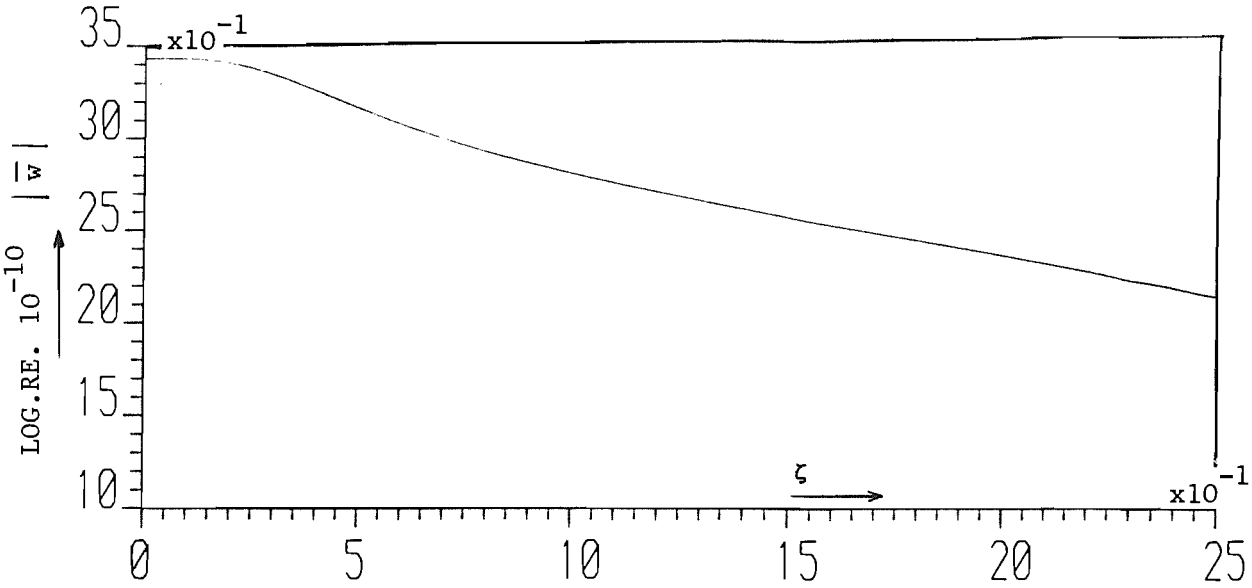

Fig5.2(a): Frequency = 8 Hz

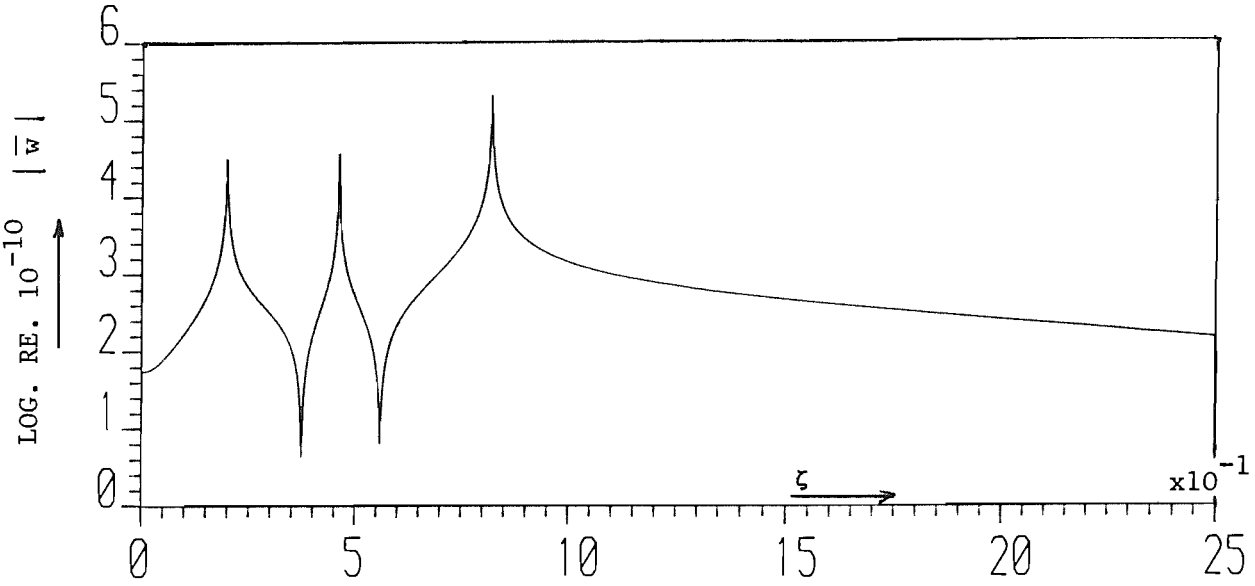

Fig 5.2(b): Frequency = 32 Hz

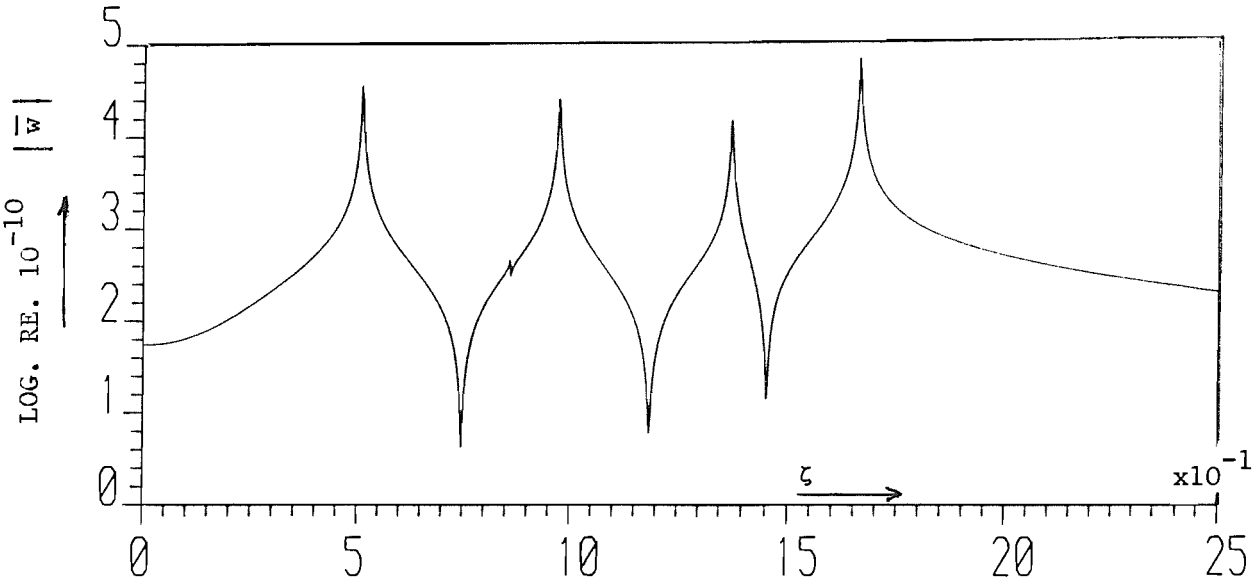

Fig 5.2(c): Frequency = 64 Hz

Fig 5.2: Amplitude Of Transformed Vertical Motion, $|\bar{w}|$, With Clarborough Parameters, η = 0.002

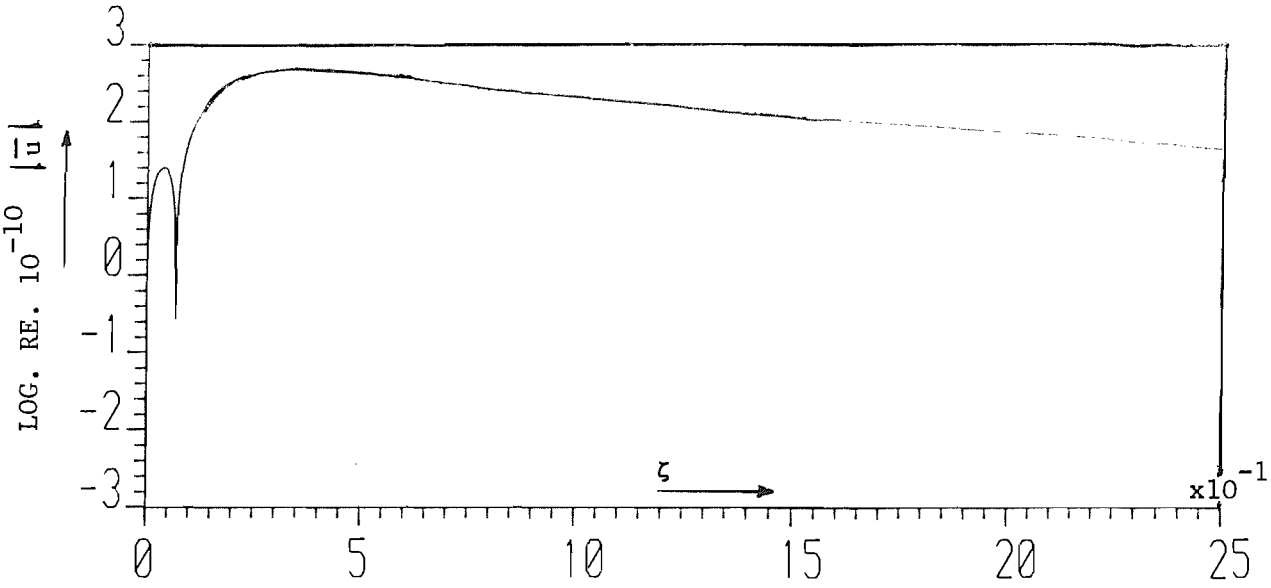

Fig 5.3(a): Frequency = 4 Hz

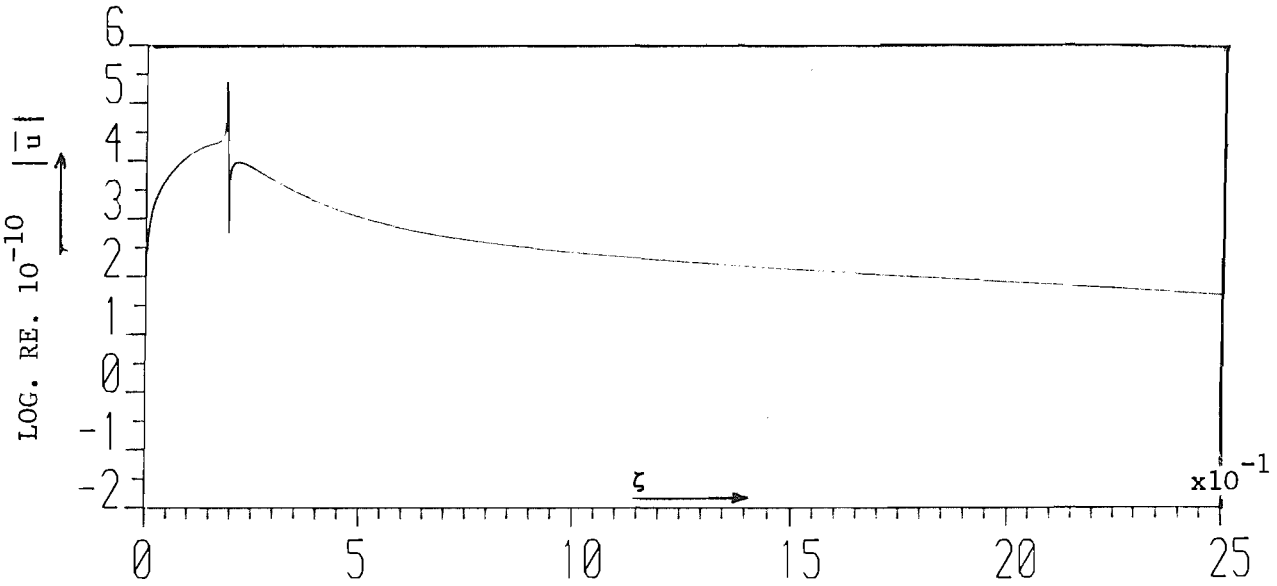

Fig 5.3(b): Frequency = 16 Hz

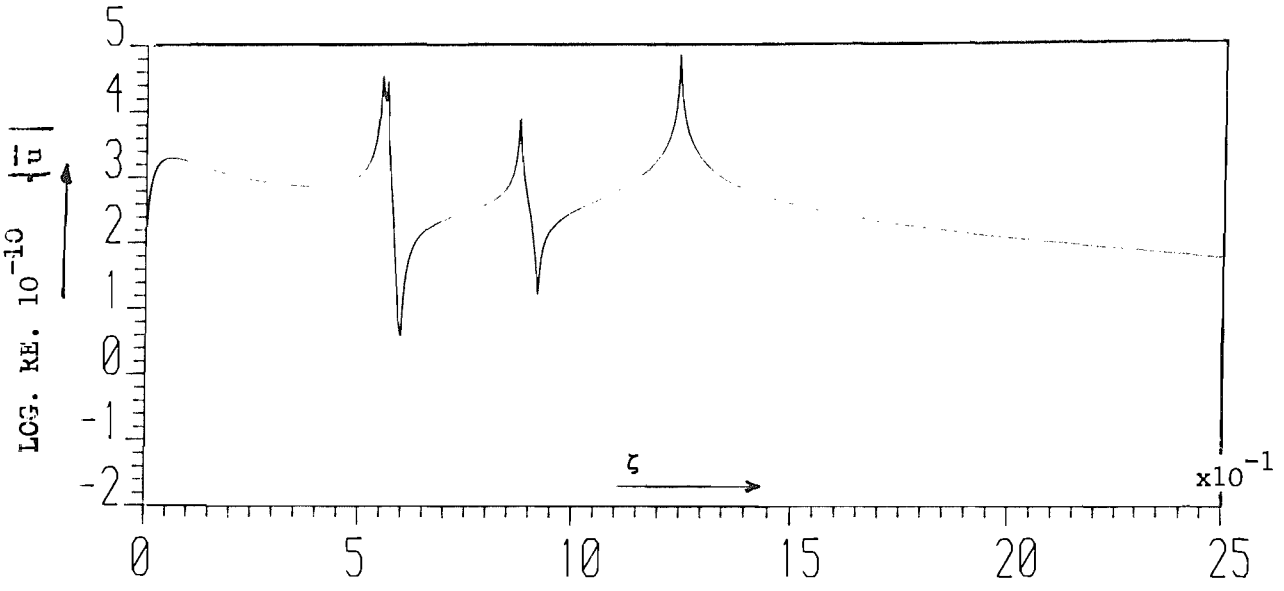

Fig 5.3(c): Frequency = 48 Hz

Fig 5.3: Amplitude Of Transformed Horizontal Motion, $|\bar{u}|$, With Clarborough Parameters, $\eta = 0.002$

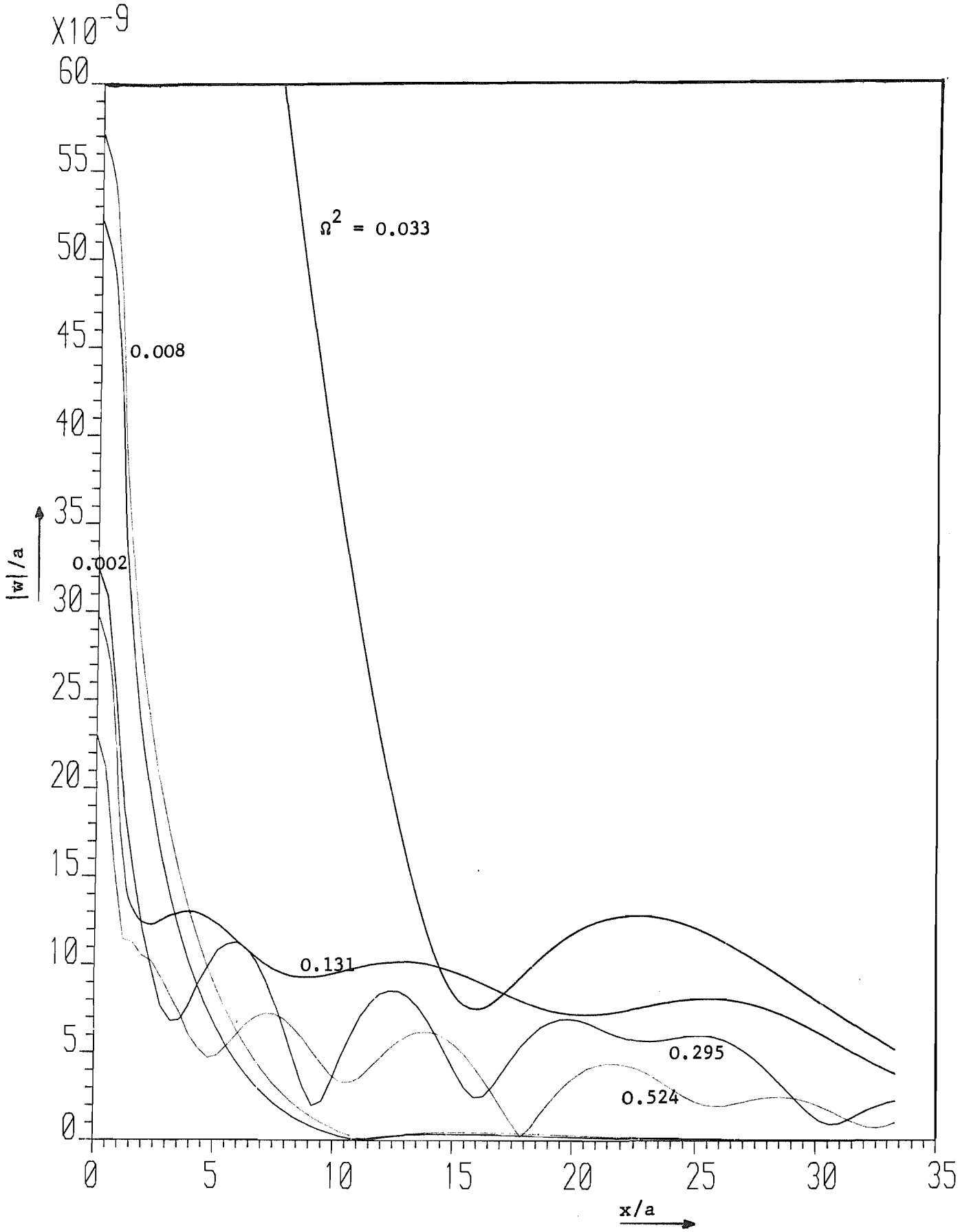

Fig 5.4: Non-Dimensional Vertical Motion Amplitude |w|/a, Against Distance, For Ω^2 = 0.002, 0.008, 0.033, 0.131, 0.295 and 0.524

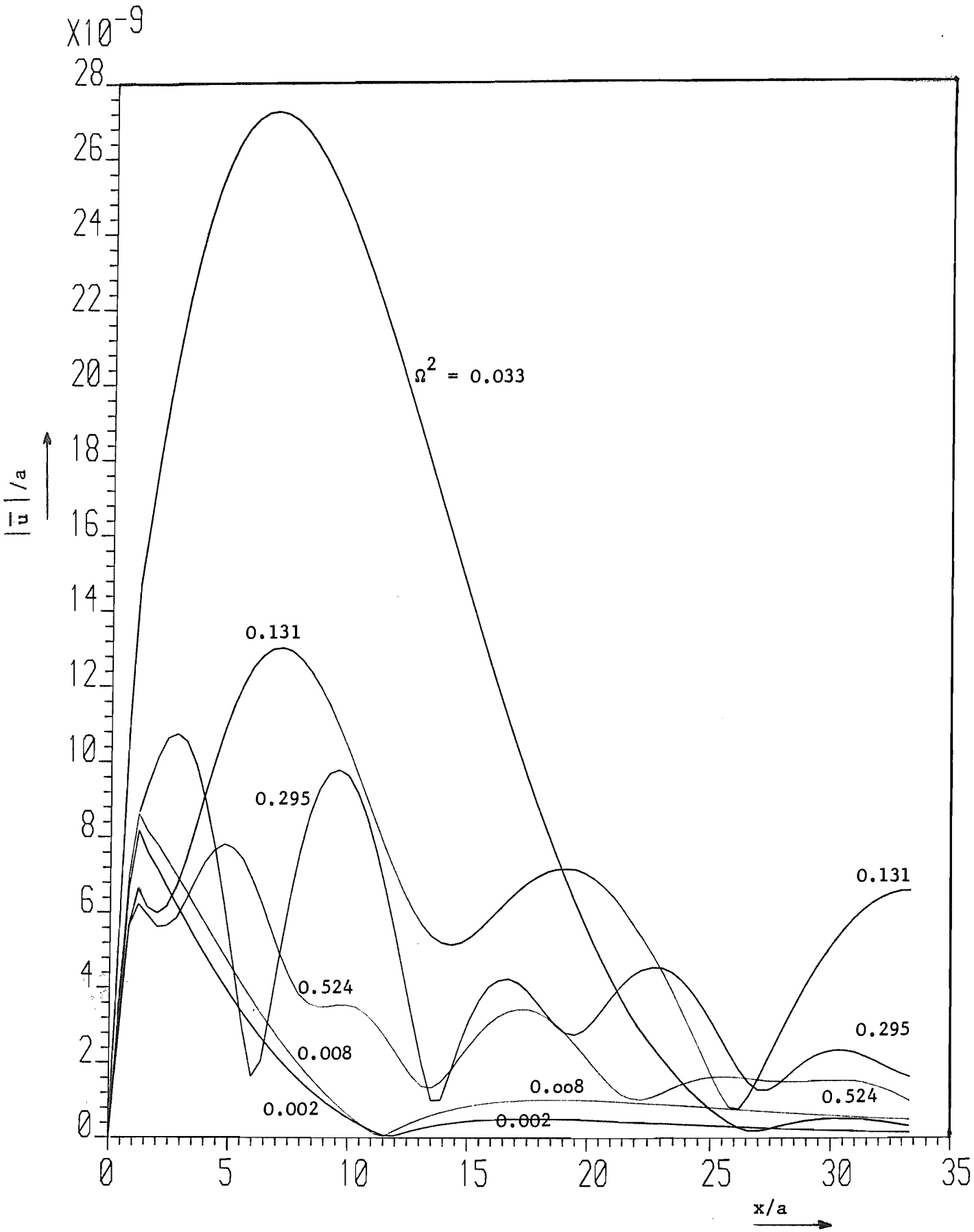

Fig 5.5: Non-Dimensional Horizontal Amplitude, $|\bar{u}|/a$, Against Distance For Six Frequencies.

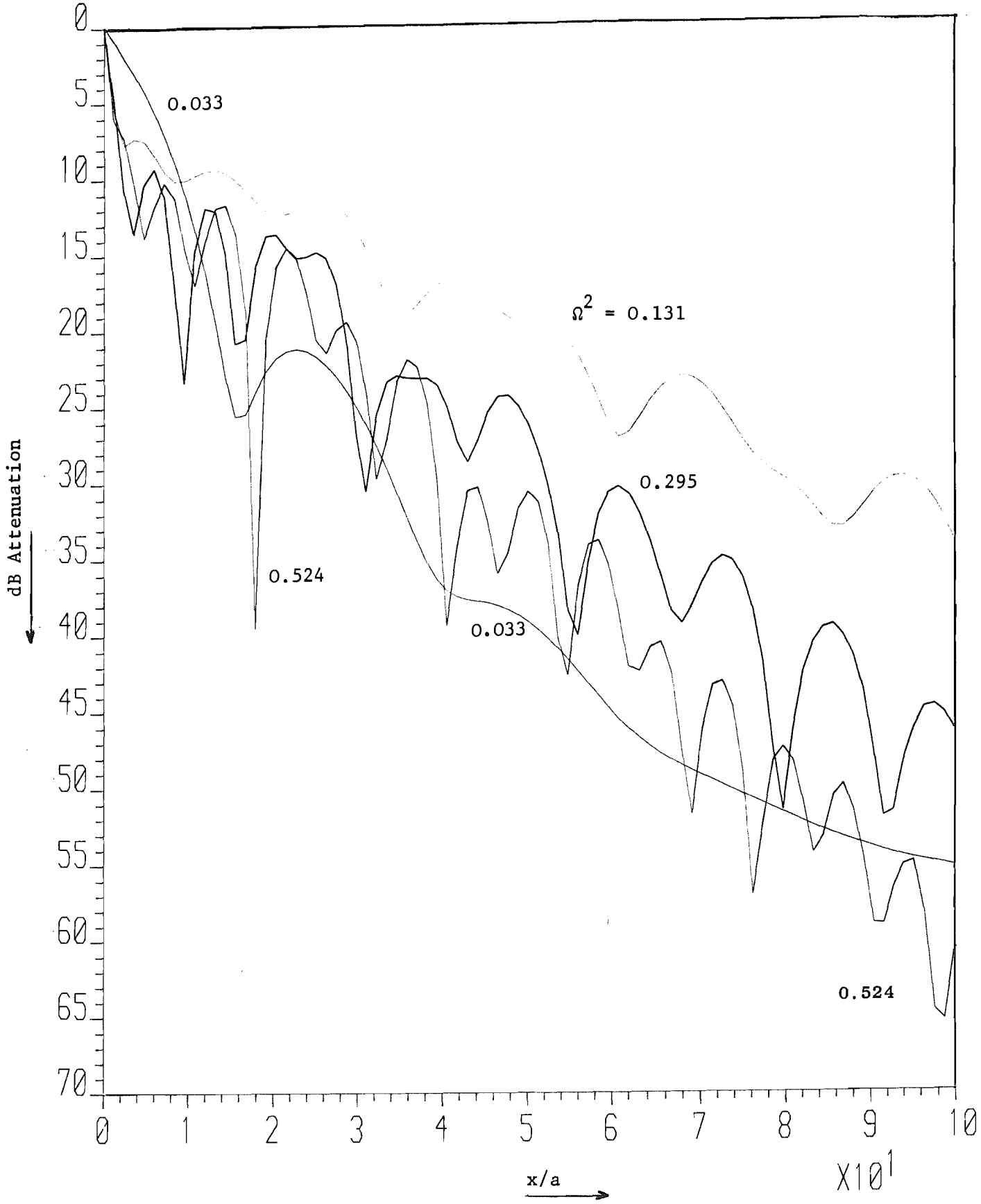

Fig 5.6: Non-Dimensional Vertical Motion Attenuation, Against Distance, η = 0.1, For Four Frequencies.

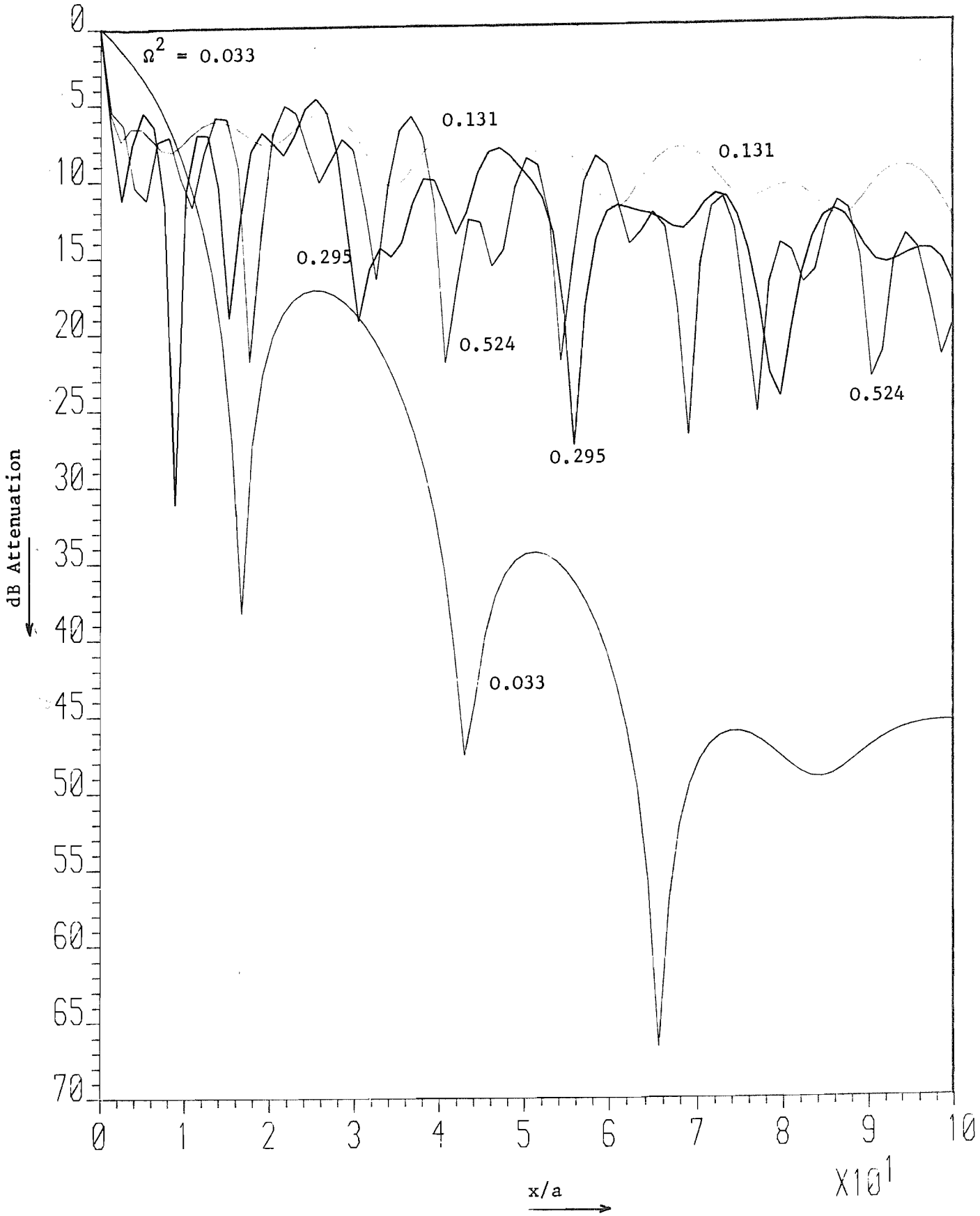

Fig 5.7: Non-Dimensional Vertical Motion Against Distance, η = 0.02, For Four Frequencies.

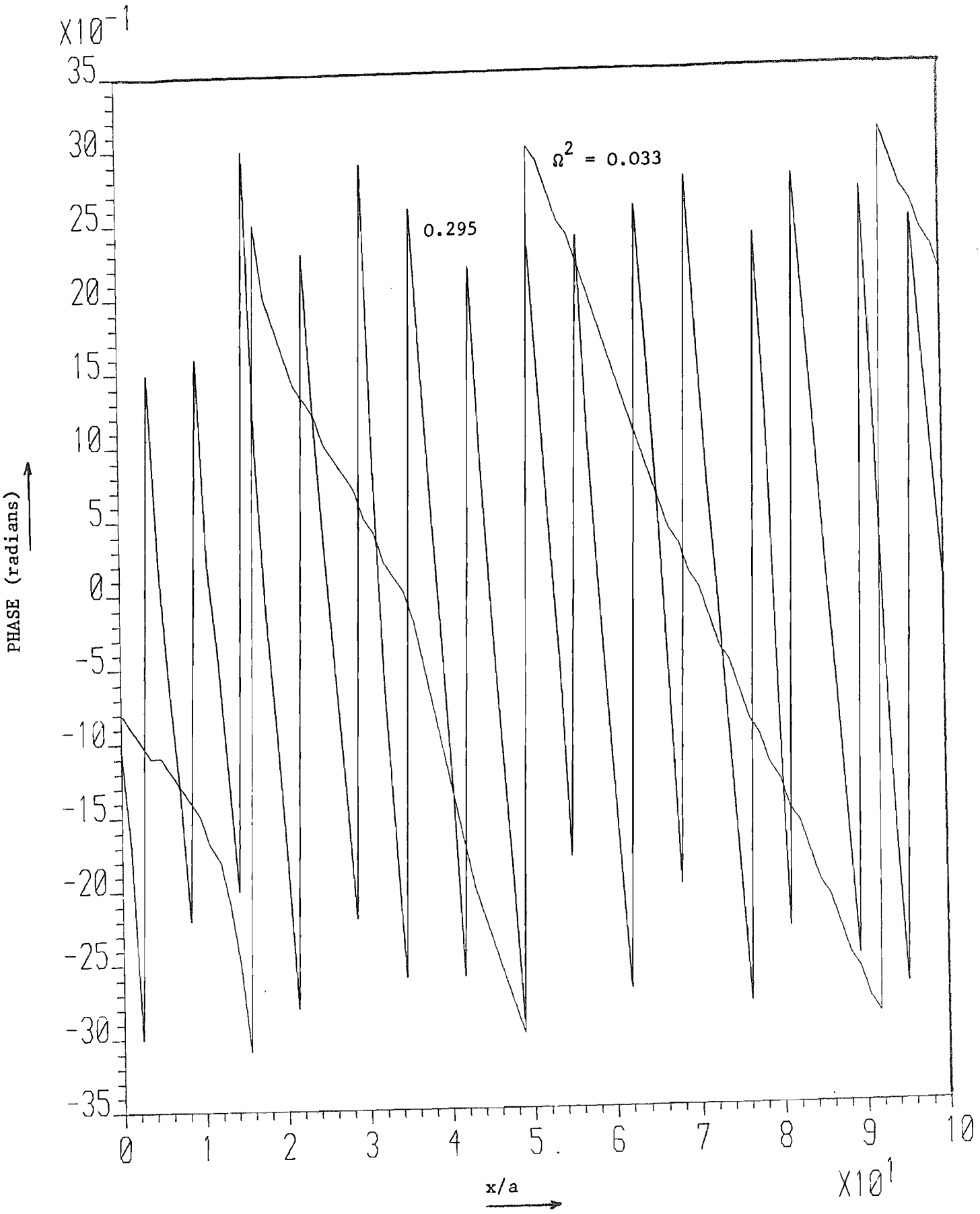

Fig 5.8: The Phase Change Corresponding To Fig 5.6, For $\Omega^2 = 0.033$, And 0.295

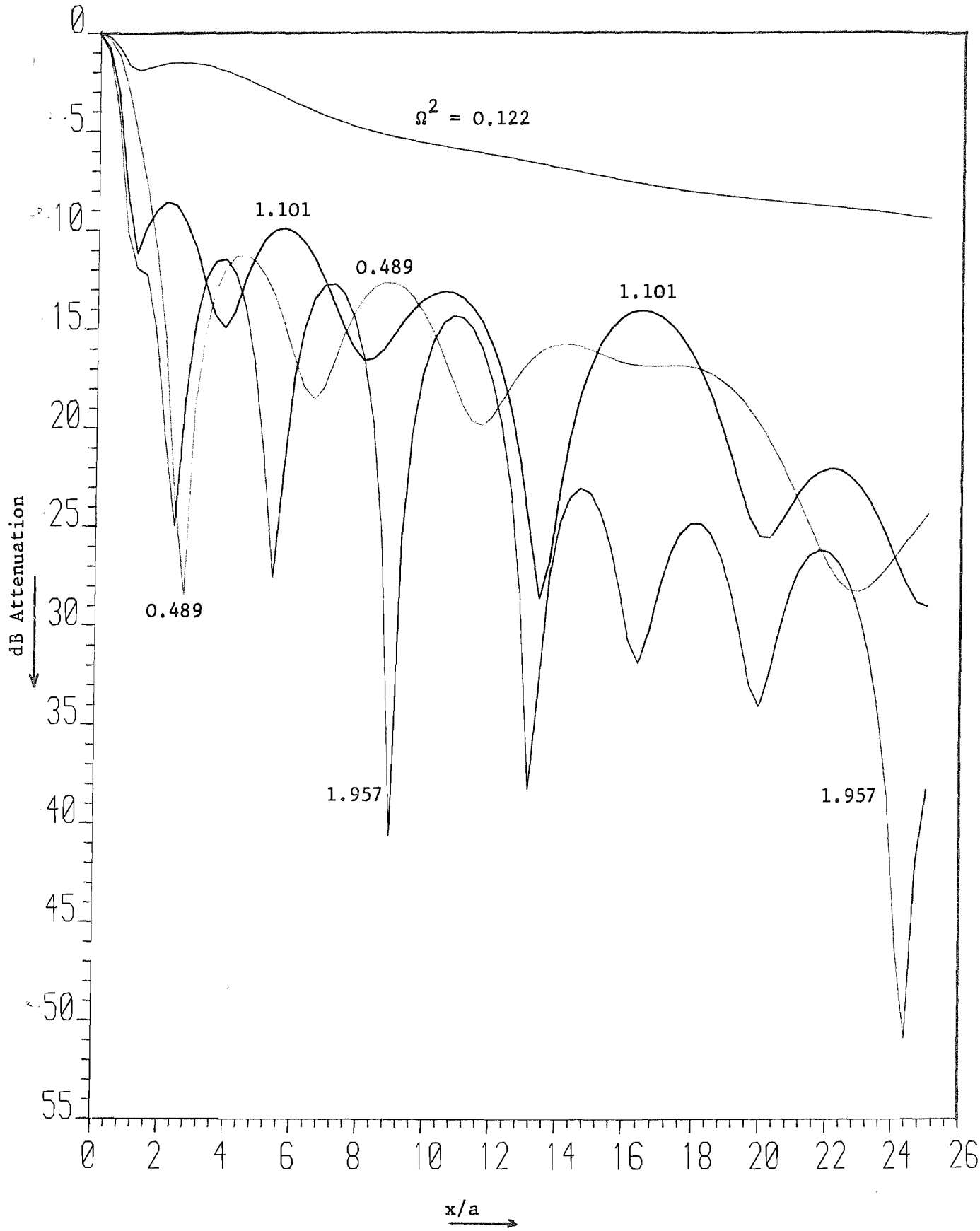

Fig 5.9: As Fig 5.6, But For Different Non-Dimensional Frequencies; This Figure Is Applicable To The Checkerhouse Test-Site

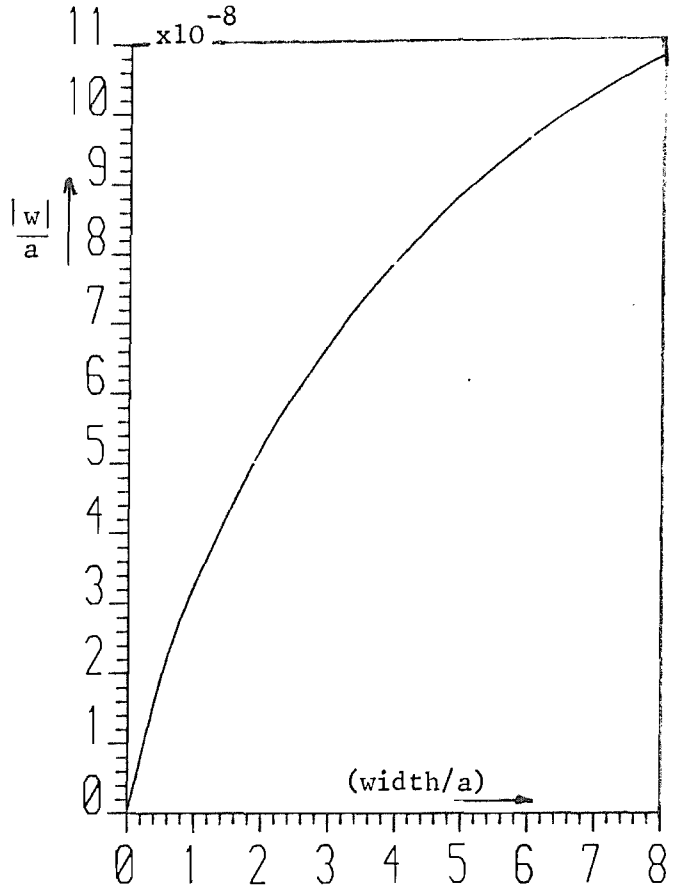

Fig 5.10(a): Frequency = 4 Hz

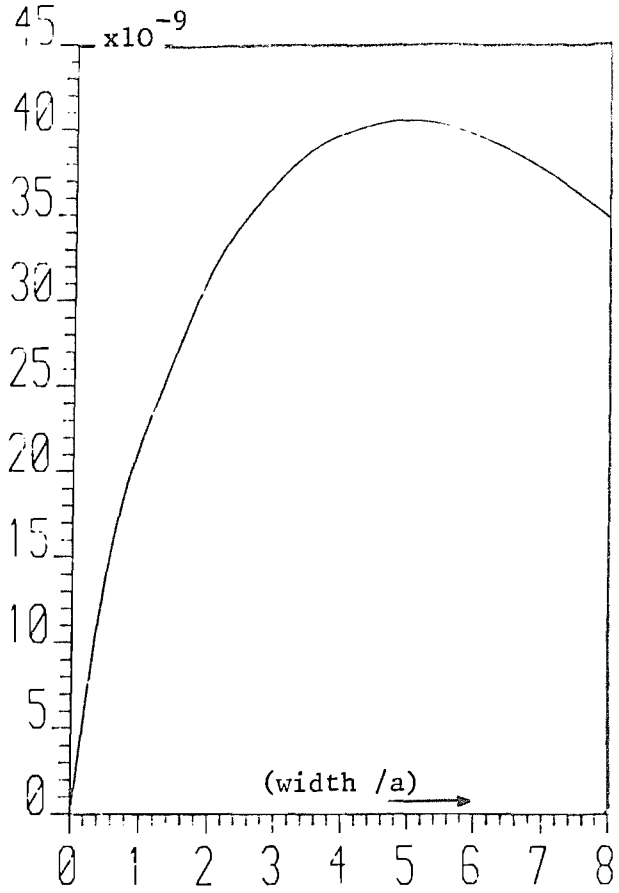

Fig 5.10(b): Frequency = 32Hz

Fig 5.10: Effect On Displacement At Centre Of Load Of Varying Load Width, Bedrock Model, With Constant Load/Unit Width, $\eta = 0.02$

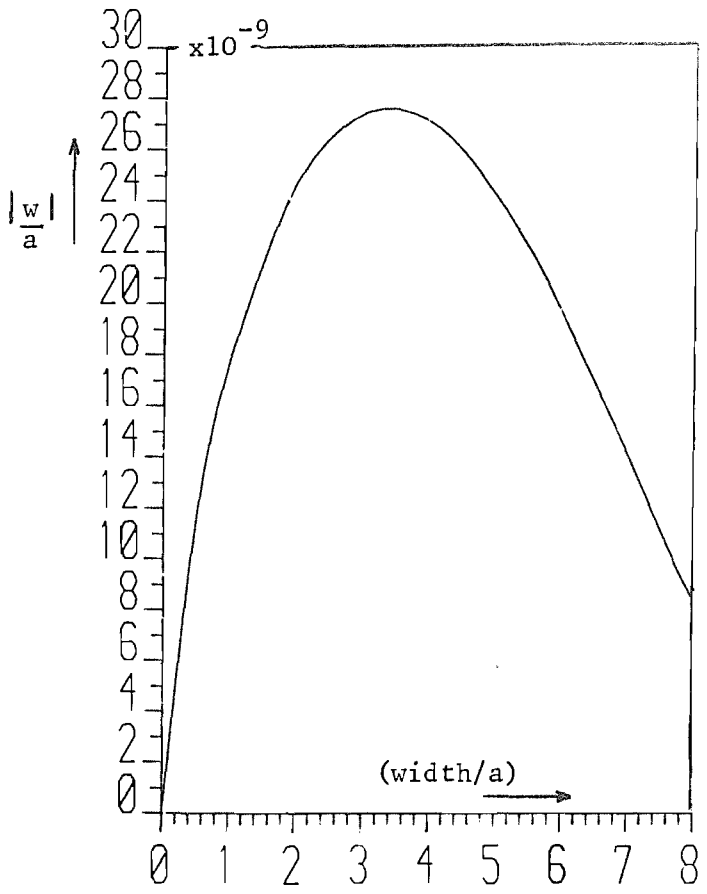

Fig 5.10(c): Frequency = 64Hz

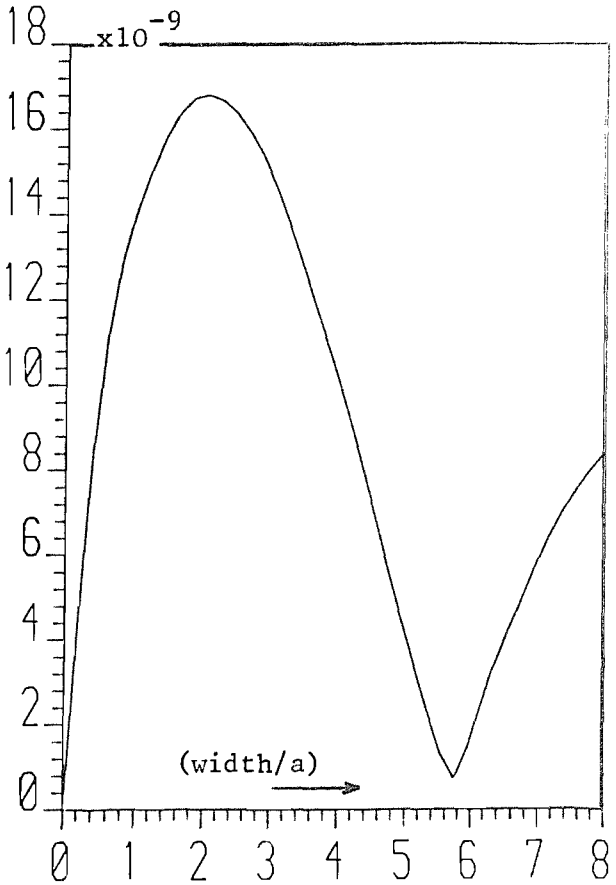

Fig 5.10(d): Frequency = 100Hz

FIG 5.11 A Representation of the maximum deflections experienced under the load

The displacements shown are derived from data for the Clarborough test site, with a load frequency of 32Hz and a ground loss factor of 0.1. No allowance has been made for phase differences, so this actual configuration could not occur; instead, (continued below)

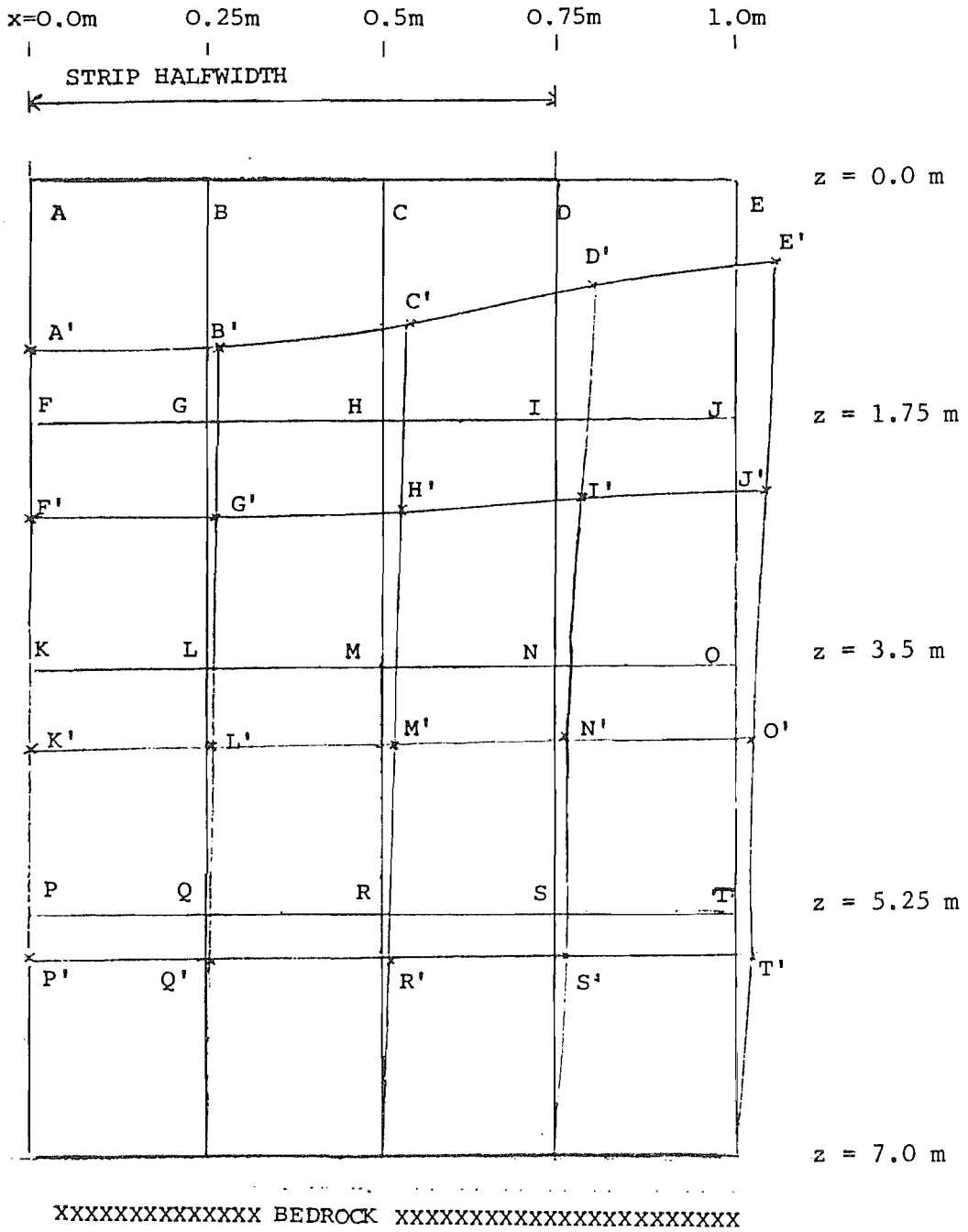

the diagram indicates the maximum deflections. In it, point A moves to A' etc. The diagram has been scaled with a ratio of 1:50 in the Z direction, and 1:10 in the x-direction. The displacements have been multiplied by 10^6 in both directions. Each scaling is arbitrary and chosen to make the diagram more informative.

5.4 Discussion

The wavenumber domain graphs, Figures 5.2 and 5.3, have been plotted with a low loss factor and using log scales to accentuate their peaks. The absence of peaks in Figures 5.2(a) and 5.3(a) shows that no propagation can occur at these frequencies, as predicted by Figure 4.1. The lowest frequency of propagation is a function of both the material properties and the depth of the layer. The effect of varying the depth alone is shown in Table 6.2. Figure 4.1 can be used to explain the location of the peaks in Figures 5.2 and 5.3. For a given frequency, the wavenumbers given in Table 5.1 are very close to the wavenumbers of the natural modes at that frequency. Exact agreement is impossible, because these natural modes are for a layer without damping, and so their wavenumbers are real. The wavenumbers of the waves in a damped medium are complex, but as the damping for Figures 5.2 and 5.3 is so low, the imaginary parts of the wavenumbers are small. These figures show the variation of $|\bar{u}|$ and $|\bar{w}|$ along the real ζ axis, primarily because this is the axis of integration.

These wavenumber domain graphs are significantly different to those of the half-space (Figures 3.2 and 3.3). Although above about 30 Hz the Rayleigh wave is again the dominant propagating wave, no contributions now appear at the shear or compression wavenumbers. Instead, the wavenumbers of the propagating modes produced by their interaction appear (and in fact, the Rayleigh wave is also a result of their interaction).

The calculated near-field displacements are shown in Figures 5.4 and 5.5. There are several striking features of these graphs. The $\Omega^2 = 0.002$ and 0.008 components, which equate with 4 and 8 Hz at Clarborough, decay rapidly, each having a minimum near $x/a = 11.5$. The graphs of phase change for these frequencies, which are not shown, reveal no propagation, or zero phase change, except at $x/a = 11.5$. Here, there is a jump of 180° in phase. It seems that the elastic nature of the layer, and its constraint at $z = 7$ m, reduce the indentation of the strip to practically zero at $x/a = 11.5$. It is as if the layer 'buckles' at this distance, the phase changes by 180°, and the displacements beyond $x/a = 11.5$ are a reaction to the stresses induced in the layer at that distance. These further displacements

become negligible after a short distance which depends on the layers' elasticity. Because these displacements are so small, and because the displacement at $x/a = 11.5$ is almost zero, these frequencies do not appear in the attenuation graphs (Figures 5.6, 5.7 and 5.9) which are for a greater distance and use a log scale.

From Figures 5.4 and 5.5, it is clear that propagation is possible at $\Omega^2 = 0.033$ (or 16 Hz for Clarborough). This frequency, for Clarborough, is close to 16.4 Hz, the frequency of intersection of the first two natural modes, shown in Figure 4.1. This "resonant frequency" is also given by Warburton [80], who found that his undamped layer had an infinite response when

$$\cot(a_0 R\eta') = 0 \qquad (5.28)$$

where

$$a_0 = k_2 r_0, \qquad R = h/r_0, \qquad \eta' = k_2/k_1 \qquad (5.29)$$

and r_0 is the radius of the disc load. In fact, equation (5.28) is independent of r_0, and is identical to equation (4.18) with $c_i = c_1$. Therefore the first frequency predicted by equation (5.28) for Clarborough is 16.4 Hz, and the second is 49.3 Hz, from Table 4.1.

The relative amplitude of the 16 Hz response can be seen clearly in curve 'H' of Figure 8.6, which shows the direct receptance for the layer as a function of frequency.

The first third of the phase change shown in Figure 5.8 applies to the smaller distance shown in Figure 5.4. The minimum in the $\Omega^2 = 0.033$ vertical motion component at about $x/a = 16$, corresponds to a locally faster rate of change of phase (or larger wavenumber) in Figure 5.8. The phase change graphs for each frequency have the same characteristic associated with their minima, which can only clearly be seen for $\Omega^2 = 0.033$. Likewise, the maxima in these curves occur when the wavenumber is locally smaller. The average wavenumber for the whole range is always close to the first mode wavenumber of Figure 4.1, being slightly larger because of the damping. This is predicted by the wavenumber domain graphs, which show more information is associated with this wave than any other. In the region of the minima, where the

total disturbance travels even more slowly than the first propagating wave (this cannot be called the first 'mode' in the same sense as in the last Chapter, as here the damping will change its form), destructive interference produces a wave slower than any of the contributing waves. Conversely, in the region of a maximum, constructive interference results in a wavespeed faster than the first propagating wave, and therefore a smaller wavenumber.

At $\Omega^2 = 0.033$, only two propagating waves can exist, and so the interference 'pattern' is simple. The complexity of the interference pattern increases discretely with increasing frequency, because a new propagating wave appears at discrete frequencies. (Also, increased frequency means decreased wavelength, and so the 'density' of the pattern increases.) However, this trend cannot continue indefinitely, even though the number of natural modes is infinite. Kobori *et al* [39] have shown that depending on the depth of the layer, h, for (ηf) large enough the layer solution is the same as the half-space solution. This is not surprising, since large damping or short wavelengths make the boundary conditions at the bottom of the layer practically irrelevant. This tendency for the solutions to merge is suggested in Figure 7.18, which shows the half-space and layer solutions in the same graph, for 64 Hz. At very high frequency, the interference pattern is due to the Rayleigh "extraneous roots" (see Section 9.5.2). It is possible that these extra waves contribute to the complicated interference patterns of Figures 5.4 and 5.5.

With the half-space model, it was found that the vertical motion direct receptance of the load is inversely proportional to frequency, with an infinite static solution. The bedrock boundary conditions require a finite static solution (see Figure 8.6), and also because of the resonance which can occur in the layer, the displacement under the load does not decrease monotonically with increasing frequency. The 16 Hz case (with Clarborough parameters) is an obvious example of this, but it can also be seen that the 48 Hz curve in Figure 5.4, which is near to another (undamped) resonance frequency of 49.3 Hz, produces a larger response at the load than 32 Hz. The receptance graph, Figure 8.6, shows this clearly. The horizontal motion (Figure 5.5) also shows that the 16 Hz and 48 Hz inputs produce large responses near the load.

In particular, Figure 5.5 shows that 16 Hz ($\Omega^2 = 0.033$) is a special case: the amplitude at the edge of the load, marked by the inflection at $|w|/a \simeq 14.8$, is nearly twice that of any other frequency.

The only known results which can in any way be compared with these, are from Waas [79]. He considered the somewhat different problem of a disc embedded in an inhomogeneous layer over bedrock. He gives a non-dimensionalised figure of displacements against distance, which can be matched with the $\Omega^2 = 0.131$ case here. The results are of a very similar form, despite the models' differences.

From the results in this Chapter and the bedrock receptance Figures in Chapter 8, it is clear that the bedrock undamped resonant frequencies below 64 Hz are given by the natural frequencies of a one dimensional rod, and by the turning frequency of the fourth mode.

Figure 5.6 shows the extension of Figure 5.4 to $\kappa/a = 100$, using a dB log scale for each graph. Figure 5.7 is similar, the only difference being that $\eta = 0.02$. The reduction in damping greatly reduces the attenuation. In the bedrock model, there is no "radiation damping" as in the half-space, and all the energy is trapped in the layer. Hence the internal damping is the only cause of dissipation. The Clarborough 16 Hz (or $\Omega^2 = 0.033$) curves can be misleading, because the reference value at $\kappa/a = 0$ is so much larger than for the other frequencies. So the greater attenuation of these curves does not imply that their displacement amplitudes are smaller than the others. The lower damping (Figure 5.7) does not inhibit the interference effect in the 16 Hz curve, and the minimum at $\kappa/a \simeq 16$ now appears to be the first of several minima, which are much less clearly defined with larger damping. The 32 Hz ($\Omega^2 = 0.131$) curve also has an almost regular interference pattern, but the higher frequency graphs are more complex.

Figure 5.9, the equivalent attenuation graph for Checkerhouse, is included here principally to put the Clarborough 16 Hz resonance into perspective. The lowest non-dimensionalised frequency in Figure 5.9, $\Omega^2 = 0.122$, corresponds to 16 Hz at Checkerhouse. Likewise, the higher frequencies are equivalent to 32, 48 and 64 Hz at Checkerhouse. The

interference pattern for each curve is less dense than in Figures 5.6 and 5.7, because the wavespeeds and therefore wavelengths are double those of Clarborough:

Checkerhouse wavespeeds: $c_1 = 889\ ms^{-1}$, $c_2 = 567\ ms^{-1}$
$c_R = 513\ ms^{-1}$ (5.30)

At Checkerhouse, the main resonant frequency is at $889/(4 \times 20) = 11.11$ Hz. Also, at 16 Hz there are only two propagating waves. Therefore the 16 Hz curve is not a resonance case, and shows little sign of interference. Its (unshown) phase change with distance reveals a wavenumber slightly larger than the first modes', due to the damping. It is attenuated least because it is the lowest frequency (see Section 2.2).

Figure 5.10 shows the effect on direct receptance of varying the width of the load. The graphs can be compared with similar ones for the half-space, in Figure 3.10. Compared with the half-space, the bedrock reduces the amplitudes slightly. The maximum displacement per frequency is for a different width than in the half-space, because clearly the "resultant wavelength" (see the last part of Section 3.5) will also be different. However, at the higher frequencies, when the bedrock and half-space solutions start to merge, the graphs are quite similar.

Figure 5.11 shows a representation of the deflections under the load. The spread of material to the edge of the load is clear. Also, a "buckling" of material near the layer base is apparent, with the displacement to T' being larger than O', for example. The boundary condition requires zero displacement at the bottom of the layer.

CHAPTER 6

FREE VIBRATION IN AN ELASTIC LAYER OVER AN ELASTIC HALF-SPACE

6.1 Introduction

In this Chapter, the ground is modelled as an elastic, homogeneous, isotropic layer, over-lying an elastic, homogeneous, isotropic half-space, of different material properties to the layer. The natural modes of free vibration are analysed, and the results are used to help explain the forced response due to an harmonic strip load, presented in the next Chapter.

Ground vibration literature contains much work on the natural propagating modes in a layer over a half-space. The case of a liquid layer, which is less complicated than the corresponding ground layer problem, due to the lack of shear waves in the liquid, was first investigated by Pekeris [62], who considered isovelocity water over an homogeneous water bottom. The extension to other velocity structures, by perturbation of the Pekeris solution, is presented by Williams [86], and sound propagation in a channel with "lossy" boundaries is considered by Bucher [8]. The case of a liquid layer over a solid half-space is treated by Pack [84]. Although the methods of these workers are inappropriate for the present problem, their solutions can help explain phenomena occuring in the solid layer problem.

Previous work on the ground model of an elastic layer over an inflexible half-space, is considered in Chapters 4 and 5. The extension of Lord Rayleigh's original work on surface waves [67], to include waves propagating at the interface of two solid media, was begun by Stoneley [73]. In the present problem, his work relates to waves at the interface of the layer and half-space. Fu [18] has shown that the free wave solution for the present problem, when the layer depth is much larger than the wavelength, is described by the product of the period equations for the Rayleigh and Stoneley waves. However, Fu also demonstrates that the interaction between the Rayleigh and Stoneley waves in a layer is negligible, provided the wavelength of interest is greater than the layer depth. In any case, Scholte and Sezawa and Kanai [10,34] have shown that "true" Stoneley waves (see the next paragraph) can only exist under

special circumstances. The relevance of these considerations to the present problem is considered in Section 6.5.

The expression "true Stoneley wave" is used by Phynney [65] to distinguish between the wave investigated by Stoneley and the related "leaking Stoneley wave" which can exist with exceptional combinations of layer and half-space material properties. Phynney summarises the original work of Gilbert and Laster on this subject [83]. "Leaky" modes arise from the so-called extraneous roots of the period equation; their place in the present ground model solution is considered in Section 6.5. Fu attempted a physical interpretation of the extraneous roots [87], and Phynney has approached the problem using the contour integration formulation, leading to asymptotic expressions for ground displacements, used in much previous work (see for example the classic work of Lamb, [45]. Subsequent workers have used more recent and more powerful techniques to cope with more complicated load boundary conditions). In this formulation, the leaky modes appear as poles on Riemann sheets other than the principal sheet of integration. Chapman [12] has helped to clarify the significance of the leaky modes.

It should be noted that the expression "leaky" mode, coined by acousticians concerned with sound propagation in water, can be slightly misleading to a structural engineer. The complex behaviour of these inhomogeneous waves, with energy flowing from the layer into the half-space, where no reflection occurs at infinity, does not match the usual definition of "mode" as applied to structures.

Several workers in this field give dispersion figures for the natural modes. Tolstoy and Usdin [77] use the interference principle of waveguide propagation, to produce period equations for a variety of liquid and solid layer combinations, including the model under consideration here. They give dispersion curves (the variation of wavespeed with wavenumber) for the first two natural modes. Kuhlemeyer [43] has also produced dispersion curves for the first two modes, using a Finite Element formulation of the "elastic foundation" problem. Newlands [54] has used a similar mathematical formulation to that of Section 6.5 here, to produce an approximation to the period equation valid for large values of ζd, where ζ is the wavenumber and d the layer depth. The results of this

work are found to agree closely with Newlands' approximation for (ξd) > 25, provided his material properties are used.

The mathematical analysis presented here is similar to that of Fu, and Newlands [18,54]. By substituting for the displacements in Navier's elastodynamic equations with potential functions, and assuming harmonic waves with no transverse motion (which is the form of waves produced by the strip load of Chapter 7), a solution is sought for the relevant boundary conditions, zero surface stresses, and continuity of stresses and displacements at the layer/half-space interface. This gives the period equation as a determinant equated to zero. Fu merely checks this equation for the special cases d=0 and d=∞, when the equation reduces to the period equation of the Rayleigh and Stoneley waves respectively, and Newlands gives an approximate solution for large wavenumber. A solution for smaller wavenumbers is algebraically very complicated.

However, an alternative method of obtaining the dispersion curves is now possible, due to the work of Wittrick and Williams [89]. Their method allows the eigenvalue solution of the non-linear dynamic stiffness matrix for the elastic foundation model, subject to the matrix having a minimum number of layers. The method, and also the minimum number of layers required, is explained in Section 6.3. The only limitation of the method is that the solution wavenumbers (the eigenvalues) must be real. This excludes solutions for "leaky" modes, which have complex wavenumbers. Fortunately, modes with complex wavenumbers only exist for mode wavespeeds greater than the shear wavespeed in the half-space, which is typically much higher than the body wavespeeds in the layer, and so dispersion curves can be deduced for much of the wavenumber region of interest (see Figure 6.2).

The shapes of the natural modes could be derived directly from the solution of the stiffness matrix described above, but to give accurate shapes of the higher order modes would require many layers and therefore much computation. A more elegant method is to solve the period equation derived in Section 6.2, for a particular natural frequency and wavenumber pair. This immediately yields the displacements due to the corresponding mode, both in the layer and the half-space.

6.2 Analysis of Free Vibration in an Elastic Layer Over-Lying an Elastic Half-Space

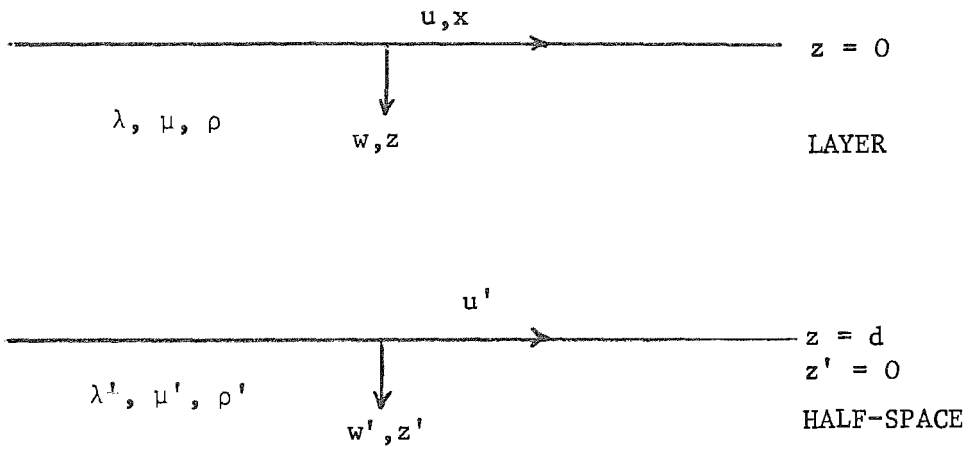

Fig 6.1: Diagram of Ground Structure Model

Figure 6.1 shows the model of the ground structure used in this analysis, known here as the "elastic foundation" model. The layer and half-space have different material properties, and their interface lies along the plane Z=d. The grounds' surface is the plane Z = 0.

Navier's elastodynamic equations are required (see Section 3.2):

$$(\lambda+\mu)\,\underline{\nabla}\Delta + \mu\nabla^2\underline{v} = \rho\,\frac{\partial^2\underline{v}}{\partial t^2} \qquad (6.1)$$

where $\underline{v}$ is the vector of displacements u and w, and $\Delta = \frac{\partial u}{\partial x} + \frac{\partial w}{\partial z}$.

Introducing potential functions Φ and H (see Section 3.2), for the displacements u and w in the layer, such that:

$$u = \frac{\partial\phi}{\partial x} - \frac{\partial H}{\partial z}\,; \qquad w = \frac{\partial\phi}{\partial z} + \frac{\partial H}{\partial x} \qquad (6.2)$$

then for harmonic motion of angular frequency ω, equation (6.1) separates into two wave equations:

$$\nabla^2\phi + k_1{}^2\phi = 0 \qquad (6.3)$$

and $$\nabla^2 H + k_2^2 H = 0 \qquad (6.4)$$

where k_1, k_2 are the compression and shear wavenumbers respectively defined by

$$k_1^2 (\lambda+2\mu) = \mu k_2^2 = \rho\omega^2 \qquad (6.5)$$

The harmonic solutions for ϕ and H are of the form:

$$\phi = \phi(Z)e^{i(\omega t-\zeta x)}$$
$$H = H(Z)e^{i(\omega t-\zeta x)} \qquad (6.6)$$

where ζ is the wavenumber (or rate of change of phase) of horizontal waves. Substituting equation (6.6) in equations (6.4) and (6.5) and suppressing the $e^{i\omega t}$ term, leads to:

$$\phi''(Z) - (\zeta^2-k_1^2)\,\phi(Z) = 0 \qquad (6.7)$$

and $$H''(Z) - (\zeta^2-k_2^2)\,H(Z) = 0 \qquad (6.8)$$

where the " denotes double differentiation w.r.t. time. It should be remembered that ' indicates a property in the half-space.

For the half-space, introduce potential functions θ and G, such that the half-space displacements u' and w' are given by:

$$u' = \frac{\partial\theta}{\partial x} - \frac{\partial G}{\partial z}, \quad w' = \frac{\partial\theta}{\partial z} + \frac{\partial G}{\partial x} \qquad (6.9)$$

For continuity at the interface, the horizontal wavenumber ζ must be the same in both the layer and the half-space. Therefore for harmonic θ and G, we have:

$$\theta''(Z') - (\zeta^2 - k_1'^2)\,\theta(Z') = 0 \qquad (6.10)$$

$$G''(Z') - (\zeta^2 - k_2'^2)\, G(Z') = 0 \qquad (6.11)$$

where

$$k_1'(\lambda' + 2\mu') = \mu' k_2' = \rho'\omega^2 \qquad (6.12)$$

Putting

$$\left.\begin{aligned} \alpha^2 &= \zeta^2 - k_1^2 \;; \quad \beta^2 = \zeta^2 - k_2^2 \\ \alpha'^2 &= \zeta^2 - k_1'^2; \quad \beta'^2 = \zeta^2 - k_2'^2 \end{aligned}\right\} \qquad (6.13)$$

gives the following solutions to equations (6.7), (6.8), (6.10), and (6.11):

$$\phi(Z) = A_1 e^{-\alpha z} + A_2 e^{\alpha z} \qquad (6.14)$$

$$H(z) = B_1 e^{-\beta z} + B_2 e^{\beta z} \qquad (6.15)$$

$$\theta(z) = C_1 e^{-\alpha' z'} + C_2 e^{\alpha' z'} \qquad (6.16)$$

$$G(z) = D_1 e^{-\beta' z'} + D_2 e^{\beta' z'} \qquad (6.17)$$

where A_i, B_i, C_i, D_i, i=1 or 2, are constants of integration. On physical grounds, C_2 and D_2 must be zero, as no reflection of energy occurs at infinity. Therefore, substituting equations (6.14)to (6.17) into equations (6.2) and (6.9) gives:

$$u = -i\zeta e^{-i\zeta x}(A_1 e^{-\alpha z} + A_2 e^{\alpha z}) + \beta e^{-i\zeta x}(B_1 e^{-\beta z} - B_2 e^{\beta z}) \qquad (6.18)$$

$$w = \alpha e^{-i\zeta x}(-A_1 e^{-\alpha z} + A_2 e^{\alpha z}) - i\zeta e^{-i\zeta x}(B_1 e^{-\beta z} + B_2 e^{\beta z}) \qquad (6.19)$$

$$u' = -i\zeta C_1 e^{-\alpha' z'} e^{-i\zeta x} + \beta' D_1 e^{-\beta' z'} e^{-i\zeta x} \qquad (6.20)$$

$$w' = -\alpha' C_1 e^{-\alpha' z'} e^{-i\zeta x} - i\zeta D_1 e^{-\beta' z'} e^{-i\zeta x} \qquad (6.21)$$

The continuity of displacement at the interface boundary condition requires $u=u'$, $w=w'$ at $z = d$, $z'=0$.

Therefore equations (6.18) and (6.20) give:

$$-i\zeta(A_1 e^{-\alpha d} + A_2 e^{\alpha d}) + \beta(B_1 e^{-\beta d} - B_2 e^{\beta d}) = -i\zeta C_1 + \beta' D_1 \qquad (6.22)$$

and equations (6.19) and (6.21) give:

$$\alpha(-A_1 e^{-\alpha d} + A_2 e^{\alpha d}) - i\zeta (B_1 e^{-\beta d} + B_2 e^{\beta d}) = -\alpha' C_1 - i\zeta D_1 \qquad (6.23)$$

Multiplying equation (6.22) by $(i\zeta/\beta')$ and then adding to equation (6.23) gives the following expression for C_1:

$$C_1 = \frac{1}{\zeta^2 - \alpha'\beta'} \left\{ \begin{array}{c} A_1 e^{-\alpha d}(\zeta^2 - \alpha\beta') + A_2 e^{\alpha d}(\zeta^2 + \alpha\beta') + i\zeta B_1 e^{-\beta d}(\beta - \beta') \\ -i\zeta B_2 e^{\beta d}(\beta + \beta') \end{array} \right\} \qquad (6.24)$$

Likewise, multiplying equation (6.22) by $(\alpha'/i\zeta)$ and then subtracting equation (6.23), gives D_1:

$$D_1 = \frac{-1}{\zeta^2 - \alpha'\beta'} \left\{ \begin{array}{c} A_1 e^{-\alpha d} i\zeta(\alpha - \alpha') - A_2 e^{\alpha d} i\zeta(\alpha + \alpha') - B_1 e^{-\beta d}(\zeta^2 - \alpha'\beta) \\ -B_2 e^{\beta d}(\zeta^2 + \alpha'\beta) \end{array} \right\} \qquad (6.25)$$

The relevant stress components in the layer are defined:

$$\tau_{zz} = \lambda\frac{\partial u}{\partial x} + (\lambda + 2\mu)\frac{\partial w}{\partial z} \qquad (6.26)$$

$$\tau_{zx} = \mu\left(\frac{\partial u}{\partial z} + \frac{\partial w}{\partial x}\right) \qquad (6.27)$$

The equivalent half-space stress equations are obtained by substituting primed quantities in equations (6.26) and (6.27).
From equations (6.18) to (6.21), we have:

$$\frac{\partial u}{\partial x} = -\zeta^2 e^{-i\zeta x}(A_1 e^{-\alpha z} + A_2 e^{\alpha z}) - i\zeta\beta e^{-i\zeta x}(B_1 e^{-\beta z} - B_2 e^{\beta z}) \qquad (6.28)$$

$$\frac{\partial u}{\partial z} = \alpha i\zeta e^{-i\zeta x}(A_1 e^{-\alpha z} - A_2 e^{\alpha z}) - \beta^2 e^{-i\zeta x}(B_1 e^{-\beta z} + B_2 e^{\beta z}) \qquad (6.29)$$

$$\frac{\partial w}{\partial x} = \alpha i\zeta e^{-i\zeta x}(A_1 e^{-\alpha z} - A_2 e^{\alpha z}) - \zeta^2 e^{-i\zeta x}(B_1 e^{-\beta z} + B_2 e^{\beta z}) \qquad (6.30)$$

$$\frac{\partial w}{\partial z} = \alpha^2 e^{-i\zeta x}(A_1 e^{-\alpha z} + A_2 e^{\alpha z}) - i\zeta\beta e^{-i\zeta x}(-B_1 e^{-\beta z} + B_2 e^{\beta z}) \qquad (6.31)$$

$$\frac{\partial u'}{\partial x} = -\zeta^2 C_1 e^{-\alpha' z'} e^{-i\zeta x} - i\zeta\beta' D_1 e^{-i\zeta x} e^{-\beta' z'} \qquad (6.32)$$

$$\frac{\partial u'}{\partial z'} = \alpha' i\zeta C_1 e^{-\alpha' z'} e^{-i\zeta x} - \beta'^2 D_1 e^{-i\zeta x} e^{-\beta' z'} \qquad (6.33)$$

$$\frac{\partial w'}{\partial x} = \alpha' i\zeta C_1 e^{-i\zeta x} e^{-\alpha' z'} - \zeta^2 D_1 e^{-i\zeta x} e^{-\beta' z'} \qquad (6.34)$$

$$\frac{\partial w'}{\partial z'} = \alpha'^2 C_1 e^{-i\zeta x} e^{-\alpha' z'} + i\zeta\beta' D_1 e^{-i\zeta x} e^{-\beta' z'} \qquad (6.35)$$

Equations (6.28) to (6.35) can now be used with equations (6.26) and (6.27), to apply the stress boundary conditions. The stress components are continuous, at z=d, z'=0; therefore equating τ_{zz} at z=d with $\tau'_{z'z'}$ at z'= 0 and cancelling the term $e^{-i\zeta x}$ gives:

$$(A_1e^{-\alpha d}+ A_2e^{\alpha d})\{(\lambda+2\mu)\alpha^2-\lambda\zeta^2\} + 2\mu i\zeta\beta\ (B_1e^{-\beta d}- B_2e^{\beta d})$$

$$= C_1\ (\alpha'^2\ (\lambda' +2\mu')- \zeta^2\lambda') + 2\mu' i\zeta\beta' D_1 \qquad (6.36)$$

Similarly, continuity of τ_{zx} gives:

$$2\mu\alpha i\zeta\ (A_1e^{-\alpha d} - A_2e^{\alpha d}) - \mu(\beta^2+\zeta^2)\ (B_1e^{-\beta d} + B_2e^{\beta d})$$

$$= \mu'(2\alpha' i\zeta C_1 - (\beta'^2 + \zeta^2)\ D_1\ ) \qquad (6.37)$$

At the free surface, z=0, and $\tau_{zz} = 0$, yield

$$(A_1+A_2)\ \{\alpha^2(\lambda+2\mu) - \lambda\zeta^2\} + 2\mu i\zeta\beta(B_1-B_2) = 0 \qquad (6.38)$$

Similarly, at z=0, $\tau_{zx} = 0$, therefore

$$2\alpha i\zeta\mu(A_1-A_2) - \mu(\beta^2+\zeta^2)\ (B_1+B_2) = 0 \qquad (6.39)$$

Equations (6.24) and (6.25) (for C_1 and D_1) can now be substituted into equations (6.36) and (6.37) giving:

$$A_1e^{-\alpha d}\ \{E-F.O + H.U\} + A_2e^{\alpha d}\ \{E-F.P -H.V\} + B_1e^{-\beta d}\{G-F.S-H.Q\}$$

$$+ B_2e^{\beta d}\{-G + F.T - H.R\} = 0 \qquad (6.40)$$

and

$$A_1 e^{-\alpha d}\{W-X.O-Z.U\} + A_2 e^{\alpha d}\{-W-X.P+Z.V\}$$

$$+ B_1 e^{-\beta d}\{-Y-X.S+Z.Q\} + B_2 e^{\beta d}\{-Y+X.T+Z.R\} = 0 \qquad (6.41)$$

where:

$$\left.\begin{aligned} E &= (\lambda+2\mu)\alpha^2 - \lambda\zeta^2 = 2\mu\zeta^2 - (\lambda+2\mu)k_1^2 \\ F &= (\lambda'+2\mu')\,\alpha'^2 - \lambda'\zeta^2 = 2\mu'\zeta^2 - (\lambda'+2\mu')k_1'^2 \end{aligned}\right\} \qquad (6.42)$$

$$G = 2\mu i\zeta\beta; \qquad H = 2\mu' i\zeta\beta' \qquad (6.43)$$

$$O = \frac{\zeta^2-\alpha\beta'}{\zeta^2-\alpha'\beta'}\,; \quad P = \frac{\zeta^2+\alpha\beta'}{\zeta^2-\alpha'\beta'}\,; \quad Q = \frac{\zeta^2-\alpha'\beta}{\zeta^2-\alpha'\beta'}\,; \quad R = \frac{\zeta^2+\alpha'\beta}{\zeta^2-\alpha'\beta'}, \qquad (6.44)$$

$$S = \frac{i\zeta(\beta-\beta')}{\zeta^2-\alpha'\beta'}\,; \qquad T = \frac{i\zeta(\beta+\beta')}{\zeta^2-\alpha'\beta'} \qquad (6.45)$$

$$U = \frac{i\zeta(\alpha-\alpha')}{\zeta^2-\alpha'\beta'}\,; \qquad V = \frac{i\zeta(\alpha+\alpha')}{\zeta^2-\alpha'\beta'} \qquad (6.46)$$

$$W = 2\mu\alpha i\zeta\,; \qquad X = 2\mu'\alpha' i\zeta \qquad (6.47)$$

$$Y = \mu(\beta^2+\zeta^2)\,; \qquad Z = \mu'(\beta'^2+\zeta^2) \qquad (6.48)$$

Putting $\{A\} = [A_1 \;\; A_2 \;\; B_1 \;\; B_2]^T$ (6.49)

equations (6.38) to (6.41) can be written as

$$[M]\{A\} = 0 \qquad (6.50)$$

so that for non-trivial solutions, the determinant of [M] must equal zero. We have:

$$\det[M] = \begin{vmatrix} (E-F.O+H.U).e^{-\alpha d} & (E-F.P-H.V).e^{\alpha d} & (G-F.S-H.Q).e^{-\beta d} & (-G+F.T-H.R).e^{\beta d} \\ (W-X.O-Z.U).e^{-\alpha d} & (-W-X.P+Z.U).e^{\alpha d} & (-Y-X.S+Z.Q).e^{-\beta d} & (-Y+X.T+Z.R).e^{\beta d} \\ E & E & G & -G \\ W & -W & -Y & -Y \end{vmatrix} = 0 \qquad (6.51)$$

Equation (6.51) is the period equation for the elastic foundation model, and has been found algebraically too complicated to be solved analytically [18,54].

In Section 6.3, an alternative method for finding the natural frequencies of the system is described. Once these are known, equation (6.50) can be solved to give A_1, A_2, B_1 and B_2 to within an arbitrary mutliplicative constant. Substitution of these into equations (6.24) and (6.25), and then (6.18) to (6.21), gives the modeshapes.

6.3 Numerical Solution of the Dynamic Stiffness Matrix and its Application to Finding the Modeshapes

Because it is not practical to solve equation (6.51) analytically, an alternative approach to find the natural frequencies of the layer will be used. By a simple combination of the analysis in Chapters 3 and 5, the dynamic stiffness matrix for the elastic foundation model can be derived. This derivation is actually performed in Chapter 7 (see equation (7.3)), but this dynamic stiffness matrix will also be used here. The matrix, denoted [T], is such that

$$[T]\ [\bar{W}] = [\bar{\tau}] \qquad (6.52)$$

where $[\bar{W}]$ is the vector of Fourier transformed vertical and horizontal displacements, and $[\bar{\tau}]$ is the vector of the corresponding stresses, at each of several sub-layers composing the surface layer. It is necessary

to divide the layer into these sub-layers, to avoid computational problems described in Chapter 7.

If the load in this forced response problem is removed, setting the stress vector $[\bar{\tau}]$ to zero (all elements of $[\bar{\tau}]$ other than the top two are zero due to the stiffness matrix formulation - see Ch. 7), the equation for free vibrations results:

$$[T]\ [\bar{W}] = 0 \qquad (6.53)$$

Clearly non-trivial solutions will correspond to [T] having a zero determinant.

Throughout this analysis, the exact matrix [T] will be used, not a linear approximation to the matrix, as used in the "bedrock" work of Chapter 4. Matrix [T] is non-linear, and so a special method due to Wittrick and Williams [89] will be used to find its eigenvalues. This method allows the solution for the natural frequencies of the system which correspond to a given real wavenumber. The method wil now be described, using the notation of [89].

A quantity called the Sign Count of [T], denoted s{T}, must be defined. This is most easily defined in terms of the upper triangular form of [T], denoted T^{Δ}, which is the equivalent form of [T] with only zeroes below the leading diagonal. This is derived by subtracting the necessary fractions of the first row of [T] from each of the other rows, in order to make the first element of each other row equal zero. The modified second row is then used in a similar fashion, to reduce the second element of each subsequent row to zero, and so on for all the rows. The sign count s{T} is then equal to the number of negative elements on the diagonal of T^{Δ}. Also requiring definition are the quantities $J(\omega^*)$ and $J_o(\omega^*)$. $J(\omega^*)$ is the number of natural frequencies of [T] which exist below the fixed chosen frequency ω^*, and $J_o(\omega^*)$ is the number of natural frequencies of [T] which exist below ω^*, if constraints are imposed at every sub-layer interface (including the top and bottom of the layer) to prevent any motion at those depths, ie. the displacement vector $\underline{D}$ describing the motion at the sub-layers is made zero.

Then the algorithm deduced by Wittrick and Williams states that

$$J(\omega^*) = J_o(\omega^*) + s\{T(\omega^*)\} \qquad (6.54)$$

This relation is proved in a lucid manner in [89].

With equation (6.54), computation of the dispersion curves shown in Figures 6.2 and 6.3 is straightforward. For a chosen frequency ω^*, $J_o(\omega^*)$ can be reduced to zero by making the height of each sub-layer less than a critical height. This critical height can be found easily, by a modification to the dynamic stiffness matrix for the "bedrock" model (see Chapter 4), which describes a layer with a free surface, lying on an inflexible half-space. If no motion is allowed at either the base or the surface of the layer, then the conditions for the calculation of $J_o(\omega^*)$ for a single layer are satisfied. Provided every sub-layer has the same height, they are all identical, and so $J_o(\omega^*)$ for each layer is the same. Because of the form of the dispersion curve for this layer with fixed surfaces, the lowest natural frequency of a propagating wave corresponds to that of the fundamental mode at zero wavenumber (see Fig. 4.1 for the equivalent "bedrock" model dispersion curve). Reducing the layer height increases this lowest frequency, and so by making the height sufficiently small, this lowest frequency will exceed ω^*. The program EFEIG, which performs this calculation, is listed in Appendix B, and its results are given in the next section.

If the number of sub-layers, n, is now chosen large enough to make the height of each sub-layer of $T(\omega^*)$, less than the critical height calculated by the above method, equation (6.54) reduces to:

$$J(\omega^*) = s\{T(\omega^*)\} \qquad (6.55)$$

Computation of the sign count of $T(\omega^*)$, for a chosen wavenumber ζ, is a fast and simple process. The natural frequencies ω_n, which exist for ζ, and are less than ω^* can be found using a bisection method based on reducing ω^*, and finding the change (if any) in the integer value of $s\{T(\omega^*)\}$. Program EFIND uses this approach to plot the dispersion curves in Figures 6.2 and 6.3, and program EIGFREQ calculates individual natural frequency and wavenumber pairs very accurately, using quadruple

precision, to be used in plotting the modeshapes. Program EIGFREQ is closely related to program EFIND, which is listed in Appendix B.

Once the natural frequency for a particular wavenumber is known from program EIGFREQ, equation (6.50) can be used to give the constants of equation (6.49), to within an arbitrary constant. A slight complication is that this constant is in general complex. However, because the modeshapes are described by real values, the ratio of the real and imaginary parts of the arbitrary constant can be determined. As explained at the end of Section 6.2, the modeshapes can then be calculated. Program MODE2 in Appendix B evaluated and plotted the modeshapes in Figures 6.4 to 6.7.

6.4 Results

6.4.1 Material Properties

The material properties used in this chapter match those of previous Chapters, and correspond to properties measured experimentally at the British Rail test-site "Clarborough", which has a layer depth of 7m. These are summarised and listed in Table 2.2. Additionally, the relevant wavespeeds are listed in Table 6.1:

Wavespeed	Layer	Half-Space
Compression Wavespeed (ms^{-1})	459.4	3007.3
Shear Wavespeed (ms^{-1})	262.7	1880.3
Rayleigh Wavespeed (ms^{-1})	241.9	1707.2

TABLE 6.1: Wavespeeds in layer and half-space, elastic foundation model

The Rayleigh wavespeeds are calculated from equation (4.14).

6.4.2 Results for the Determination of the Minimum Required Size of the Dynamic Stiffness Matrix

As explained in Section 6.3, the dynamic stiffness matrix for the layer must have sufficient sub-layers to ensure that each layer, if it were held rigid at each interface, would allow no wave propagation below the maximum frequency of interest. Table 6.2 gives the results from program EFEIG, which divides the 7m layer at Clarborough into integer numbers of sub-layers, and then computes the lowest value of the fundamental frequency. Because EFEIG uses a linearised approximation to the dynamic stiffness matrix, the program further sub-divides each sub-layer into sufficient layers to make the linear approximation valid (see Chapter 4 for an explanation of the sufficient conditions).

Number of sub-layers	Depth of each sub-layer (m)	Lowest value of fundamental frequency (Hz)
1	7	18.7806
2	3.5	37.5612
3	2.333	56.3418
4	1.75	75.1224
5	1.4	93.9030

TABLE 6.2 The effect of layer depth on the fundamental frequency of a layer held rigid at both interfaces

For the frequency range of interest, which is below 64Hz, it is clear that four sub-layers each of height 1.75m are required for the eigenvalue solution of the dynamic stiffness matrix.

Note that the lowest fundamental frequency is inversely proportional to the layer depth, for this layer with fixed boundaries. Also, these boundary conditions produce a higher value of the lowest fundamental frequency than in the "bedrock" model (Chapter 4), as can be expected from

the greater stiffness. In fact, the bedrock lowest fundamental frequency for a given layer depth is exactly half that of the layer rigid at both surfaces, and so it is 9.4Hz for a 7m layer.

6.4.3 Description of the Figures

Figures 6.2 and 6.3 were produced by the program EFIND. Figure 6.2 shows the variation of wavenumber with frequency for the first six natural modes, for wavenumbers greater than k_2', the shear wavenumber in the half-space. For reference purposes, three extra lines have been superimposed on the graph, to show the variation of wavenumber with frequency of the compression and shear waves in the layer, and the shear wave in the half-space. The variation of the Rayleigh wavenumber for the layer, is coincident wth the first mode above 30Hz. Figure 6.3 is a different interpretation of the information shown in Figure 6.2. Here wavespeed variation with frequency for the first six natural modes is shown. Because of the great variation in wavespeeds, a log scale has been used. Reference points on the scale show the Rayleigh, shear and compression wavespeeds in the layer, and the Rayleigh wavespeed in the half-space . The half-space shear wavespeed is shown as a line across the graph, to show the limit of the solution.

Figure 6.4 shows the variation of amplitude (to within an arbitrary constant) of the vertical and horizontal motion components of the first and second modes, plotted against non-dimensional depth. Variations in both the layer and half-space are shown, for a pair of frequencies for each mode. Figure 6.5 is similar to Figure 6.4, but shows the third mode amplitude variations, for four different frequencies. The lowest frequency graph shows the shape of the third mode at a wavenumber close to k_2'. Figure 6.6 shows three graphs of the fourth modeshapes; the lowest frequency is again for a wavenumber near to k_2'. Figure 6.7 follows the same pattern as Figures 6.4 to 6.6, with two graphs for each of the fifth and sixth modeshapes.

Figures 6.4 to 6.7 were all plotted by the program MODE2, after initially finding very accurate values of the natural frequencies for chosen wavenumbers. To ensure good solutions of equation (6.50), these frequencies were found to 14 decimal places. Table 6.3 gives the first ten decimal places of all the natural frequencies used in the Figures. In addition, the natural frequency of the first mode at very low wavenumber is given.

Mode Number	Natural Frequency (Hz)	Wavenumber (ζ)
1	0.0027118335	0.00001
1	14.7154135863	0.35
1	57.7484706315	1.5
2	14.8140575665	0.2
2	41.9628403395	0.8
3	20.1225704611	0.07
3	29.8069828493	0.3
3	44.1564817126	0.6
3	59.8292569719	1.0
4	32.8675640479	0.11
4	38.6191778612	0.4
4	58.5943808847	0.8
5	40.1606909848	0.14
5	54.9652960654	0.5
6	57.1908625770	0.2
6	62.5359477427	0.55

TABLE 6.3: Natural frequencies of mode shapes shown in Figures

6.4.4 Comparison with previous results

Previous work has produced dispersion curves for the first two natural modes [43,54,77] the form of which is similar to the first and second mode curves in Figure 6.3. Direct comparison is not possible, since different material properties have been used in each case. However, Newlands [54] has found the following approximate relation valid for large (ζd):

$$\tan\{\zeta d(c^2/c_2^2-1)^{1/2}\} = \frac{4(c^2/c_2^2-1)^{1/2}(1-c^2/c_1^2)^{1/2}S-(2-c^2/c_2^2)^2\,T}{4(c^2/c_2^2-1)^{1/2}(1-c^2/c_1^2)^{1/2}T + (2-c^2/c_2^2)^2 S} \qquad (6.56)$$

where $S = \begin{vmatrix} -\zeta & 0 & -\zeta & -(\zeta^2-k_2'^2)^{1/2} \\ (\zeta^2-k_1^2)^{1/2} & -\zeta & -(\zeta^2-k_1'^2)^{1/2} & -\zeta \\ -2\zeta(\zeta^2-k_1^2)^{1/2} & (2\zeta^2-k_2^2) & 2\zeta(\zeta^2-k_1'^2)^{1/2}\mu'/\mu & (2\zeta^2-k_2'^2)\mu'/\mu \\ (2\zeta^2-k_2^2) & 0 & (2\zeta^2-k_2'^2)\mu'/\mu & 2\zeta(\zeta^2-k_2'^2)^{1/2}\mu'/\mu \end{vmatrix}$

and $T = \begin{vmatrix} -\zeta & -(\zeta^2-k_2^2)^{1/2} & . & . \\ (\zeta^2-k_1^2)^{1/2} & 0 & . & . \\ -2\zeta(\zeta^2-k_1^2)^{1/2} & 0 & . & . \\ (2\zeta^2-k_2^2) & 2\zeta(\zeta^2-k_2^2)^{1/2} & . & . \end{vmatrix}$

where the 3rd and 4th columns of T are identical with those of S, and the parameters have the same definitions as before, with k_1', k_2', μ' representing the compression wavenumber, shear wavenumber and shear modulus in the half-space, respectively.

Newlands tabulates values of (ζd) for the first five modes, for a range of c/c_2, where c is the mode wavespeed. He uses material properties defined by $\mu'/\mu=\lambda'/\lambda=20/9$; $\rho'/\rho=5/4$; $\mu=\lambda$, $\mu'=\lambda'$. These material properties were used as a check with the present method, and it was found that for $(\zeta d) > 25$, the difference between the two sets of results was less than 1%.

6.5 Discussion

6.5.1 Analysis of the Results

The significance of the work in this Chapter is in its application to the forced response in the elastic foundation model. In this respect Figure 6.2 shows the principal results, which can be applied directly to

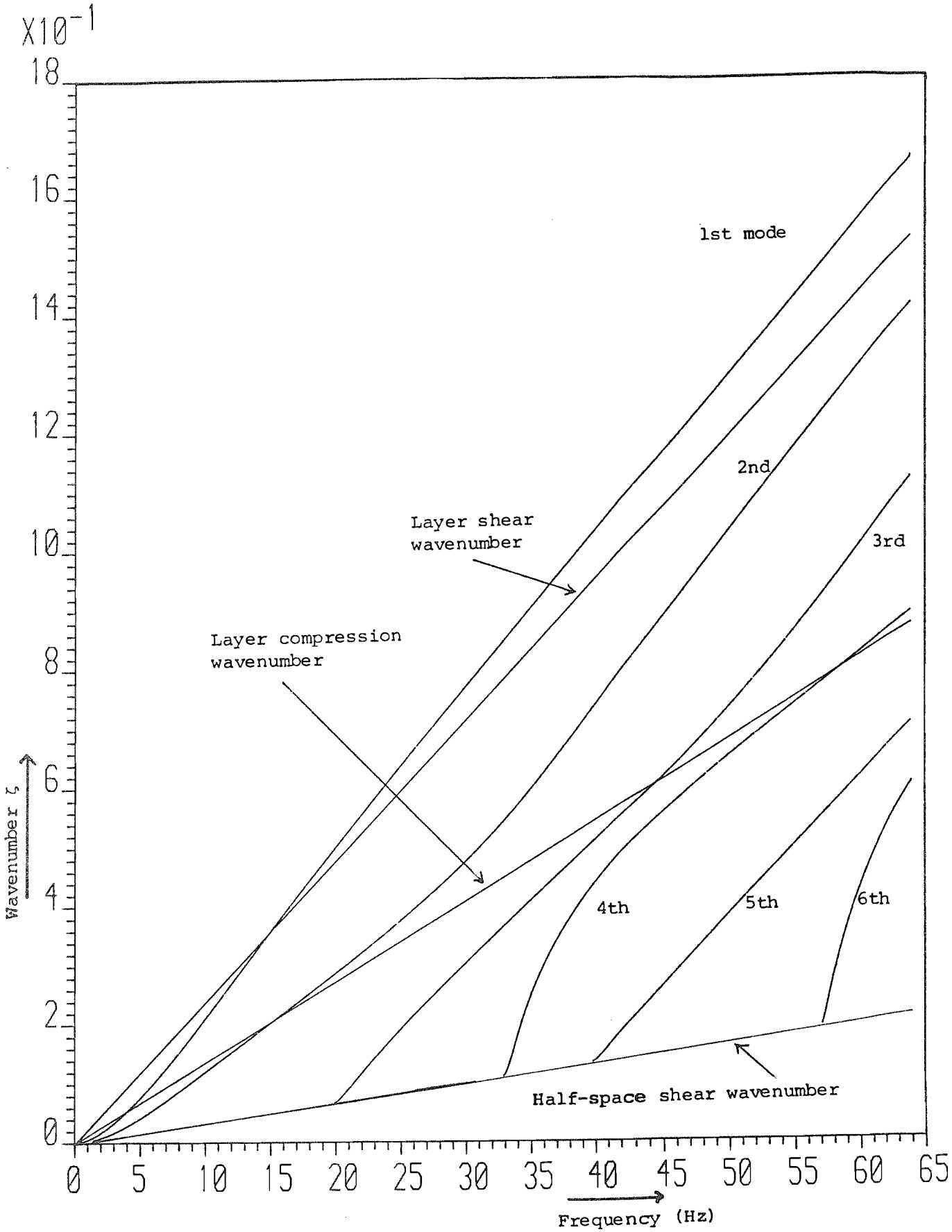

FIGURE 6.2 Wavenumber versus frequency: The first six natural modes of propagation in the elastic foundation layer

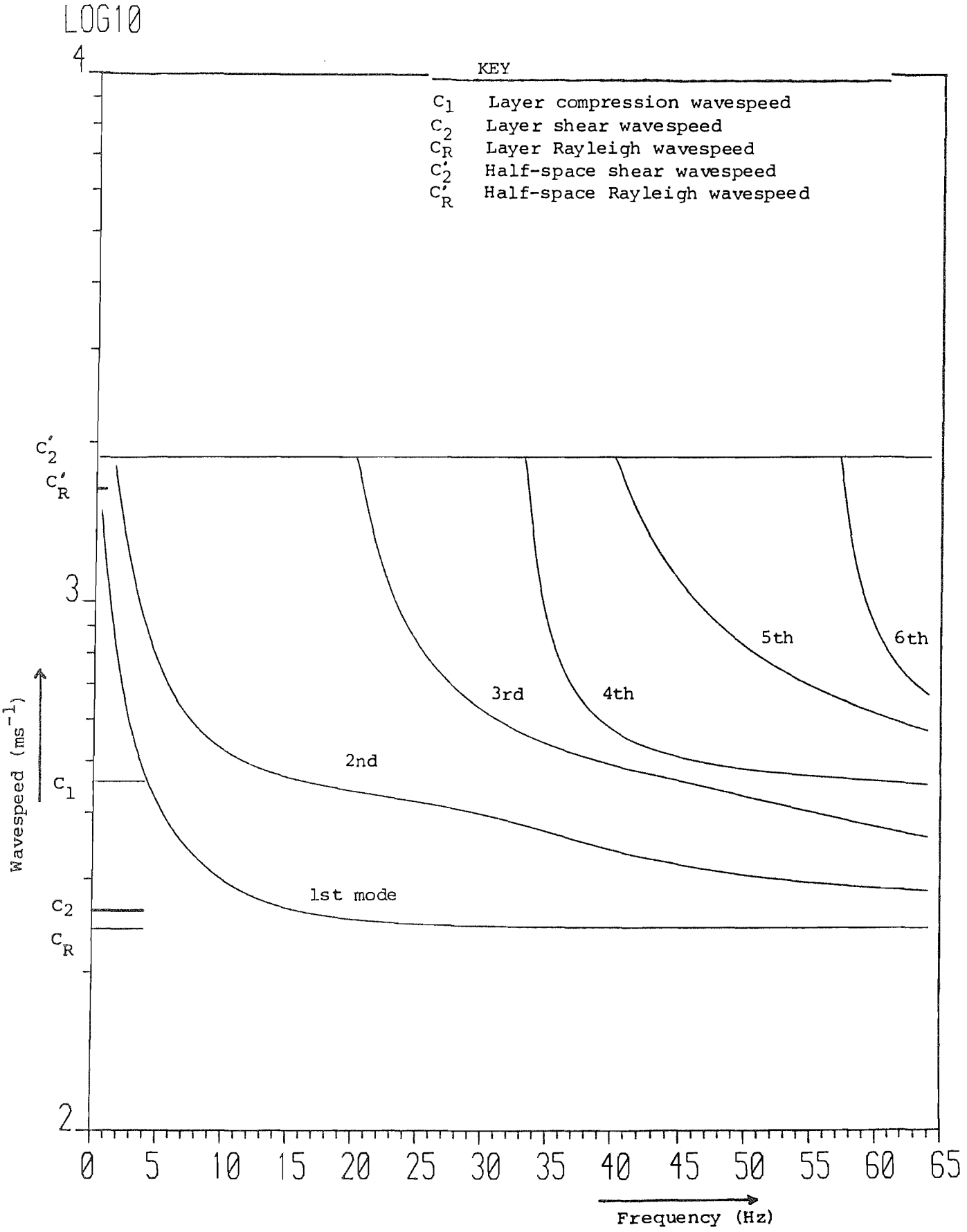

FIGURE 6.3 Wavespeed versus Frequency: The first six natural modes of propagation in the elastic foundation model

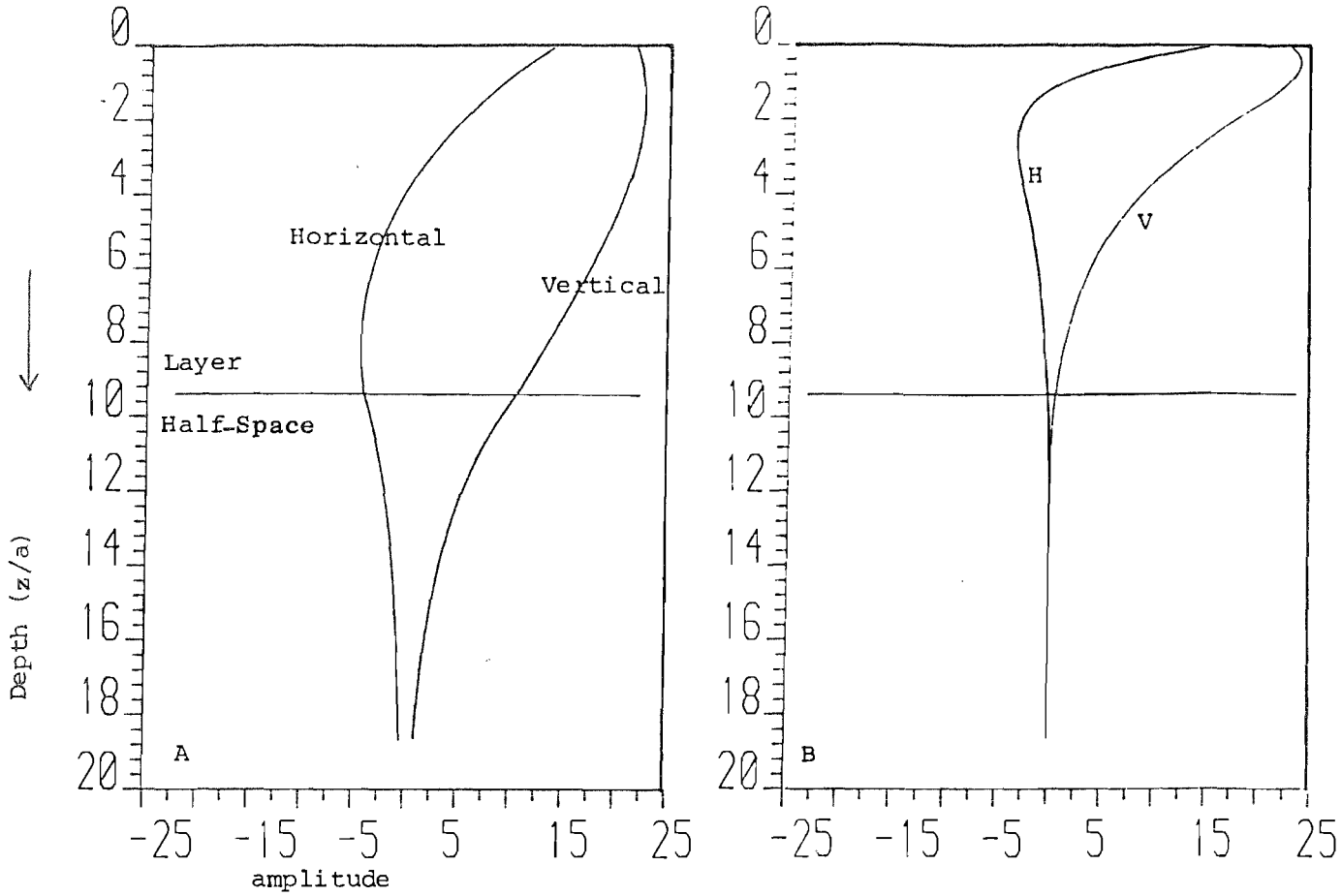

FIGURE 6.4 Vertical and horizontal components of 1st and 2nd modeshapes (All equivalent axes are the same)

GRAPH	MODE NO.	FREQUENCY
A	1st	14.72
B	1st	57.75
C	2nd	14.81
D	2nd	41.96

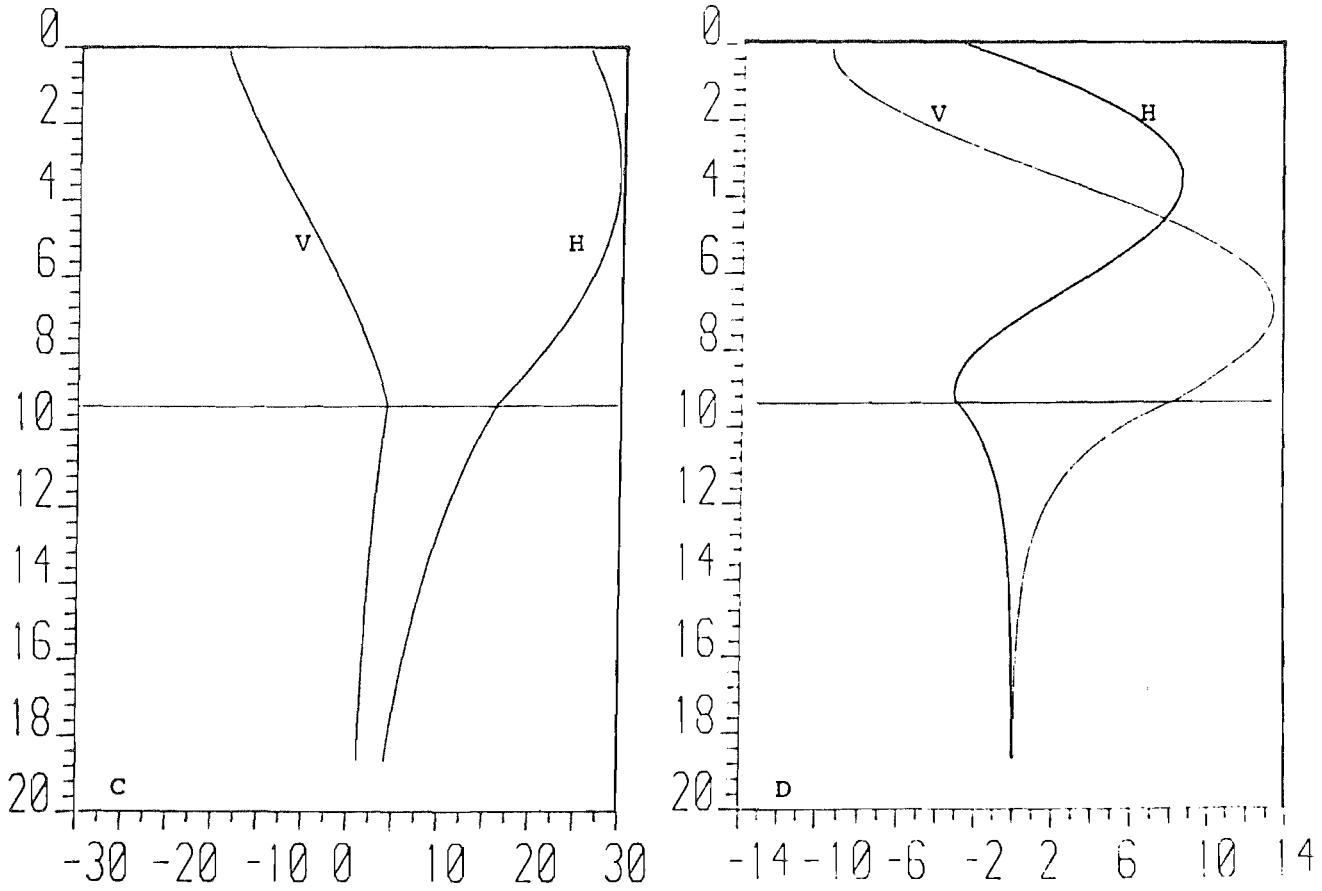

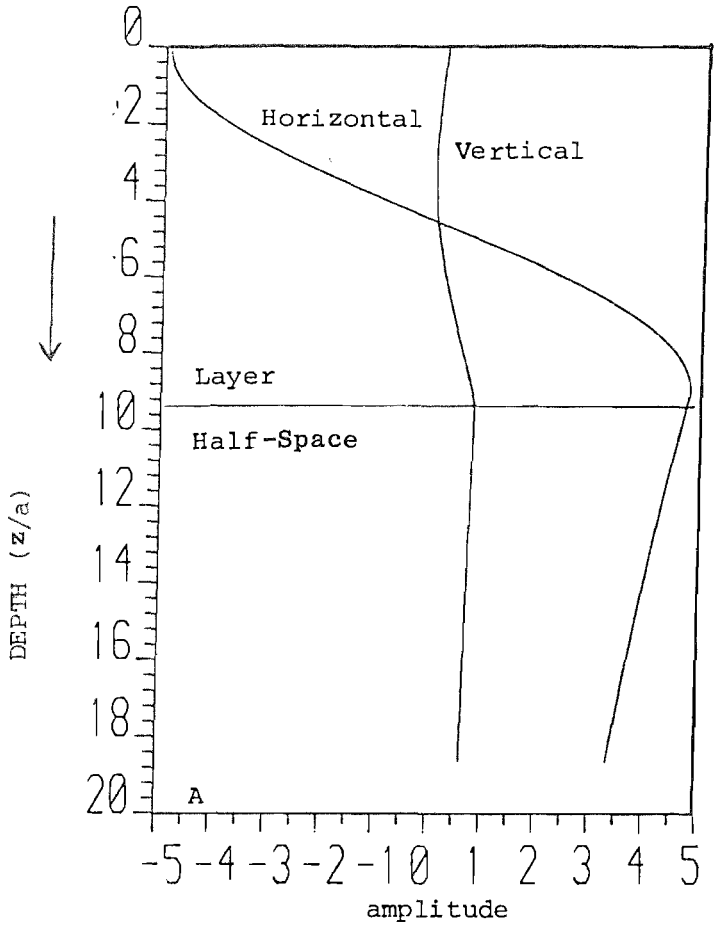

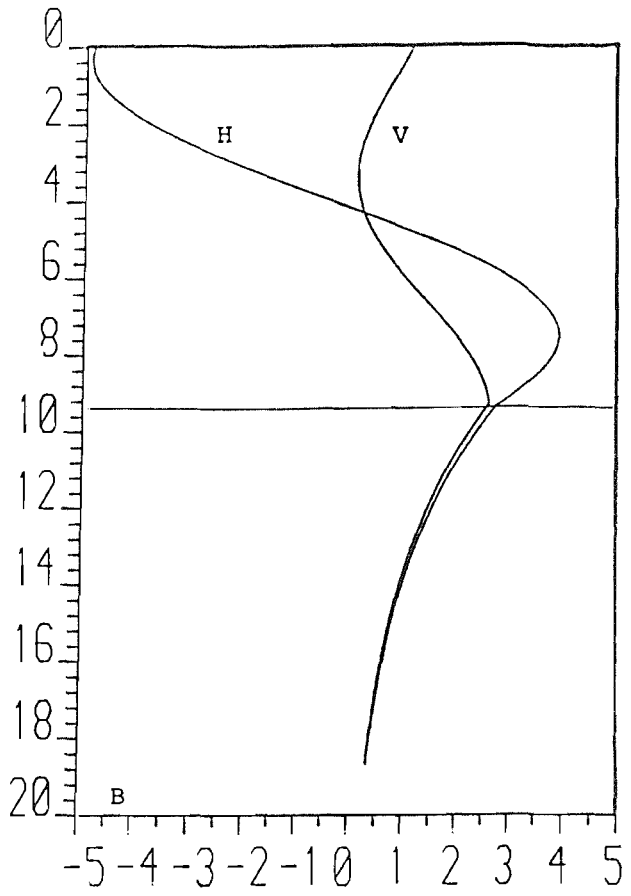

FIGURE 6.5 Vertical and horizontal components of the 3rd modeshapes (All equivalent axes are the same)

GRAPH	MODE NO.	FREQUENCY
A	3rd	20.12
B		29.81
C		44.16
D		59.83

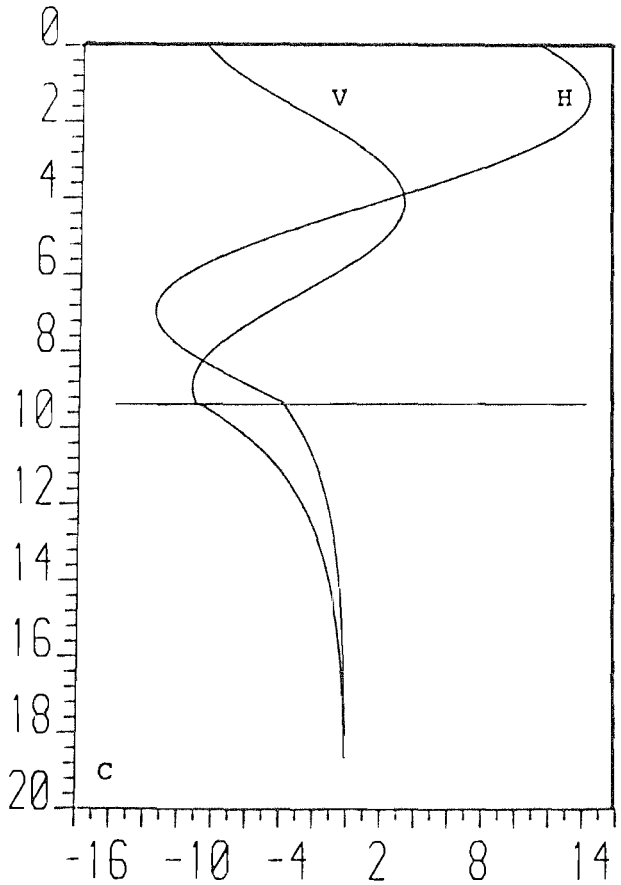

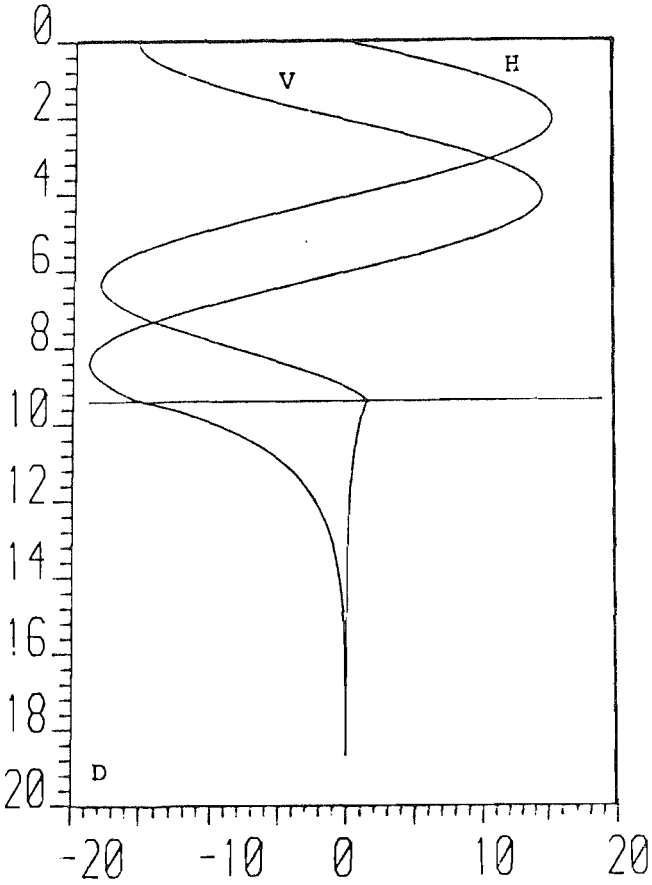

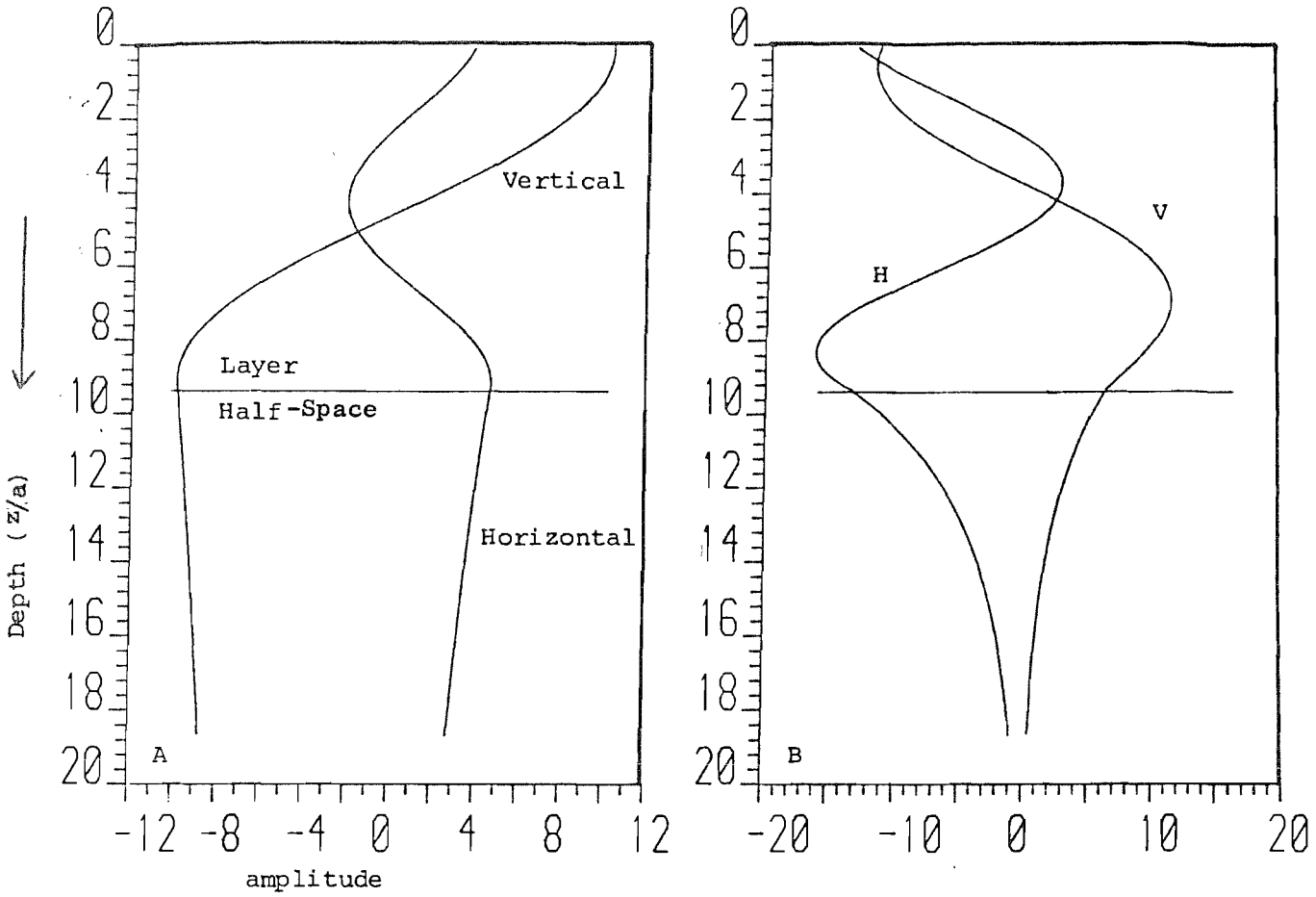

FIGURE 6.6 Vertical and horizontal components of the 4th modeshape

(All equivalent axes are the same)

GRAPH	MODE NO.	FREQUENCY
A		32.87
B	4th	38.62
C		58.59

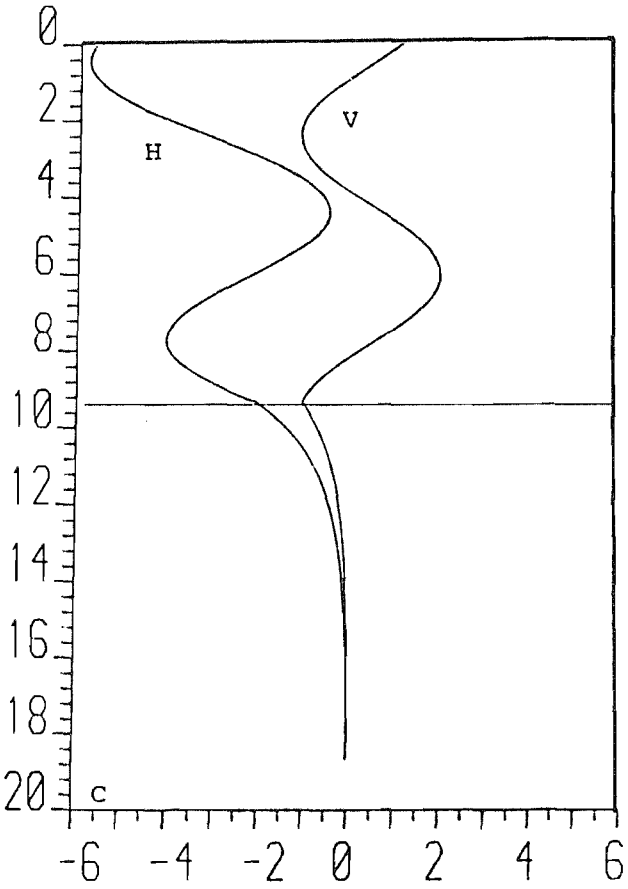

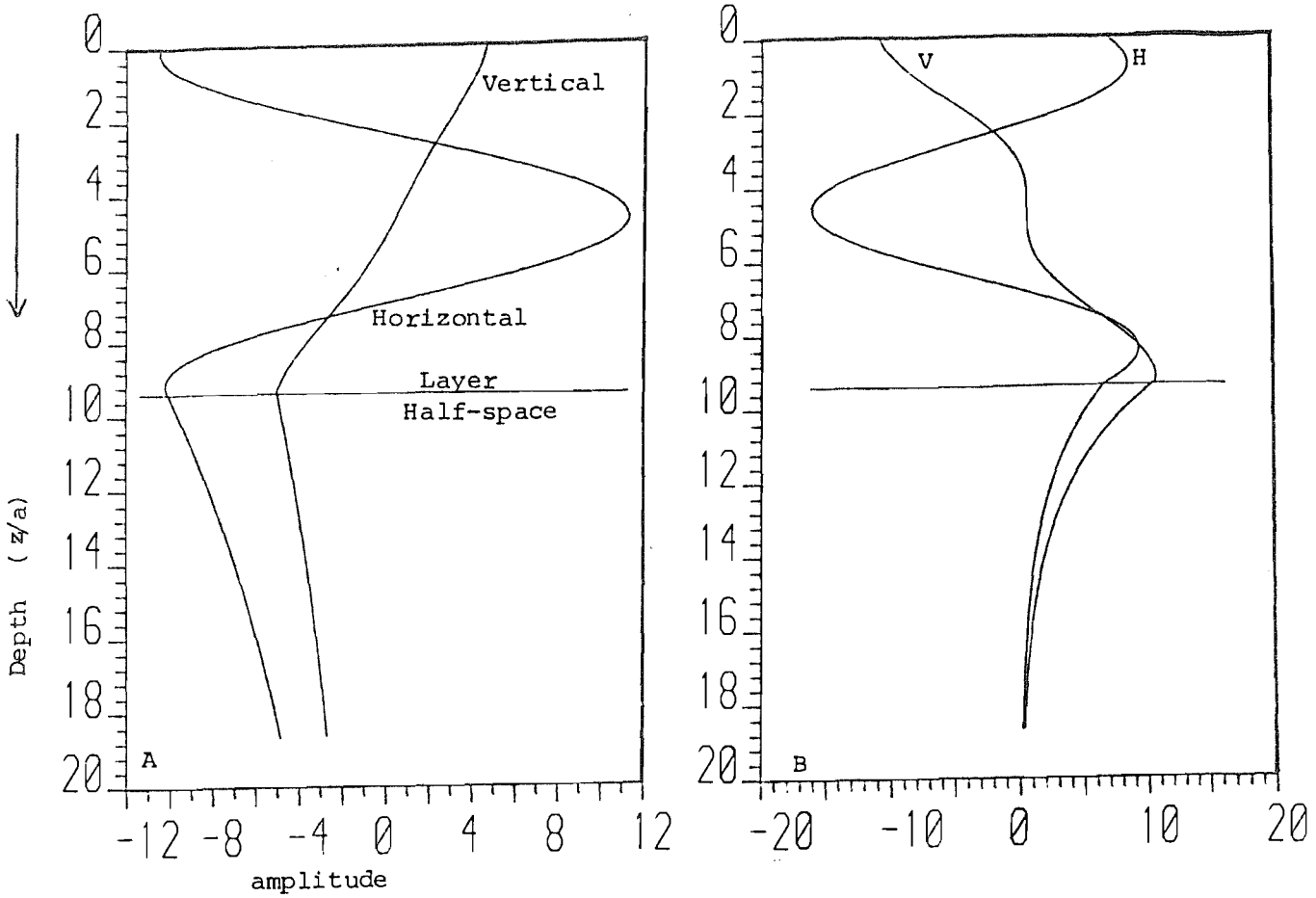

FIGURE 6.7 Vertical and horizontal components of 5th and 6th modeshapes
(All equivalent axes are the same)

GRAPH	MODE NO.	FREQUENCY
A	5th	40.16
B	5th	54.97
C	6th	57.19
D	6th	62.54

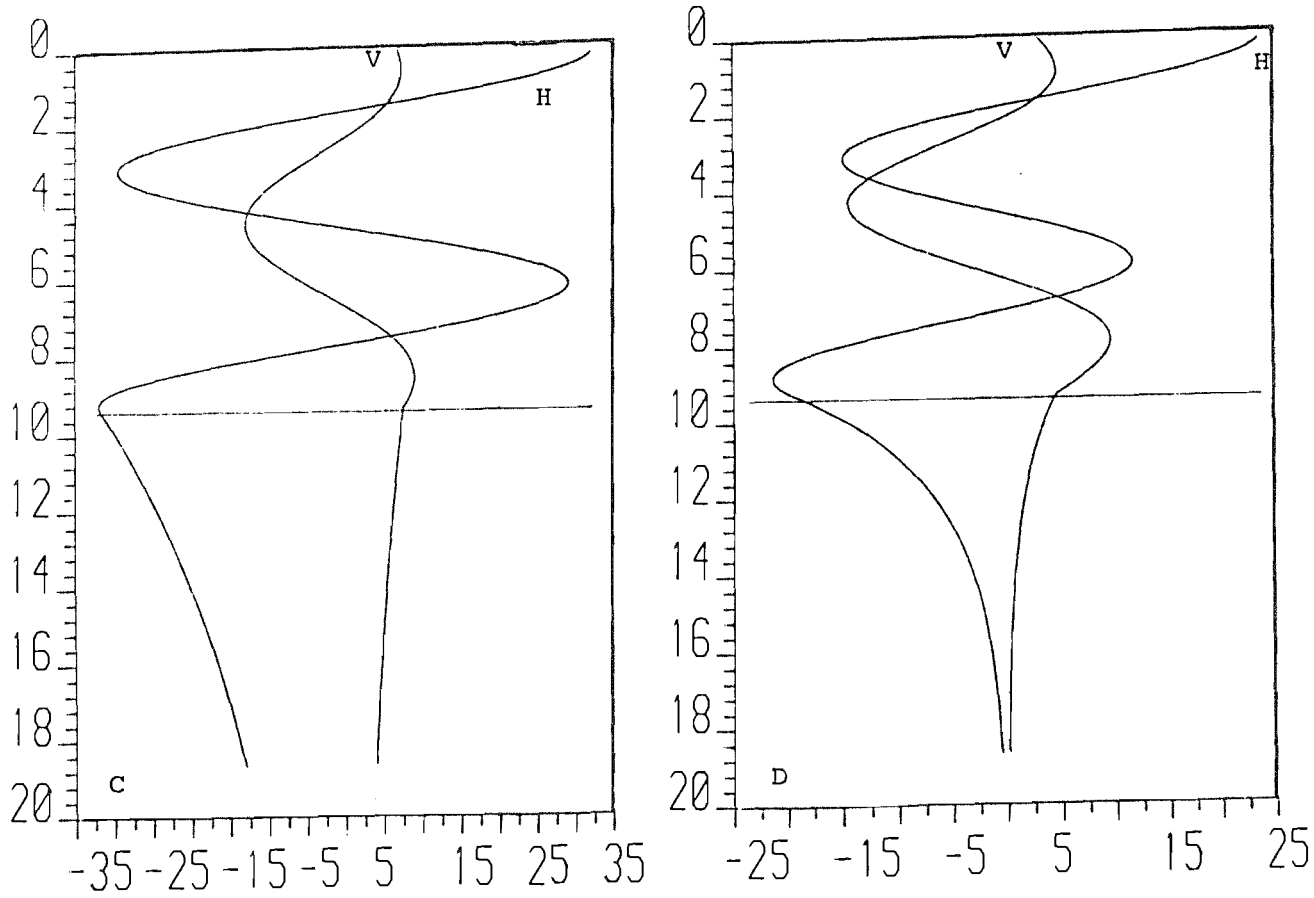

understanding the results of Chapter 7. For a chosen exciting frequency, the wavenumbers of the resulting natural modes can be found immediately. At frequencies where a mode may have a "leaky" contribution to the total forced response, the real part of the wavenumber of the leaky mode can be found indirectly, by studying the forced response "wavenumber domain" variation of transformed vertical and horizontal motion (see Figures 7.3 and 7.5). In these wavenumber domain figures, which are plotted for individual frequencies, each mode produces a peak in the variation of $\bar{u}$ and $\bar{w}$ (Fourier transformed horizontal and vertical motion, respectively). Referring to Figure 6.2, if a frequency say f_c, is chosen just below the frequency at which a mode dispersion curve meets the "half-space shear wavenumber" line, the corresponding wavenumber domain plot for f_c will show a peak at low wavenumber, which only appears for a small frequency range below f_c. This peak must relate to the "leaky" form of the mode, and the relative size of the peak is a measure of the relative contribution to the forced response of that mode. In the past (for example [18] and [54]) these "inhomogeneous" waves have been neglected, but the results of Chapter 7 show they can have some effect. In particular, the receptance figures for the elastic foundation model (Figs. 8.20-8.25) show peaks at 33 Hz, which is just above the leaky "cut-off" for the fourth mode. From equation (6.13), it can be seen that the 'leaky' transition occurs when $\zeta = k_2'$, making β' complex. The transition from homogeneous to inhomogeneous wave can clearly have an important effect. Further discussion of the leaky modes can be found in Section 6.5.2.

Although Figure 6.2 is of most use in the interpretation of forced response results, Figure 6.3 is a more conventional dispersion diagram, and more suitable for physical interpretation. Only the first mode has a real wavenumber for the whole frequency range. At large frequencies, the first mode wavespeed tends to the Rayleigh wavespeed in the layer. It is well known that the Rayleigh wave amplitudes are very small beyond one wavelength below the surface [67]. With the Clarborough material properties used here, the Rayleigh wavelength equals the layer depth at about 35Hz. Above this frequency, the first mode wavespeed is very close to the Rayleigh wavespeed. Kuhlemeyer [43] found that at very low frequencies, the first mode wavespeed approaches the Rayleigh wavespeed in the half-space. Both the Rayleigh wavespeeds, for the layer and

half-space (i.e., in the case of the half-space, this is the speed of the Rayleigh wave which would exist if the layer were a vacuum) are tabulated in Table 6.1. If the wavespeed of the first mode is calculated using the first entries in Table 6.3, it is found that at about 0.0027Hz, the mode wavespeed equals $1703.9ms^{-1}$, which is close to the half-space Rayleigh wavespeed of $1707.2ms^{-1}$. At such a low frequency this wavespeed produces a very long wavelength, and the layer depth becomes insignificant, appearing only as a "skin" on the half-space with almost no effect on the wave motion.

Kuhlemeyer also found that at high frequency, the modes of order two and above approach the layer shear wavespeed. In Figure 6.3 this tendency can only be seen in the second mode; a greater frequency range would show the other modes behaving similarly. The effect of the compression wavespeed, however, can be seen in three modes, the 2nd, 3rd and 4th. All these dispersion curves inflect along a line through c_1 on the wavespeed axis. Every mode is the result of a different interaction between the compression and shear waves; the inflections in the dispersion curves, and their asymptotic approach to the shear wavespeed, indicate which body wave dominates the behaviour. The first mode, which (for all practical purposes) is a Rayleigh wave for frequencies outside the frequency range allowing the interface to interfere with the mode, is a surface wave caused by reflection of the body waves at the free surface.

Comparison of Figs 6.2 and 6.3 with the bedrock model dispersion curves (Figs 4.1 and 4.2) reveals that some surprising behaviour in that model was due to the inflexible half-space boundary condition. With the physically more realistic boundary conditions imposed here, which allow movement at the bottom of the layer, no two mode dispersion curves ever cross, and the fourth mode does not possess the derivative $df/d\zeta=0$ at non-zero ζ. (These characteristics can only be seen true in Figs 6.2 and 6.3, for wavespeeds less than C_2', the half-space shear wavespeed. However, analysis of the forced response wavenumber domain peaks, as explained earlier in this Section, indicates that the real part of the wavenumber, for the dispersion curves below the C_2' line in Figure 6.2, will not alter these characteristics). Also, the modes are shifted to lower frequencies, as could be expected with these boundary conditions.

The effect of boundary conditions restraining motion at both the "surfaces" of the layer, is mentioned briefly in Section 6.4.2. Graphs A and B in Figure 6.4 show the development of the Rayleigh wave, as frequency increases. In Graph A, it is clear that the frequency is too low for a fully developed Rayleigh wave, as the layer half-space interface affects the modeshape. In Graph B, the frequency has been nearly quadrupled, and the vertical and horizontal components resemble the variation with depth described by many authors. In particular, Kolsky [41] shows that the vertical component varies according to:

$$e^{-(1-k^2\alpha^2)^{1/2}\zeta z} - \left(\frac{2}{2-k^2}\right)e^{-(1-k^2)^{1/2}\zeta z} \qquad (6.57)$$

while the horizontal component varies according to:

$$e^{-(1-\alpha^2k^2)^{1/2}\zeta z} - \left\{\frac{2(1-\alpha^2k^2)^{1/2}(1-\alpha^2)^{1/2}}{2-\alpha^2(1+k^2)}\right\} e^{-(1-\alpha^2)^{1/2}\zeta z} \qquad (6.58)$$

where $\alpha = C_2/C_1$, $k=C_R/C_2$, and C_1,C_2 and C_R are the compression, shear and Rayleigh wavespeeds respectively. Kolsky's notation has been changed and his expressions altered slightly. From Table 6.1, $k=0.921$ and $\alpha=0.572$, for the material properties used here.

Analysis of equation (6.57) reveals that it can never equal zero for $z\geq 0$, but differentiation with respect to z yields a turning point at $\zeta z=0.493$, or alternatively, as $\zeta=2\pi/\lambda$, where λ is the wavelength, at $z = 0.078\lambda$.

Equation (6.58), if equated to zero, predicts zero horizontal motion at a depth of 0.096λ. Differentiation gives a turning point at a depth of 0.361λ. In all the Figures 6.4 to 6.7, depth is shown non-dimensionalised; the non-dimensionalised Rayleigh wavelength for a frequency of 57.75Hz is $\lambda/a=5.61$. Computing the depths $z/a = 0.078\lambda/a$, $0.0961\lambda/a$ and $0.361\lambda/a$ for $\lambda/a=5.61$, reveals that the turning points and horizontal motion "zero" shown in Graph B of Fig 6.4 are all close to the corresponding Rayleigh wave depths. It is therefore apparent that the

first mode will become indistinguishable from the Rayleigh wave at high frequencies.

The second mode shapes, shown in Graphs C and D of Figure 6.4, suggest that as with the first mode, the modeshape only fully develops at high frequency. Symmetry of the modeshapes cannot be expected, as the top and bottom boundary conditions in the layer are not equal. However, most of the modeshapes in Figures 6.4 to 6.7, for the modes of order greater than one, are clearly "almost" either symmetric or anti-symmetric, suggesting they are "corruptions" of either symmetric or anti-symmetric modes which exist in a layer with symmetric boundary conditions. The plane of this "quasi-symmetry" is at $z/a = 4\ ^{2}/_{3}$. In Figure 6.5, for example, the horizontal component of the third mode is nearly anti-symmetrical about this plane, while the vertical component is nearly symmetrical. Conversely, the fourth and fifth modes have nearly anti-symmetrical vertical components and nearly symmetrical horizontal components (Figs 6.6 and 6.7). The sixth mode follows the same pattern as the third. All these higher modes develop fuller more complex shapes at higher frequencies.

For each of the 3rd, 4th, 5th and 6th modes, the lowest frequency graph in Figures 6.5 to 6.7 shows the mode just above the cut-off at the half-space shear wavenumber (Fig 6.2). In these graphs the decay of amplitude of vibration in the half-space is very slow - this is predicted by equations (6.20) and (6.21), for very small β'. These waves which cause large displacements in the half-space and yet are still "trapped" because their wavespeeds are too low for coupling with the half-space shear wave (see the next Section), appear to have a considerable effect on the forced response. In the elastic foundation receptance Figures of Chapter 8, peaks of varying size appear near the frequencies 20.12Hz, 32.87Hz, 40.16Hz and 57.19Hz, which are the frequencies where the individual modes are just below the half-space shear wavespeed.

6.5.2 The importance of Leaky and Stoneley Waves

It is clear from the discussion at the end of the previous section, that a mode near to transition from "trapped" to "leaky" has a significant effect on the response. Logically, a mode which is leaky and

loses energy to the half-space will have less effect at some distance from the source than a trapped mode, although it is possible for energy radiated into the half-space to be diffracted back into the layer [12]. "Leaky" waves have been studied for some years ([12,65,74,84,87]) but it is difficult to relate waves studied by these workers to the individual modes analysed here. However, their work helps to explain the mechanism of "leaky" propagation. In the notation of this Chapter, a "leaky" mode always has a complex wavenumber, and is an "inhomogeneous" wave - it changes its form as it propagates along the layer. This is because energy is continuously lost to the half-space. Stump [74] explains that the energy is lost through coupling with the body waves in the half-space, and that this coupling is only possible if the speed of the mode exceeds the speed of the coupling body wave. Some individual leaky waves, which exist with particular material property combinations of the layer and half-space, have been discussed by several authors. At high Poisson's ratio, above ν=0.45, a leaky wave denoted by P_1 is known to exist, which couples with the half-space compression wave. Phynney [65] describes a "leaky" Stoneley interface wave which exists between a liquid layer and a solid, and loses energy to compression waves in the liquid.

"True" Stoneley waves, as mentioned in Section 6.1, are not "leaky"; they are generalised Rayleigh waves which exist at the interface of two media, and decay rapidly in both media away from the interface. However, these waves are in general of theoretical interest only, as they require special conditions to prevail before they can develop. Stoneley was originally concerned with the "Wiechert" surface of discontinuity deep inside the earth, where the compression wavespeeds in each medium, and the shear wave speeds in each medium, are almost equal. Newlands, and Tolstoy and Usdin [54,77] both find that Stoneley waves do not contribute to their solutions, for their chosen material properties. Tolstoy and Usdin comment that if Stoneley waves did exist, then an extra dispersion curve could be expected to appear in Figs 6.2 and 6.3, which would be asymptotic to a line very close to the first (Rayleigh) wave mode. However, the work of Scholte [10] makes it clear that Stoneley waves cannot exist with the material properties used here. His equations 1 and 2 give values of (μ/μ') as a function of (ρ/ρ'), in the notation of Section 6.2. For Stoneley waves to exist between two media, the ratio

μ/μ' must lie between the values given by these two equations; this condition corresponds to $C_1 \simeq C_1'$ and $C_2 \simeq C_2'$. Table 6.1 shows that these conditions are not satisfied.

CHAPTER 7

INFINITE STRIP LOAD ACTING ON AN ELASTIC LAYER OVER AN ELASTIC HALF-SPACE

7.1 Introduction

The free vibrations of the "elastic foundation" ground structure model are analysed in Chapter 6, where the contributions of previous workers are discussed. In this Chapter, the complementary elastic foundation near-field forced response of a strip-load is studied, which does not appear to have been examined before. Some previous results for the direct receptance of a strip on the elastic foundation are mentioned in Chapter 8; additionally, Newlands [54] has considered a line-load. However, the bulk of the results in this Chapter cannot be compared with any previous work.

Following the forced response work of Chapters 3 and 5, internal damping characterised by the loss factor η is present in the layer, and also the under-lying half-space. The damping mechanism is explained in Section 2.2. The method of analysis is an extension of the work in Section 5.2. Here, the dynamic stiffness matrix for the elastic foundation layer is derived by effectively combining the half-space and layer stiffness matrices.

The results are non-dimensional, and although they cannot be compared with any independent work, comparison is possible with the half-space and bedrock results. In fact, Figures 7.12 to 7.20 show the results from each ground structure model, for a given frequency, combined in single graphs. The Figures preceding these follow the pattern established in Chapters 3 and 5, and show (i) transforms of horizontal and vertical motion components in the wavenumber domain; (ii) horizontal and vertical motion components plotted against distance, using linear and dB 'attenuation' scales; and (iii) the effect varying the strip width has on the direct receptance, with a constant force per unit width.

7.2 ANALYSIS OF THE ELASTIC FOUNDATION MODEL

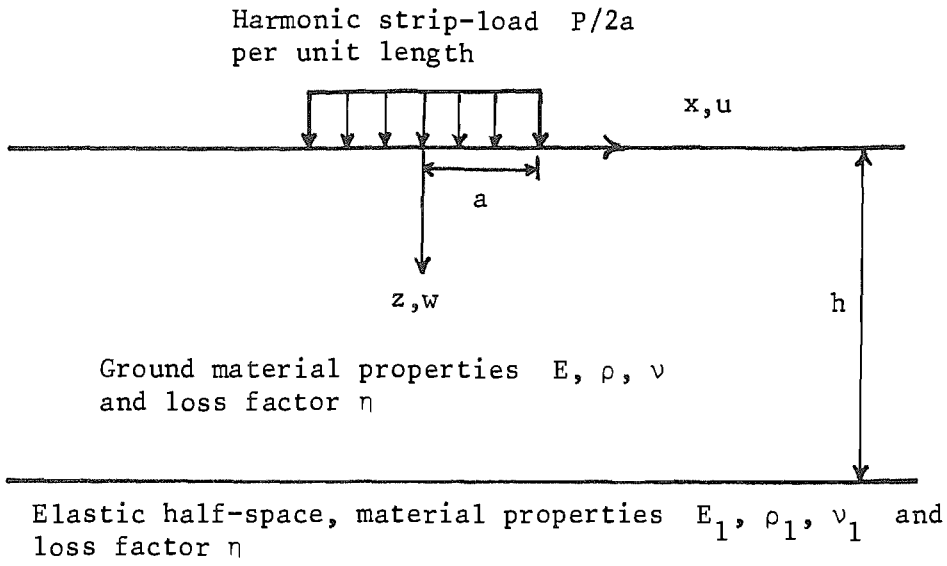

FIGURE 7.1: The "Elastic Foundation" Model with Infinite Strip Load

Figure 7.1 shows the key elements of the model. An isotropic, elastic, homogeneous layer with material damping (loss factor) η, of depth 'h' covers an isotropic, elastic, homogeneous half-space of different material properties but with the same level of material damping. The uniform load acts on an infinite strip of width '2a', and the contact is 'smooth' - there is no shear stress. The load moves vertically and harmonically.

Much of the analysis of this problem is identical to the solution of the 'bedrock' model, given in Section 5.2, so this will not be repeated here. In Section 5.2, a dynamic stiffness matrix [T] (see equation (5.25)) is derived, such that

$$[T][\bar{W}] = [\bar{\tau}] \qquad (7.1)$$

where

$$[\bar{\tau}] = [-i\bar{\tau}_{zz}(0),\ -\bar{\tau}_{zx}(0),\ i\bar{\tau}_{zz}(h),\ \bar{\tau}_{zx}(h)]^T$$

and (7.2)

$$[\bar{w}] = [i\bar{w}(0),\ \bar{u}(0),\ i\bar{w}(h),\ \bar{u}(h)]^T$$

where $\bar{\tau}_{ij}$ are the transforms of stress components; $\bar{u}$, $\bar{w}$ are the transforms of horizontal and vertical motion, respectively; and the '0' and 'h' in round brackets refer to the position in the layer to which each quantity refers.

Because of computational difficulties described in Chapter 5, it is necessary to sub-divide the single layer into several exactly similar layers, each of height 'd' (say). If there are three layers, so that d = h/3, the formulation becomes:

$$\begin{bmatrix} \blacksquare & \blacksquare & 0 & 0 \\ \blacksquare & \blacksquare & \blacksquare & 0 \\ 0 & \blacksquare & \blacksquare & \blacksquare \\ 0 & 0 & \blacksquare & \blacksquare \end{bmatrix} \begin{bmatrix} i\bar{w}(0) \\ \bar{u}(0) \\ i\bar{w}(d) \\ \bar{u}(d) \\ i\bar{w}(2d) \\ \bar{u}(2d) \\ i\bar{w}(3d) \\ \bar{u}(3d) \end{bmatrix} = \begin{bmatrix} -i\bar{\tau}_{zz}(0) \\ -\bar{\tau}_{zx}(0) \\ 0 \\ 0 \\ 0 \\ 0 \\ i\bar{\tau}_{zz}(3d) \\ \bar{\tau}_{zx}(3d) \end{bmatrix} \qquad (7.3)$$

where each shaded 4 × 4 matrix is equal to [T], with the relevant additions of elements where the intersections cross (shown by cross hatching).

With the bedrock model, the elements of $[\bar{w}]$ corresponding to movement at the bottom of the layer ($i\bar{w}(3d)$ and $i\bar{u}(3d)$ in the equation above) were zero. This reduced the problem to one of six equations in six

unknowns, as the stress components $\bar{\tau}_{zz}(0)$ and $\bar{\tau}_{zx}(0)$ are known (see equation (3.35)). They are

$$\bar{\tau}_{zz}(0) = -\frac{P}{2\pi}\frac{\sin\zeta a}{\zeta a}$$
$$\bar{\tau}_{zx}(0) = 0 \qquad (7.4)$$

Now that deformation is allowed at the bottom of the layer, the components $\bar{w}(3d)$ and $\bar{u}(3d)$ are no longer zero. However, a solution can be found in a fashion similar to the bedrock problem, as now the stresses $\bar{\tau}_{zz}(3d)$ and $\bar{\tau}_{zx}(3d)$ can be found. The simplest method to achieve this uses the equality of stresses above and below the layer/ half-space interface, i.e.,

$$\begin{bmatrix}\bar{\tau}_{zz}(3d)\\ \bar{\tau}_{zx}(3d)\end{bmatrix} = \begin{bmatrix}\bar{\tau}'_{zz}(z'=0)\\ \bar{\tau}'_{zx}(z'=0)\end{bmatrix} \qquad (7.5)$$

where $\bar{\tau}'_{zz}$ is the stress component in the half-space, and z' is the vertical direction in the half-space.

Likewise, the components $\bar{u}$ and $\bar{w}$ above and below must match. From equation (3.39), replacing the right hand side of the equation by $[\bar{\tau}'_{zz}(z'=0), \bar{\tau}'_{zx}(z'=0)]^T$

$$\begin{bmatrix}\bar{u}'(0')\\ \bar{w}'(0')\end{bmatrix} = \begin{bmatrix}i & \beta\\ -\alpha & i\zeta\end{bmatrix}\begin{bmatrix}2\mu\zeta^2 - (\zeta+2\mu)k_1^2 & -2\mu i\zeta\beta\\ -2\mu\alpha i\zeta & -\mu(2\zeta^2-k_2^2)\end{bmatrix}^{-1}\begin{bmatrix}\bar{\tau}'_{zz}(0')\\ \bar{\tau}'_{zx}(0')\end{bmatrix} \qquad (7.6)$$

which leads to

$$\begin{bmatrix}\bar{\tau}'_{zz}(0')\\ \bar{\tau}'_{zx}(0')\end{bmatrix} = \begin{bmatrix}2\mu\zeta^2 - (\zeta+2\mu)k_1^2 & -2\mu i\zeta\beta\\ -2\mu\alpha i\zeta & -\mu(2\zeta^2-k_2^2)\end{bmatrix}\begin{bmatrix}-\alpha & i\zeta\\ i\zeta & \beta\end{bmatrix}^{-1}\begin{bmatrix}\bar{w}'(0')\\ \bar{u}'(0')\end{bmatrix} \qquad (7.7)$$

Performing this matrix inversion and multiplication, followed by introducing the coefficient 'i' to the $\bar{\tau}_{zz}(0')$ and $\bar{w}'(0')$ terms, gives:

$$\begin{bmatrix} i\bar{\tau}'_{zz}(0') \\ \bar{\tau}'_{zx}(0') \end{bmatrix} = \begin{bmatrix} i\bar{\tau}_{zz}(3d) \\ \bar{\tau}_{zx}(3d) \end{bmatrix} = \begin{bmatrix} \frac{(\lambda+2\mu)\beta k_1^2}{\alpha\beta-\zeta^2} & \frac{2\mu\alpha\beta\zeta-2\mu\zeta^3+(\lambda+2\mu)\zeta k_1^2}{\alpha\beta-\zeta^2} \\ \frac{2\mu\alpha\beta\zeta-2\mu\zeta^3+\mu k_2^2\zeta}{\alpha\beta-\zeta^2} & \frac{\mu\alpha k_2^2}{\alpha\beta-\zeta^2} \end{bmatrix} \times \begin{bmatrix} i\bar{w}(3d) \\ \bar{u}(3d) \end{bmatrix} \qquad (7.8)$$

Or, defining [R] as the (2 × 2) matrix in equation (7.8) where:

$$R = \begin{bmatrix} R_{11} & iR_{12} \\ -iR_{21} & R_{22} \end{bmatrix} \qquad (7.9)$$

gives

$$\begin{bmatrix} i\bar{\tau}_{zz}(3d) \\ \bar{\tau}_{zx}(3d) \end{bmatrix} = \begin{bmatrix} R_{11} & iR_{12} \\ -iR_{21} & R_{22} \end{bmatrix} \begin{bmatrix} i\bar{w}(3d) \\ \bar{u}(3d) \end{bmatrix} \qquad (7.10)$$

Equation (7.3) can now be modified: if the signs of equation (7.10) are changed and the LHS is added to the bottom two elements of the stress matrix, in equation (7.3) (producing two zero sums), then the matrix [R] must be added to the bottom right corner of the (8 × 8) dynamic stiffness matrix.

As the surface stresses are known (equation (7.4)), we now have eight equations in eight unknowns, which can be solved for the transformed displacements $[\bar{w}]$. The solution method and results are presented in Section 7.3.

7.3 Results

Program EF64H2, which is listed in Appendix B with some brief notes, is representative of several closely related programs used in this work. The program uses NAG library routines to solve equation (7.10) for discrete values of ζ. This yields values of $\bar{w}(\zeta,z=0)$ and $\bar{u}(\zeta,0)$, which are inverse transformed using a numerical technique described in Appendix A, to give the displacement on the surface of the ground.

Figures 7.2 to 7.5 show the real and imaginary parts of Fourier transformed horizontal and vertical components of motion, non-dimensionalised (to become $(a\bar{u})$ and $(a\bar{w})$ respectively), and for various frequencies. A low loss factor has been used in each of these Figures to accentuate the peaks. Table 7.1 lists the Rayleigh, shear and compression wavenumbers for zero damping, and also the wavenumber location of peaks in these Figures. The dimensional frequencies relate to the Clarborough test-site (see Table 2.2 for the material properties), with the strip half-width $a = 0.75$. The corresponding non-dimensional frequencies in the layer and the half-space are tabulated in Table 7.2. The method of non-dimensionalising is explained in Section 3.3.

Freq. (Hz)	Theoretical (η=0) wavenumbers (ak_1)	(ak_2)	(ak_R)	Non-dimensionalised Wavenumber ($a\zeta$) Location of major peaks in Figs., η = 0.002
4.0	0.041	0.072	0.078	0.021, 0.041
8.0	0.082	0.143	0.156	0.066, 0.115
16.0	0.164	0.287	0.312	0.165, 0.291
19.25	0.197	0.345	0.375	* 0.035, 0.21, 0.36 (η = 0.02)
32.0	0.328	0.574	0.623	0.0683, 0.261, 0.392, 0.620
33.0	0.338	0.592	0.643	* 0.085, 0.28, 0.415, 0.64
38.5	0.395	0.691	0.749	* 0.065, 0.3, 0.36, 0.52, 0.75
48.0	0.492	0.861	0.935	0.253, 0.463, 0.516, 0.733, 0.935
56.5	0.579	1.013	1.100	* 0.1, 0.4, 0.58, 0.68, 0.92, 1.1
64.0	0.656	1.148	1.246	0.532, 0.671, 0.843, 1.063, 1.247

* – these peak locations were measured from the figures; the others are from discrete data.

Table 7.1: Non-dimensionalised Wavenumbers

Frequency (Clarborough) (Hz)	Ω^2 (Layer)	Ω^2 (Half-Space)
4.0	0.002	0.00004
8.0	0.008	0.00017
16.0	0.033	0.00068
19.25	0.047	0.00099
32.0	0.131	0.00273
33.0	0.139	0.00290
38.5	0.189	0.00395
48.0	0.295	0.00614
56.5	0.408	0.00850
64.0	0.524	0.01090

Table 7.2: Non-dimensionalised frequencies

Most of the remaining Figures show non-dimensionalised amplitudes plotted against distance; additionally, some Figures show phase change plotted against distance. All parameters in the Figures are non-dimensional, except for the frequency. Figures 7.6 and 7.7 show vertical and horizontal amplitude respectively, for each of the six frequencies 4, 8, 16, 32, 48 and 64 Hz. The loss factor $\zeta = 0.1$, and the range covered is $(x/a) \leq 33^1/_3$. The same range is used in Chapters 3 and 5, to aid comparison. Figures 7.8 and 7.9 give similar information to Figure 7.6, but over the larger range $(x/a) \leq 100$, using a dB log scale to show attenuation. In Figure 7.9 the damping has been reduced to $\eta = 0.02$.

Figure 7.10 shows the phase change of two of the frequency components plotted in Figure 7.9, 4 Hz and 32 Hz. Figure 7.11 shows the effect varying the strip width has on the displacement at the centre of the strip, with a constant force per unit width, for the frequencies 1.5, 32, 64 and 100 Hz. The loss factor is $\eta = 0.02$ to exaggerate the maxima and minima.

Figures 7.12 to 7.20 are a comparison of the half-space, bedrock and elastic foundation models' results. Figure 7.12 shows the results from each model, for vertical amplitude and a frequency of 8 Hz, plotted over $(x/a) \leq 33^1/_3$. Figure 7.13 shows the equivalent three phase changes, and Figures 7.14 and 7.15 correspond to Figures 7.12 and 7.13, but are for

the horizontal component of motion. Figures 7.16 and 7.17 give the amplitude and phase change, respectively, of the vertical component of motion at 16 Hz, for each model. Similarly, Figures 7.18 and 7.19 are for 64 Hz, and give the vertical and horizontal components' amplitudes, respectively, for each model.

Figure 7.20 compares the vertical motion direct receptances for all three models, over the frequency range $1 < f \leq 64$ Hz, using a log scale for the amplitude.

7.4 Discussion

The interpretation of the bedrock model forced response results in Chapter 5 was made possible by the free vibration work of Chapter 4. Likewise, the elastic foundation model free vibration work of Chapter 6 is essential to this discussion. Figures 7.2 to 7.5 all show the variation of Fourier transformed displacements with wavenumber. The main features of these graphs are distinct peaks, the wavenumber locations of which are predicted by the free vibration work. Each peak represents a propagating wave, and is related to a particular natural mode; this can be clearly seen by comparing Table 7.1 with Figure 6.2 (provided the values in the Table are first dimensionalised for the Clarborough test-site, by dividing by $a = 0.75$). Table 7.1 shows that above about 30 Hz, the first peak is at the Rayleigh wavenumber. (A convention that the 'first' peak is defined as the peak at largest wavenumber will be adhered to.) The relative size of this peak indicates the relative importance of the associated propagating wave. Unlike the half-space model, but in common with the bedrock model, peaks do not in general occur at the shear or compression wavenumbers. The coincidence of the first peak with the compression wavenumber at 4 Hz, at $(a\zeta) = 0.041$, can be seen in Figure 6.2 to be unique to that frequency (for the first mode). Each dispersion curve in Figure 6.2 shares this characteristic at a distinct frequency.

Although Figure 6.2 'predicts' that six propagating waves (corresponding to the free vibration modes) will exist at 64 Hz, only five peaks are evident in Figure 7.2(c). Accordingly, there are only

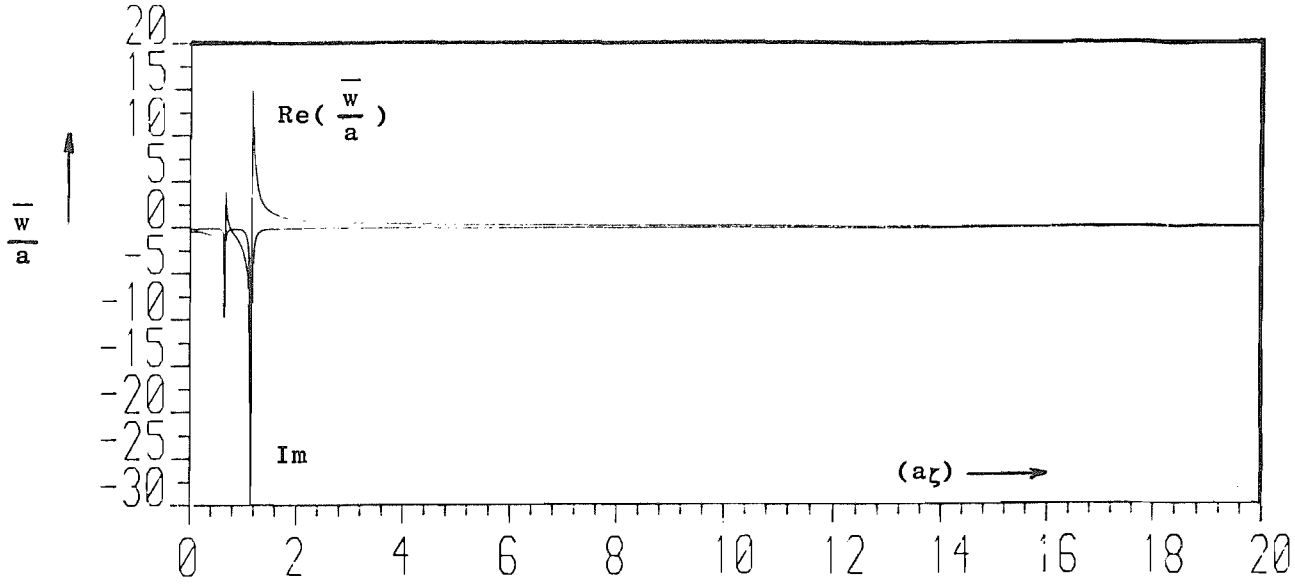

Fig 7.2(a): Frequency = 8 Hz

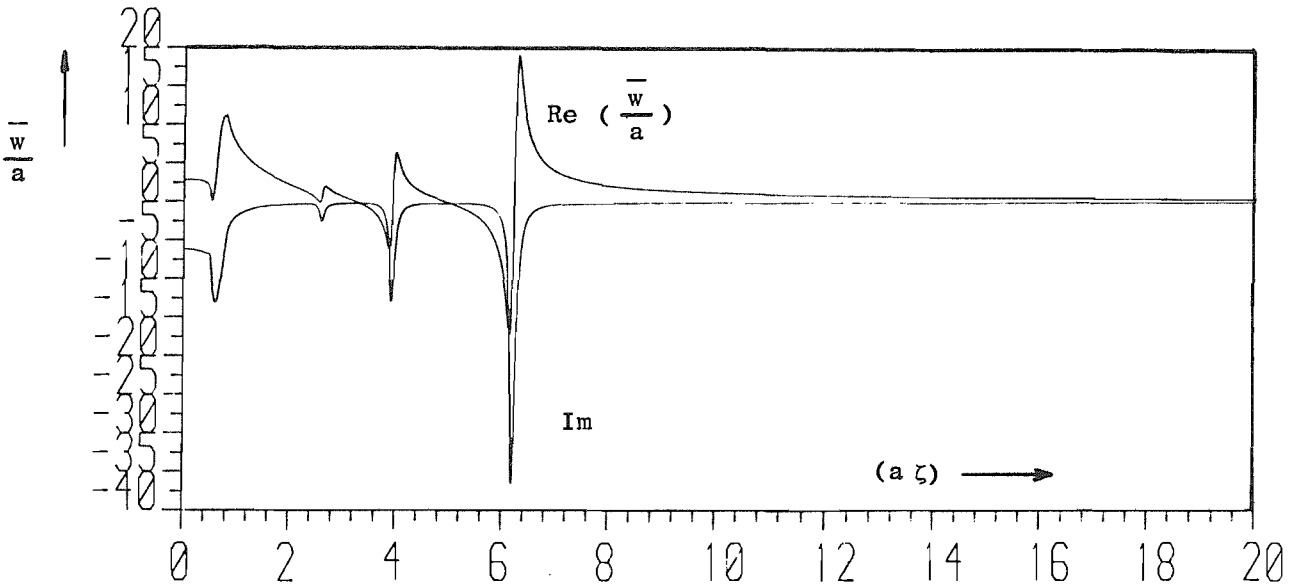

Fig 7.2(b): Frequency = 32 Hz

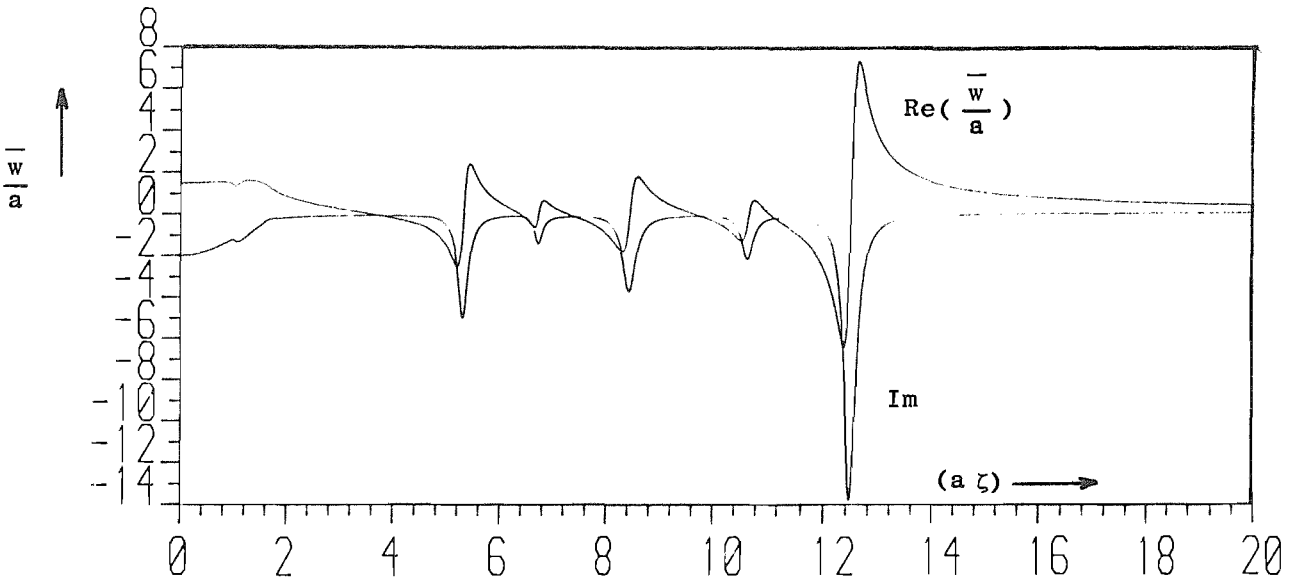

Fig 7.2(c): Frequency = 64 Hz

Fig 7.2: Non-Dimensionalised Transformed Vertical Motion Plotted Against Wavenumber For the Elastic Foundation Model, η=0.02

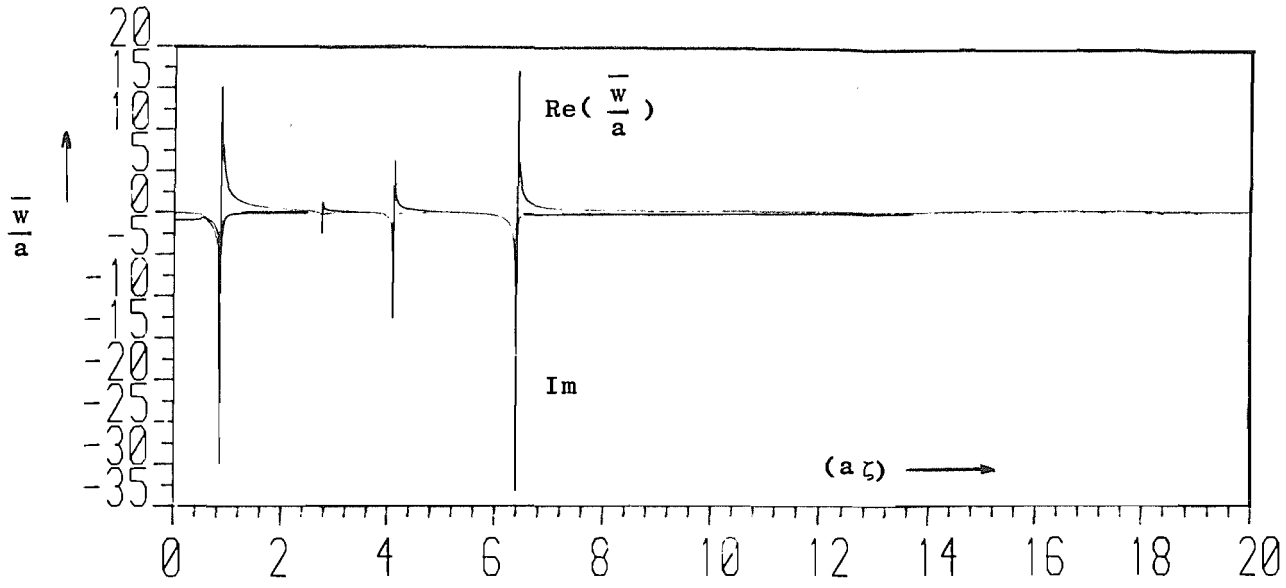

Fig 7.3 (a): Frequency = 33 Hz

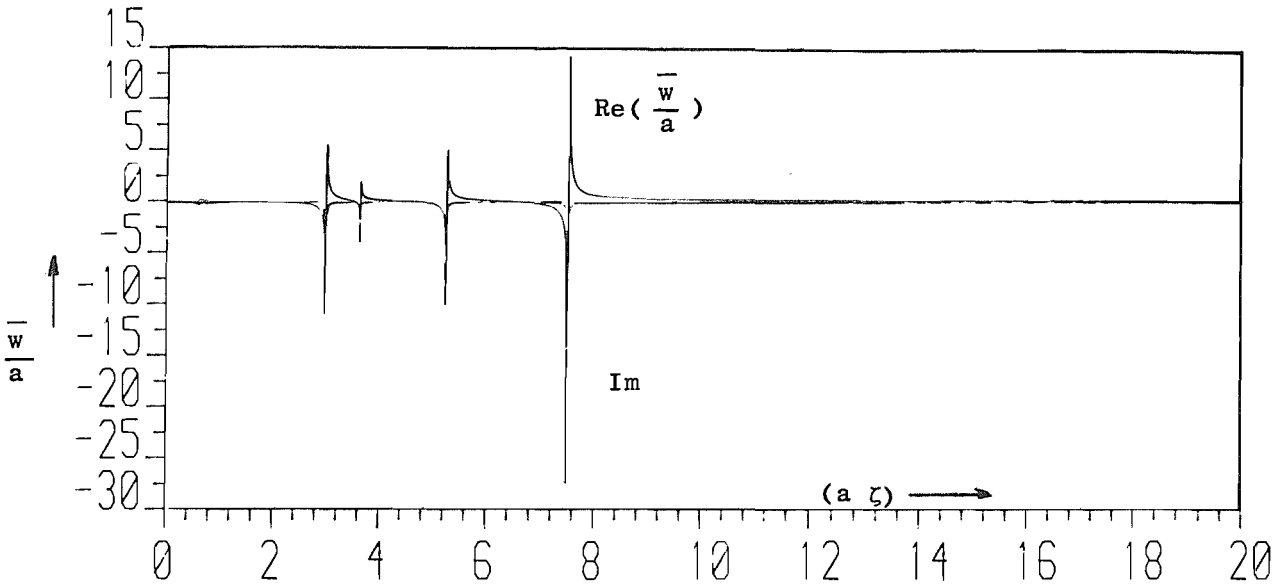

Fig 7.3(b): Frequency = 38.5 Hz

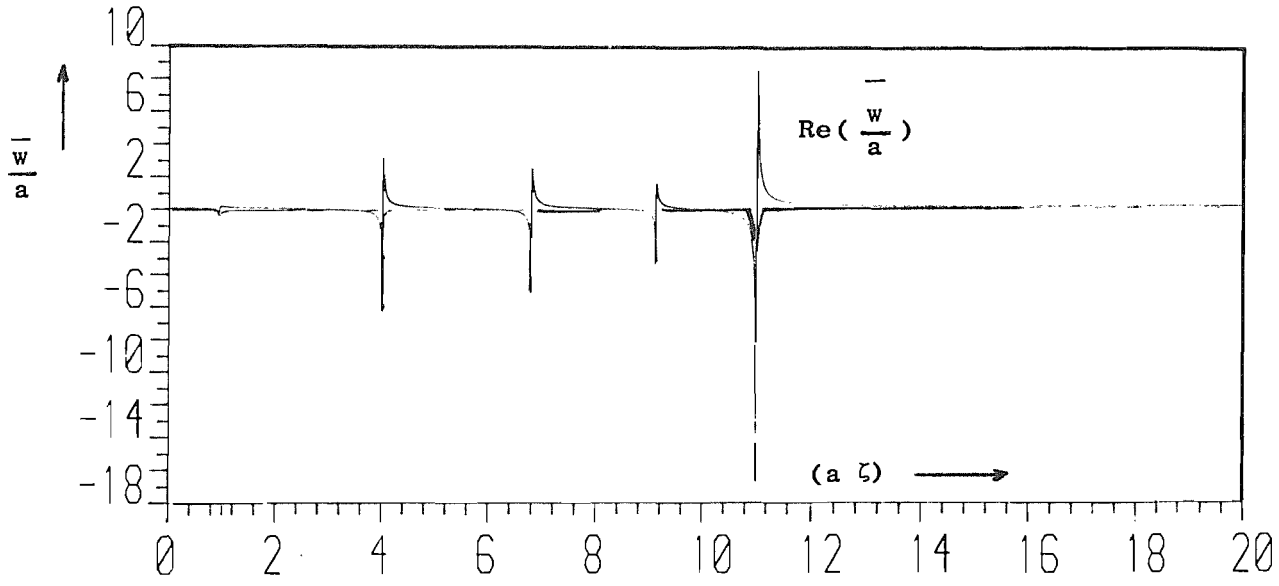

Fig 7.3(c): Frequency = 56.5 Hz

Fig 7.3: Non-Dimensionalised Transformed Vertical Motion Plotted Against Wavenumber, For the Elastic Foundation Model $\eta = 0.02$

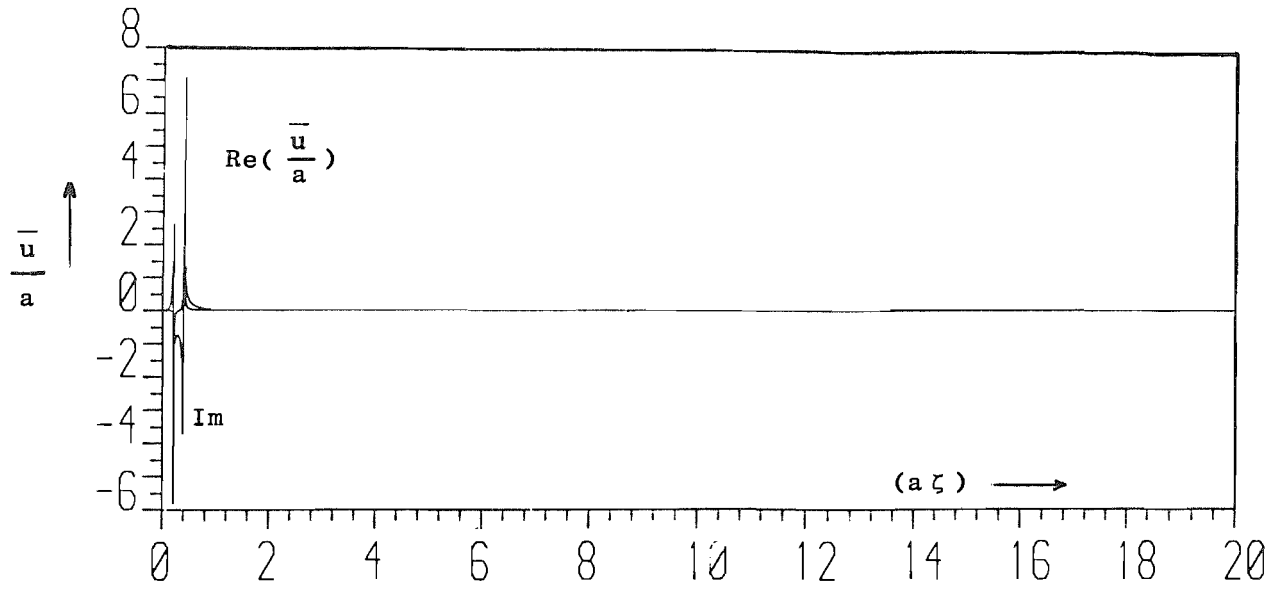

Fig 7.4(a): Frequency = 4 Hz

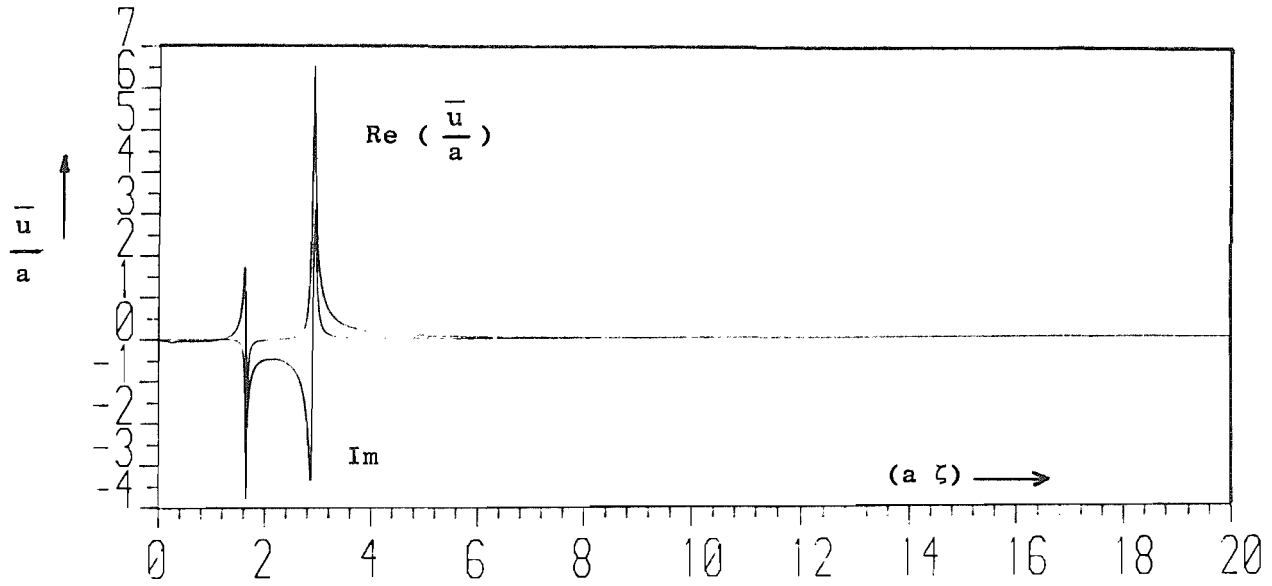

Fig 7.4(b): Frequency = 16 Hz

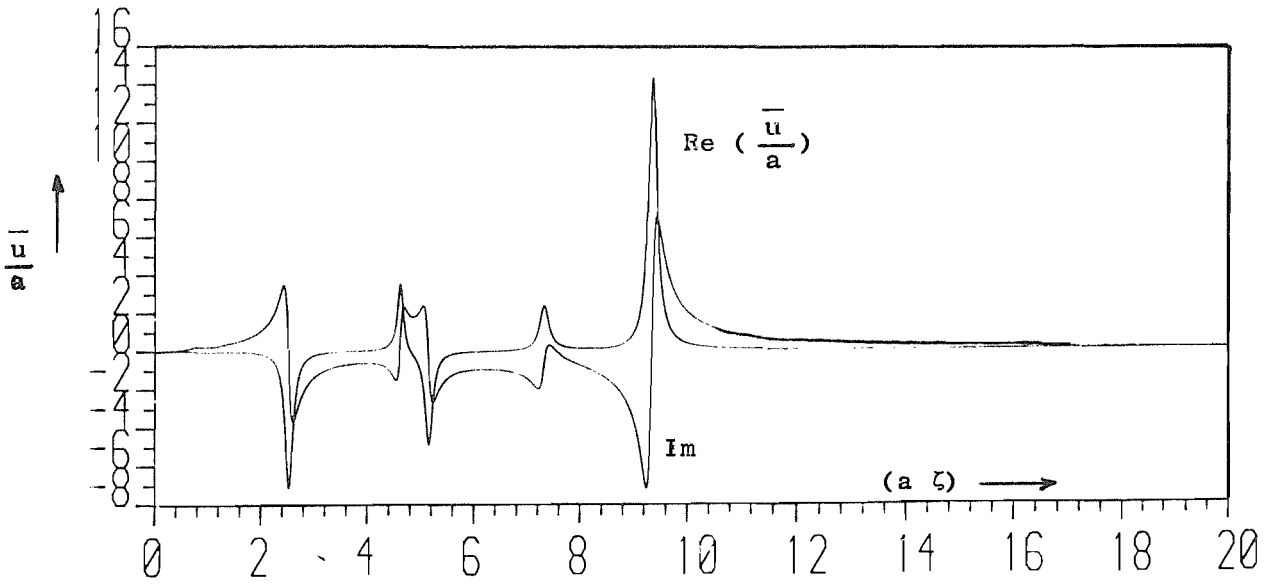

Fig 7.4(c): Frequency = 48 Hz

Fig 7.4: Non-Dimensionalised Transformed Horizontal Motion Plotted Against Wavenumber, Elastic Foundation Model, $\eta = 0.02$

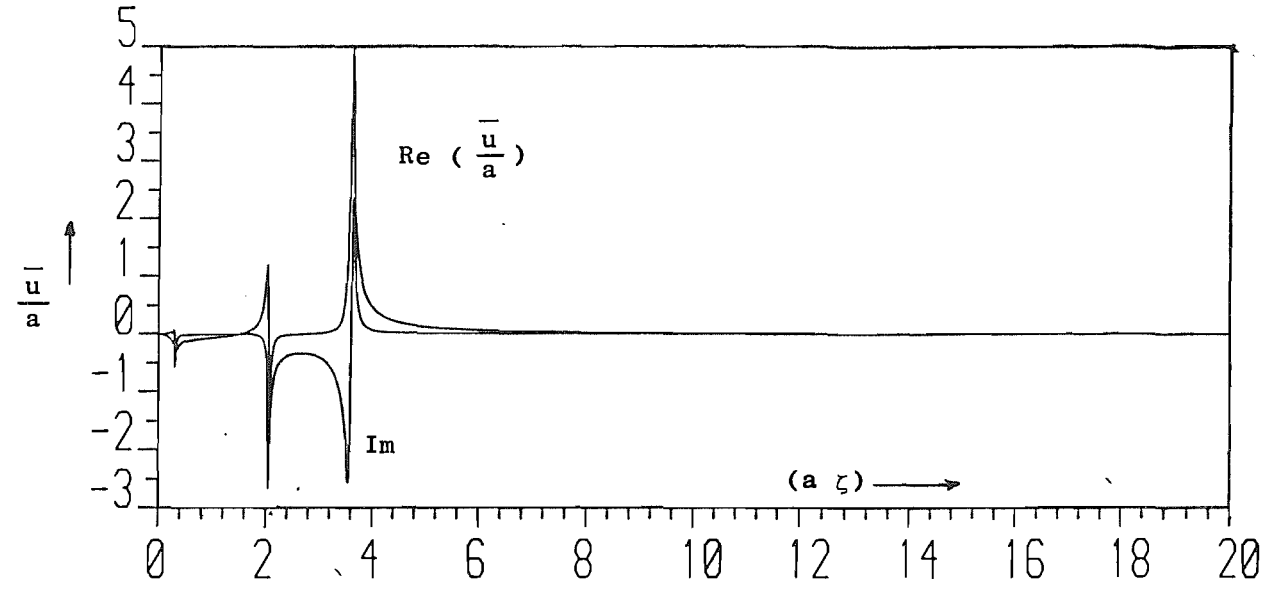

Fig 7.5(a); Frequency = 19.25 Hz

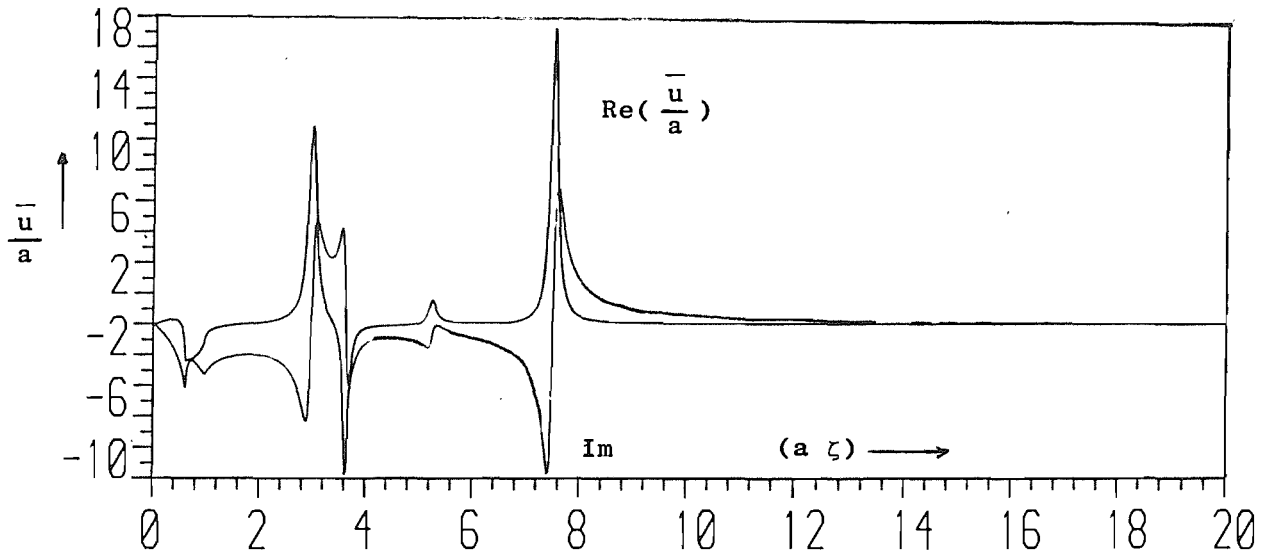

Fig 7.5(b): Frequency = 38.5 Hz

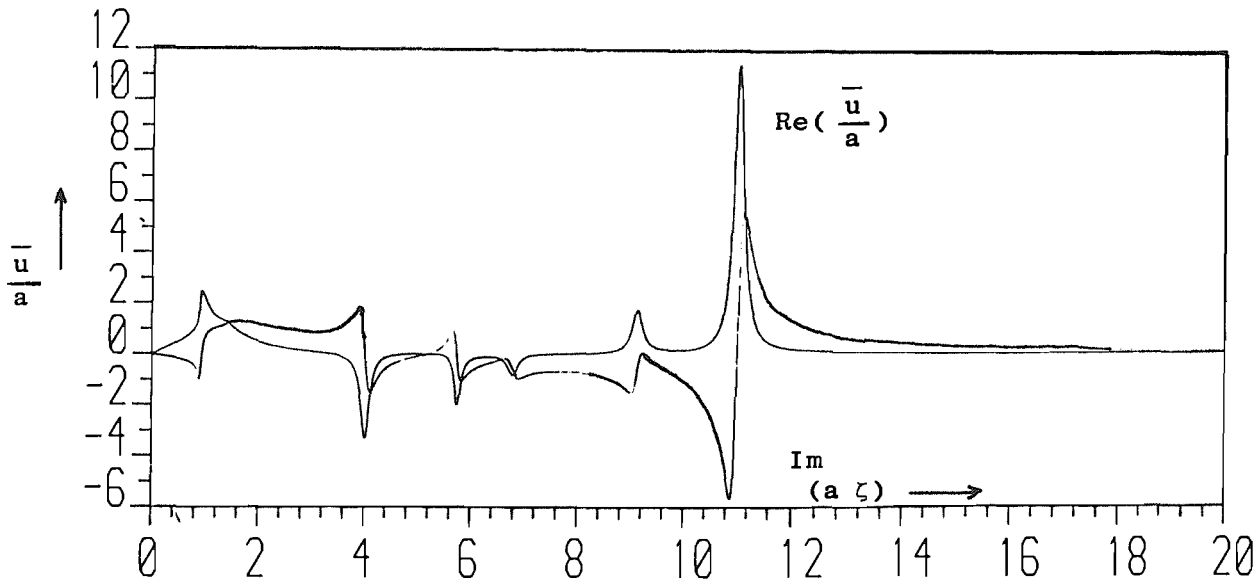

Fig 7.5(c): Frequency = 56.5 Hz

Fig 7.5: Non-Dimensionalised Transformed Horizontal Motion Plotted Against Wavenumber, Elastic Foundation Model, $\eta = 0.02$

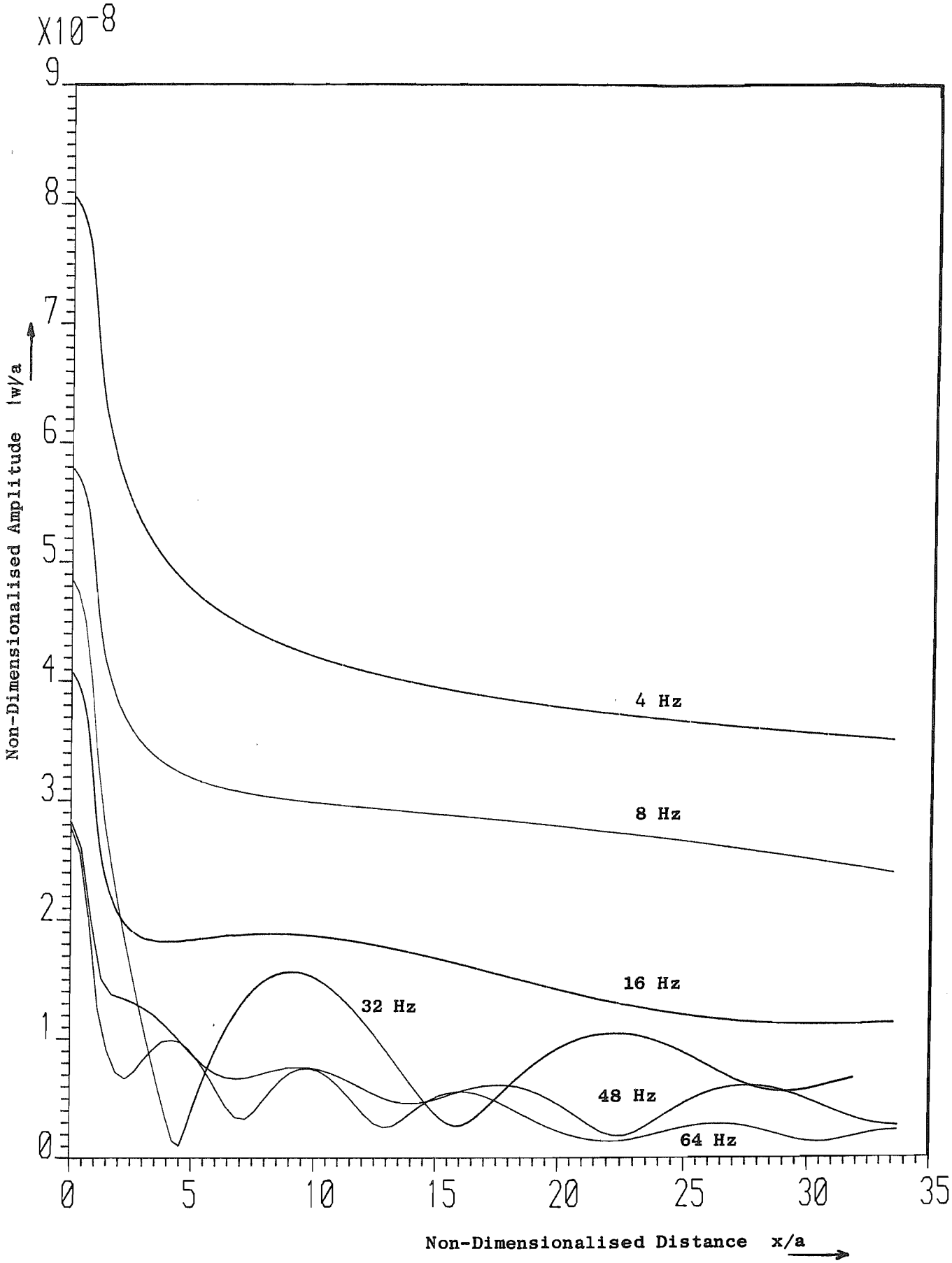

Fig 7.6: Vertical Non-Dimensionalised Amplitude of Motion, Elastic Foundation Model, At Six Frequencies, Plotted Against Distance, $\eta = 0.1$

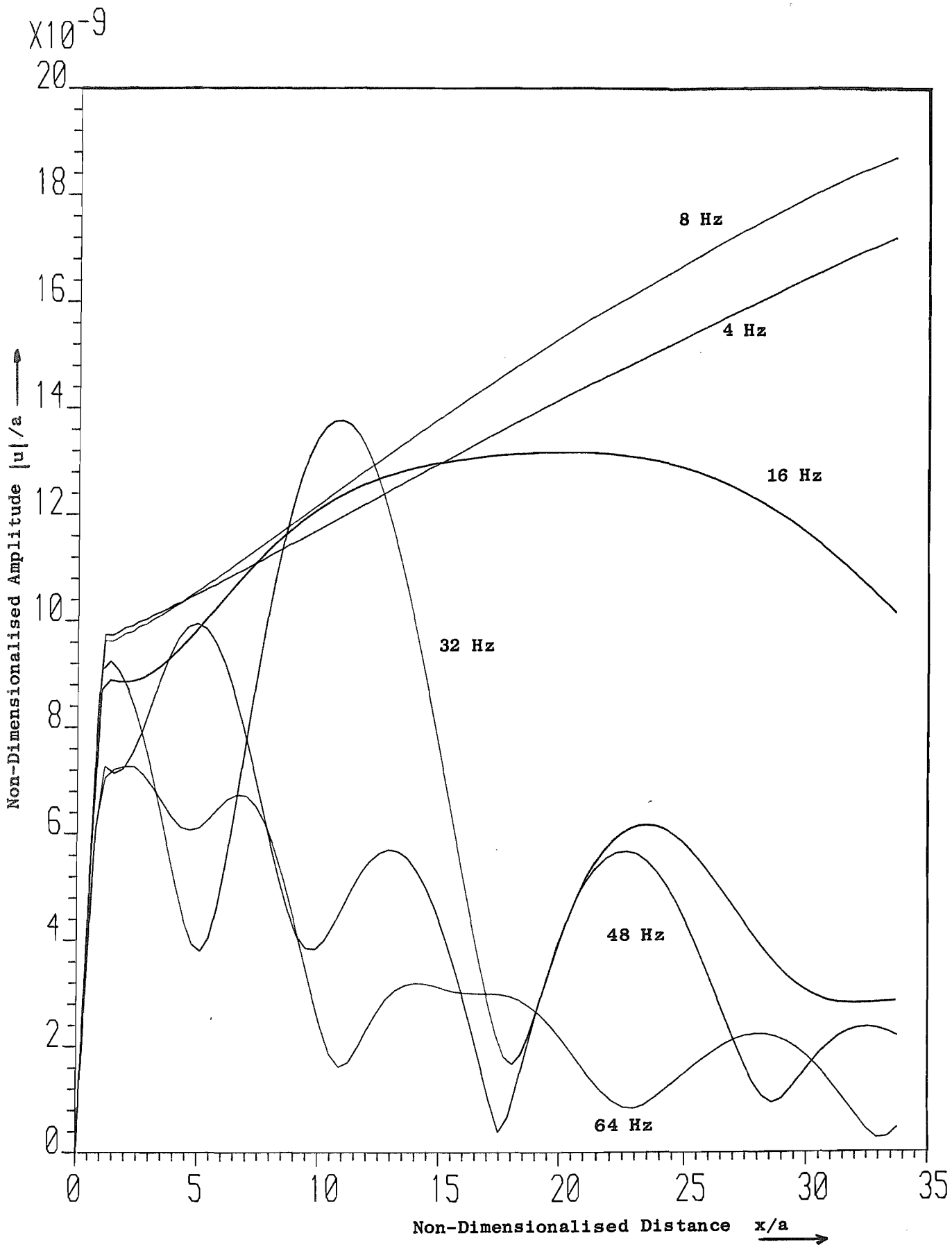

Fig 7.7: Horizontal Non-Dimensionalised Amplitude of Motion, Elastic Foundation Model, At Six Frequencies, Plotted Against Distance, $\eta = 0.1$

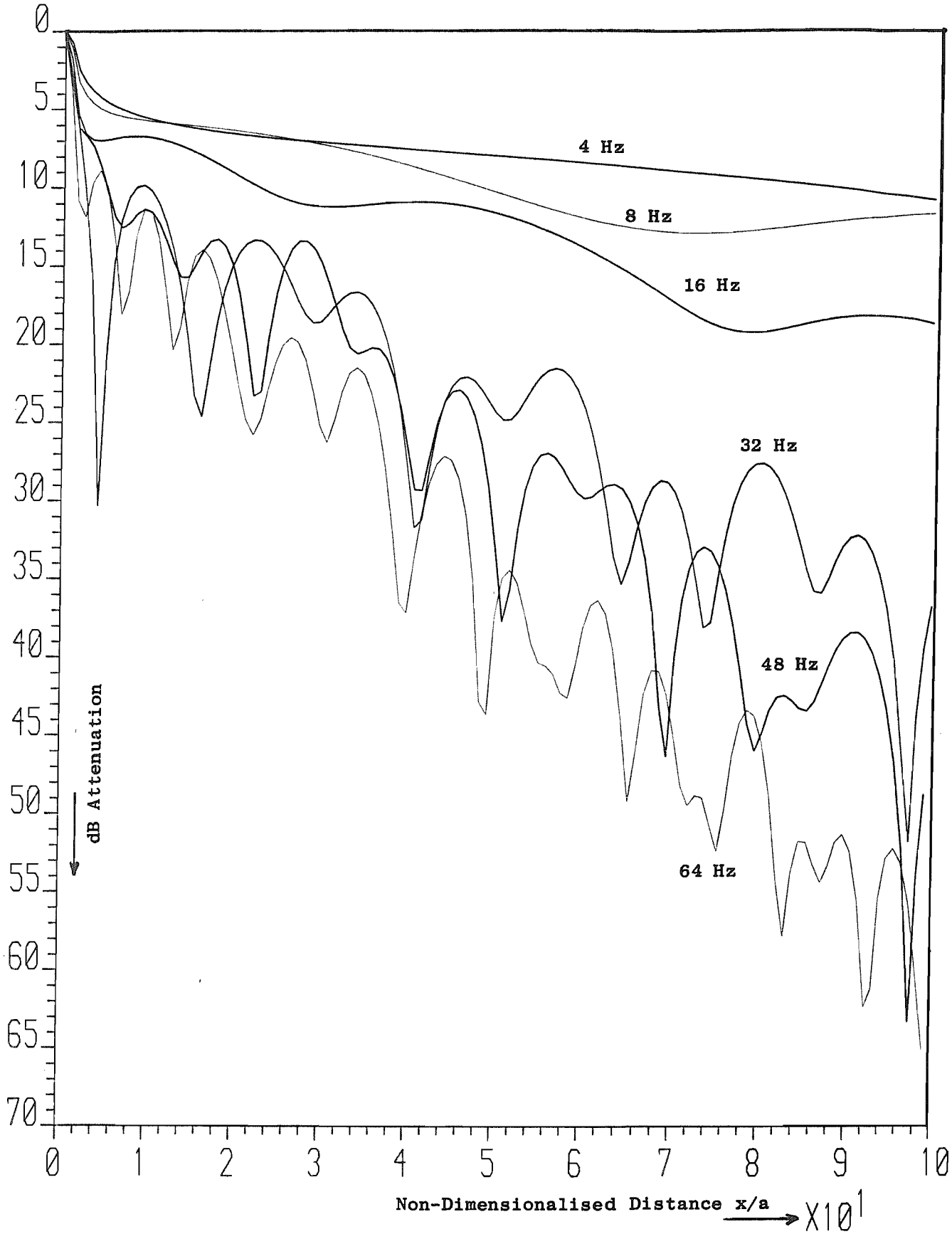

Fig 7.8: dB Attenuation of Vertical Motion At Six Frequencies, $\eta = 0.1$

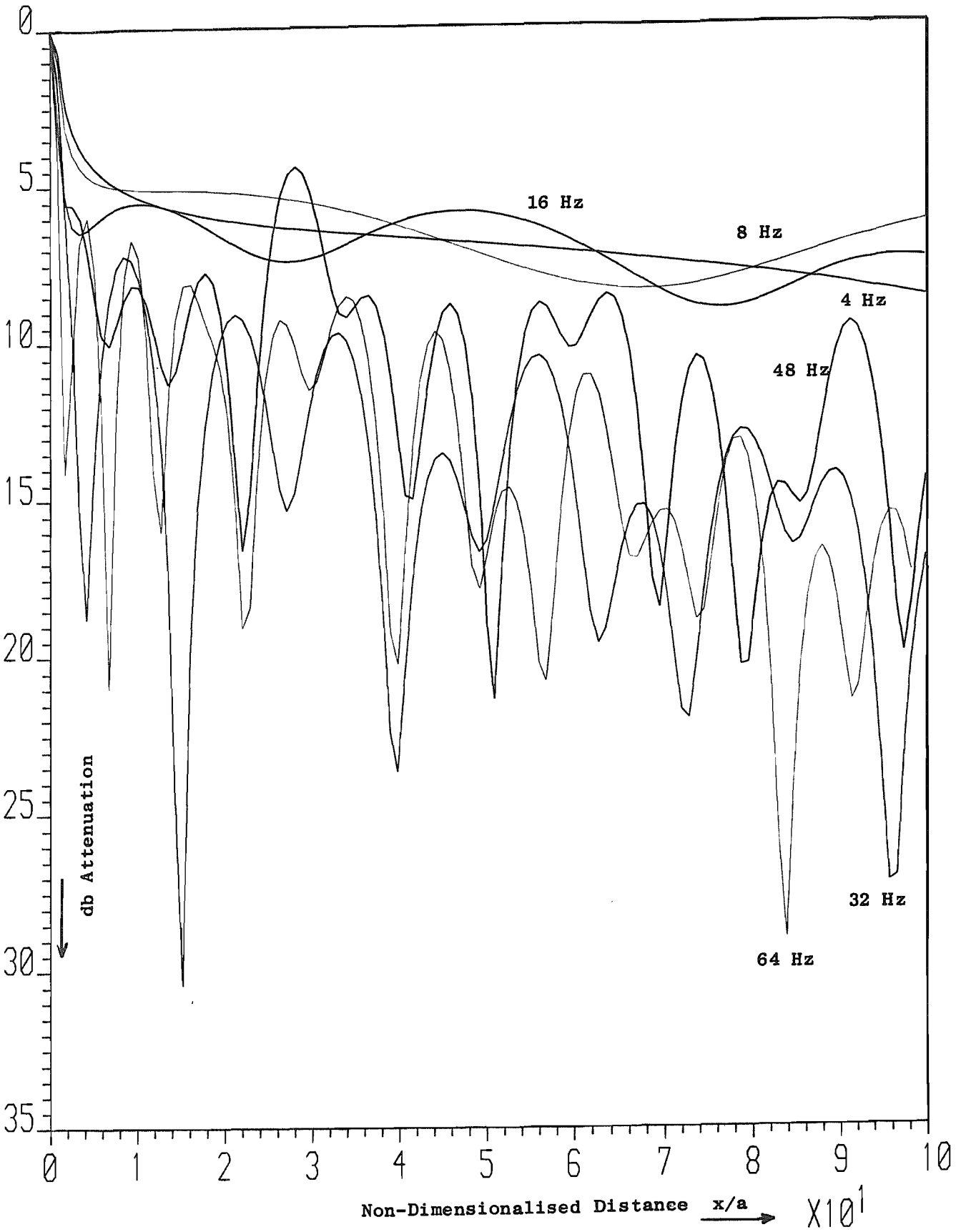

Fig 7.9: dB Attenuation of Vertical Motion At Six Frequencies, $\eta = 0.02$

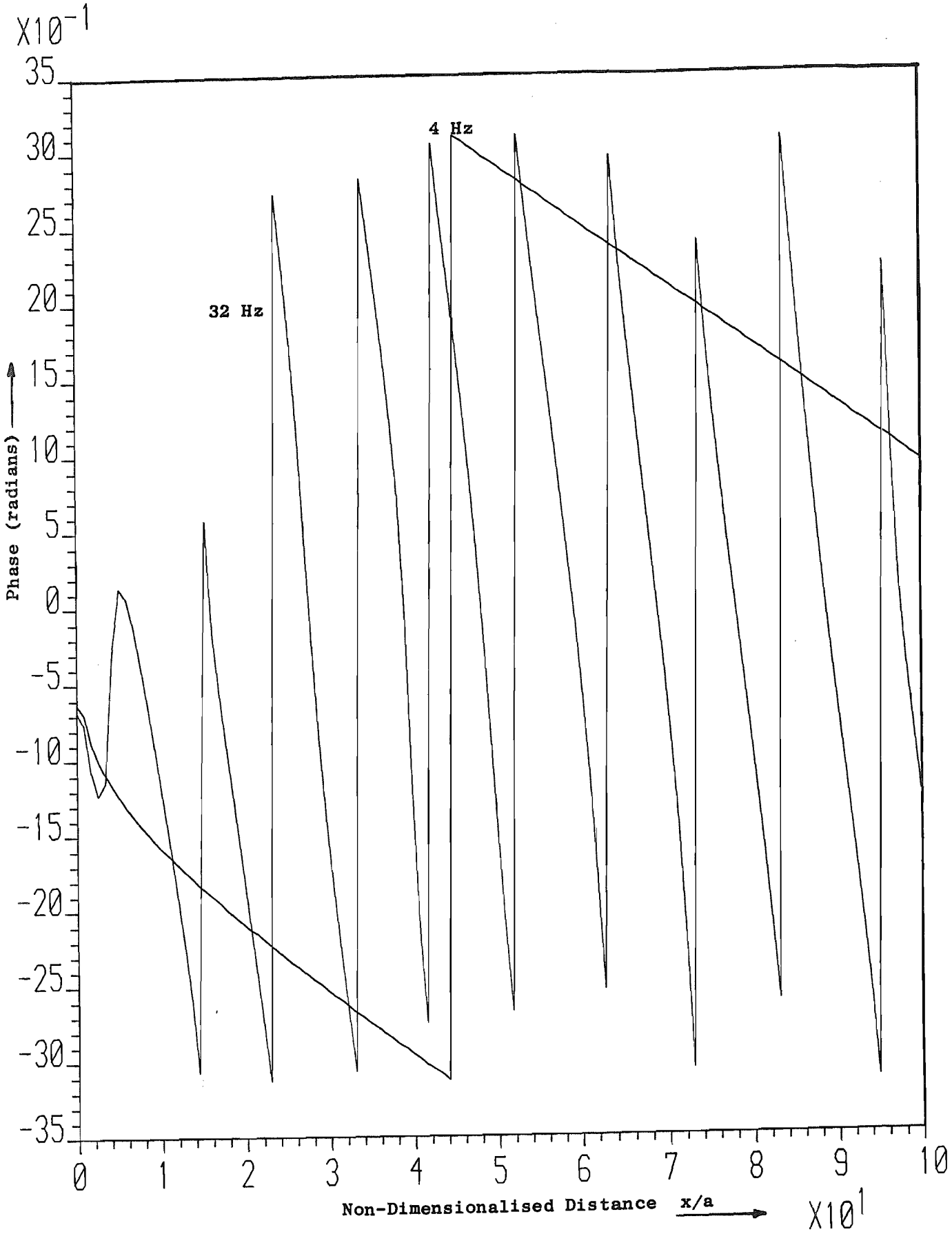

Fig 7.10: Phase Change of Vertical Motion Against Distance, $\eta = 0.1$, at 4Hz and 32 Hz

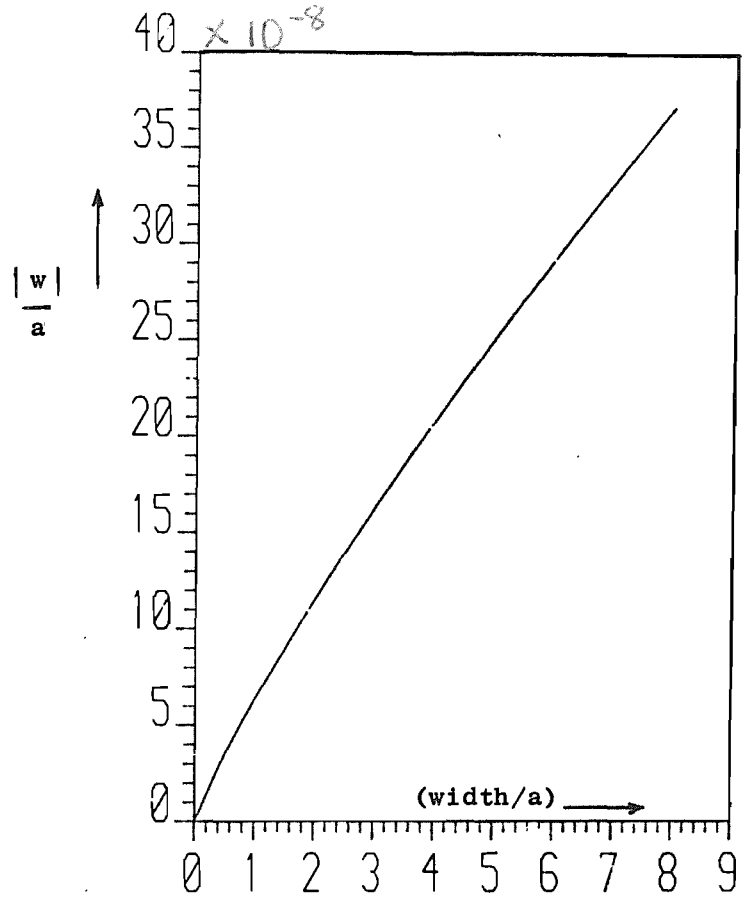

Fig 7.11(a): Frequency = 1.5 Hz

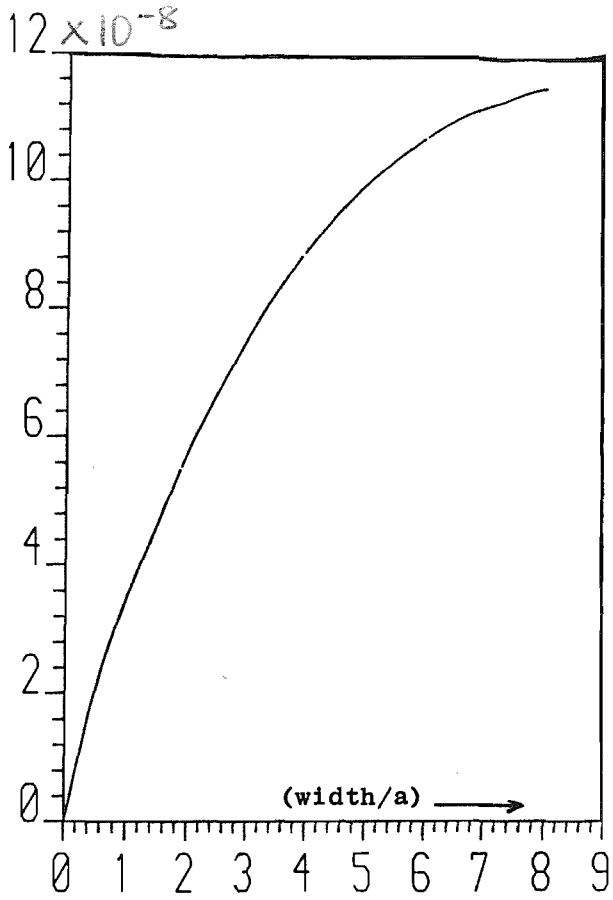

Fig 7.11(b): Frequency = 32 Hz

Fig 7.11: The Effect on Displacement At the Centre Of The Strip Of Varying The Strip Width, With Force per Unit Width Constant.

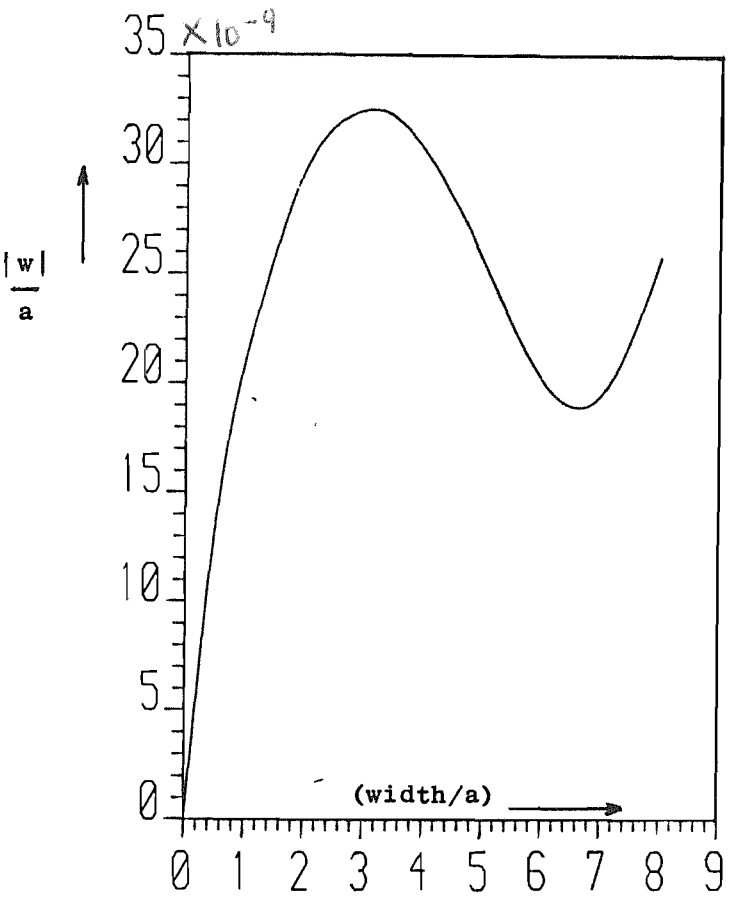

Fig 7.11(c): Frequency = 64 Hz

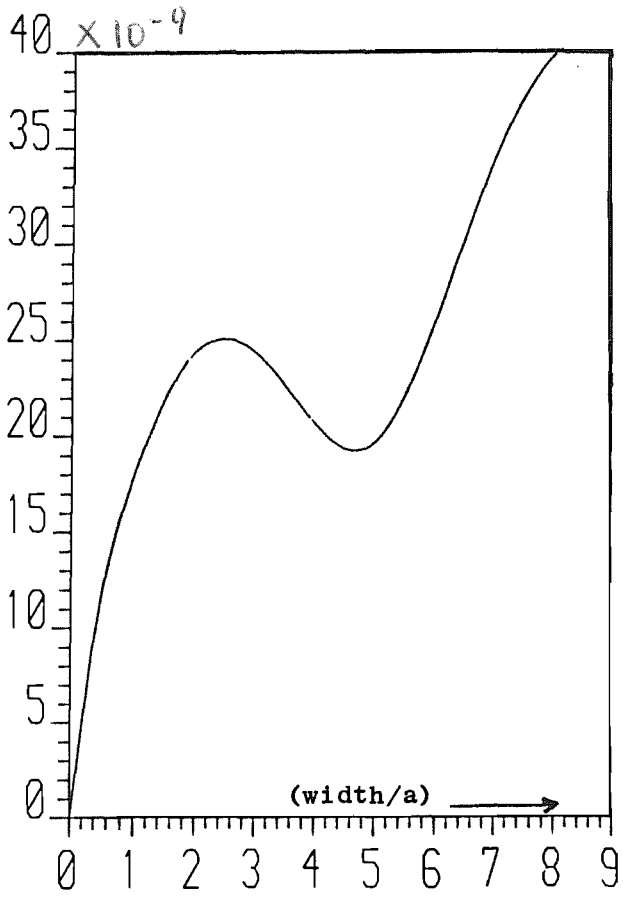

Fig 7.11(d): Frequency = 100 Hz

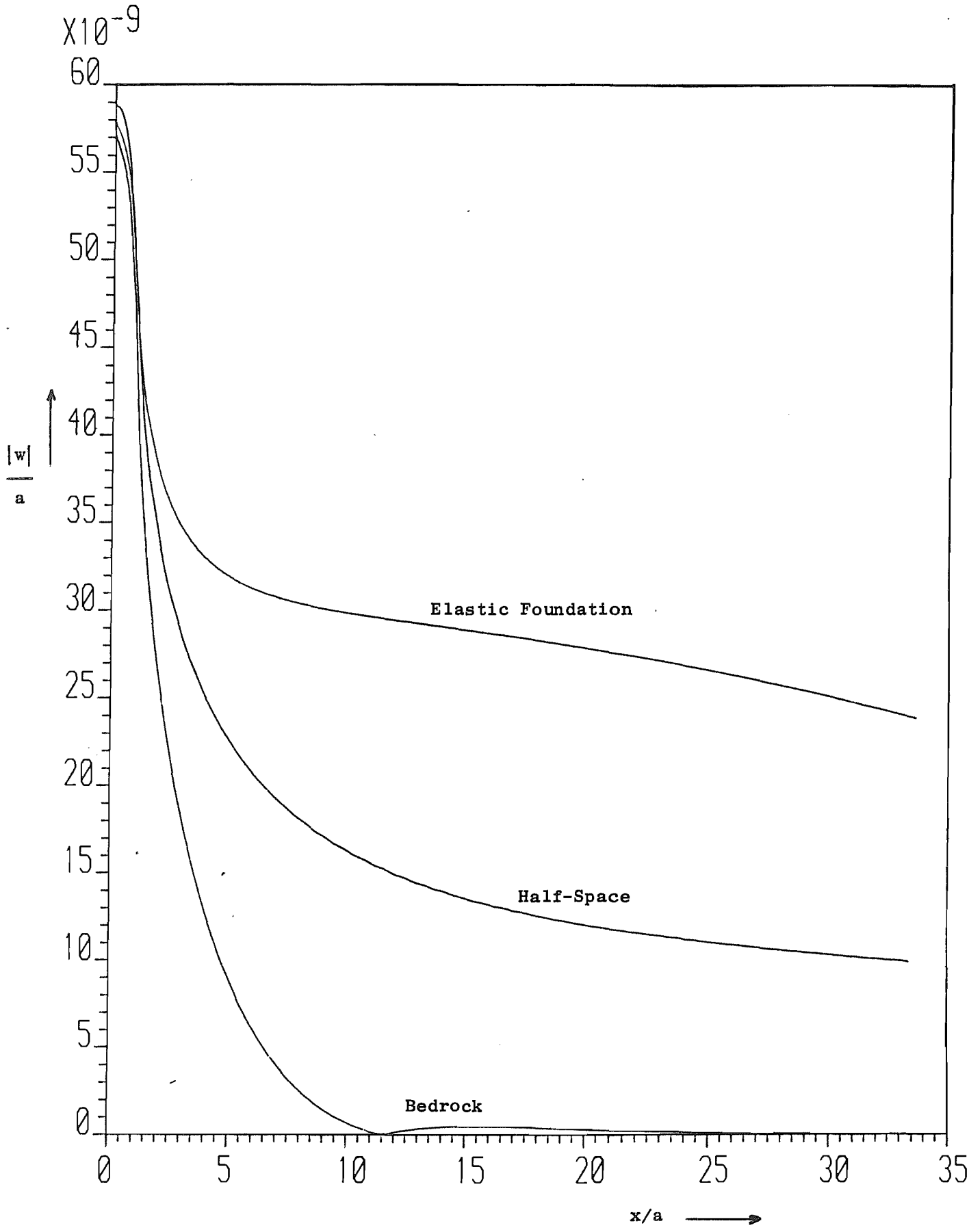

Fig 7.12: Vertical Amplitude Against Distance Predicted By The Half-Space, Bedrock And Elastic Foundation Models, At 8 Hz

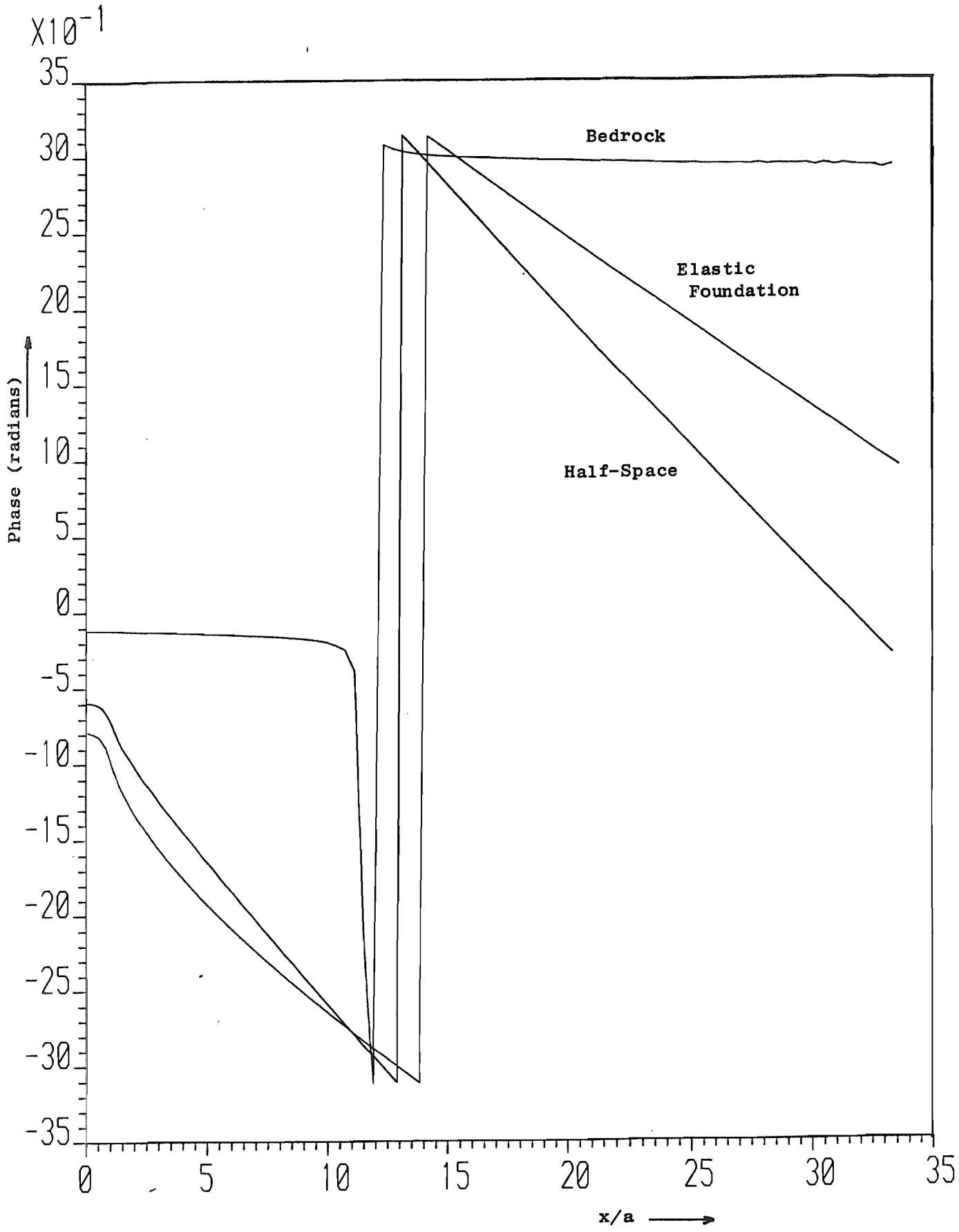

Fig 7.13: The Phase Change Corresponding To Fig 7.12

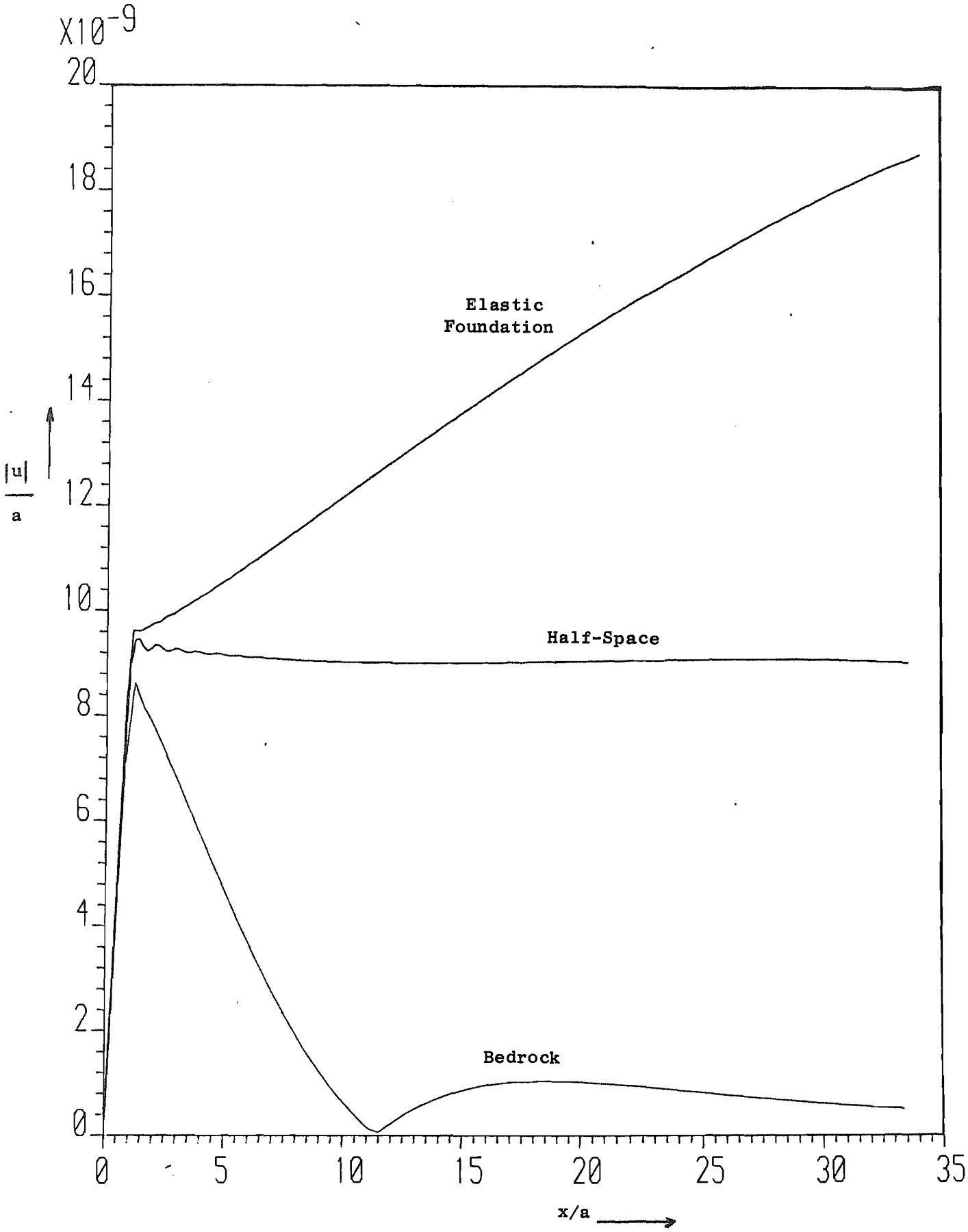

Fig 7.14: Horizontal Amplitude Against Distance Predicted By The Half-Space, Bedrock And Elastic Foundation Models, At 8 Hz

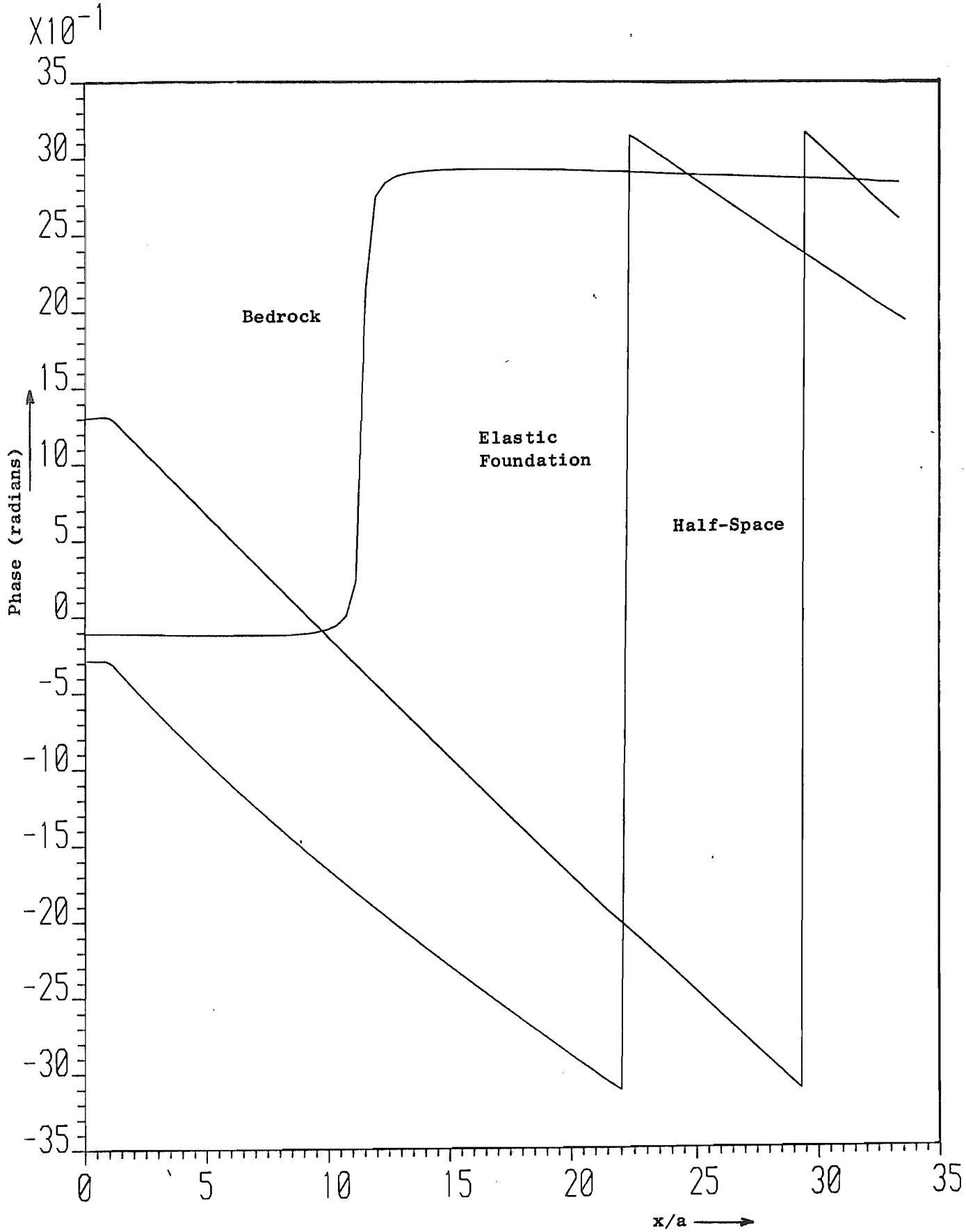

Fig 7.15: The Phase Change Corresponding To Fig 7.14

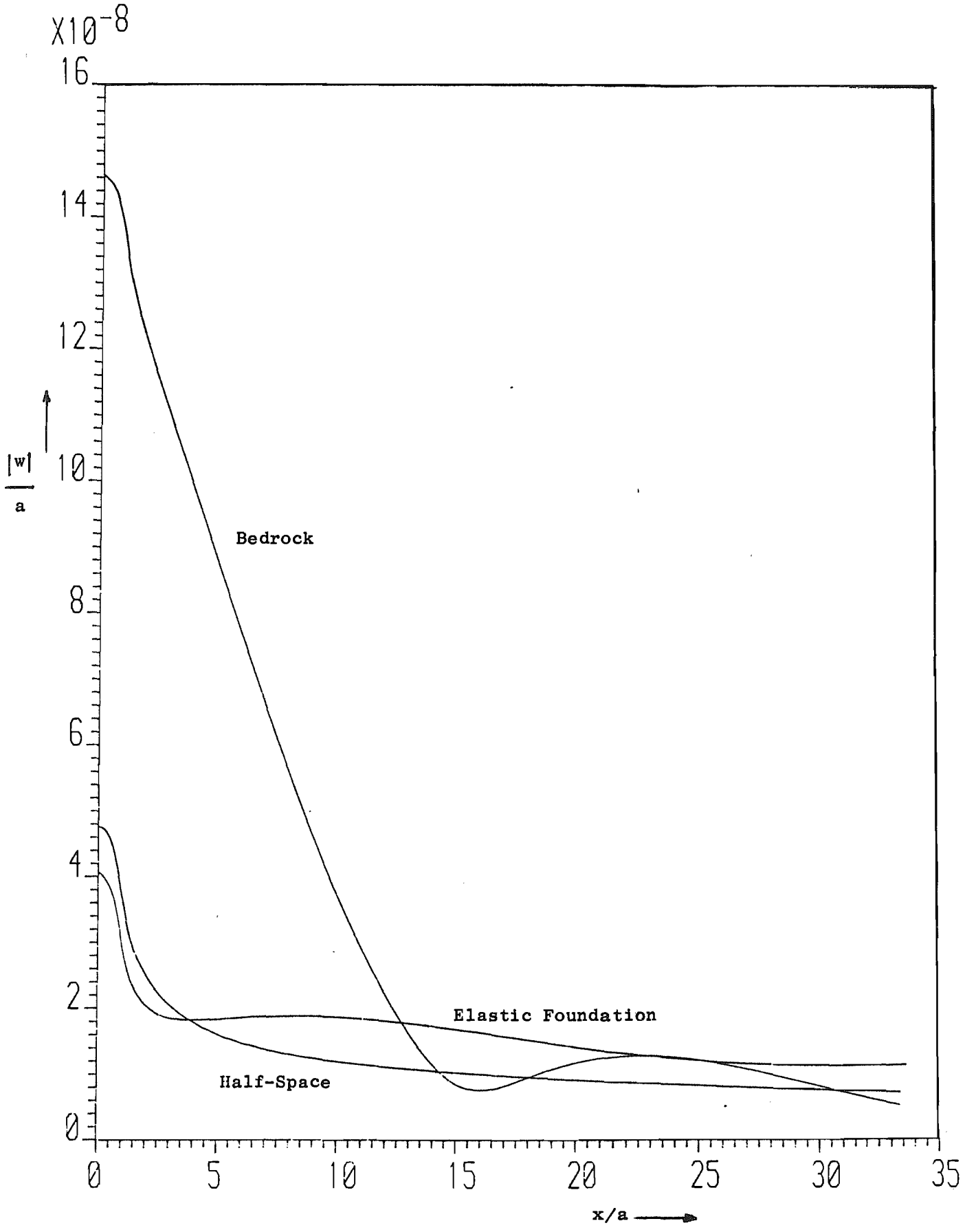

Fig 7.16: Vertical Amplitude Against Distance Predicted By The Half-Space, Bedrock And Elastic Foundation Models, At 16 Hz

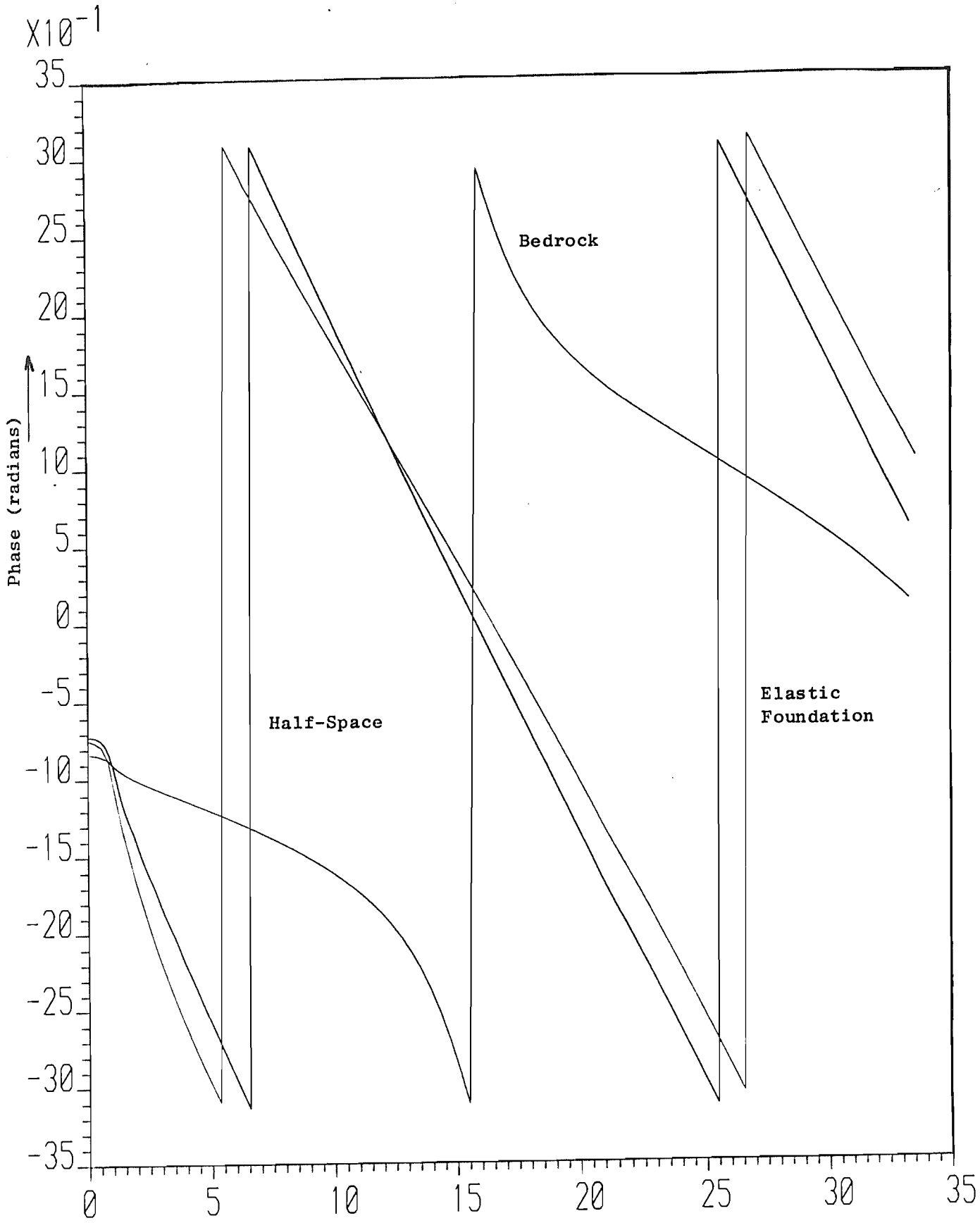

FIg 7.17: The Phase Change Corresponding To Fig 7.16

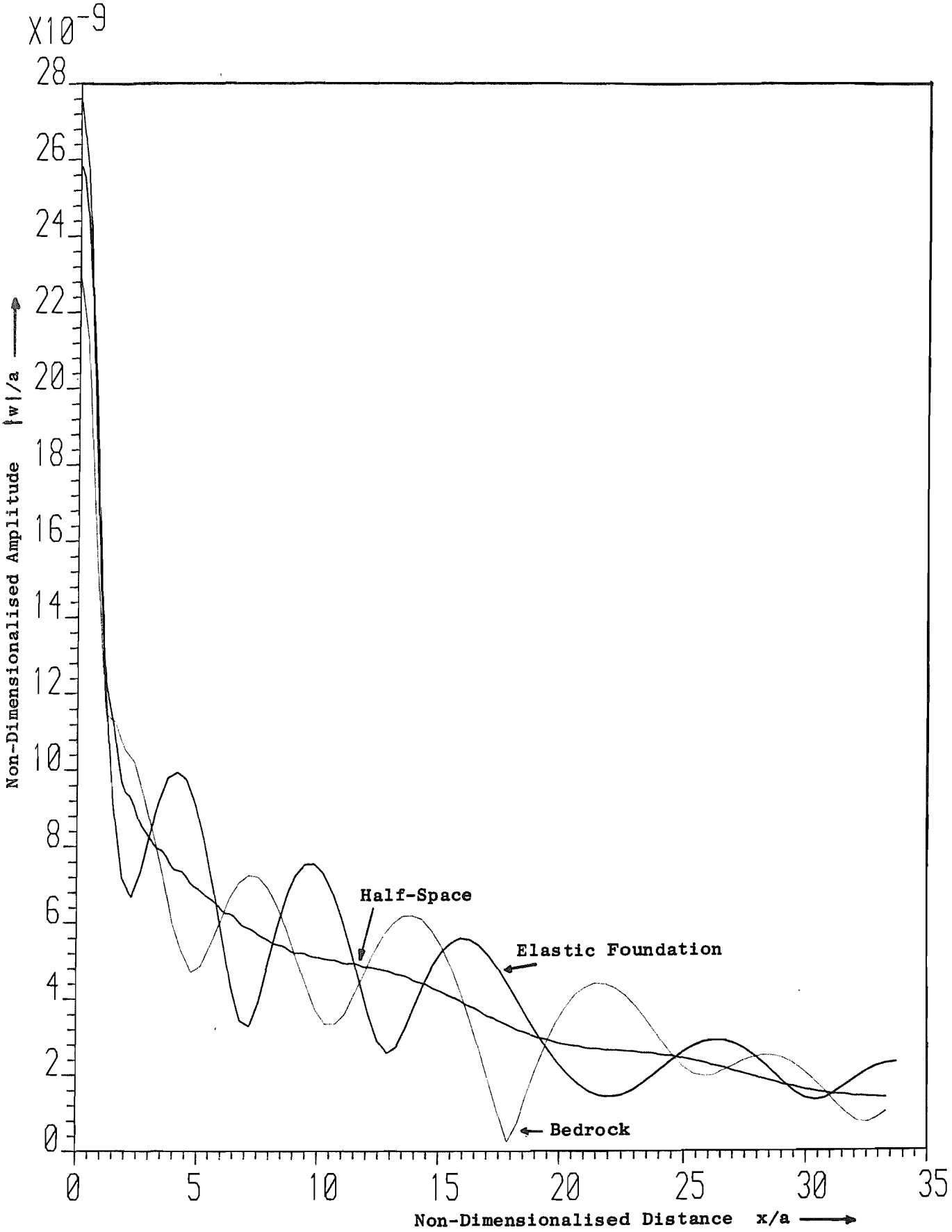

Fig 7.18: A Combination Of Vertical Motion Predicted By The Half-Space, Bedrock And Elastic Foundation Models, Frequency = 64 Hz, Loss Factor = 0.1

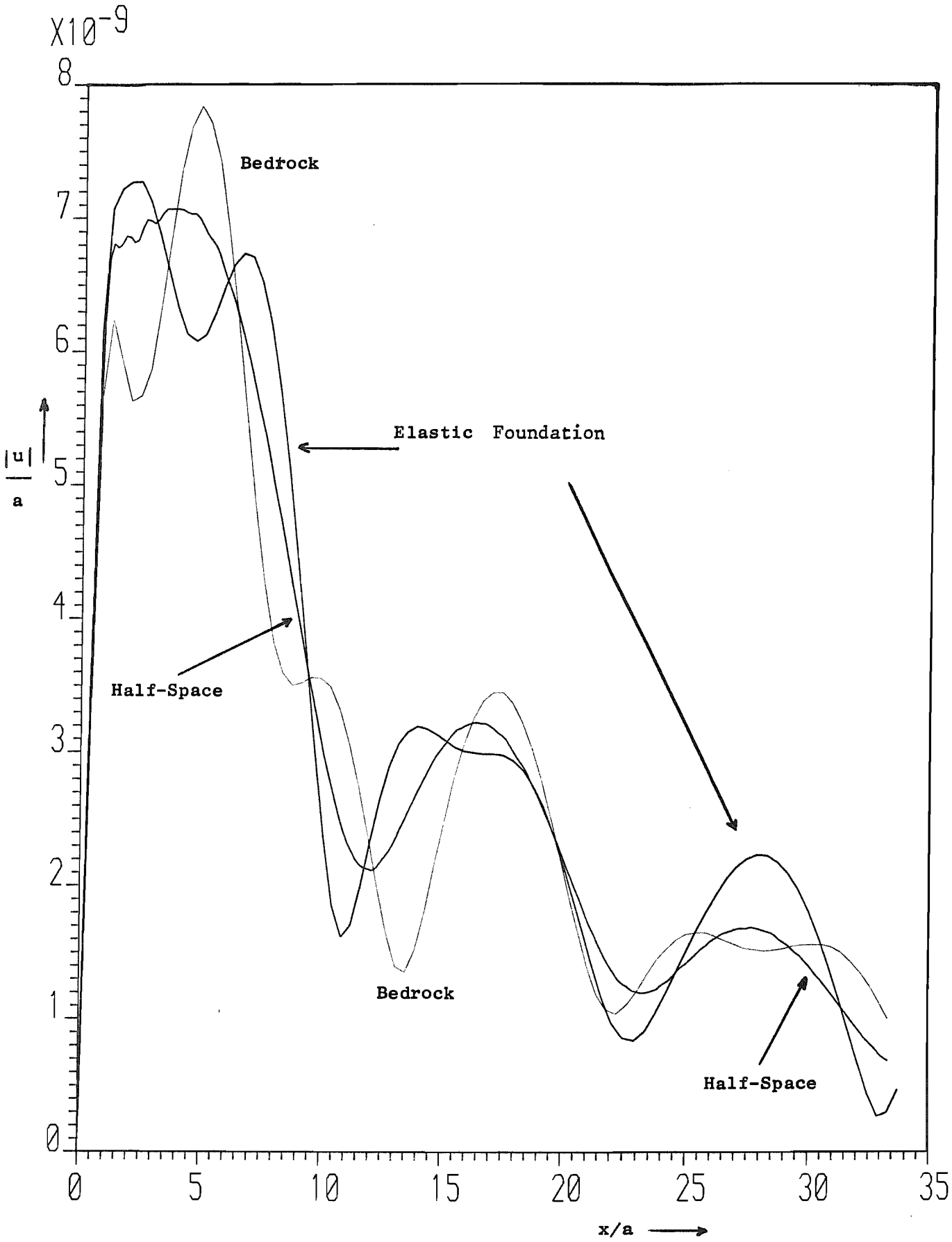

Fig 7.19: A Combination Of Horizontal Motion Predicted By The Half-Space, Bedrock And Elastic Foundation Models, Frequency = 64 Hz, $\eta = 0.01$

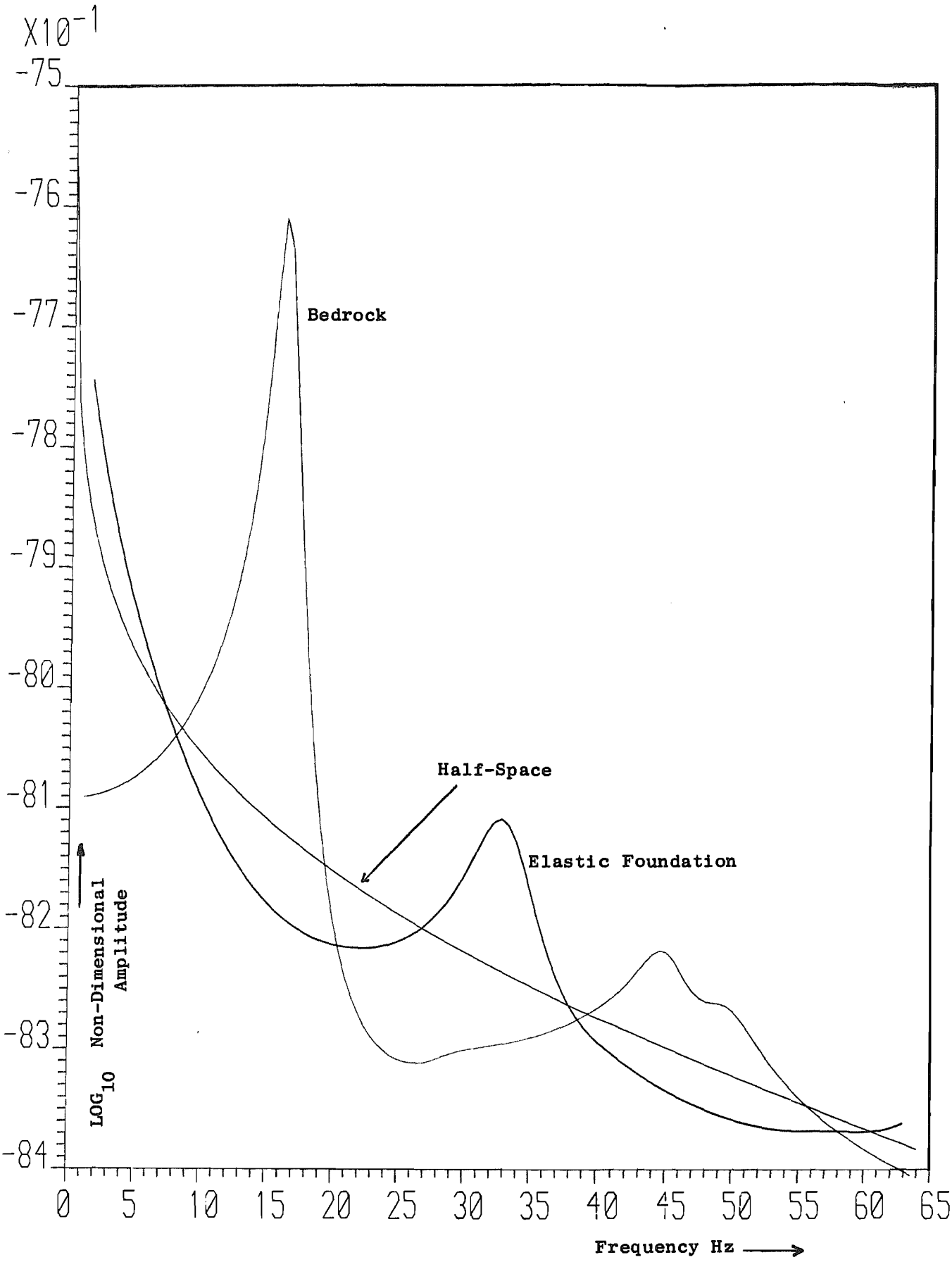

Fig 7.20: Direct Receptance For The Half-Space, Bedrock And Elastic Foundation Models.

five entries in the 'peaks' column of Table 7.1 for 64 Hz. This is because a linear amplitude scale in Figure 7.2(c) allows the sixth propagating wave's peak to be dwarfed by the other peaks. A log scale would reveal the additional peak at approximately ($a\zeta$) = 0.45.

Figures 7.3 and 7.5 show the tranformed displacements at frequencies for which one of the waves is 'leaky'. Therefore, the location of the matching low wavenumber peaks in these graphs cannot be predicted with Figure 6.2 (the leaky waves are discussed in Section 6.5.2). As a 'leaky' wave has a complex wavenumber, the relevant peak in these Figures is located at the real part of the wavenumber. Two of the frequencies chosen for Figures 7.3 and 7.5, 9.25 Hz and 38.5 Hz, are just below the frequencies at which the 3rd and 5th modes respectively become leaky (Figure 6.2). The other two frequencies, 33.0 Hz and 56.5 Hz, are just above the equivalent 'transition' frequencies for the 4th and 6th modes respectively. The first mode/propagating wave has a real wavenumber for all frequencies, and the 2nd mode/propagating wave is only 'leaky' at very small frequency. Figure 6.2 also shows that only these first six modes can exist below 64 Hz. (It should be remembered that damping has the effect of slightly increasing the frequency at which '$\zeta = 0$' phenomena occur.) Figures 7.3 and 7.5 show that the leaky waves, which lose energy to the half-space, make less of a contribution to the propagating disturbance than the 'trapped' waves. However, the 33.0 Hz and 56.5 Hz graphs show that at a frequency just above the transition between the 'leaky' and 'trapped' states, the relevant wave makes an important contribution. This is particularly true of the 4th mode/propagating wave; the sudden appearance of this trapped, propagating wave has a marked effect on the receptance graphs, shown in Figures 7.20 and 8.20 to 8.25. This is also discussed in Section 6.5.1.

As with the bedrock model, all peaks other than the first peak, which is associated with the Rayleigh wave, can be expected to tend to the shear wavenumber, with increasing frequency.

Figure 7.6 shows the amplitude of vertical motion plotted against distance, for six frequencies. The equivalent non-dimensional frequencies are given in Table 7.2. As with the bedrock model, it is

found that the higher frequencies result in more complicated variations of displacement. This is because more propagating waves exist at high frequencies, as can be seen in Figures 7.2 to 7.5, and so the interference patterns are more complicated. In common with the half-space model results, the lower frequencies dominate the response largely because of the infinite static response of these models. Additionally, it has been shown in Section 2.2 that the hysteretic damping present has more effect, per unit distance, on the propagation of higher frequency waves.

In common with the bedrock model, it is possible that the waves associated with the Rayleigh equation extraneous roots, which are discussed in Section 9.5.2, contribute to the interference patterns.

The amplitude of displacement under the load does not decrease monotonically with increasing frequency; in this respect the results are unlike those of the half-space model, but similar to those of the bedrock model. This can be clearly seen in Figure 7.20, and in the case of the elastic foundation model is attributable to the appearance of the 4th propagating wave, above 30 Hz. There is also evidence that the 6th propagating wave, which appears at about 56 Hz, causes a second much smaller peak, and a third peak, presumably associated with the appearance of another propagating wave, will occur at a frequency greater than 64 Hz.

The interference in the horizontal motion amplitude (Figure 7.7) is more pronounced than in the vertical motion (Figure 7.6), because in the former case the displacements are not dwarfed in comparison with the displacements at the strip. The strip-edge at $(x/a) = 1$ has a greater effect on the horizontal than the vertical motion, and the 4 Hz and 8 Hz components of horizontal motion propagate so strongly, that they are monotonically increasing in amplitude throughout the range shown.

Figures 7.8 and 7.9 emphasise certain features of Figure 7.6, and demonstrate the effect of reducing damping to $\eta = 0.02$ (in Figure 7.9). In comparing these Figures, it should be noted that the amplitude scales are not the same, but rather fit the data. The greater attenuation of the higher frequencies, and also their more complex displacements, are clear. As with the half-space and bedrock models,

the reduced damping greatly reduces the attenuation of amplitude of the higher frequencies, and does not suppress the interference patterns as much as the higher damping (although this second effect in Figure 7.9 is also due to the changed scale). An interference effect of long 'wavelength' can be seen in the 4 Hz curve, most clearly in Figure 7.9. Figure 7.9 also shows that in ground with low internal damping, there may exist 'zones' on the surface where the largest contribution to displacement is of a high frequency, such as for 48 Hz near (x/a) = 30. A similar effect can be seen in Figure 7.7, for the 32 Hz component near (x/a) = 12. However, this conclusion is only possible with a graph such as Figure 7.9, if the reference values for each curve at (x/a) = 0 are known. Although the 4 Hz component is more attenuated than the 48 Hz component near (x/a) = 30, their magnitudes are also a function of their displacements at (x/a) = 0.

Figure 7.10 shows the phase change with distance of the two frequency components 4 and 32 Hz, for $\eta = 0.02$. The loss factor has little effect on the appearance of these curves - the wavelength, determined by the distance required to change phase by $2\pi^c$, is shortened slightly by increased η. As with the phase change graphs in previous Chapters, the apparent discontinuities in the lines are a convenience for graph-plotting, to confine the scale to $\pm\pi$. Failure of each line to reach $\pm\pi$ is due to inadequate resolution. The rate of change of phase is identical to the wavenumber of the propagating disturbance (or the sum by superposition of all the propagating waves). Measuring this change in Figure 7.10 for the 4 Hz component, reveals that its wavenumber is very close to the wavenumber of the dominant peak in Figure 7.4(a). Only two waves can propagate at 4 Hz, and the one corresponding to the first mode of free vibration clearly dominates. However, Figure 7.10 shows that the 32 Hz component does not have a constant wavenumber for $(x/a) \leq 100$, and the average value is not so close to the wavenumber of the first peak (the Rayleigh wavenumber at this frequency). The changes in wavenumber are related to the maxima and minima in the 32 Hz components of Figures 7.6 and 7.7; this relationship also applies to the bedrock model, and is discussed in Section 5.4.

Figure 7.11(b), (c) and (d) can be compared directly with Figures 3.10 and 5.10(b), (c) and (d), since they are all for the same

frequencies and loss factor. The first graph in each case ((a)) is not at the same frequency, due to numerical problems in the solution, but each one serves its purpose of showing the trend as frequency increases. They all show the effect on displacement at the centre of the strip, of varying the strip-width, with constant force per unit width. The graphs all exhibit a similar pattern of troughs and peaks. In Section 3.5, for the half-space model, it is suggested that the location of these troughs and peaks, which is frequency dependent, is because of the "resultant wavelength" of the shear, compression and Rayleigh waves. This wavelength is deduced from Miller and Pursey's calculated energy distribution among the waves [57]. The different boundary conditions in the three models produce peaks and troughs of different amplitude, but because their locations are so close, it seems reasonable to extend the "resultant wavelength" hypothesis to this model too, particularly for the high frequencies, for which the solutions merge.

Figures 7.12 to 7.20 are a comparison of the forced response results of the three ground structure models so far considered: the half-space, bedrock and elastic foundation with a strip-load. The first four Figures are all for 8 Hz, and show the vertical components of motion, and their phase change, and the horizontal components of motion, and their phase change, respectively, for each model. Although all three have similar amplitudes under the load, the rest of the solutions are quite different. The bedrock model does not allow propagation of vibration at this frequency, and so the displacements in the near-field are much smaller than produced with the half-space model. Equally, the elastic foundation model results in greater near-field displacements than the half-space, because at this low frequency a long wavelength is produced, and much more energy is trapped near the surface by the layer than by the half-space.

The phase change due to the bedrock model, shown here in Figures 7.13 and 7.15 for the 8 Hz case, has been discussed in Section 5.4. It reveals the lack of propagation. In the case of the half-space, it reveals the dominance of the Rayleigh wave. The somewhat faster wave represented by the longer wavelength in the elastic foundation, shows the dominance of the propagating wave connected with the first mode of free vibration. The ratio of this wavespeed and the Rayleigh wavespeed can be

approximated from Figure 6.3, by reading the wavespeed of the first mode for 8 Hz. The Rayleigh wavespeed is marked on the wavespeed scale. This gives an approximate ratio, because no damping exists in the free vibration analysis.

Figures 7.16 and 7.17 show the vertical component of motion and its phase change, respectively, for each model, at a frequency of 16 Hz. These results represent a considerable departure from the 8 Hz case, as 16 Hz not only allows propagation in the bedrock model, but is a resonance frequency. This phenomenon is discussed in Section 5.4. As a result, the bedrock model response is much greater than that of the other two models, for $(x/a) < 10$. The minimum in the bedrock amplitude at $(x/a) \simeq 16$, which is matched by a locally slower rate of propagation (see Fig. 7.17), is also discussed in Section 5.4. For the half-space and elastic foundation results in Figures 7.16 and 7.17, similar reasoning can be applied as to the 8 Hz results. A 16 Hz input also produces a fairly long wavelength compared with the layer depth (Table 3.2 gives the wavelengths for each frequency), and so the layer is effective at 'trapping' energy, in comparison with the half-space. Therefore, the elastic foundation displacements for $(x/a) > 4$ exceed those of the half-space, and the latter's wavespeed is the smaller (Fig. 7.17). Again the ratio of the wavespeeds can be approximated from Fig. 6.3.

In Figs. 7.18 and 7.19, a jump in frequency is made, to 64 Hz, and the vertical and horizontal components of motion respectively are shown, for each model. Although the many propagating waves produced in the layered models at this frequency produce complicated variations in amplitude, it is clear that the three solutions show signs of merging, with the increased frequency. The average phase changes for each model (not shown at this frequency) are also close. The layer solutions seem to fluctuate about the half-space solution, as if it were a mean value. At sufficiently high frequency, it is known (see Section 5.4) that the layer/half-space interface becomes practically irrelevant.

Figure 7.20 shows the direct receptance of the three models using a log scale to aid comparison. These curves are also reproduced and discussed in Chapter 8. The half-space and elastic foundation have infinite static responses (with the strip load; see Section 8.4), and

the elastic foundation exhibits a resonance peak near 33 Hz, because of the fourth propagating wave. The bedrock receptance curve has several resonance peaks, the most significant being the 16 Hz resonance which causes the large amplitude shown in Fig. 7.16. These bedrock resonance peaks are also a result of the behaviour of propagating waves, as discussed in Section 5.4.

CHAPTER 8

THE EFFECT OF MASSES PLACED ON THE GROUND'S SURFACE

8.1 Introduction

In this Chapter, several problems are investigated:

(i) the effect on direct receptance of a mass placed at the load;

(ii) the transfer receptance at 25 m from the load, if a mass is placed between these two points;

(iii) the transfer receptance at 25 m from the load, if two masses are placed at different points between the load and the response point.

Each of the three situations is considered with various masses, and the three ground structure models - elastic half-space, elastic layer over inflexible bedrock (the "bedrock model"), and elastic layer over an elastic half-space of different material (the "elastic foundation model") are all treated.

The first problem of a mass at the load, is an extension of the work in previous Chapters to a more realistic model. The other two problems are relevant to attempts to absorb surface vibration, by exciting masses placed there. The literature on this subject includes much work on masses on discs, on either a half-space or an elastic layer over a half-space. This work will be considered in Chapter 9. Luco and Westmann [50], in a work mainly concerned with the effect of the type of bonding between a rigid, massless strip and a half-space, give some receptance figures of interest. Alabi [2] has used a mapping finite difference model, to analyse the harmonic vertical motion of a rigid strip; he presents direct receptance graphs for various masses at the load. Gazetas and Roesset [23] also give direct receptance graphs, for each of the three ground structure models considered in this work, and an infinite strip load.

The analysis in the next section of this Chapter is based on the method of receptances. The results presented are all receptance graphs, calculated for a range of frequencies and masses which are of interest.

8.2 Analysis of the Effect of a Mass on the Ground's Surface Vibration

The method of receptances will be used, which is described by, among others, Bishop and Johnson [20].

Consider first a harmonic force acting on a mass, which rests at a point on the surface of the ground. The structure of the ground can be any of the three models considered in earlier chapters. For the purpose of finding the direct receptance of the mass-ground combination, consider the diagram shown in Fig. 8.1, which breaks the problem into elements:

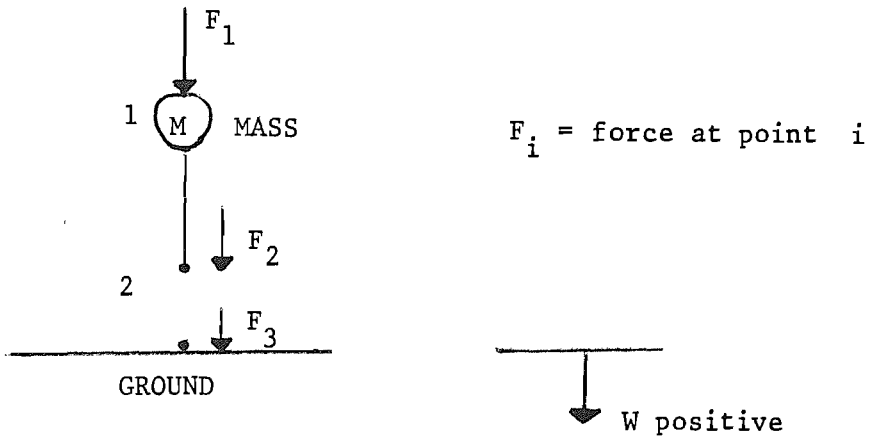

Fig. 8.1: Direct Receptance Model Diagram

By the law of action and reaction, $F_3 = -F_2$.

Considering the ground first:

$$W_2 = \beta_{22} F_3 = -\beta_{22} F_2 \qquad (8.1)$$

where W_2 is the displacement of the ground at point 2, and β_{22} is the direct receptance there; throughout, 'β_{ij}' will refer to a receptance, either direct or transfer, of the ground, and α_{ij} will similarly refer to a mass.

At the mass, which has the same displacement as the ground it rests on:

$$W_2 = \alpha_{21} F_1 + \alpha_{22} F_2 \qquad (8.2)$$

where α_{21} and α_{22} are respectively the transfer and direct receptances of the mass. Also,

$$\alpha_{21} = \alpha_{22} = \frac{-1}{M\omega^2} \qquad (8.3)$$

since the forces are harmonic.

Eliminating F_2 gives:

$$W_2 = \frac{\alpha_{22}\,\beta_{22}}{\alpha_{22} + \beta_{22}}\, F_1 \qquad (8.4)$$

which leads to

$$\frac{W_2}{F_1} = \frac{1}{\left[\,1/\alpha_{22} + 1/\beta_{22}\right]} \qquad (8.5)$$

which is the direct receptance expression required. α_{22} is given by equation (8.3) for a given frequency, and β_{22} can be deduced for a range of frequencies, and for each ground structure model, using the methods described in Chapters 3, 5 and 7.

To find the transfer receptance at a point under a mass, some distance from the applied harmonic force, a similar method can be used. Referring to the receptance model diagram shown in Fig. 8.2, the response at point 2 on the ground is:

$$W_2 = \beta_{21} F_1 + \beta_{22} F_2 \qquad (8.6)$$

Fig. 8.2: Transfer Receptance Model Diagram

The force on the mass is F_2, and so we have:

$$W_2 = - \alpha_{22} F_2 \qquad (8.7)$$

Elimination of F_2 gives:

$$\frac{W_2}{F_1} = \frac{\beta_{21}}{1 + \beta_{22}/\alpha_{22}} \qquad (8.8)$$

where α_{22} is again defined by equation (8.3). Hence the transfer receptance under a mass can be found.

Of more interest is the transfer receptance at a point beyond the mass, which itself is beyond the load; this situation is shown in Fig. 8.3:

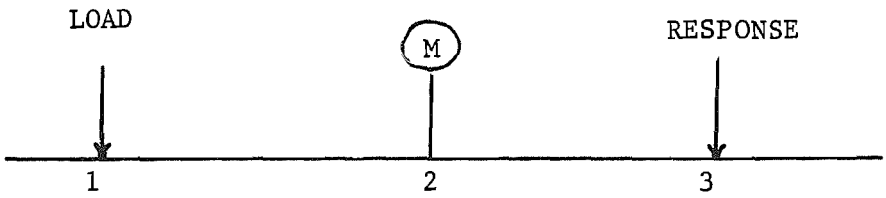

Fig. 8.3: Transfer Receptance Model Diagram, With Mass between Load and Response Point

Now if W_3 is the response at point 3,

$$W_3 = \beta_{31} F_1 + \beta_{32} F_2 \qquad (8.9)$$

where β_{3j} are transfer receptances in the same sense as before. The force F_2 acting on the mass m is given by:

$$F_2 = - \frac{1}{\alpha_{22}} W_2 \qquad (8.10)$$

Substituting for α_{22} in equation (8.10) from equation (8.3), and dividing through by F_1 gives:

$$\frac{W_3}{F_1} = \beta_{31} - \frac{\beta_{32}}{\alpha_{22}} \frac{W_2}{F_1} \qquad (8.11)$$

But (W_2/F_1) is given by equation (8.8), and so

$$\frac{W_3}{F_1} = \beta_{31} - \frac{\beta_{32}\,\beta_{21}}{(\alpha_{22} + \beta_{22})} \qquad (8.12)$$

This expression gives the transfer receptance at point 3, due to a force at point 1 and a mass at point 2.

If a second mass is introduced, the situation shown in Fig. 8.4 is reached:

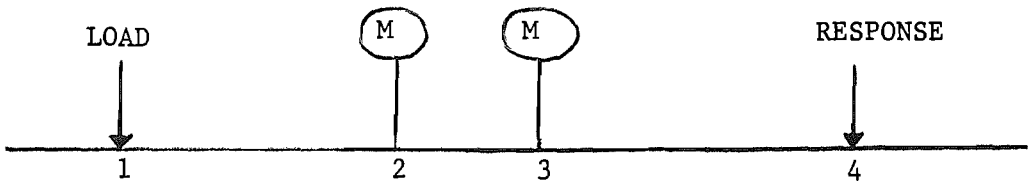

Fig. 8.4: Transfer Receptance Model Diagram, With Two Masses Between Load and Response Point

Now $$W_4 = \beta_{41} F_1 + \beta_{42} F_2 + \beta_{43} F_3 \qquad (8.13)$$

and with analysis similar to the one mass case, the expression

$$\frac{W_4}{F_1} = \beta_{41} - \frac{\beta_{42}\,\beta_{21} + \beta_{43}\,\beta_{31}}{\alpha_{22} + \beta_{22}} \qquad (8.14)$$

can be deduced. With equation (8.14) the transfer receptance at point 4, with a load at point 1, and two intervening masses, can be calculated.

8.3 Results

The receptance expressions in equations (8.5), (8.12) and (8.14) have been evaluated for a range of frequencies, and for several masses. The distances between the load, masses and response point, and also the magnitude of the masses chosen, were all suggested by British Rail R&D. The masses were 0, 1, 3 and 10 tonnes for the transfer receptance graphs, and a larger range of eight masses for the direct receptance graphs. The masses were always distributed over a strip the same width as the exciting force. The transfer receptance was calculated at a point 25 m from the load. The mass was placed at several positions, the closest to the load being 3 m. When two masses were placed on the surface, they were always of the same magnitude.

The ground material properties correspond to those measured at the Clarborough test-site, and are given in Table 2.2. The loss factor of the ground's damping used is, $\eta = 0.1$.

The results show a non-dimensional quantity plotted against a dimensional one, which is unusual. Non-dimensional vertical amplitude, at a specified distance from the centre of the strip load, is plotted against frequency measured in Hz. This is to facilitate comparison with the results in other Chapters, where non-dimensional amplitudes are shown plotted against non-dimensional distance for a fixed frequency. These fixed frequencies are given in both non-dimensional form, and dimensional form, with particular reference in the latter case to Clarborough. For the non-dimensional extension to other test sites, such as Checkerhouse, see Chapter 3.

Figures 8.5, 8.6 and 8.7 show direct receptance at $x = 0$, with a variety of masses, for the half-space, bedrock and elastic foundation models respectively. Figs. 8.8 to 8.11 show receptance for the half-space model, with one mass at varying positions, and Figs.8.12 and 8.13 show receptance with two masses in the half-space model. Figs. 8.14 to 8.17 are bedrock receptance graphs with one mass, and Figs. 8.18 and 8.19 are similar but with two masses. Figs. 8.20 to 8.23 are receptance graphs for the elastic foundation model, with one mass, and Figs. 8.24 and 8.25 show the results with two masses.

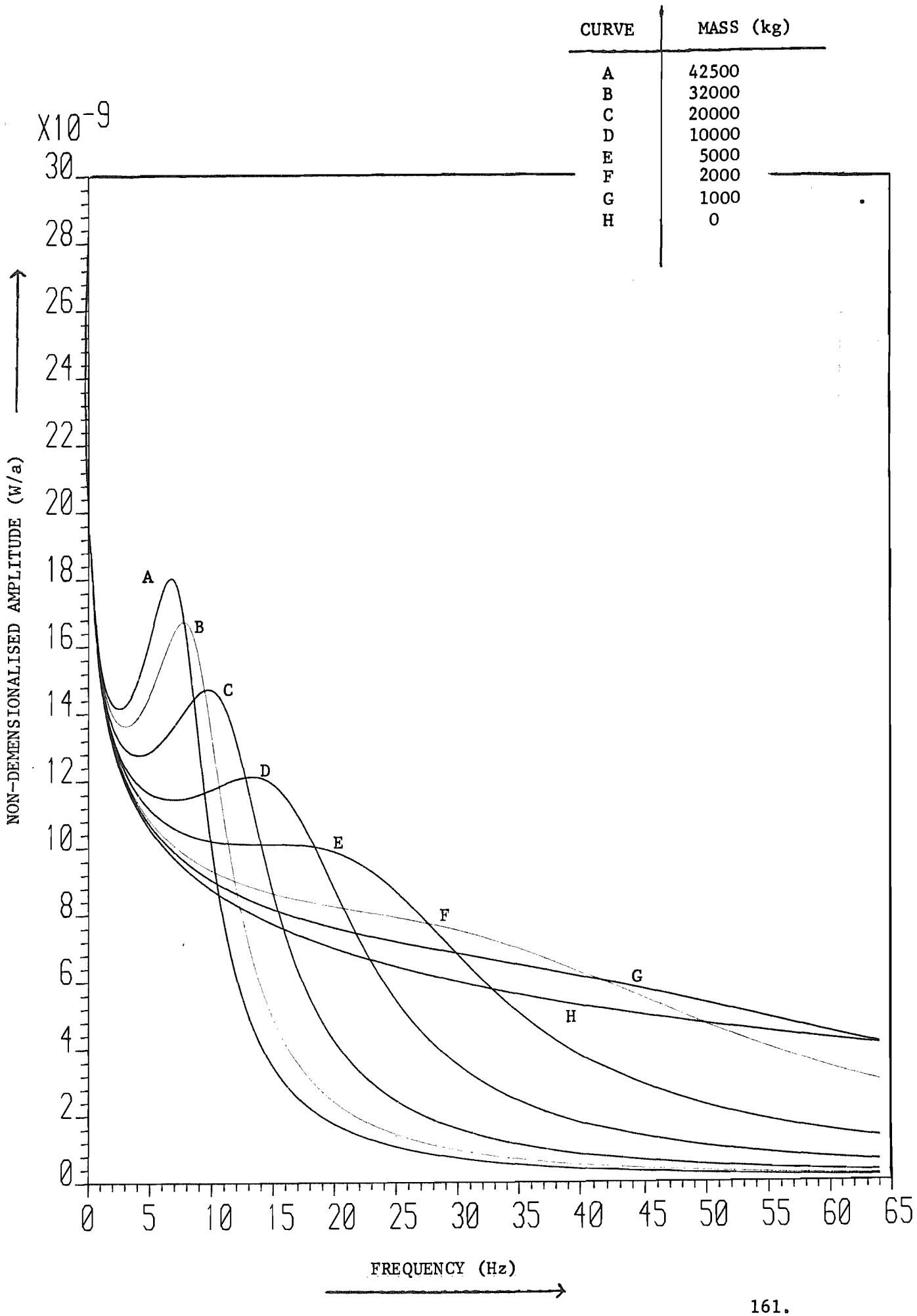

FIG. 6.5 Direct Receptance for the Halfspace Model

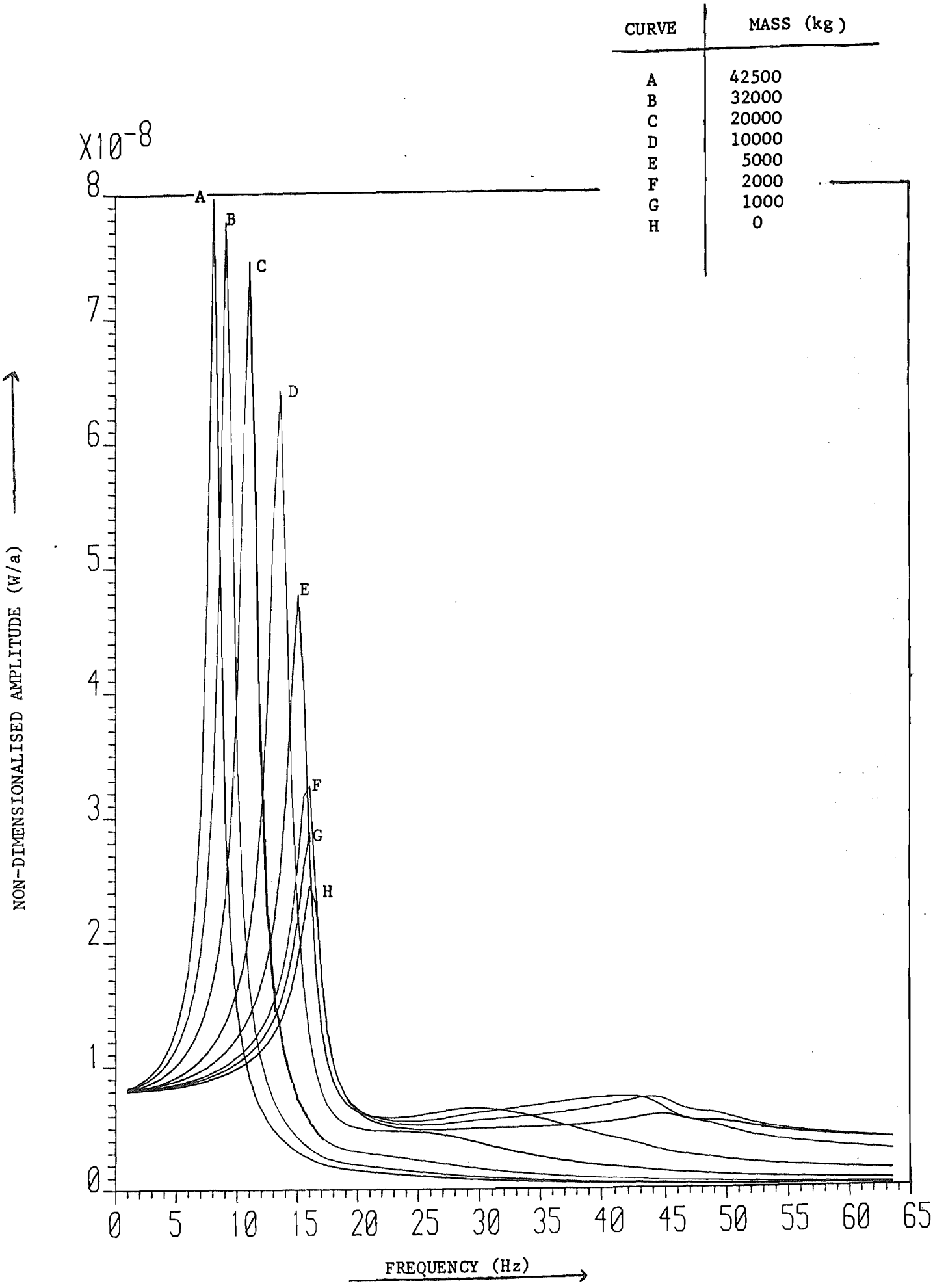

FIG. 8.6 Direct Receptance for the Bedrock Model

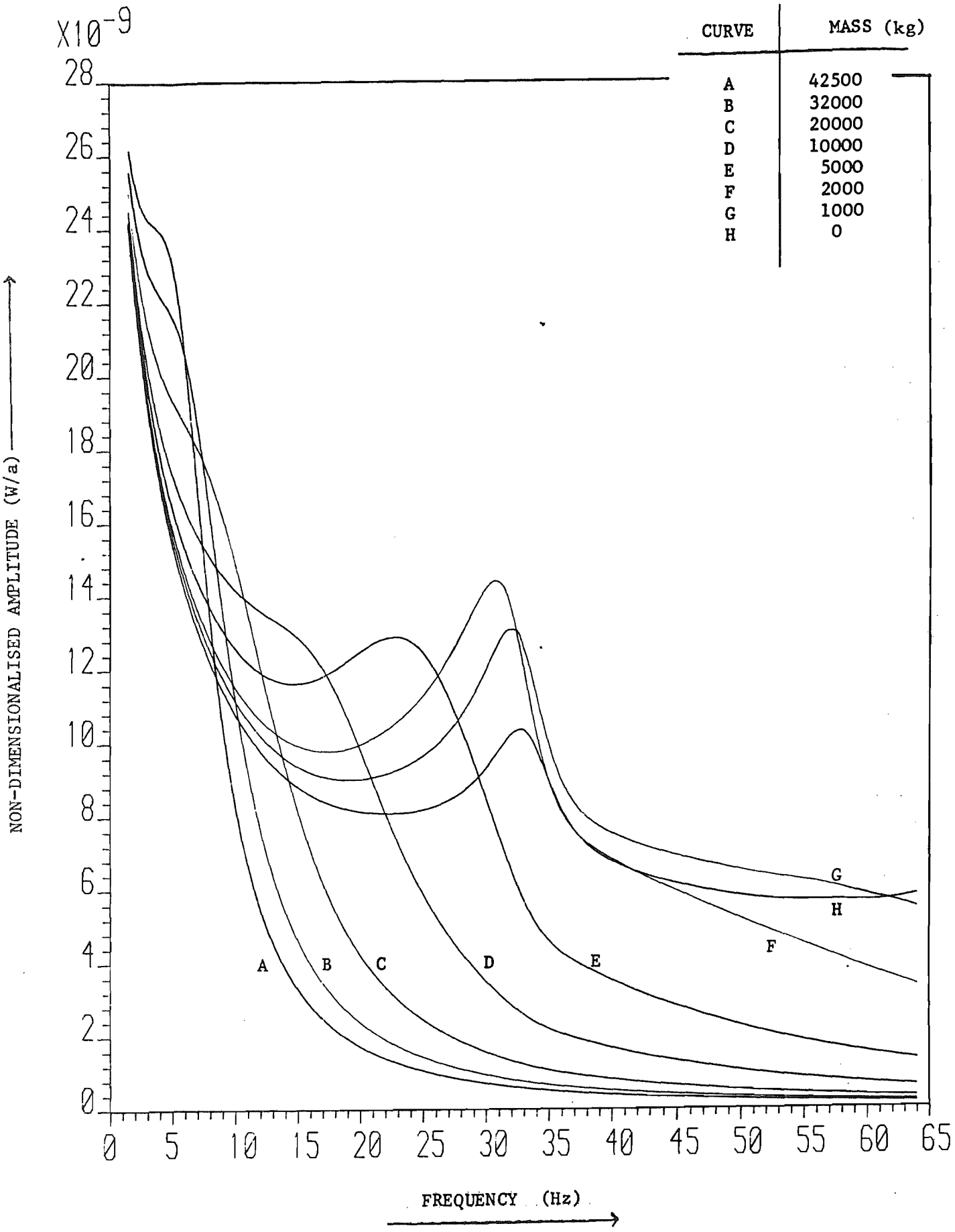

FIG. 8.7 Direct Receptance for the Elastic Foundation Model

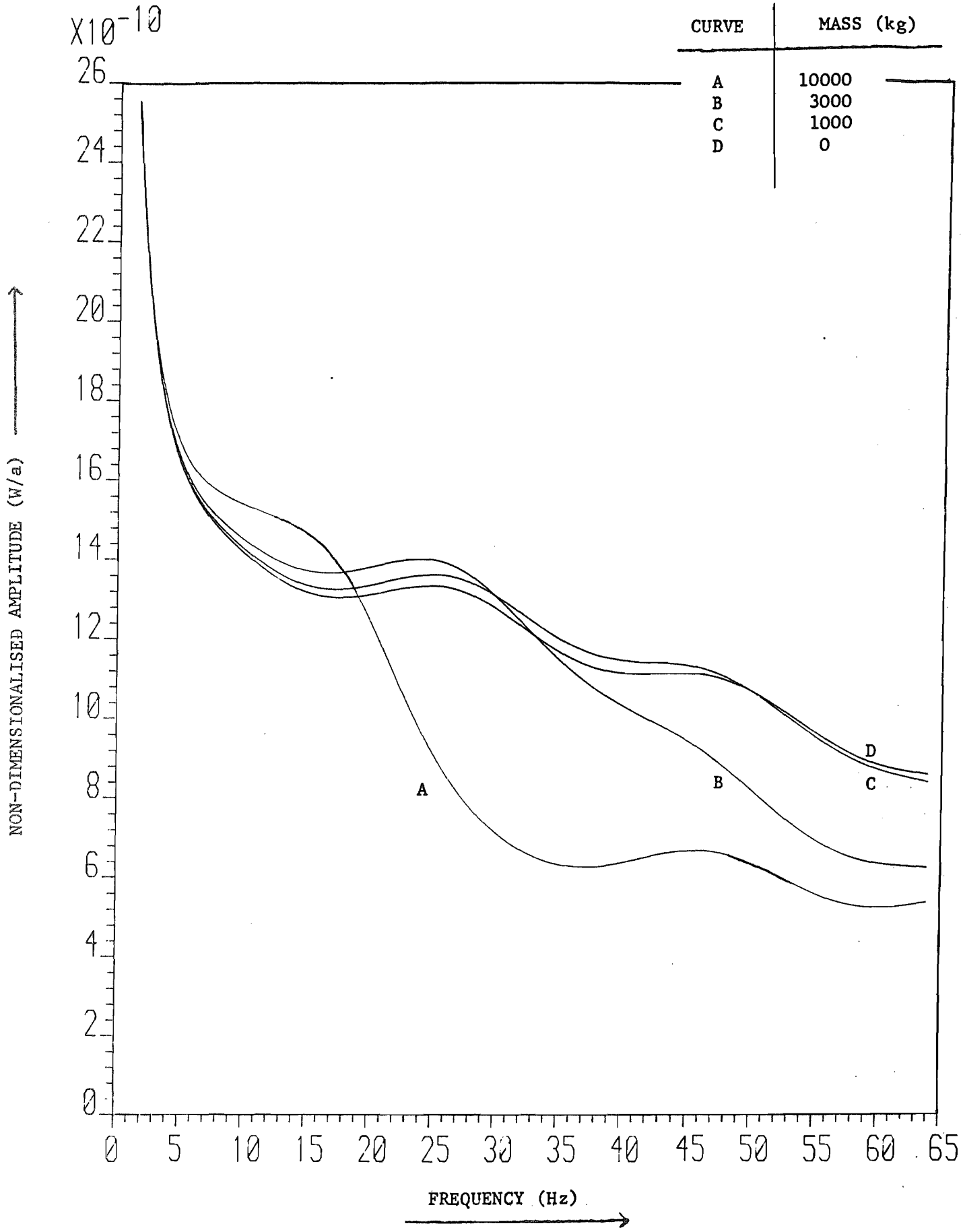

FIG. 8.8 Transfer Receptance at 25m, Halfspace Model, with a Mass at 3m.

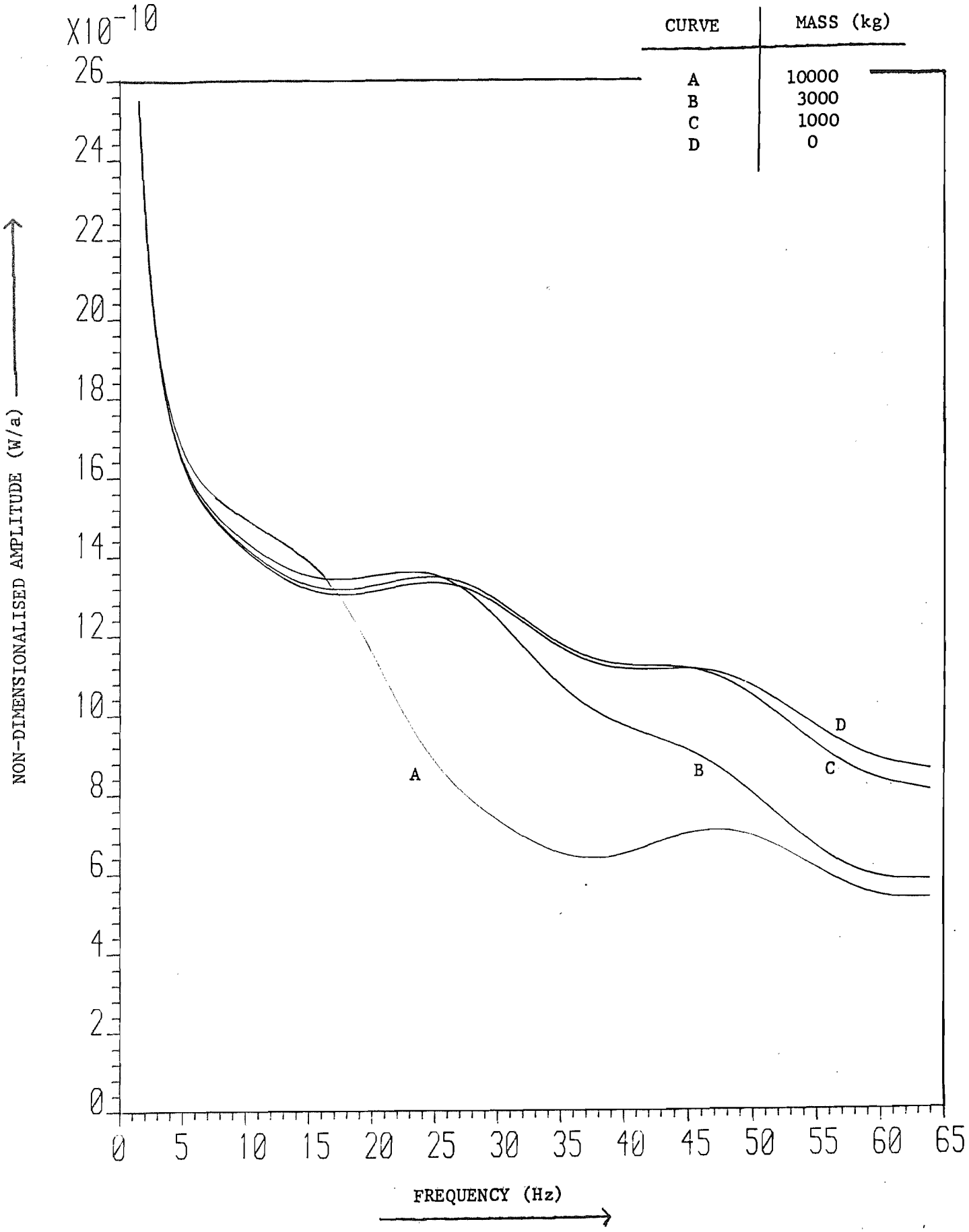

FIG. 8.9 Transfer Receptance at 25m, Halfspace Model, with a Mass at 5.5m

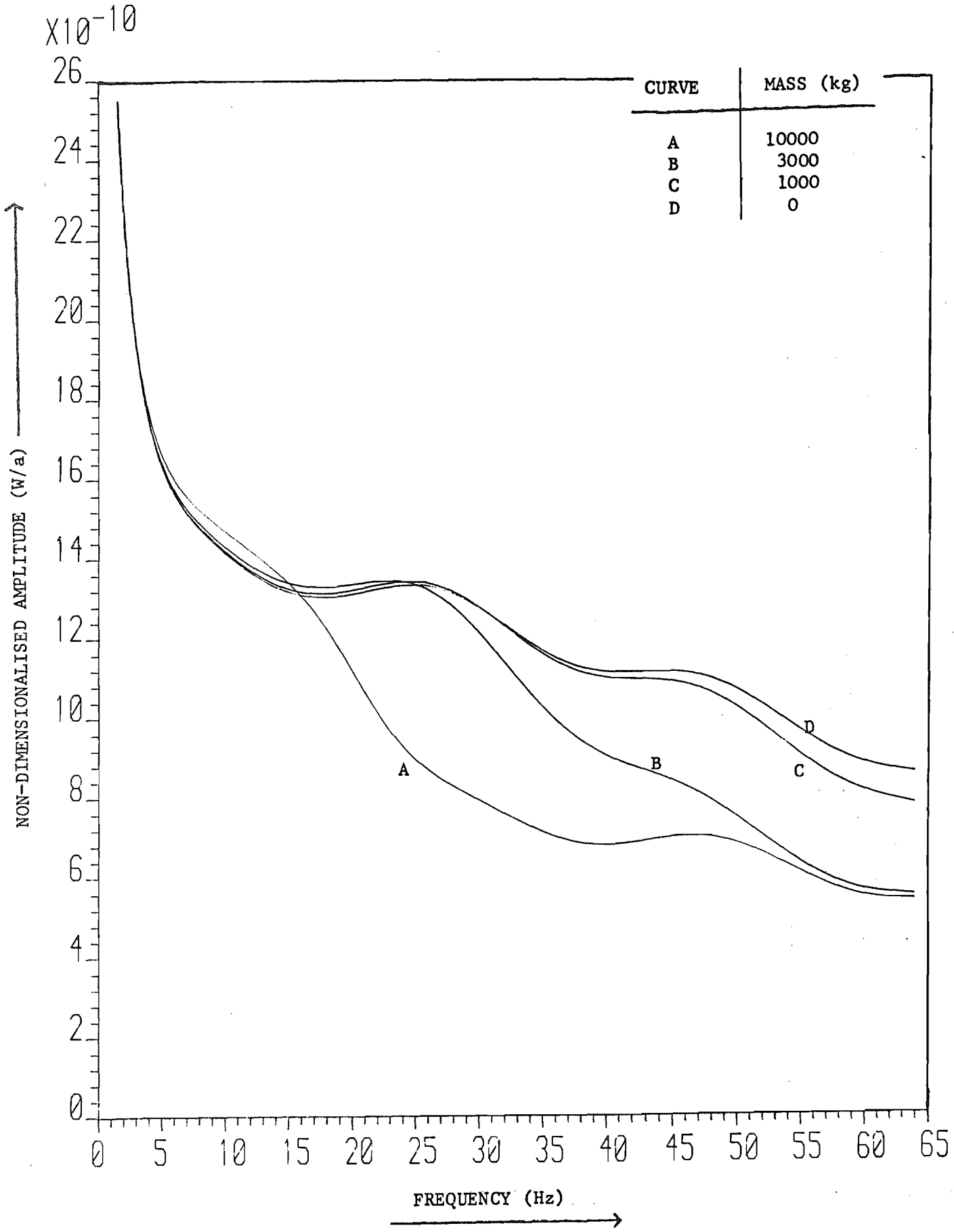

FIG. 8.10 Transfer Receptance at 25m, Halfspace Model, with a Mass at 10m.

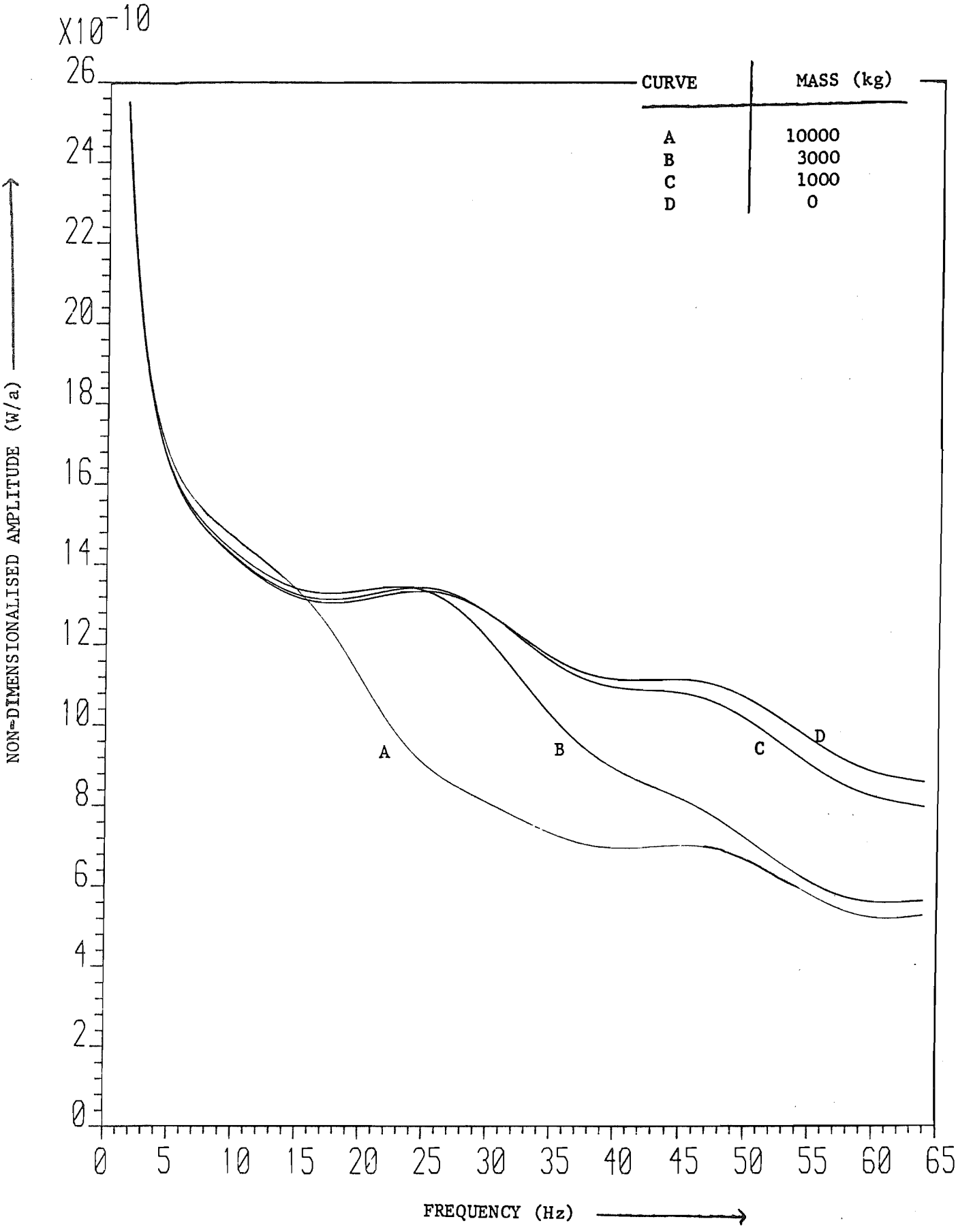

FIG. 8.11 Transfer Receptance at 25m, Halfspace Model, with a Mass at 12.5m.

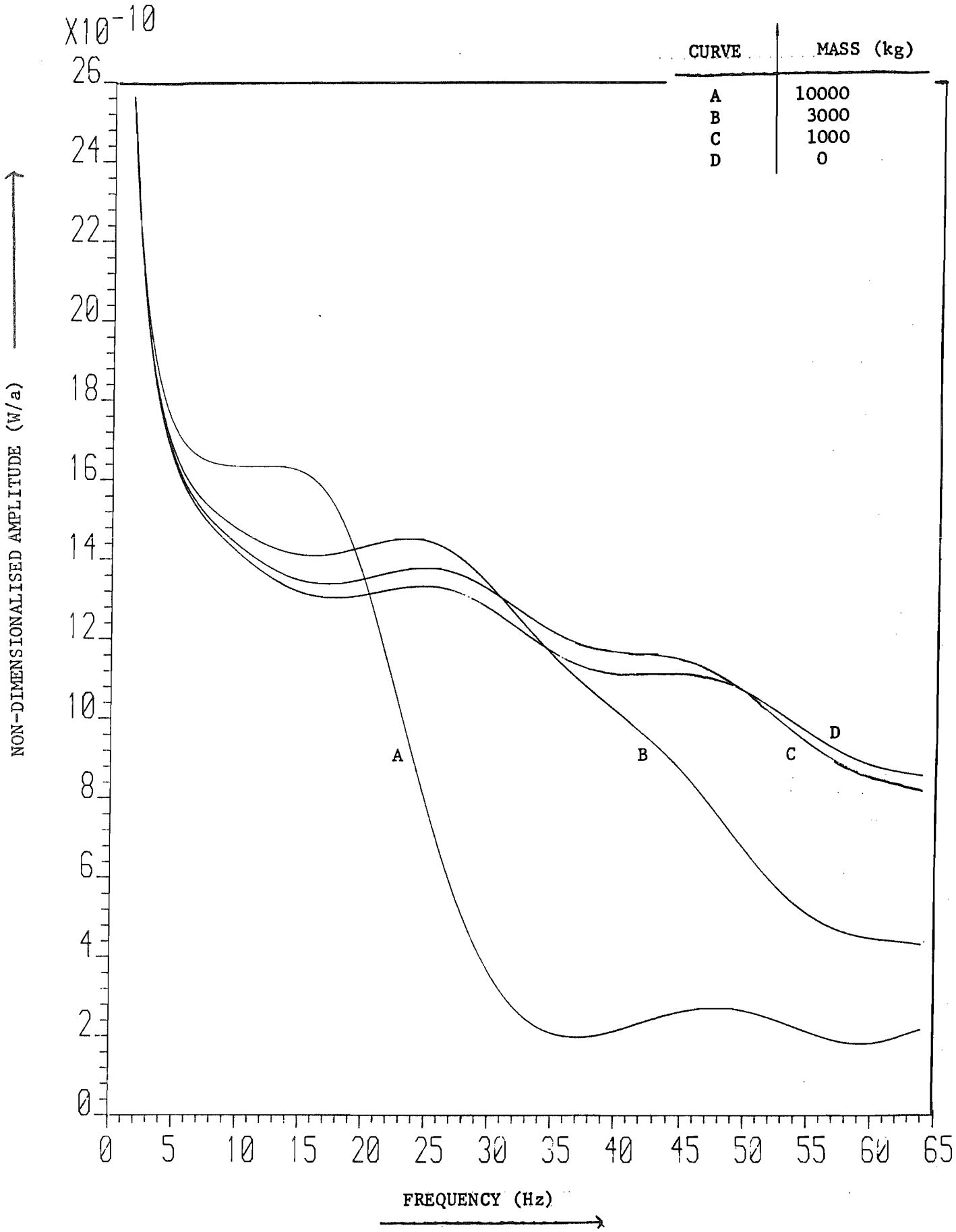

FIG. 8.12 Transfer Receptance at 25m, Halfspace Model, with Masses at 3 & 5.5 m

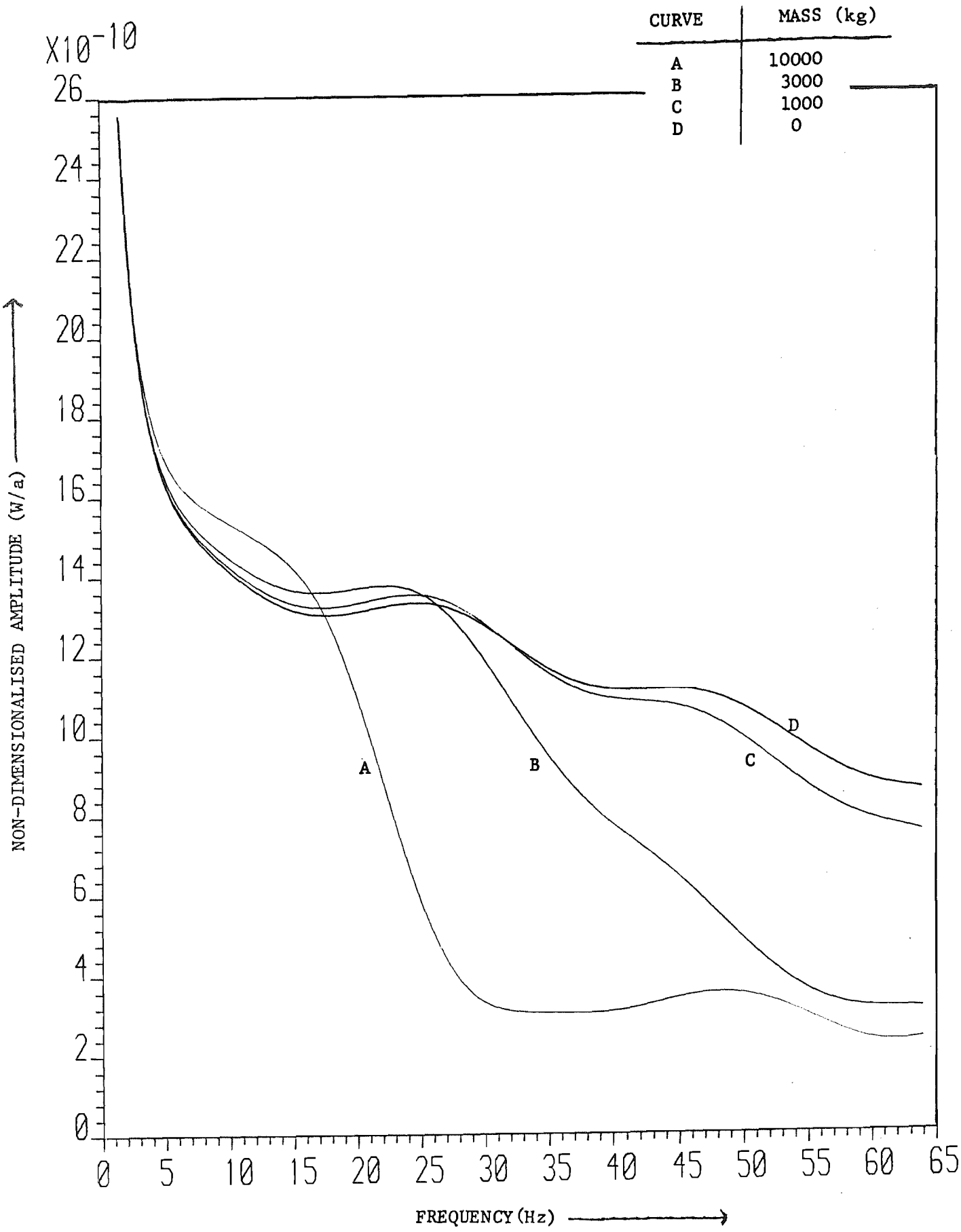

FIG. 8.13 Transfer Receptance at 25m, Halfspace Model, with Masses at 10 & 12.5m.

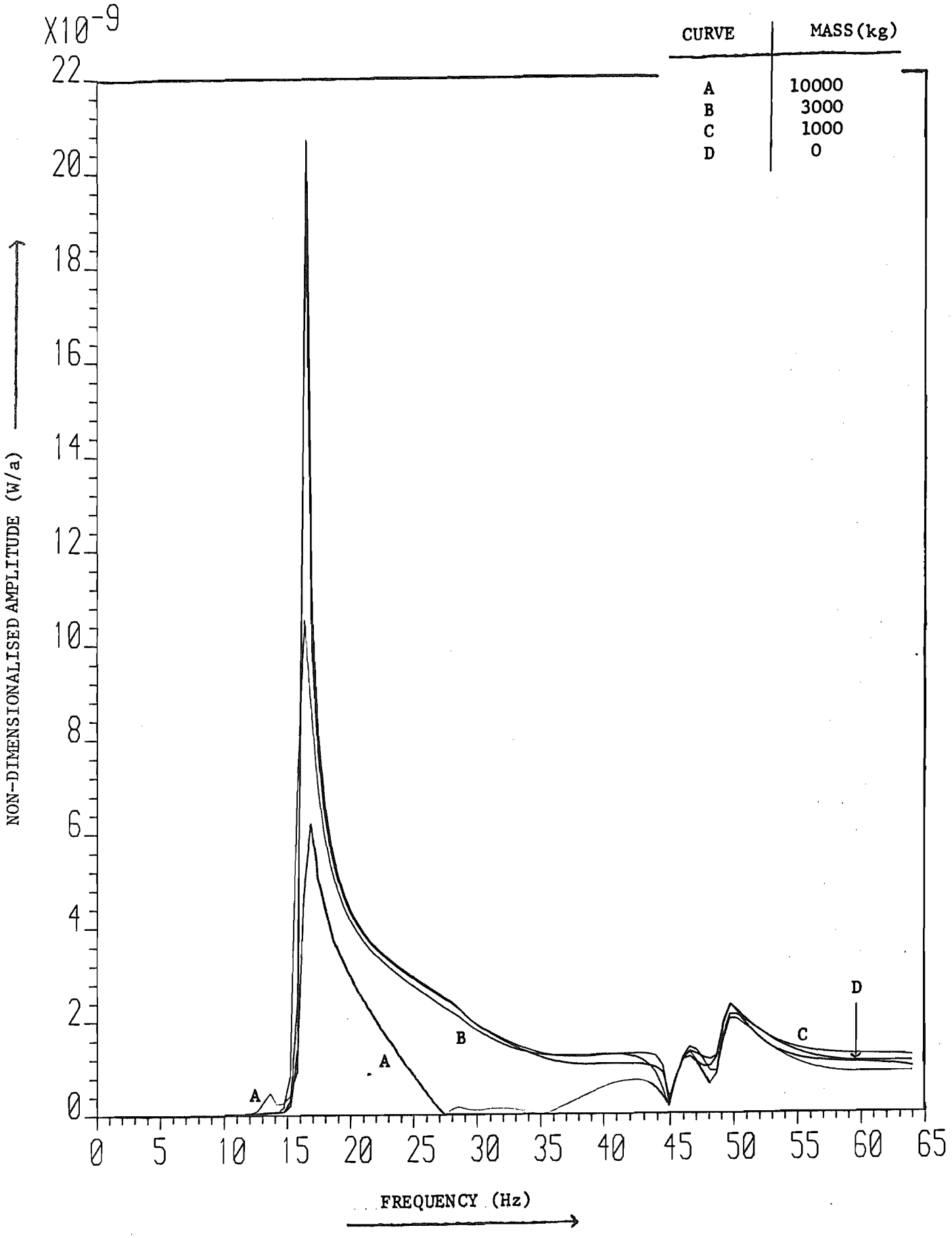

FIG. 8.14 Transfer Receptance at 25m, Bedrock Model, with a Mass at 3m.

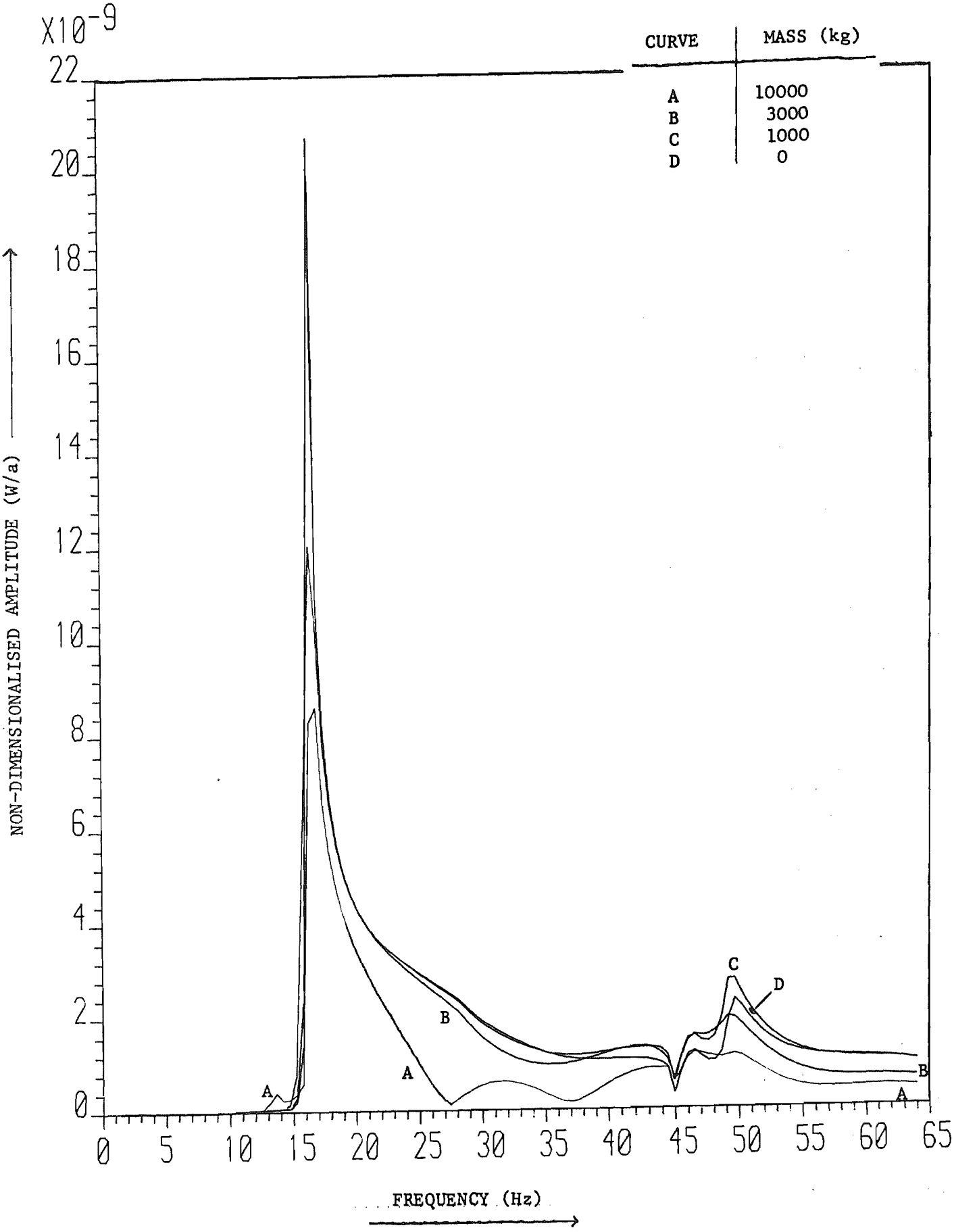

FIG. 8.15 Transfer Receptance at 25m, Bedrock Model, with a Mass at 5.5m.

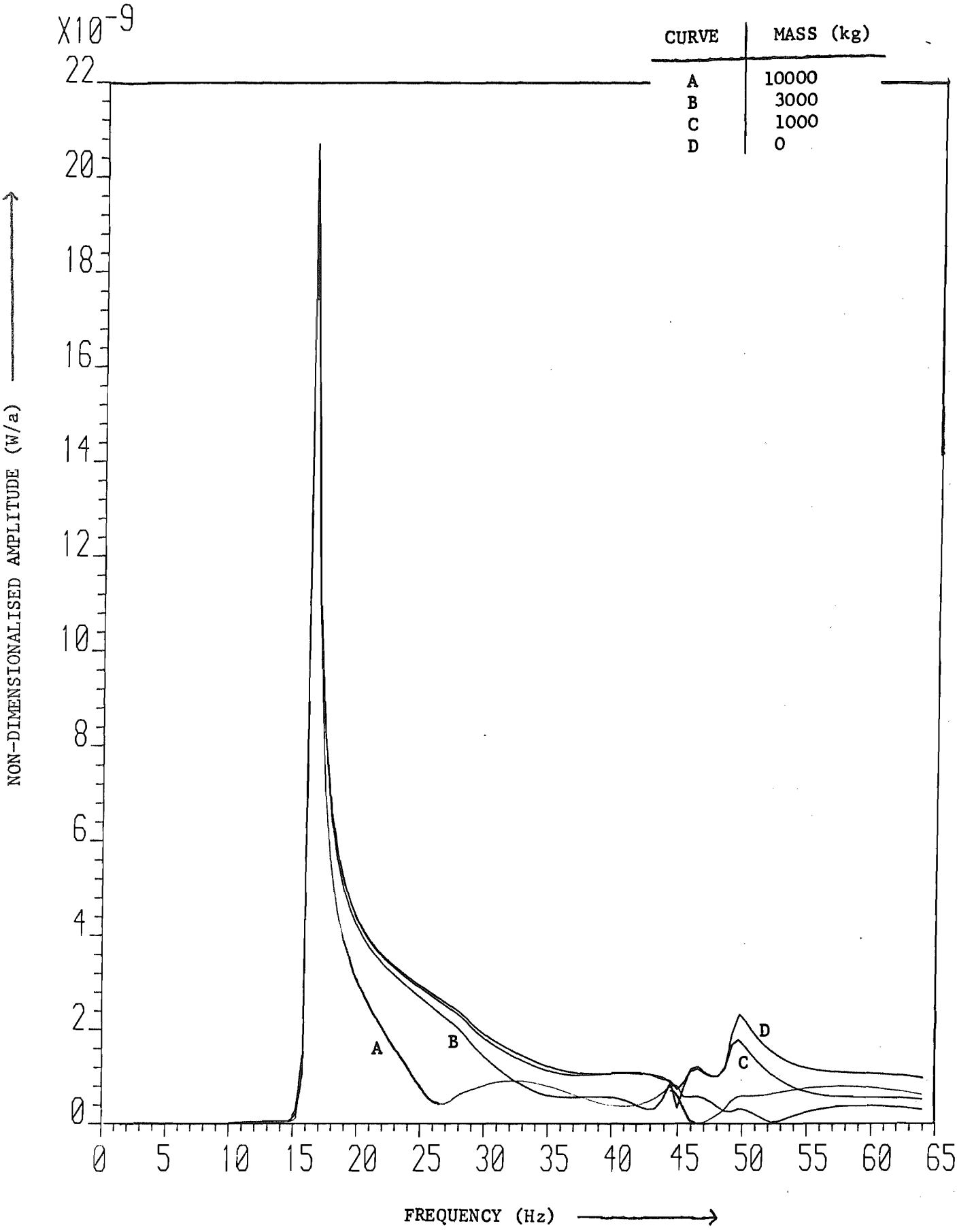

FIG. 8.16 Transfer Receptance at 25m, Bedrock Model, with a Mass at 10m.

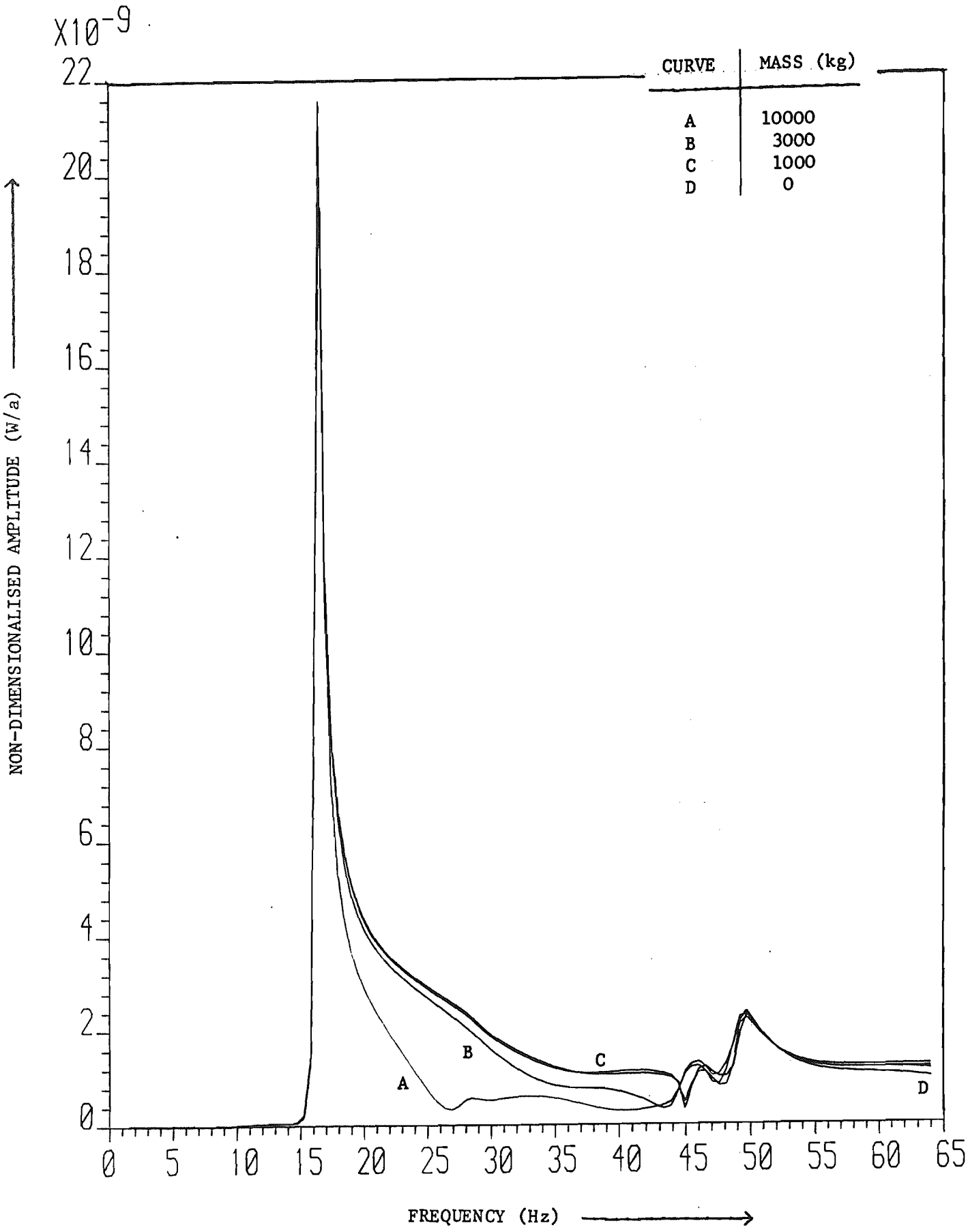

FIG. 8.17 Transfer Receptance at 25m, Bedrock Model, with a Mass at 12.5m.

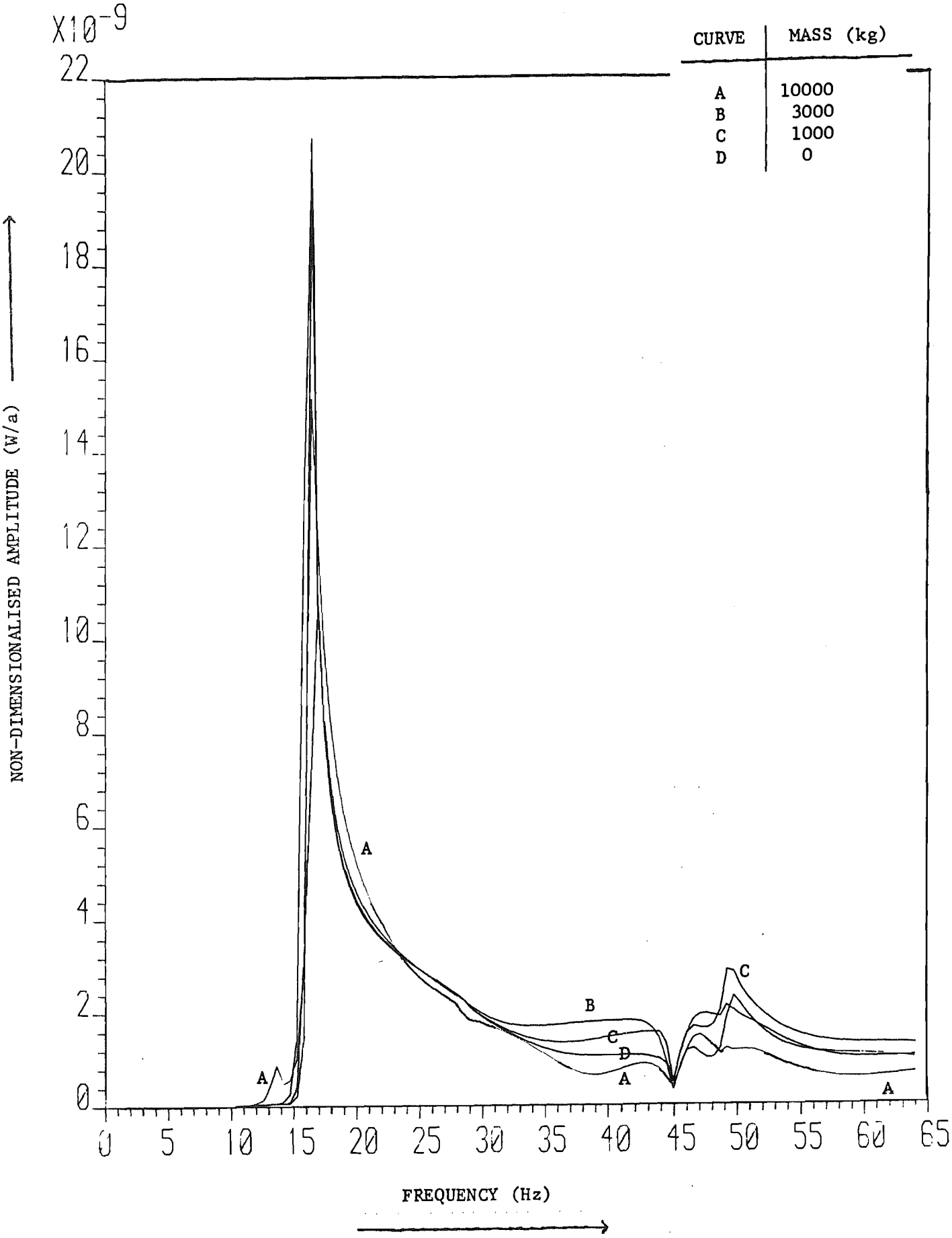

FIG. 8.18 Transfer Receptance at 25m, Bedrock Model, with Masses at 3 & 5.5 m.

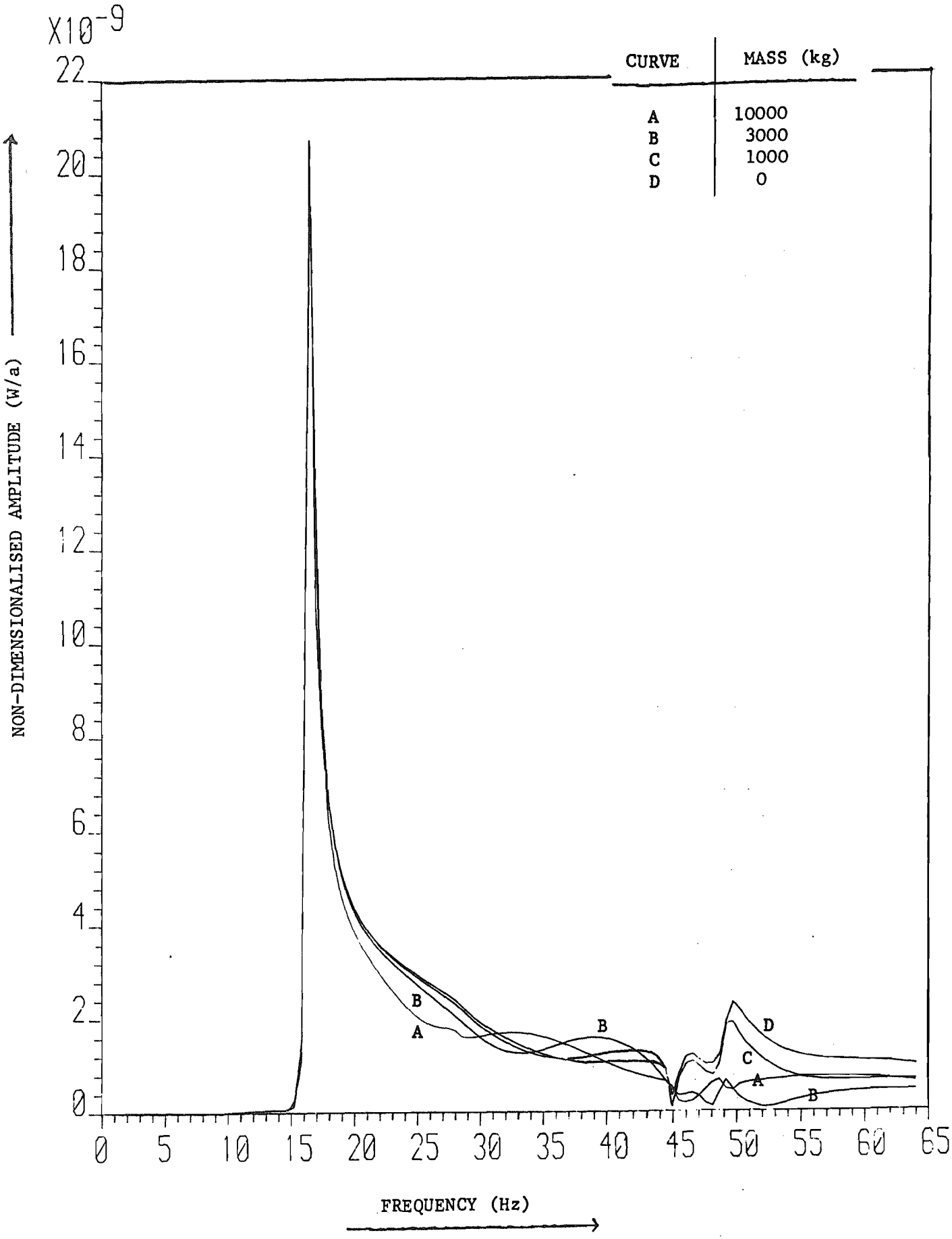

FIG. 8.19 Transfer Receptance at 25m, Bedrock Model, with Masses at 10 & 12.5m.

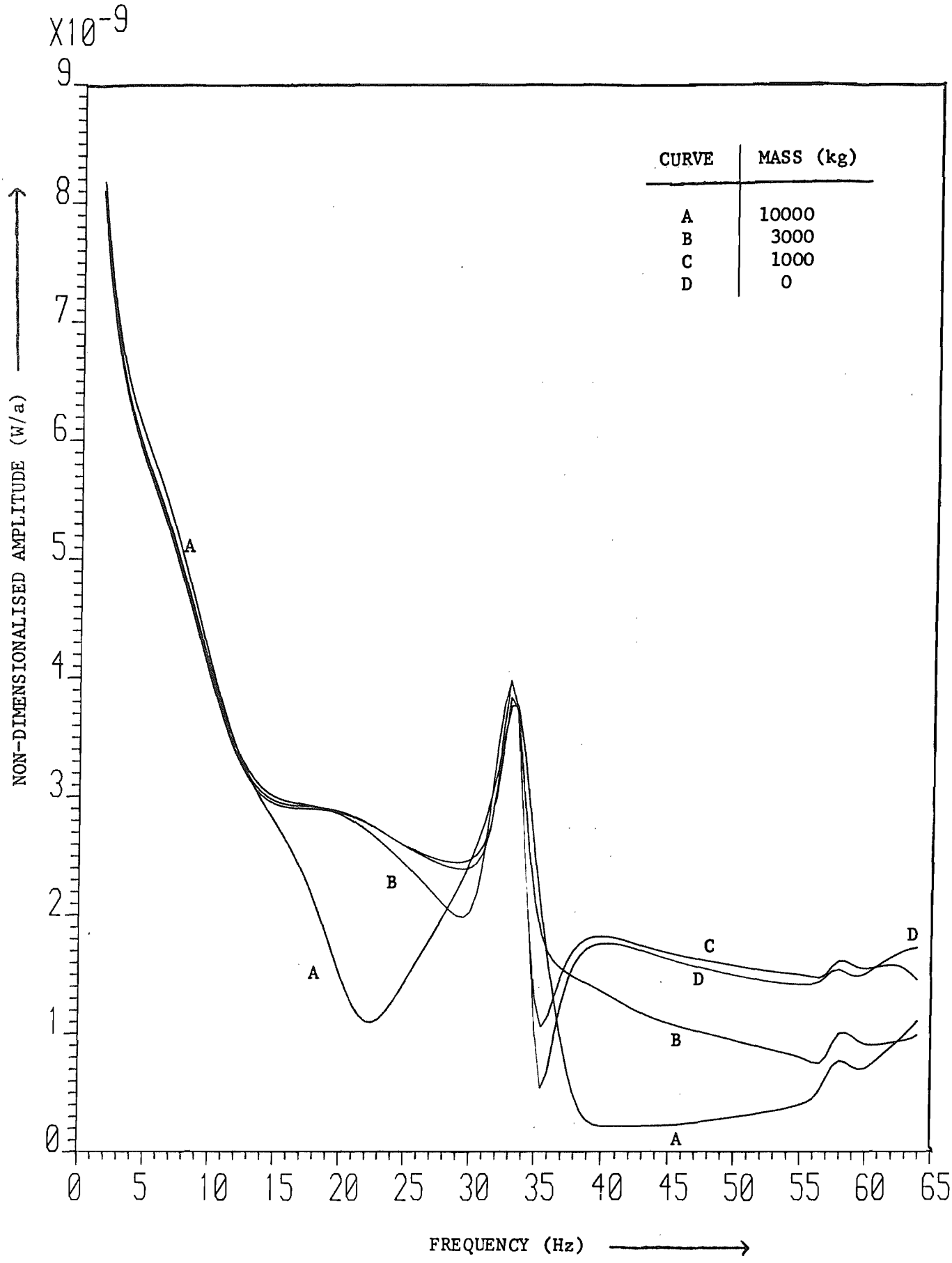

FIG. 8.20 Transfer Receptance at 25m, Elastic Foundation Model, with a Mass at 3m.

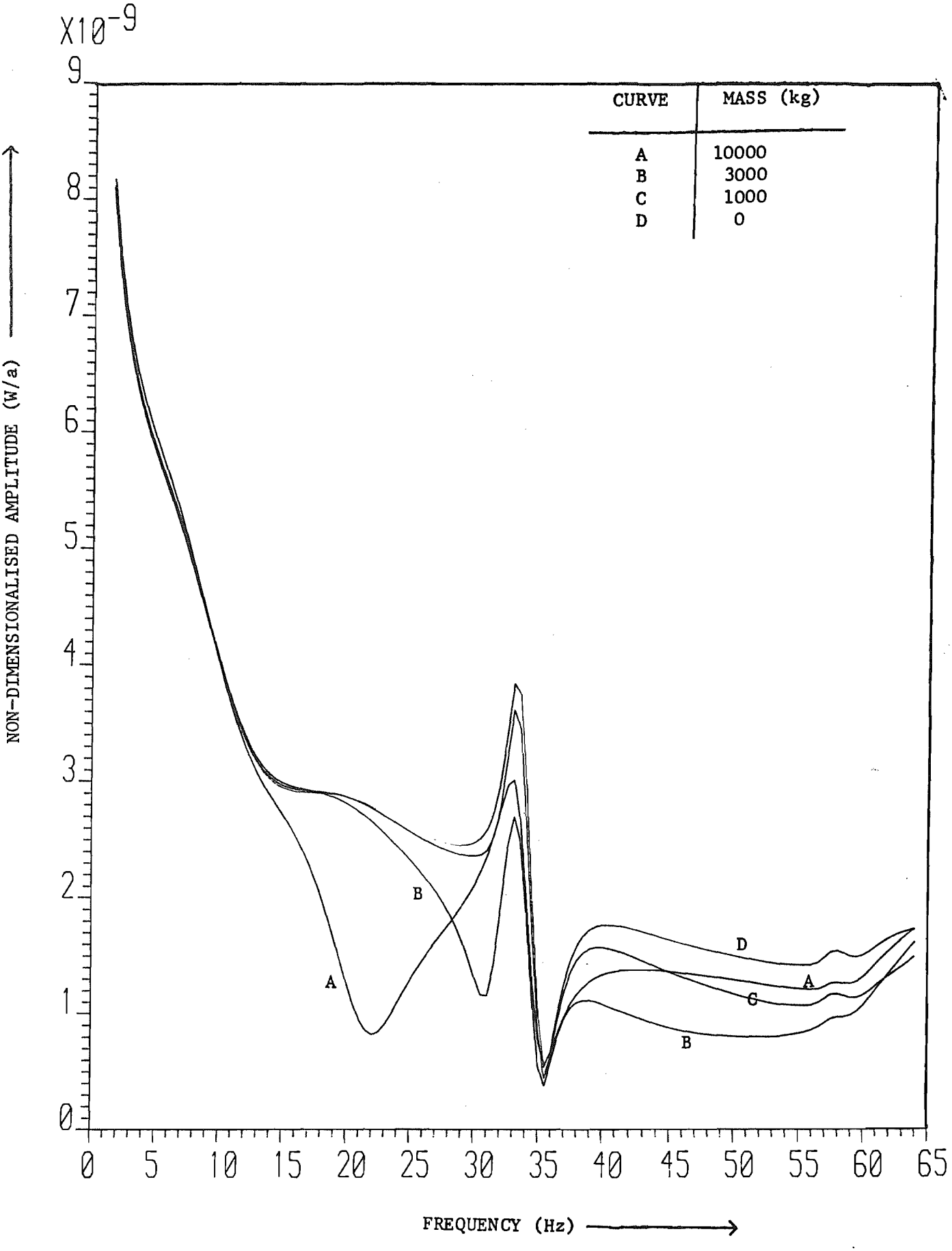

FIG. 8.21 Transfer Receptance at 25m, Elastic Foundation Model, with a mass at 5.5m.

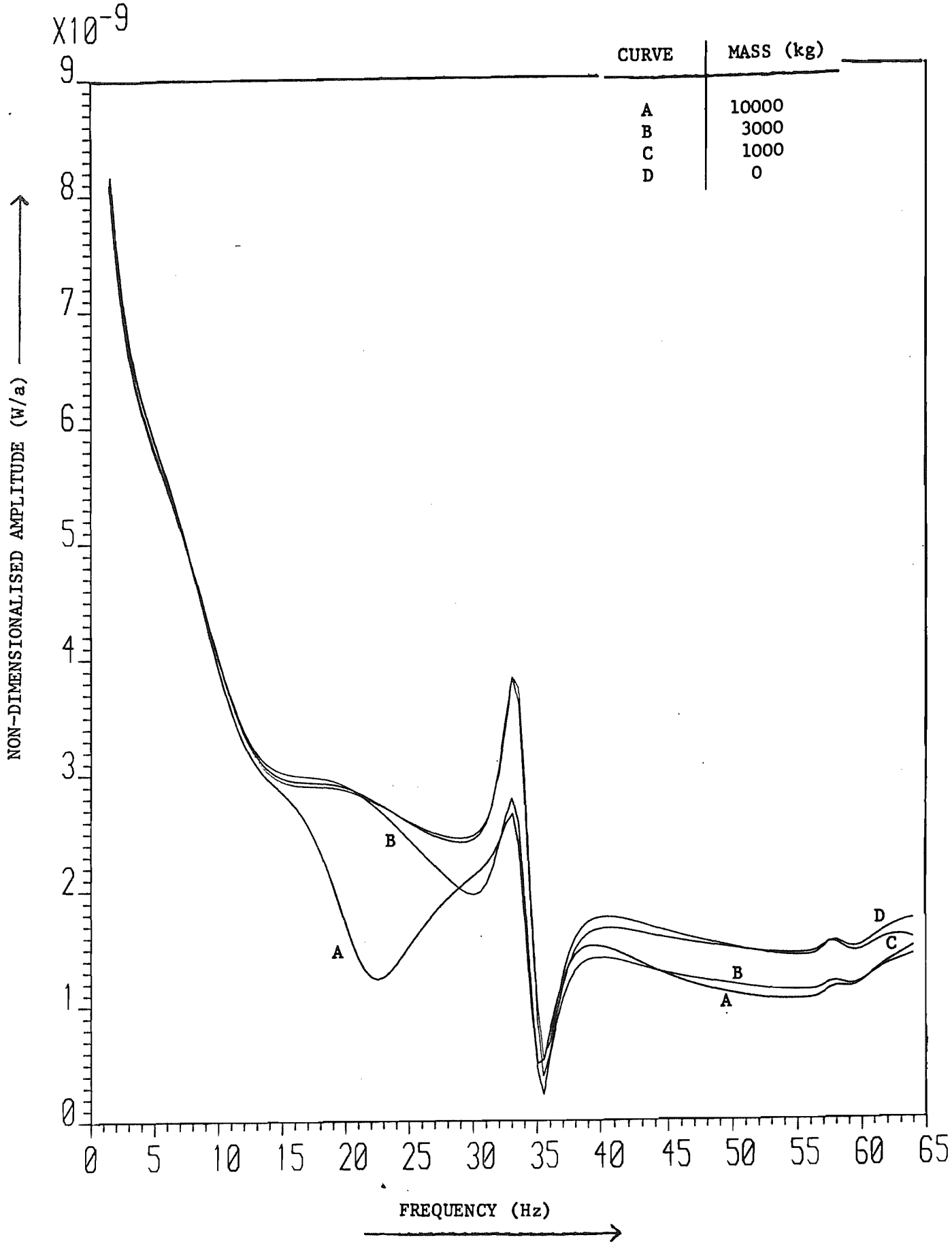

FIG. 8.22 Transfer Receptance at 25m, Elastic Foundation Model, with a Mass at 10m.

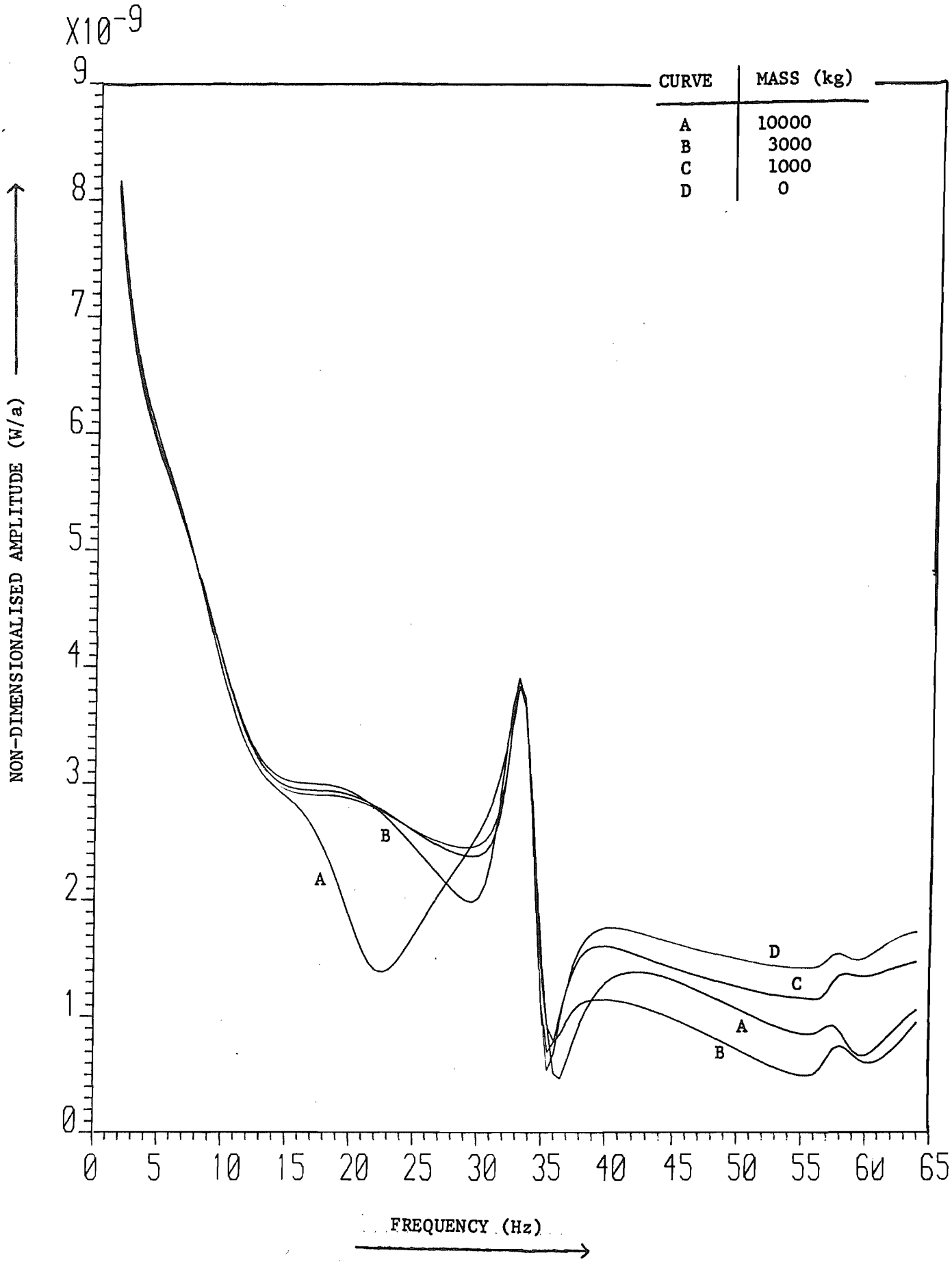

FIG. 8.23 Transfer Receptance at 25m, Elastic Foundation Model, with a Mass at 12.5m.

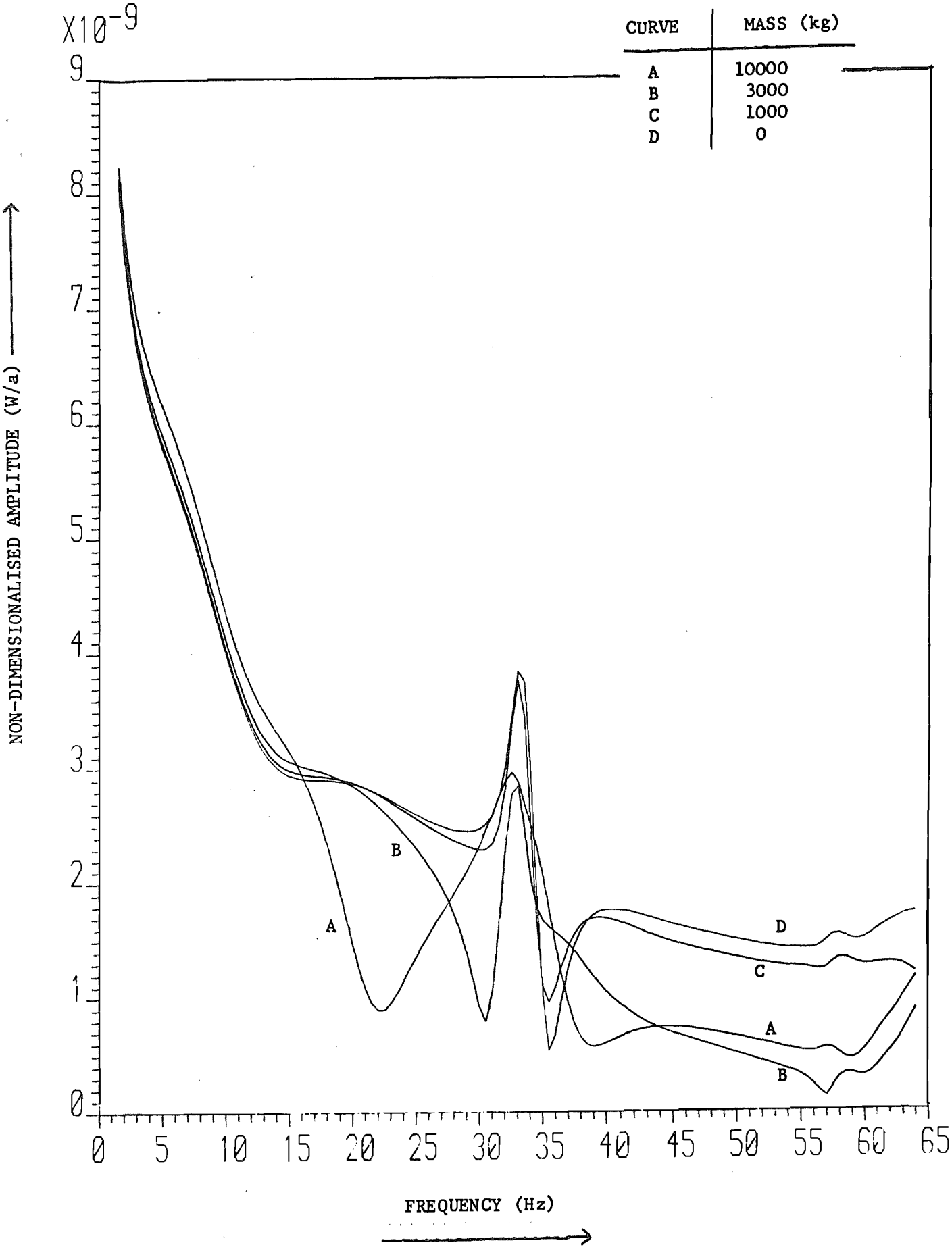

FIG. 8.24 Transfer Receptance at 25m, Elastic Foundation Model, with Masses at 3 & 5.5 m.

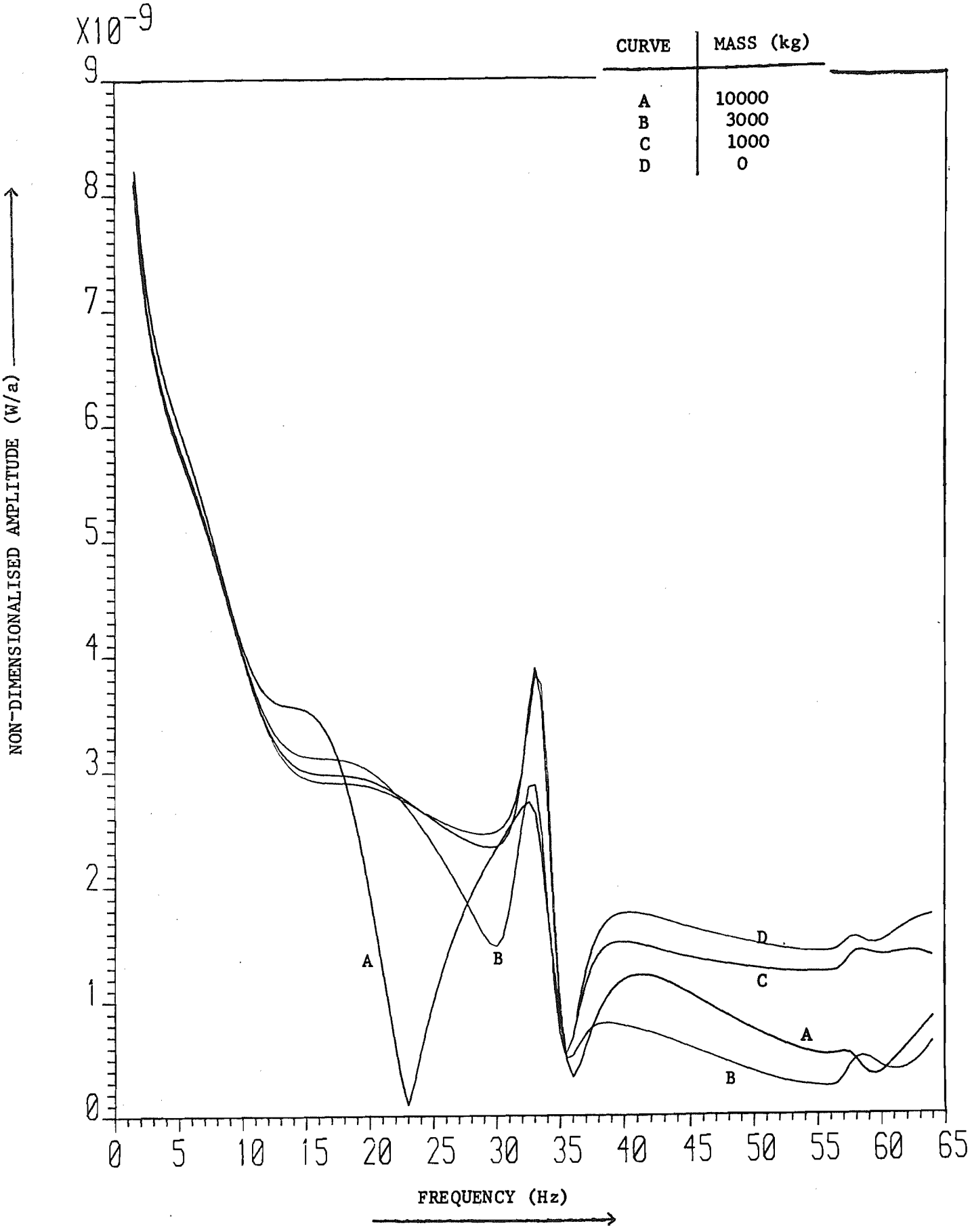

FIG. 8.25 Transfer Receptance at 25m, Elastic Foundation Model, with Masses 10 & 12.5m.

8.4 Discussion

Although the results presented are principally for the response 25 m from the load, masses have only been considered at positions up to 12.5 m from the load. This is because a symmetry exists in the model, which results in a mass at n metres ($n \leq 25$) from the load, producing the same receptance graph as a mass at (25-n)m from the load. Similarly, for the two mass case, a mass M1 at x metres and a mass M2 at y metres ($x, y \leq 25$), is an equivalent case to a mass M1 at (25-x)m and a mass M2 at (25-y)m. This symmetry is predictable from the receptance expressions, in equations (8.12) and (8.14). Considering the slightly simpler equation (8.12), the terms β_{31}, α_{22} and β_{22} will not vary between case one (a mass at n metres) and case two (a mass at (25-n) metres), while the terms β_{22} and β_{21} will by their definition exchange values, so resulting in exactly the same transfer receptance at 25m in both cases. Note that the symmetry observed here may not exist in a more general situation.

This discussion will focus on the half-space, bedrock and elastic foundation results in turn, with cross-references to each model to consider common features. The first Figure in the results section, Fig. 8.5, shows the direct receptance with the half-space model and various masses. Above about 10 Hz, the form of this graph is familiar and accords with the general shape of rigid disc solutions (see Waas [79], for example). The zero mass curve H is monotonic decreasing, indicating that the peak in the other curves is a mass resonance. However, at low frequency , the curves tend to very large receptances, which is at variance with the solutions for loads on finite areas. This is because the static solution for a infinite strip has infinite vertical receptance. The proof of this is implicit in the work of Timoshenko and Goodier [53], who obtain a static solution for a strip by superposing static line load solutions. Their response is finite, because they assume that at some depth d below the centre of the load, the vertical motion becomes zero. Their finite solution then depends on a factor log d. In a true half-space, the vertical displacement is only zero at infinity, and so an infinite receptance results. Alternatively, a static analysis of the problem yields the expression:

$$W = K \int_0^\infty \frac{\sin \zeta a \cos \zeta x \, d\zeta}{\zeta^2} \qquad (8.15)$$

where W is the vertical displacement at the centre of the strip, K is a constant, a is the strip half-width, and ζ is the wavenumber. This integral is improper due to its singularity at $\zeta = 0$, and predicts infinite response [15].

Infinite receptance, or "compliance", is also found in the work on rigid strip solutions of Gazetas and Luco and Westmann [21, 50].

In common with the receptance Figs. 8.6 and 8.7, for the bedrock and elastic foundation models respectively, the curves for larger masses have peaks of greater magnitude and at lower frequency than the smaller masses, as usual.

Figs. 8.8 to 8.13 show the effect of masses on the half-space transfer receptance. They show that the effectiveness of a mass in reducing the response at some distance, is dependent on the position and size of the mass, and also the frequency range of interest. Any of the masses in any of the positions will increase the response between 5 and 15 Hz, but above 20 Hz the effect is generally helpful. It is clear that a mass as small as 1 tonne has little effect, even when two are used in unison, as shown in Figs. 8.12 and 8.13. The 10 tonne mass causes a substantial reduction in response above 20 Hz, particularly when two 10 tonne masses are used, but this latter case significantly amplifies the response between 5 and 15 Hz. The "wavyness" superimposed on even the zero mass curves (which provide a useful reference for comparing the Figures), is assumed due to interference between the different propagating waves (see section 9.5.2).

In Fig. 8.6, which is a direct receptance graph for the bedrock model, with various masses, each curve tends to a finite value at zero frequency, which is required by the rigid boundary condition at the base of the layer. Although the method of solution does not allow computation of the static displacement, it is clear that all the curves tend to a value of about $W = (0.8 \times 10^{-8}).a$ at zero frequency. Each mass has the same static displacement, as in the original solution of Navier's equations, the gravity body force was neglected. As a unit force was used to produce this displacement, its reciprocal will give the equivalent stiffness of the layer. A value of $a = 0.75$ has been used for the Clarborough model, giving a stiffness $K = 166.7$ MKgm^{-2}.

The main peak of each curve in Fig. 8.6 is a combination of two effects: (a) the mass, and (b) at 16 Hz the first two modes of vibration propagate with the same wavenumber, so magnifying the response (see the free vibration analysis of Chapter 4). Effect (b) also explains why curve H, for zero mass, exhibits a large peak too. The smaller peaks at higher frequencies are also explained by the behaviour of natural modes, which are all analysed in Chapter 4.

The transfer receptance Figures for the bedrock model, nos. 8.14 to 8.19, all show practically zero response below 12 Hz. This was also predicted by the free vibration analysis, which showed that the bedrock model "waveguide" effect prevented propagation at lower frequencies. The principal peak is again related to the frequency at which the first two natural modes propagate in unison, but at this distance from the source, the centre of the peak has increased 1 Hz to about 17 Hz. The other peaks, between 45 and 50 Hz, have also shifted, although the increase is about 2 Hz. The author is unaware of a physical explanation for this phenomenon, which has also been observed by others. In particular, the O.R.E. of the International Union of Railways [30] have found the following empirical relation, which closely applies here:

$$\frac{f_o d}{C_1} = K$$

where f_o = the peak frequency at the load, d = the distance to the response point from the load, C_1 = the compression wavespeed, and K is the frequency shift at distance d. The dependence on C_1 suggests the shifting phenomenon is caused by the behaviour of the compression wave.

Although direct comparisons are obviously impossible between solutions for a flexible, infinite strip, and a rigid disc, a similarity of form can be expected, particularly for the bedrock model, which predicts finite static response for both a strip and a disc. Waas [79] has analysed a rigid disc on a layer over a rigid base, with similar dimensions and material properties to those used here. His Fig. 38 shows direct receptance, and he too finds a major peak in each curve, with smaller peaks at higher frequencies, in virtually the same ratios to the results presented here. He also finds that the zero mass case

has the smallest of the main peaks, at a slightly higher frequency than any of the others.

Direct receptance graphs of a very similar form to those given here, can also be found in the work of Gazetas and Roesset [23], for a strip load, and the three ground structure models used here.

Figs. 8.14 to 8.19 show that it is less easy to generalise about the effect of masses, than in the half-space model. A one tonne mass in most of the positions considered, increases response at 25 m over most of the frequency range, and so is of no use as an isolator. A single ten tonnes mass, placed close to the load at 3 or 5.5 m, substantially reduces both the amplitude of the main peak, and the response from 20 to 40 Hz, but this first effect is lost if the mass is placed at 10 m or 12.5m. However, a mass close to the load increases response between 12 and 15 Hz, which is not the case at 10 or 12.5 m.

The most surprising feature of these Figures is the effect of two masses. Whereas with the half-space model, two masses were better isolators than one mass for most of the frequency range, the opposite is true in the bedrock model. The large reduction between 20 and 40 Hz caused by the single mass, is almost completely lost, with a slight improvement at higher frequencies. These results suggest that a large single mass placed near to the load, is the best isolator in the bedrock model, for most of the frequency range.

Fig. 8.7 shows the direct receptance for the elastic foundation model. As in the half-space model, the static response of each curve is infinite. This characteristic has apparently disguised peaks which are caused by mass resonance. The smaller peaks at higher frequency are mass-independent, as evidenced by the peak in the zero mass curve; these peaks are probably caused by the natural mode behaviour (see Section 7.4). It is shown in the free vibration analysis of the elastic foundation model in Chapter 6, that no two modes share the same wavenumber at any frequency, and so the sharp peaks characteristic of the bedrock model cannot be expected. Comparison of Fig. 8.7 with the bedrock receptance Fig. 8.6, reveals that because energy is not trapped in the layer in the elastic foundation model, the curves are smoother and the peak displacements smaller.

Physically the elastic foundation model can be considered a "compromise" between the half-space and bedrock models, and the results of Figs. 8.20 to 8.25 feature aspects of the solutions for the other two models. They show the effect on transfer receptance of one or two masses. All the curves approach larger responses near zero frequency, as with the half-space model, although the amplitudes are greater now, as more energy is retained by the layer. A rectangular load solution might exhibit peaks in the region 5 to 15 Hz.

The principal peak in each Figure is shifted to a slightly higher frequency than the corresponding peak in Fig. 8.7, although the magnitude of the shift is less than predicted by the equation $K = (f_o d)/C_1$, an equation which seems to be better matched with the bedrock model. In each of the Figs. 8.20 to 8.25, curve A has a pronounced minimum near 23 Hz, and curve B has a minimum mear 30 Hz. Logically, these minima are near the frequencies of the peaks of corresponding curves in Fig. 8.7. Only the 10 tonnes and 1 tonne cases can be matched exactly, since no curve for 3 tonnes has been plotted in Fig. 8.7. However, if the position of the peak of a 3 tonnes curve is estimated in Fig. 8.7, by extrapolating between the 2 and 5 tonnes curves (E and F), it is clear that the peak will be near 30 Hz. The mass has 'absorbed' much energy in this frequency range, leaving the response in this range reduced at distance. Any minimum which might have appeared in curve C in Fig. 8.21, has apparently been lost in the large peak near 35 Hz caused by the 4th mode/propagating wave.

As in the half-space results, two masses are more effective isolators than one mass for much of the frequency range, but the reverse is true below about 20 Hz. Also, the effect of a second mass is less dramatic than in the half-space, with the exception of the effect at 23 Hz of two 10 tonnes masses placed at 10 and 12.5 m. Of all the mass and distance combinations, a single 10 tonnes mass placed at 3 m, is most effective at absorbing energy above 40 Hz. As with the other two ground structure models, the results suggest that the effectiveness of isolators is heavily dependent on the frequency range of interest, and the relative positions of load, mass and response point. In general a large mass is much more effective than a small one. Probably the safest and most economical use of an isolator, is a single heavy mass close to the load.

This analysis could be improved by including the receptance to horizontal mass motion, and rocking motions. However, some comparisons have been made with experimental results produced by British Rail [32]. Results from a test site at Uttoxeter, where a shallow 3 m layer covers a firmer material, show some agreement with the form of the bedrock model results here. A large peak in the Uttoxeter transfer receptance graphs is almost independent of the position of the measuring point, and below this frequency little propagation occurs.

Comparison of experimental results with the other two ground structure models (half-space and elastic foundation), is made difficult by the infinite static response.

CHAPTER 9

A THREE-DIMENSIONAL MODEL: A RECTANGULAR LOAD ON A HALF-SPACE

9.1 Introduction

9.1.1 Relevant previous work

The two founders of research into ground vibrations were Lord Rayleigh and Professor Lamb. Rayleigh [67] discovered the existence of a surface wave restricted to near the free surface of a half-space, now known as the Rayleigh wave. Knowledge of the existence and behaviour of this wave is necessary to explain experimentally observed ground vibrations. Lamb [45] was the first to consider the waves propagated and vibration caused by line and point sources, acting on the surface of an elastic half-space. His approach to the problem has guided much of the subsequent work. As an extension of Lamb's work, Love [49] considered the static displacements of a rectangular or circular load on a half-space, using the potential method due to Boussinesq.

Since these early theoretical studies, most workers in this field have been motivated by the requirements of civil engineering, for example to improve machine foundation design and avoid damage-causing resonance. For this reason, they have studied the direct receptance of loads, rather than the vibrations caused on the surface surrounding the load. Reissner [81], and later Miller and Pursey [56], considered a constant stress acting over a disc, which is a convenient shape to analyse in cylindrical coordinates, and leads naturally to use of the Hankel transform. Miller and Pursey incorporated viscoelastic damping into their model, and produced asymptotic expressions for the surface displacements, valid in the far-field.

Bycroft [9] used a stress distribution under the disc closer to that produced by a rigid disc, in an attempt to simulate a machine foundation more closely. He based his stress distribution on the static stress distribution, which can be calculated exactly (see Richardson's Appendix [68], for example), and his results have been shown adequate for low frequency [4]. Bycroft also considered a disc on an elastic stratum.

Awojobi and Grootenhuis [4] and Robertson [70] tackled the genuine rigid circular body problem, which involves mixed boundary conditions of constant displacement under the disc, and zero stresses on the surrounding surface. This leads to dual integral equations, from which Awojobi and Grootenhuis obtain approximate expressions for the stress distributions, by combining series solutions to the integrals (neglecting the integrands' singularities), with asymptotic expressions for the contributions from these singularities. They show receptance graphs for the circular body, and also find the "correction mass" which must be added to the body if a static stress distribution is assumed, and the resonant frequencies of the body are desired. Robertson also gives receptance graphs, produced with a series solution.

In a later piece of work, Awojobi [3] again considered a rigid circular body, but resting on 'Gibson soil', which is defined as incompressible with a shear modulus proportional to depth, such that $\mu = kz$, where k is a constant and z the depth. He, too, produces direct receptance graphs.

In an extension to the work of these authors, Luco and Westmann [51] have studied the effect on the vibrations of a rigid disc of varying Poisson's ratio. Their solution of the key integrals involves the numerical integration methods of Filon [1] and Simpson's Rule [35]. Zeng and Cakmak [16] have used orthogonal series expansions to approximate the stress and displacement under a rigid disc, and Lin [46] has investigated the effect on the rigid disc's stress distribution and receptance, of varying the half-space hysteretic loss factor, η. Richardson studied the coupling of the motion of two discs, using Bycroft's stress distribution under the discs, and approximating the resulting integrals using Longman's method for oscillating integrals [47,48].

Richardson, Webster and Warburton [69] have considered some combinations of circular bodies and excitations on or beside the bodies. They have used Bycroft's stress distribution under the bodies, and approximated the infinite integrals with Longman's technique. They have found that the vertical mode of excitation propagates with greater effect than the rocking or horizontal modes, and that a mass some distance from the excitation point can be strongly excited.

Balakrishna and Nagaraj [66] give some useful expressions for predicting the natural frequencies of excited bodies, which are applicable to the rectangular load studied here. One expression, which they attribute to Converse, gives good agreement with the resonant frequencies found in this work, as shown in Section 9.5.3.

Some more recent workers have been interested in the effect of layers in the ground of different material properties, or of the effect of non-circular loads. Warburton [80] has looked at the forced vibrations of a circular body, resting on an elastic layer over an inflexible half-space (the "bedrock" model used with an infinite strip load, as in Chapter 5), with Bycroft's approximation to the stress distribution under the body. Waas [79] has used the Finite Element Method, to study the vertical motion of a disc on both a half-space and the "bedrock" ground structure model, using hysteretic damping. His bedrock results resemble, in form, those of Chapter 5. Luco [52] worked on the problem of a rigid disc resting on a viscoelastic layer, which in turn over-lies an elastic half-space. He gives graphs of the impedance functions. He chose constant hysteretic damping in preference to Kelvin-Voigt viscous damping, because laboratory tests have shown this to be a better approximation to the anelastic behaviour of soils. In effect, his model of the ground is the same as that studied with an infinite strip load in Chapter 7. Girardi [24] has considered the effect of torsion applied to a disc, which lies on the "bedrock" ground structure.

Kausel, Roesset and Waas [37] have used the Finite Element Method to approximate the swaying and rocking impedance functions, of irregular footing shapes on layered media, which they find tend to the half-space solutions for high frequency. Kobori, Minai and Suzuki [39] have studied the vibration of a massless rectangular load, resting on an hysteretically damped "bedrock" ground structure. They find that the natural propagating modes have a similar effect on the surface vibration, to the results of Chapter 5 for an infinite strip on a "bedrock" structure. Their solution method, which has to contend with a double Fourier inverse transformation which cannot be performed analytically, uses the coordinate transformation $\beta = \zeta \cos\theta$, $\gamma = \zeta \sin\theta$, where β and γ are the transform variables, in order to reduce the θ-integral to finite limits. Gaul [19] uses the same transformation to study the

vibrations due to a square loaded by a uniform harmonic stress, and resting on a half-space which is hysteretically damped. He is concerned with surface vibrations in the near-field of the load, and for this reason his work is closest to the main results here. As explained in Section 9.4.2, his parameters have been used with the solution method of this Chapter, and good agreement found.

Experimentally, Chae [11] has investigated non-circular foundations in some depth, and discovered that the same load acting on a rectangular area produces greater deflection than on the same circular area. He has also found that the resonant frequency of a rectangular mass is lower than the resonant frequency of an equal circular mass. He has modified the previously held "equivalent radius", used to compare solutions due to circular and rectangular bodies, from one based on equivalent area, to one based on equivalent perimeter lengths. This new equivalent radius will be used in Section 9.5.3.

9.1.2 The scope of work in this Chapter

In this Chapter, the surface vibrations due to an harmonically loaded rectangular strip are studied. The dimensions of the strip are chosen to approximate those of a railway sleeper. The stress is uniformly distributed, and the contact is 'smooth' ; there are no shear stresses under the load. Although a rigid strip would be a closer approximation to a sleeper, it has been assumed that on the free surface around the strip, the difference in behaviour caused is not pronounced. The strip rests on an isotropic, homogeneous, elastic half-space, which exhibits constant hysteretic damping. Only a vertical harmonic force is applied to the strip, as this is considered the most important component of vibration induced in a sleeper by a passing train. However, the method can easily be altered to accommodate different loading conditions.

Unlike the infinite strip load studied in previous Chapters, the elastodynamic equations (equation (9.1)) must now be solved in three dimensions, not two. The approximate solution is obtained by double Fourier transforming the partial differential equations which describe the vibration, solving these in the transform domain, and then using numerical techniques to inverse transform and give the near-field surface displacements. The requisite analysis, which follows [40] is given in

Section 9.2, and the numerical solution described in Section 9.3. Section 9.4 describes the results, which form three groups of figures:

(i) the integrand functions which must be inverse transformed. and which give useful information about the propagating wave components, which assemble to cause the surface displacements;

(ii) vertical and horizontal motion amplitudes and phase changes plotted against distance, for each of four frequencies;

(iii) direct and transfer receptance figures, with various masses either placed at the load, or at a response point some distance from the load, or finally at a point in beween the load and response point.

9.2 The Analysis of the Surface Vibration Caused by a Vibrating Rectangular Strip

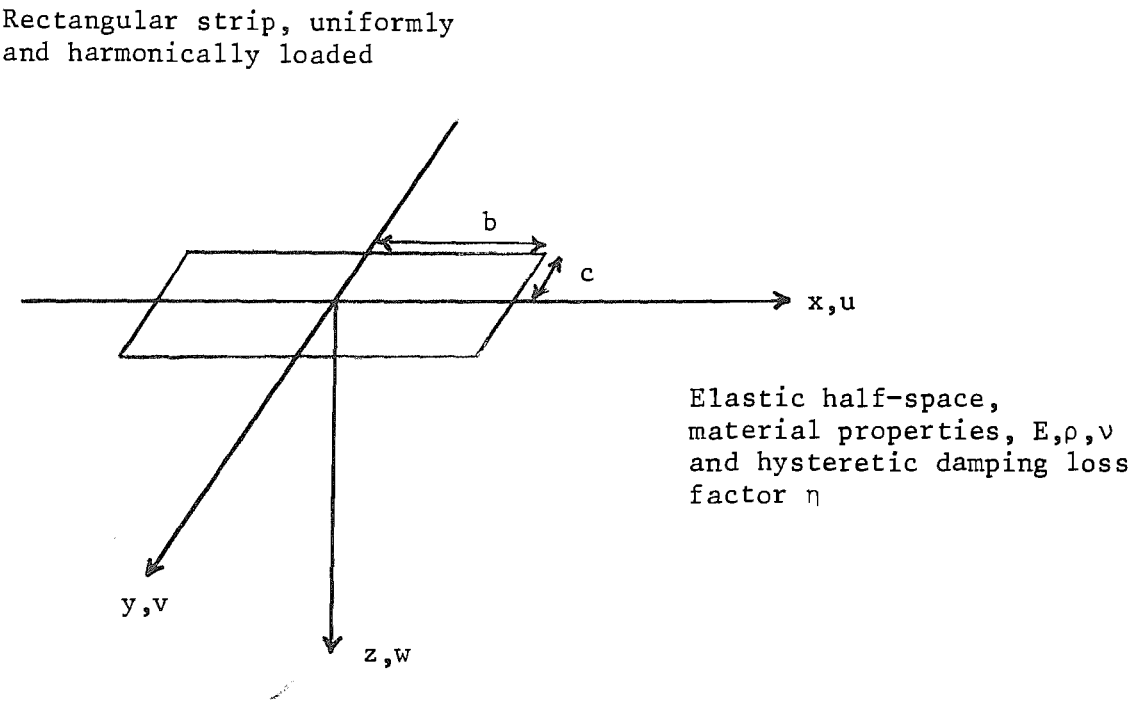

Fig. 9.1: Diagram of Rectangular Load on Half-Space

Figure 9.1 shows the coordinate system and rectangular strip dimensions of the model to be analysed. The rectangle has sides of length 2b and 2c, and is aligned with respect to the coordinate axes as shown. It rests on a homogeneous, isotropic, elastic half-space, which has material properties E, ρ and ν in the usual notation, and exhibits hysteretic damping of vibrations characterised by a loss factor η. An harmonic vertical load acts uniformly over the rectangle, and the contact is 'smooth' - no shear stresses exist at the surface.

The behaviour of the half-space is described by Navier's elastodynamic equations (see Appendix A [26], for example). In the absence of a body force, these can be written:

$$(\lambda + \mu)\underset{\sim}{\nabla}\ \nabla.\underset{\sim}{u} + \mu\nabla^2\underset{\sim}{u} = \rho\ddot{\underset{\sim}{u}} \qquad (9.1)$$

where λ and μ are as usual the Lamé constants, $\underset{\sim}{u}$ is the vector of the three components of displacement, and " $\ddot{}$ " denotes double differentiation with respect to time. "$\underset{\sim}{\nabla}$" denotes the gradient, "$\nabla.$" the divergence, and "∇^2" is the Laplacian operator.

The stress-strain relations can be written:

$$\tau_{ij} = \lambda\epsilon_{kk}\delta_{ij} + 2\mu\epsilon_{ij}$$

where (9.2)

$$\epsilon_{ij} = \frac{1}{2}(u_{i,j} + u_{j,i})$$

where τ_{ij} are the stress components, ϵ_{ij} are the strain components as defined, δ_{ij} is the Kronecker delta, and the summation convention applies.

If the motion is harmonic with frequency ω, then equation (9.1) can be expanded into the three component equations:

$$(\lambda + \mu)\frac{\partial\Delta}{\partial x} + \mu\nabla^2 u + \rho\omega^2 u = 0 \qquad (9.3)$$

$$(\lambda + \mu)\frac{\partial \Delta}{\partial y} + \mu\nabla^2 v + \rho\omega^2 v = 0 \qquad (9.4)$$

$$(\lambda + \mu)\frac{\partial \Delta}{\partial z} + \mu\nabla^2 w + \rho\omega^2 w = 0 \qquad (9.5)$$

where the dilatation $\Delta = \frac{\partial u}{\partial x} + \frac{\partial v}{\partial y} + \frac{\partial w}{\partial z}$. (9.6)

Taking the differential of equations (9.3) to (9.5) with respect to x, y and z respectively, and dividing through by ρ, gives the following three equations:

$$\frac{\lambda + \mu}{\rho}\frac{\partial^2}{\partial x^2}\Delta + \frac{\mu}{\rho}\frac{\partial}{\partial x}\nabla^2 u + \omega^2\frac{\partial u}{\partial x} = 0 \qquad (9.7)$$

$$\frac{\lambda + \mu}{\rho}\frac{\partial^2}{\partial y^2}\Delta + \frac{\mu}{\rho}\frac{\partial}{\partial y}\nabla^2 v + \omega^2\frac{\partial v}{\partial y} = 0 \qquad (9.8)$$

$$\frac{\lambda + \mu}{\rho}\frac{\partial^2}{\partial z^2}\Delta + \frac{\mu}{\rho}\frac{\partial}{\partial z}\nabla^2 w + \omega^2\frac{\partial w}{\partial z} = 0 \qquad (9.9)$$

Summing equations (9.7) to (9.9) and simplifying gives:

$$\frac{\lambda + 2\mu}{\rho}\nabla^2\Delta + \omega^2\Delta = 0 \qquad (9.10)$$

Putting

$$k_1^2 = \frac{\omega^2}{c_1^2}, \quad \text{where} \quad c_1^2 = \frac{\lambda + 2\mu}{\rho} \qquad (9.11)$$

gives $$(\nabla^2 + k_1^2)\Delta = 0. \qquad (9.12)$$

To solve equation (9.12), the double Fourier transform is required, defined by

$$\bar{f}(\beta,\gamma,z) = \frac{1}{2\pi}\int_{-\infty}^{\infty}\int_{-\infty}^{\infty} f(x,y,z)e^{-i(\beta x+\gamma y)}dxdy \qquad (9.13)$$

The transform of a double partial differential can be shown to be:

$$\frac{1}{2\pi}\int_{-\infty}^{\infty}\int_{-\infty}^{\infty}\frac{\partial^2 g}{\partial x^2}\, e^{-i(\beta x+\gamma y)}dxdy = -\beta^2\bar{g}(\beta,\gamma,z) \qquad (9.14)$$

Now Fourier transforming equation (9.12) gives:

$$(\frac{d^2}{dz^2} - \beta^2 - \gamma^2 + k_1^2)\bar{\Delta} = 0 \qquad (9.15)$$

Putting $\alpha_1^2 = (\beta^2 + \gamma^2 - k_1^2)$ (9.16)

and integrating equation (9.15) gives

$$\bar{\Delta} = Ae^{-\alpha_1 z} + Be^{\alpha_1 z} \qquad (9.17)$$

where A and B are constants of integration. However, B must be zero, otherwise incoming waves exist, and no reflection is allowed at $z = \infty$. Hence

$$\bar{\Delta} = Ae^{-\alpha_1 z} \qquad (9.18)$$

The Fourier inversion of equation (9.18) gives

$$\Delta(x,y,z) = \frac{1}{2\pi} \int_{-\infty}^{\infty} \int_{-\infty}^{\infty} A(\beta,\gamma)e^{-\alpha_1 z + i(\beta x + \gamma y)} d\beta d\gamma \qquad (9.19)$$

Now equations (9.3) to (9.5) can be Fourier transformed; also dividing through by ρ gives:

$$(\frac{\lambda + \mu}{\rho})(-i)\beta\bar{\Delta} + \frac{\mu}{\rho}(-\beta^2 - \gamma^2 + \frac{d^2}{dz^2})\bar{u} + \omega^2\bar{u} = 0 \qquad (9.20)$$

$$(\frac{\lambda + \mu}{\rho})(-i)\gamma\bar{\Delta} + \frac{\mu}{\rho}(-\beta^2 - \gamma^2 + \frac{d^2}{dz^2})\bar{v} + \omega^2\bar{v} = 0 \qquad (9.21)$$

$$(\frac{\lambda + \mu}{\rho})\frac{d\bar{\Delta}}{dz} + \frac{\mu}{\rho}(-\beta^2 - \gamma^2 + \frac{d^2}{dz^2})\bar{w} + \omega^2\bar{w} = 0 \qquad (9.22)$$

Substituting into equations (9.20) to (9.22) from equation (9.18), and multiplying through by ρ/μ gives

$$(\frac{d^2}{dz^2} - \beta^2 - \gamma^2 + \frac{\rho\omega^2}{\mu})\bar{u} = \frac{\lambda + \mu}{\mu} i\beta Ae^{-\alpha_1 z} \qquad (9.23)$$

$$(\frac{d^2}{dz^2} - \beta^2 - \gamma^2 + \frac{\rho\omega^2}{\mu})\bar{v} = \frac{\lambda + \mu}{\mu} i\gamma A e^{-\alpha_1 z} \qquad (9.24)$$

$$(\frac{d^2}{dz^2} - \beta^2 - \gamma^2 + \frac{\rho\omega^2}{\mu})\bar{w} = \frac{\lambda + \mu}{\mu} \alpha_1 A e^{-\alpha_1 z} \qquad (9.25)$$

Putting $$\alpha_2^2 = (\beta^2 + \gamma^2 - k_2^2) \qquad (9.26)$$

and $$k_2^2 = \frac{\omega^2}{c_2^2}, \quad \text{where} \quad c_2^2 = \frac{\mu}{\rho} \qquad (9.27)$$

gives:

$$(\frac{d^2}{dz^2} - \alpha_2^2)(\bar{u},\bar{v},\bar{w}) = (\frac{\lambda + \mu}{\mu})Ae^{-\alpha_1 z}(i\beta, i\gamma, \alpha_1) \qquad (9.28)$$

and

$$\frac{\lambda + \mu}{\mu} = (\frac{\lambda + 2\mu}{\mu} - 1) = (\frac{c_1^2}{c_2^2} - 1) = (\frac{k_2^2}{k_1^2} - 1) \qquad (9.29)$$

Therefore

$$(\frac{d^2}{dz^2} - \alpha_2^2)(\bar{u},\bar{v},\bar{w}) = (\frac{k_2^2}{k_1^2} - 1)Ae^{-\alpha_1 z}(i\beta, i\gamma, \alpha_1) \qquad (9.30)$$

The homogeneous solution of equation (9.30) is

$$(\bar{u},\bar{v},\bar{w}) = (B,C,D)e^{-\alpha_2 z} \qquad (9.31)$$

as waves reflected at ∞ are inadmissible.

A particular integral of equation (9.30) is [40]

$$(\bar{u},\bar{v},\bar{w}) = (i\beta, i\gamma, \alpha_1)\frac{A}{k_1^2}e^{-\alpha_1 z} \qquad (9.32)$$

Therefore, combining equations (9.31) and (9.32), the complete solution is:

$$(\bar{u},\bar{v},\bar{w}) = (i\beta, i\gamma, \alpha_1)\frac{A}{k_1^2}e^{-\alpha_1 z} + (B,C,D)e^{-\alpha_2 z} \qquad (9.33)$$

From the definition of the dilatation Δ, equation (9.6), we have after applying the Fourier transform:

$$\bar{\Delta} = -i\beta\bar{u} - i\gamma\bar{v} + \frac{d\bar{w}}{dz} \qquad (9.34)$$

But $\bar{u}$, $\bar{v}$ and $\bar{w}$ are given by equation (9.33), and inserting these in equation (9.34) gives

$$\bar{\Delta} = -i\beta\{i\beta \frac{A}{k_1^2} e^{-\alpha_1 z} + Be^{-\alpha_2 z}\} - i\gamma\{i\gamma \frac{A}{k_1^2} e^{-\alpha_1 z} + Ce^{-\alpha_2 z}\}$$

$$- \alpha_1^2 \frac{A}{k_1^2} e^{-\alpha_1 z} - \alpha_2 De^{-\alpha_2 z} \qquad (9.35)$$

Substituting in equation (9.35) for $\bar{\Delta}$ from equation (9.18), cancelling terms and rearranging, gives an expression for D:

$$D = -\frac{i}{\alpha_2}(\beta B + \gamma C) \qquad (9.36)$$

Equation (9.33) can now be rewritten:

$$(\bar{u},\bar{v},\bar{w}) = (i\beta, i\gamma, \alpha_1)\frac{A}{k_1^2} e^{-\alpha_1 z} + [B, C, -\frac{i}{\alpha_2}(\beta B + \gamma C)]e^{-\alpha_2 z} \qquad (9.37)$$

To find A, B and C, we must introduce the Fourier transformed stress boundary conditions. From equation (9.2)

$$\bar{\tau}_{xz}\,|_{z=0} = \mu(-i\beta\bar{w} + \frac{d\bar{u}}{dz})|_{z=0} = 0 \qquad (9.38)$$

Substituting for $\bar{u}$ and $\bar{w}$ from equation (9.37) leads to:

$$2i\beta\alpha_1 \frac{A}{k_1^2} + \frac{1}{\alpha_2}(\beta^2 + \alpha_2^2)B + \frac{\beta\gamma}{\alpha_2} C = 0 \qquad (9.39)$$

Similarly

$$\bar{\tau}_{yz}\,|_{z=0} = \mu(-i\gamma\bar{w} + \frac{d\bar{v}}{dz})|_{z=0} = 0 \qquad (9.40)$$

$$\Rightarrow 2i\gamma\alpha_1 \frac{A}{k_1^2} + \frac{\gamma\beta}{\alpha_2} B + \frac{1}{\alpha_2}(\gamma^2 + \alpha_2^2)C = 0 \qquad (9.41)$$

The stress component τ_{zz} is non-zero under the load; its transform from equation (9.2) is given by:

$$\bar{\tau}_{zz}|_{z=0} = (\lambda\bar{\Delta} + 2\mu \frac{d\bar{w}}{dz})|_{z=0} \qquad (9.42)$$

Therefore

$$\bar{\tau}_{zz}|_{z=0} = A(\lambda - \frac{2\mu\alpha_1^2}{k_1^2}) + 2\mu i(\beta B + \gamma C) \qquad (9.43)$$

Substituting for α_1^2 in equation (9.43) from (9.16), and noticing from equation (9.26) that

$$\beta^2 + \gamma^2 = \alpha_2^2 + k_2^2 \qquad (9.26a)$$

leads to

$$\bar{\tau}_{zz}|_{z=0} = -\mu\{(2\alpha_2^2 + k_2^2)\frac{A}{k_1^2} - 2i(\beta B + \gamma C)\} \qquad (9.44)$$

The stress at the surface is given by the imposed load:

$$\begin{aligned} \tau_{zz}|_{z=0} &= -\frac{P}{4bc} \qquad |x| < b, \quad |y| < c \\ &= 0 \qquad\quad |x| > b, \quad |y| > c \end{aligned} \qquad (9.45)$$

i.e., the surface is stress-free outside the rectangle. P is the total force acting on the rectangle, and is uniformly distributed over it.

Now from equation (9.45)

$$\bar{\tau}_{zz}|_{z=0} = \frac{1}{2\pi}\int_{-\infty}^{\infty}\int_{-\infty}^{\infty} -\frac{P}{4bc}\, e^{-i(\beta x+\gamma y)}dxdy$$

$$= -\frac{P}{8\pi bc}\int_{-c}^{c}\int_{-b}^{b} e^{-i(\beta x+\gamma y)}dxdy \qquad (9.46)$$

Evaluating this integral leads to

$$\bar{\tau}_{zz}|_{z=0} = -\frac{P}{2\pi bc} \cdot \frac{\sin \beta b \sin \gamma c}{\beta\gamma} \qquad (9.47)$$

Equations (9.39) and (9.41) are two equations for the three constants A, B and C; combining equations (9.47) and (9.44) gives the third equation necessary for a solution:

$$\mu\{(2\alpha_2^2 + k_2^2)\frac{A}{k_1^2} - 2i(\beta B + \gamma C)\} = \frac{P}{2\pi bc} \cdot \frac{\sin\beta b \sin\gamma c}{\beta\gamma} \qquad (9.48)$$

Multiplying equation (9.39) by γ, and subtracting from it equation (9.41) multiplied by β, gives, after a little algebra:

$$B = \frac{\beta}{\gamma} C \qquad (9.49)$$

Substituting this into equation (9.41) leads to:

$$\frac{2i\gamma\alpha_1}{k_1^2}A = -C\{\frac{1}{\alpha_2}(\gamma^2 + \alpha_2^2) + \frac{\beta^2}{\alpha_2}\} \qquad (9.50)$$

which, using equation (9.26), simplifies to:

$$A = \frac{ik_1^2 C}{2\gamma\alpha_1\alpha_2}(2(\beta^2 + \gamma^2) - k_2^2) \qquad (9.51)$$

Substituting equations (9.51) and (9.49) into equation (9.48) yields:

$$C = -\frac{iP}{2\pi bc\mu}\left(\frac{\sin\beta b \sin\gamma c}{\beta\gamma}\right) \cdot \frac{2\alpha_1\alpha_2\gamma}{(2(\beta^2 + \gamma^2) - k_2^2)^2 - 4\alpha_1\alpha_2(\beta^2 + \gamma^2)} \qquad (9.52)$$

where

$$(2(\beta^2 + \gamma^2) - k_2^2)^2 - 4\alpha_1\alpha_2(\beta^2 + \gamma^2) = F(\beta,\gamma) \qquad (9.53)$$

$F(\beta,\gamma)$ is the well-known Rayleigh function. This allows the expression for C to be re-written:

$$C = -\frac{iP}{2\pi bc\mu}\left(\frac{\sin\beta b \sin\gamma c}{\beta\gamma}\right).\frac{2\alpha_1\alpha_2\gamma}{F(\beta,\gamma)} \qquad (9.54)$$

Now, from equations (9.51) and (9.49)

$$A = \frac{P}{2\pi bc\mu}\left(\frac{\sin\beta b \sin\gamma c}{\beta\gamma}\right).\frac{2\alpha_1\alpha_2\beta}{F(\beta,\gamma)} \qquad (9.55)$$

$$B = -\frac{iP}{2\pi bc\mu}\left(\frac{\sin\beta b \sin\gamma c}{\beta\gamma}\right).\frac{2\alpha_1\alpha_2\beta}{F(\beta,\gamma)} \qquad (9.56)$$

With A, B and C defined as functions of β and γ, equation (9.37) gives $\bar{u}$, $\bar{v}$ and $\bar{w}$ in a form suitable for numerical inverse Fourier transformation. This process is described in the next section.

9.3 The Method of Numerically Calculating the Inverse Double Fourier Transforms

To find the displacements in the half-space, caused by the vibrating rectangle, it is necessary to inverse transform equation (9.37), where A, B and C are defined by equations (9.54), (9.55) and (9.56). Therefore the general problem is expressed by the inversion of equation (9.37):

$$(u,v,w) = \frac{1}{2\pi}\int_{-\infty}^{\infty}\int_{-\infty}^{\infty}\{(i\beta,i\gamma,\alpha_1)\,\frac{A}{k_1^2}\,e^{-\alpha_1 z} + [B,C,-\frac{i}{\alpha_2}\,(\beta B + \gamma C)]e^{-\alpha_2 z}\}$$

$$\times e^{i(\beta x+\gamma y)}d\beta d\gamma \qquad (9.57)$$

However, we are interested in the surface vibration, where $z = 0$, and if we further restrict the range of interest to the x-axis, where $y = 0$, the inverse transform is simplified:

$$(u,v,w) = \frac{1}{2\pi}\int_{-\infty}^{\infty}\int_{-\infty}^{\infty}\{(i\beta,i\gamma,\alpha_1)\,\frac{A}{k_1^2} + [B,C,-\frac{i}{\alpha_2}\,(\beta B + \gamma C)]\}e^{i\beta x}d\beta d\gamma \qquad (9.58)$$

The functions $\bar{u}$, $\bar{v}$ and $\bar{w}$ are shown plotted in the (β,γ) plane in Figs. 9.2 to 9.5, and their behaviour is such as to further simplify equation (9.58). The function $\bar{v}$ is anti-symmetric about $\gamma = 0$, with the result that the transverse displacement v along the x-axis is zero. This is required by the symmetry of the physical problem; likewise, the horizontal displacement u will be zero on the y-axis, and this is ensured by $\bar{u}$ being anti-symmetric about $\beta = 0$.

Furthermore $\bar{w}$ is symmetric in both β and γ axes, while $\bar{u}$ is symmetric in $\gamma = 0$, and as just mentioned, anti-symmetric in $\beta = 0$. These properties allow the infinite integrals to be reduced to semi-infinite integrals, as the term $e^{i\beta x}$ is the sum of a symmetric and an anti-symmetric function. Equation (9.58) reduces to:

$$u = \frac{2}{\pi}\int_0^\infty\int_0^\infty (B - \frac{\beta A}{k_1^2})\sin\beta x d\beta d\gamma \qquad (9.59)$$

and

$$w = \frac{2}{\pi}\int_0^\infty\int_0^\infty \{\alpha_1 \frac{A}{k_1^2} - \frac{i}{\alpha_2^2}(\beta B + \gamma C)\}\cos\beta x d\beta d\gamma \qquad (9.60)$$

Although methods exist for the computation of convergent infinite integrals (see, for example, Longman [47]) the upper integration limits in equations (9.59) and (9.60) can be truncated with an insignificant loss of accuracy. This is because most of the information in the (β,γ) plane is near to the Rayleigh wavenumber k_R, where $k_R^2 = \beta^2 + \gamma^2$. Denoting adequate 'cut-off' points for the integration by β_C and γ_C, equations (9.59) and (9.60) can be re-written

$$u \simeq \frac{2}{\pi}\int_0^{\gamma C}(\int_0^{\beta C}(B - \frac{\beta A}{k_1^2})\sin\beta x d\beta)d\gamma \qquad (9.61)$$

and

$$w \simeq \frac{2}{\pi}\int_0^{\gamma C}(\int_0^{\beta C}\{\alpha_1 \frac{A}{k_1^2} - \frac{i}{\alpha_2^2}(\beta B + \gamma C)\}\cos\beta x d\beta)d\gamma \qquad (9.62)$$

For large (βx), the first integration along the β axis in each of the above integrals will develop dense oscillations. The integration can be approximated accurately, for a chosen value of x (say x_1), using a method described in Appendix A. If the results of these first numerical integrations are denoted $\tilde{u}(x_1)$ and $\tilde{w}(x_1)$ such that

$$\tilde{u}(x_1) \simeq \int_0^{\beta c} (B - \frac{\beta A}{k_1^2}) \sin\beta x d\beta \qquad (9.63)$$

and

$$\tilde{w}(x_1) \simeq \int_0^{\beta c} (\alpha_1 \frac{A}{k_1^2} - \frac{i}{\alpha_2^2} (\beta B + \gamma C)) \cos\beta x d\beta \qquad (9.64)$$

then we may write

$$u(x_1) \simeq \frac{2}{\pi} \int_0^{\gamma c} \tilde{u}(x_1) d\gamma \qquad (9.65)$$

and

$$w(x_1) \simeq \frac{2}{\pi} \int_0^{\gamma c} \tilde{w}(x_1) d\gamma \qquad (9.66)$$

where throughout an expression of the form $\tilde{u}(x_1)$ means "$\tilde{u}$ evaluated for $x = x_1$".

The variations of $\tilde{u}(x_1)$ and $\tilde{w}(x_1)$ are sufficiently well-behaved, in the frequency and distance range of interest here (frequency $\leq$ 64 Hz, distance $\leq$ (x/b = 33)), to allow integration of equations (9.65) and (9.66) using several applications of Simpson's Rule.

Simpson's Rule is given by

$$\int_{x_0}^{x_{2n}} f(x)dx \simeq \frac{h}{3} \{(f_0 + f_{2n}) + 4(f_1 + f_3 + \ldots + f_{2n-1}) + 2(f_2 + \ldots + f_{2n-2})\}$$

where f_i is equal to $f(x_i)$, and h is the increment.

(Ref: any Engineering Mathematics textbook, e.g., Spencer *et al* [35])

Several applications are desirable, as then the interval used for the Rule can be varied according to the local behaviour of $\tilde{u}(x_1)$ and $\tilde{w}(x_1)$. Above $\gamma = k_R$, $\tilde{u}(x_1)$ and $\tilde{w}(x_1)$ vary smoothly, but both exhibit peaks related to the Rayleigh and compression wavenumbers (the location of which is frequency dependent), and for large x_1 (> 10) both exhibit significant oscillations for $\gamma < k_R$. (See Figs. 9.6 and 9.7, which show plots of $\tilde{w}$ against γ.)

Once $\tilde{u}(x_1)$ and $\tilde{w}(x_1)$ have been approximately evaluated for the whole range $0 \leqslant \gamma \leqslant \gamma_C$, equations (9.65) and (9.66) give $u(x_1)$ and $w(x_1)$. By then incrementing x_1, and repeating the process, the surface displacement pattern in the near-field can be found with adequate accuracy.

Note 1: The value of the expression $(\sin\beta b \sin\gamma c/\beta\gamma)$ requires attention when β or γ equal zero. Using L'Hôpital's limit theorem, it can be shown that if $\beta = 0$, then the expression $= \sin \gamma c/\gamma$, and conversely if $\gamma = 0$, then the expression $= \sin \beta b/\beta$. If both β and γ are zero, it has the value 1.

Note 2: In Section 9.1.1, it was mentioned that two previous workers reduced one infinite integral of the double inverse transform to finite limits, by means of the transformation $\beta = \zeta \cos\theta$, $\gamma = \zeta \sin\theta$. This is a more elegant approach, and may save some computation time; however, one infinite integral must still be contended with, and by the method used here, most of the computation time is spent on just the first, more involved, integration. Keeping the original expressions has the advantage that the information on each axis is known to be predominantly near $\beta, \gamma = k_R$.

9.4 Results

9.4.1 Material properties and non-dimensionalisation

In previous Chapters an attempt has been made to generalise the results, by non-dimensionalising them. However, these results are most easily interpreted as for a particular British Rail test-site, at Clarborough. The results here are presented in a similar way, to aid comparison with the previous work.

A description of the non-dimensionalising method can be found in Chapter 3. Although the Figures here, which show actual displacements or phase change plotted against distance (Figs. 9.8 to 9.13) all have non-dimensionalised scales, all the Figures are for a particular frequency (of the harmonic load) in Hz. Should the reader wish to compare these results with others, the following non-dimensionalised (frequency)^2 term should be used:

$$\Omega^2 = \frac{\omega^2 \rho b^2}{E} \qquad (9.67)$$

in the notation used before.

The four relevant non-dimensional (frequency)^2 values are tabulated below, using the Clarborough material properties:

Frequency (Hz)	4	16	32	64
$\Omega^2 = \frac{\omega^2 \rho b^2}{E}$	0.002	0.033	0.131	0.524

Table 9.1: Relevant values of the frequency parameter Ω^2.

The Clarborough material properties, as used in previous Chapters, are Young's modulus, E = 269 MNm^{-2}; density, ρ = 1550 kgm^{-3}; Poisson's ratio = 0.257. The compression, shear and Rayleigh wavespeeds with these material properties are, respectively, 459.4, 262.7 and 241.9, all ms^{-1} (see equation (4.14) for the calculation of the Rayleigh wavespeed). The values of 'b' and 'c' used are 0.75 m and 0.125 m respectively.

Figures showing actual displacements (Figs. 9.8 to 9.16) are for a load of magnitude 2π (the load is non-dimensionalised as $\bar{P} = P/Eb^2$,

which has the value $\bar{P} = 4.15 \times 10^{-8}$ for a load of 2π at Clarborough) and an hysteretic damping loss factor $\eta = 0.1$ (see Chapter 2 for a description of the damping mechanism). These figures are as used in the previous Chapters.

In Figure 9.2, which shows curves of $\bar{u}$, $\bar{v}$, $\bar{w}$ plotted against β or γ, the features of the curves have been exaggerated by reducing the loss factor η to 0.02.

9.4.2 Accuracy of the method, and comparison with other work

An example of the computer programs used to produce these results, called Program W, is listed in Appendix B. A note preceding the listing describes how other related programs can be generated, by modifying W. All the programs (except those which plot in the (β,γ) plane) use the NAG library routine D01ANF, which accomplishes the first integration of $\bar{u}$ and $\bar{w}$ resulting in values of $\tilde{u}$ and $\tilde{w}$ (these terms are defined in the last section). The NAG routine is described in Appendix A. The accuracy of this routine depends on input parameters stating the required relative accuracy, and the required absolute accuracy. In addition, the values of β_c and γ_c (defined in Section 9.3) will alter the solution. It was found that defining the relative accuracy and absolute accuracy as respectively 10^{-6} and 10^{-18}, and setting $\beta_c = \gamma_c = 20$, the results were accurate to three significant figures, on the basis of comparisons with higher required accuracy and greater β_c, γ_c.

To the author's knowledge, the only previous results which can be directly compared with those produced by the method here, are due to Gaul [19]. He gives results for two non-dimensional frequencies, showing the variation of real and imaginary parts of non-dimensional displacement up to $x/b = 8$, due to uniform loading of a square area (area b^2). He uses a Poisson's ratio $\nu = 0.4$, and incorporates hysteretic damping. However, his damping model is slightly different to the one used here, as he uses different loss factors for shear and compression - respectively, $\eta_S = 0.05$, $\eta_\lambda = 0.1$. Apart from this difference, program W was easily modified to use Gaul's square load, different Poisson's ratio and different frequency. The results showed excellent agreement with the real part of Gaul's vertical displacement, and were within 10% of the

imaginary part of the displacement. This difference is assumed due to the different damping, as effectively the loss factors were taken as $\eta_S = \eta_\lambda = 0.1$. This agreement with Gaul's results which were produced by a different method (see Section 9.5) lends weight to the results presented here.

9.4.3 Description of Figures

Figures 9.2 to 9.5 show plots of $\bar{u}$, $\bar{v}$ and $\bar{w}$ in the (β,γ) plane. Figures 9.2 to 9.5 show a surface, while Figure 9.2 effectively shows sections of the surface, with the features exaggerated by decreasing η. Figure 9.2 shows the symmetry and anti-symmetry respectively of $\bar{w}$ and $\bar{u}$ in the γ-direction, and the symmetry of $\bar{v}$ in the β-direction. The major peak in each graph is caused by the Rayleigh wave. In Figs. 9.2(a) and 9.2(c) the peak is only shifted slightly from $\gamma = k_R$, because of the damping present, but in Fig. 9.2(b), this shift is greater, because the 'section' is taken at $\gamma = 0.02$, and the peak is centred near $(k_R^2 - 0.02^2)^{1/2}$. Again, the peak is 'near' this value due to the damping.

The fact that this peak follows the locus $k_R^2 = \gamma^2 + \beta^2$ can be clearly seen in Figs. 9.3 to 9.5. These show the $\bar{u}$, $\bar{v}$ and $\bar{w}$ surfaces over part of the quarter-plane. For the frequency of 32 Hz chosen, a unit square in the (β,γ) plane is large enough to show all the behaviour of interest. The variations over the other three quarter-planes can be deduced from the one, because of the symmetry of the functions. The second, smaller peak (or trough) in these Figures, near β (or γ) = 0.45 on γ (or β) = 0, is caused by the compression wave. As was the case with the infinite strip solutions of Chapter 3, the shear wave contribution is lost in the dominant Rayleigh wave peak.

Given the symmetry of the physical problem, the horizontal and transverse motion components u and v can be expected to be related in some way, and their relationship is revealed in the algebra of Section 9.2. Combining equations (9.37), (9.54) and (9.56) leads to the equation:

$$\gamma\bar{u} = \beta\bar{v} \qquad (9.68)$$

Hence, rotating the $\bar{u}$ graphs through 90°, and interchanging the names of the β and γ axes, will produce the $\bar{v}$ graphs. Partly for this reason, Figs. 9.4(a) and 9.4(b) show the $\bar{v}$ surface observed from the (1.0,1.0) corner of the (β,γ) plane, instead of the origin as for the $\bar{u}$ surface in Figs. 9.3(a) and 9.3(b), to show more information in the four graphs.

Figures 9.5(a) and 9.5(b) show the $\bar{w}$ surface, and clearly suggest the symmetry of $\bar{w}$ in both $\beta = 0$ and $\gamma = 0$.

Figures 9.6 and 9.7 show $\tilde{w}$ curves plotted against γ, for the frequencies 4 and 64 Hz, and various values of x. These Figures show how for low frequency, increasing x has the effect of concentrating the $\tilde{w}$ information below k_R. At the higher frequency, increasing x still has this effect, which is beneficial with regard to applying Simpson's Rule, but in addition the integration is complicated by an oscillation, imposed on both real and imaginary parts of $\tilde{w}$ below k_R. Graphs of the variation of $\tilde{u}$ for increasing x and frequency would behave similarly. Figures 9.6 and 9.7 therefore show that the increments used in the applications of the Simpson's Rule, to each section of the $\tilde{w}$ or $\tilde{u}$ curve along $0 \leq \gamma \leq \gamma_C$, should be varied as x increases. Such a variation was used to produce the results here, to maximise the efficiency of the method.

Figure 9.8 shows the variation of non-dimensional vertical amplitude with distance, the amplitude plotted on a log scale, for the four frequencies considered in this Chapter: 4, 16, 32 and 64 Hz. The small "crinkles" on each curve are due to the approximate nature of the integration, and could only be removed with considerably greater computation time. However, an additional 'wavyness', evident particularly in the 64 Hz curve, is apparently due to a physical property, as explained in Section 9.5.2.

Figures 9.9 and 9.10 show the phase change with distance of each of the four frequency inputs. As in previous Chapters, there is no discontinuity in the phase change in reality; the appearance of the lines is a graphical convenience to limit the scale to $\pm\pi$. Each 'jump' should occur at exactly $\pm\pi$, and failure to do so at the higher

frequencies is due to the resolution of points being inadequate. As wavenumber is defined as rate of change of phase, the effective wavenumber of each travelling wave in this 'near-field' can be calculated graphically. In the range shown, the wavenumbers are practically constant, and are tabulated below, with the theoretical zero-damping Rayleigh wavenumber for comparison.

Frequency	Wavenumber	Rayleigh Wavenumber
4	0.115	0.103
16	0.447	0.415
32	0.860	0.831
64	1.724	1.66

Table 9.2: Wavenumbers of the Propagating Waves

The discrepancy between the Rayleigh wavenumber and the propagating wavenumber is partly due to the damping present, but the discrepancy is slightly larger than produced by a vibrating infinite strip, with the same damping (Chapter 3). An additional reason for the difference is discussed in Section 9.5.2.

Figure 9.11 is similar to Figure 9.8 but shows the change in amplitude of horizontal (u) motion (on a log scale) with distance. Because of the log scale, the zero amplitude at $x = 0$, required by symmetry, cannot be shown. A clear maximum of amplitude is achieved, for each of the four frequencies shown, at the load edge, where $x/b = 1$. Features of Fig. 9.8 are amplified in Fig. 9.11, with the regular 'wavyness' of each curve being much clearer. The 'wavelength' of this phenomenon can be easily measured from Fig. 9.11. Also, the tendency for higher frequencies to predominate in the near-field is more evident than in Fig. 9.11.

Figures 9.12 and 9.13 correspond to Figs. 9.9 and 9.10, and show the variation of the horizontal motion phase with distance. The effect of the load edge is clear in each graph, and the rates of change of phase, or wavenumbers, of each curve match their vertical motion counter-parts, with the exception of the 4 Hz graph which has a slowly increasing

wavenumber up to x/b = 20, where it achieves the 4 Hz vertical motion wavenumber.

Figures 9.14, 9.15 and 9.16 form a separate group of results, and are concerned with the effect of masses on direct and transfer receptances. Figure 9.14 shows the direct receptance of the rectangle with eight different masses, over the frequency range 2 to 64 Hz. In these three Figures, the total input load is of magnitude π. Each mass resonant frequency is clear, and the tendency of each curve to the same static value is evident. This static value is approximately $|w/b| = 2.2\times10^{-8}$, which, treating the mass on the ground as a simple, mass-spring system, and re-dimensionalising for the Clarborough properties with unit load per unit area, gives a stiffness $K = 5.08 \times 10^{8}$ Nm^{-1}. Figure 9.15 is similar to Figure 9.14, but considers the transfer receptance of a rectangular mass placed at $x/b = 4$ from the load. The same 8 masses were used as in Fig. 9.14. The purpose of Fig. 9.15 is to help interpret Fig. 9.16, which shows the response at $x/b = 33^{1}/_{3}$ from the load, if a mass is placed at $x/b = 4$. Four masses were used in this case. All the masses used are listed on the relevant Figures.

The method used to produce these receptance figures was identical to that used for the infinite strip receptances, described in Chapter 8. Equations (8.5), (8.9) and (8.13) have been used to produce Figs. 9.14, 9.15, 9.16 respectively.

9.4.4 Additional data for displacements further from the load

The near-field results presented show high frequencies producing greater displacements than low frequencies. This is known to not be the case further from the load, from experimental observation. As the amount of computation which would be required made it impractical to extend Figs. 9.8 and 9.11, vertical motion was instead computed for a small range of distance, much further from the load. The results of these computations are tabulated below, in dimensional form, for the Clarborough test-site.

Frequency (Hz)	Distance from load	|w| m × 10^{-11}	Phase of w (radians)	|(change in phase of w)|	
4	48	2.27	0.704		
	49	2.24	0.585	0.119	Av.=
	50	2.23	0.467	0.118	0.115
	51	2.19	0.359	0.108	
16	48	2.24	1.209		
	49	2.16	0.809	0.400	Av.=
	50	2.06	0.404	0.405	0.409
	51	1.97	-0.017	0.421	
32	48	1.22	0.123		
	49	1.15	-0.705	0.828	Av.=
	50	1.10	-1.567	0.862	0.816
	51	1.09	0.753	0.757	
64	48	0.21	1.427		
	49	0.19	-0.451	1.878	Av.=
	50	0.18	1.179	1.630	1.792
	51	0.16	-0.689	1.868	

Table 9.3: Additional Vertical Motion Data.

From Table 9.3 it can be seen that, sufficiently far from the load, the low frequency components dominate. However, this data is too limited to draw safe conclusions from the phase change calculations.

9.5 Discussion

9.5.1 Discussion of Figures with reference to the infinite strip load results

The bulk of work in this thesis is concerned with an infinite strip load, acting on one of three different ground structures. Surface vibrations in the vicinity of the load have been predicted. In the literature on ground vibration, very little work is concerned with surface vibrations around a load of finite area, and most of this work has been concerned with a half-space ground structure. It is probable that the Finite Element Method will prove the best tool with which to analyse more complicated ground structures. With this method, Waas [79] has already studied vibrations in the vicinity of an embedded circular load, with the 'bedrock' ground structure. Warburton [80] and Luco [52]

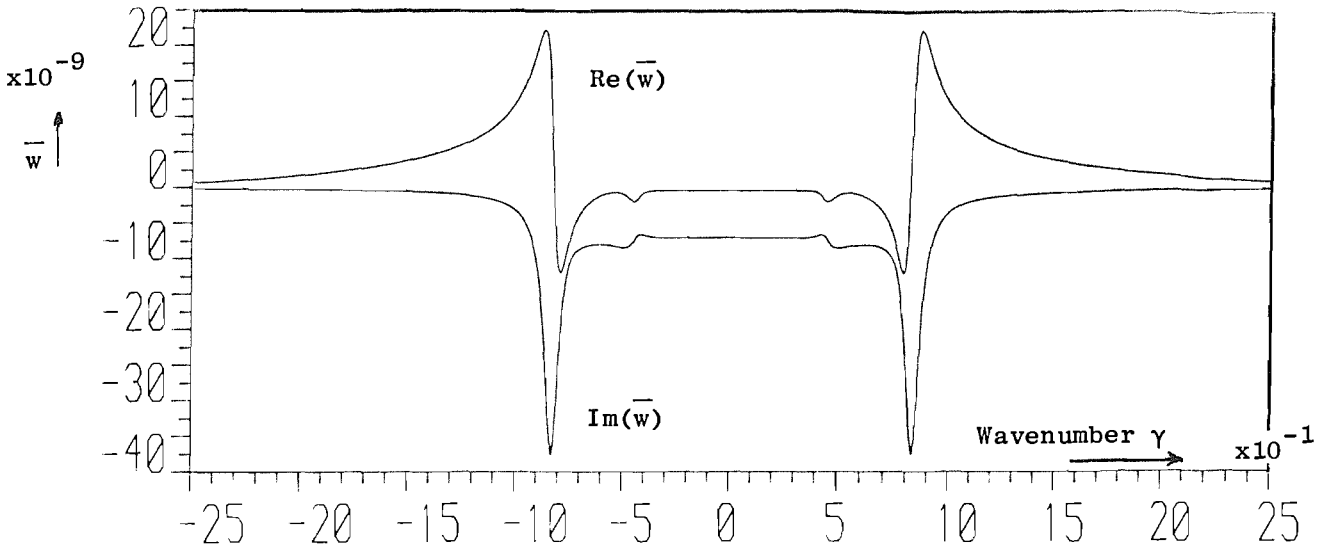

Fig 9.2(a): Transformed Vertical Motion, $\bar{w}$, against wavenumber γ for wavenumber $\beta = 0$, and frequency = 32Hz

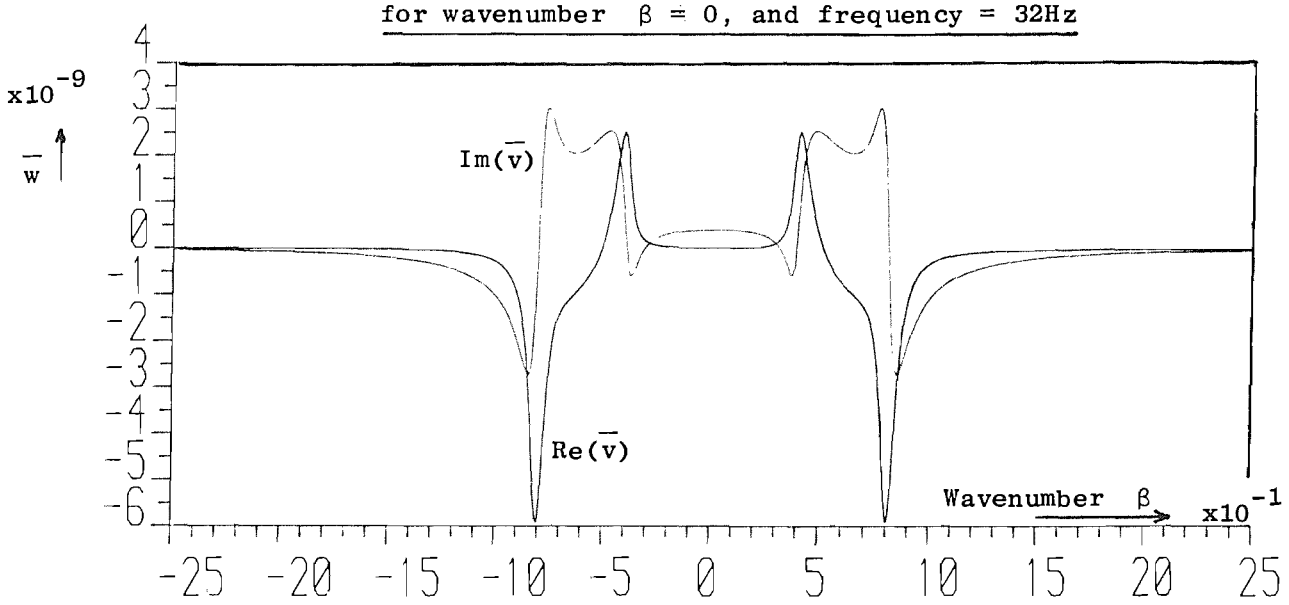

Fig 9.2(b): Transformed Transverse Motion, $\bar{v}$, against wavenmuber β for wavenumber $\gamma = 0.02$, and frequency = 32 Hz

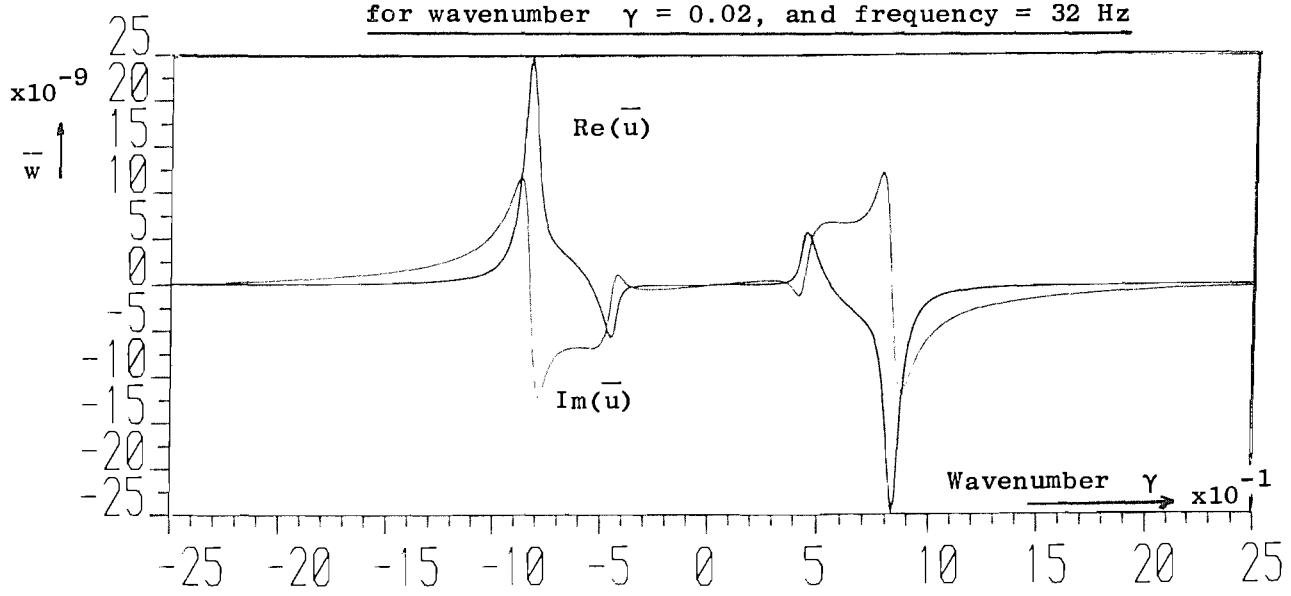

Fig 9.2(c): Transformed Horizontal Motion, $\bar{u}$, against wavenumber γ for wavenumber $\beta = 0$, and frequency = 32 Hz

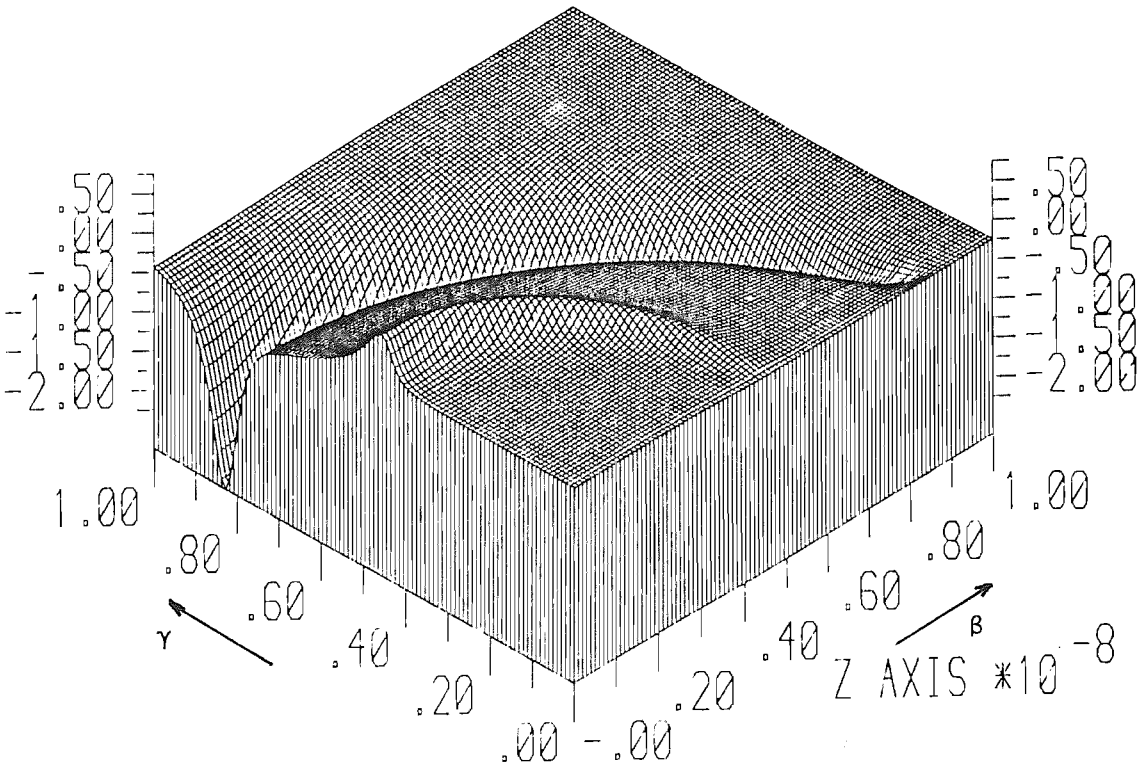

Fig 9.3(a): The Variation of the Real part of Transformed Horizontal Motion, $\bar{u}$, in the unit square $0 < \beta, \gamma < 1$, for frequency = 32 Hz

Fig 9.3(b): The Variation of the Imaginary part of Transformed Horizontal Motion, $\bar{u}$, in the unit square $0 < \beta, \gamma < 1$, for frequency = 32 Hz

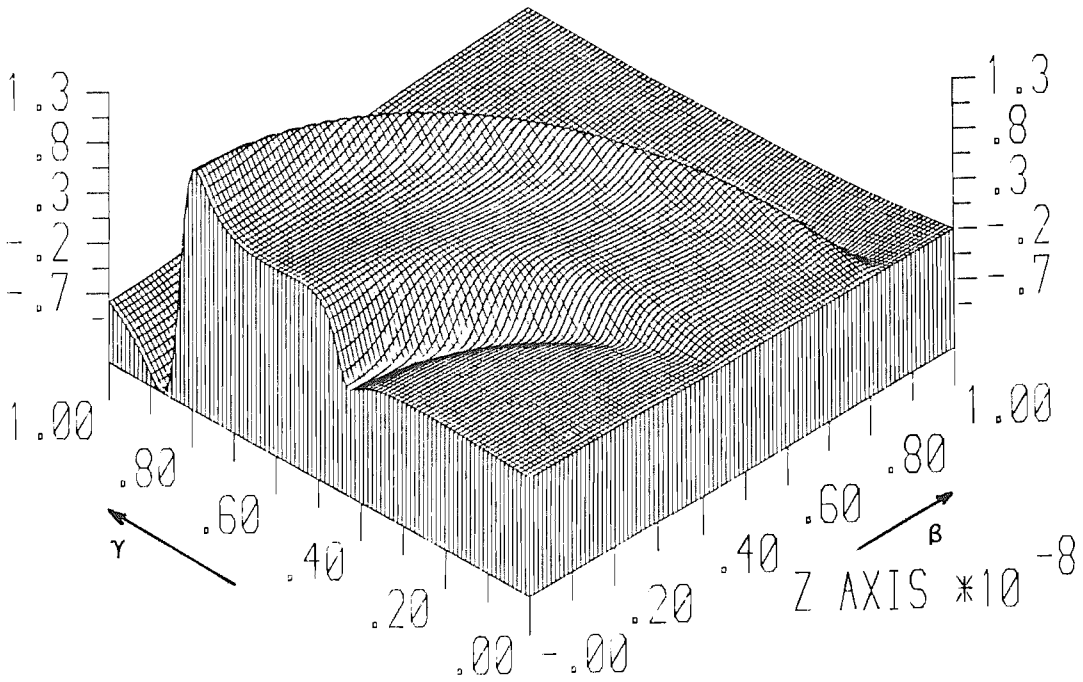

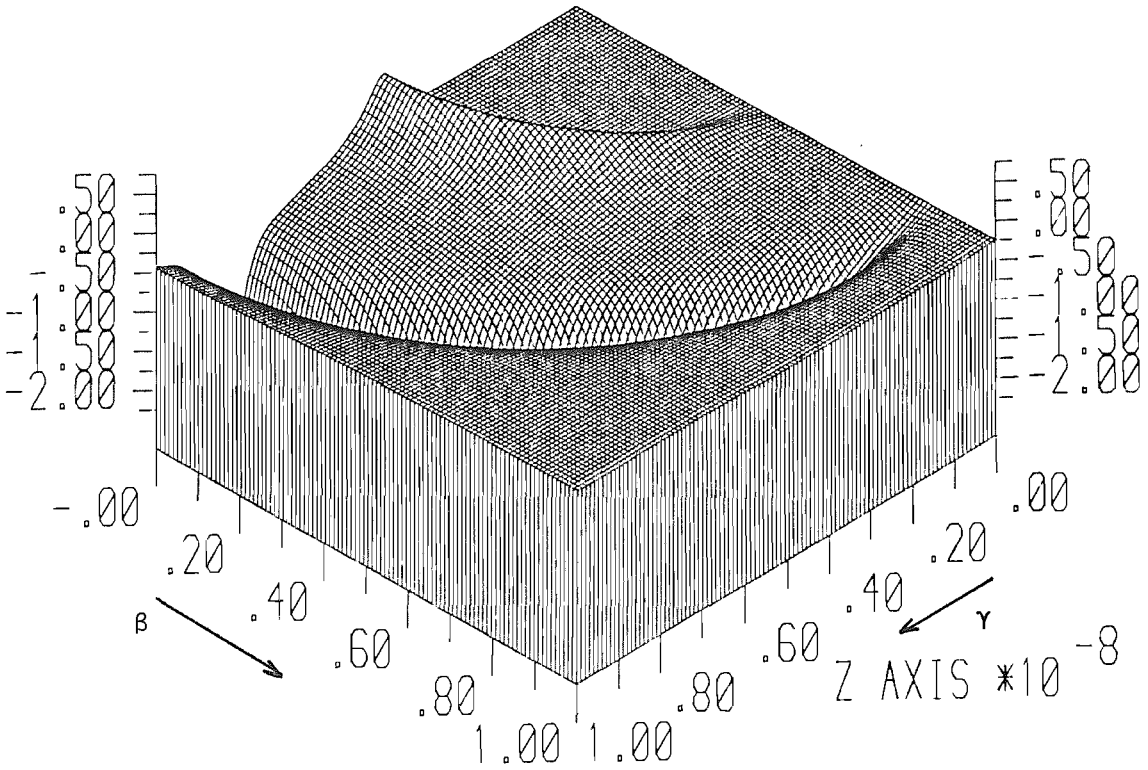

Fig 9.4(a): The Variation of the Real part of Transformed Transverse Motion, $\bar{v}$, in the unit square $0 < \beta, \gamma < 1$, frequency = 32 Hz

Fig 9.4(b): The Variation of the Imaginary part of Transformed Transverse Motion, $\bar{v}$, in the unit square $0 < \beta, \gamma < 1$, frequency = 32 Hz

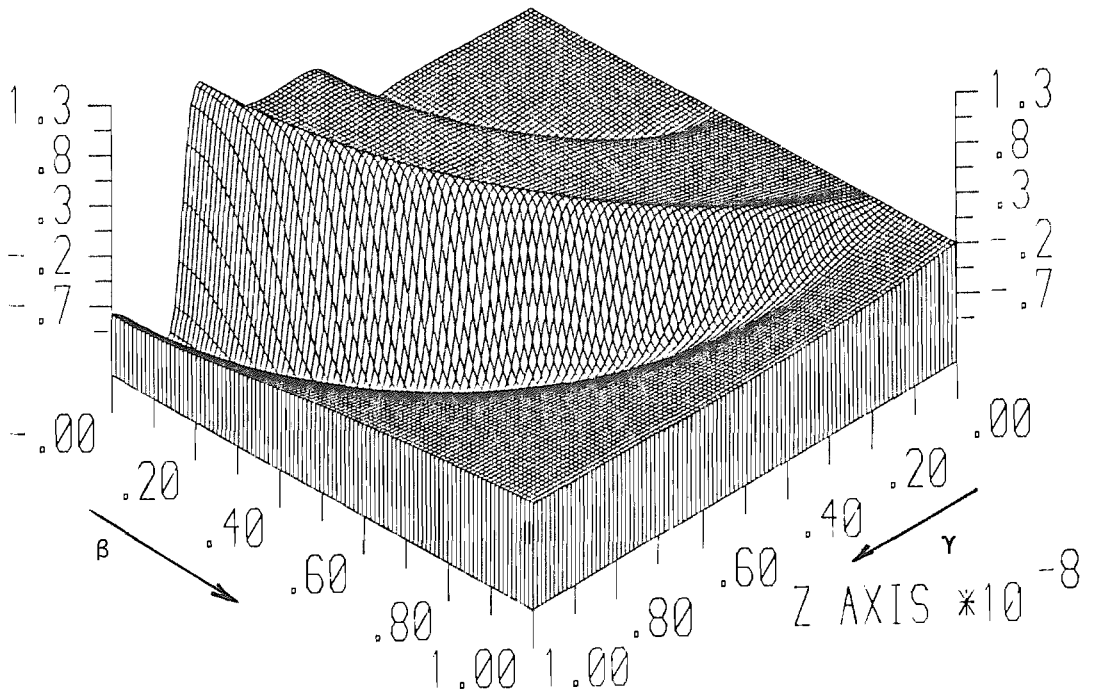

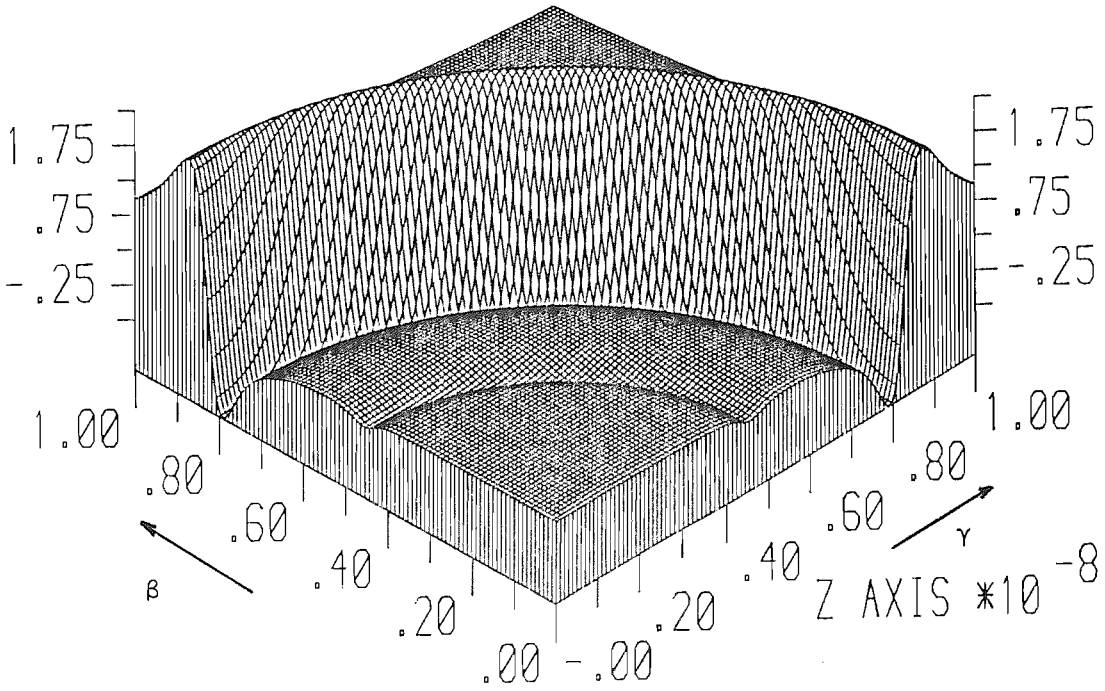

Fig 9.5(a): The Variation of the Real Part of Transformed Vertical Motion, $\bar{w}$, in the unit square $0 < \beta, \gamma < 1$, frequency = 32 Hz

Fig 9.5(b): The Variation of the Imaginary part of the Transformed Vertical Motion, $\bar{w}$, in the unit square $0 < \beta, \gamma < 1$, frequency = 32 Hz

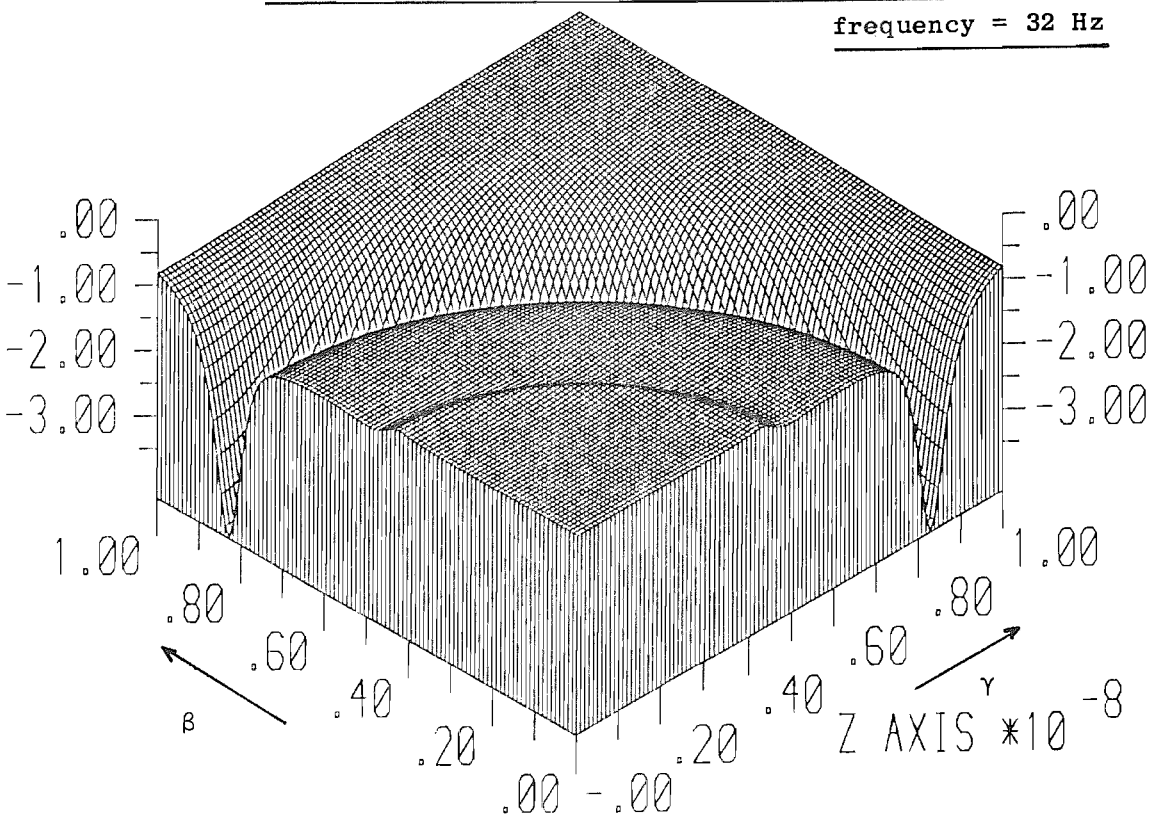

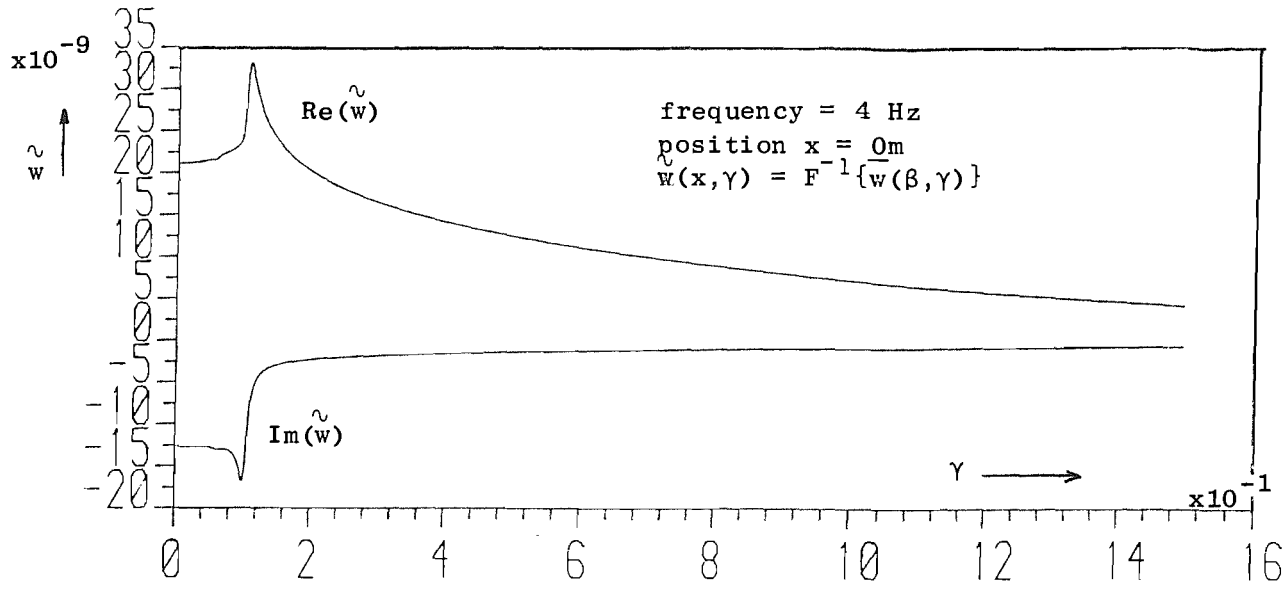

Fig 9.6(a): The function $\tilde{w}$, against wavenumber γ, produced by the first integration of $\bar{w}(\beta,\gamma)$, and evaluated at x = 0

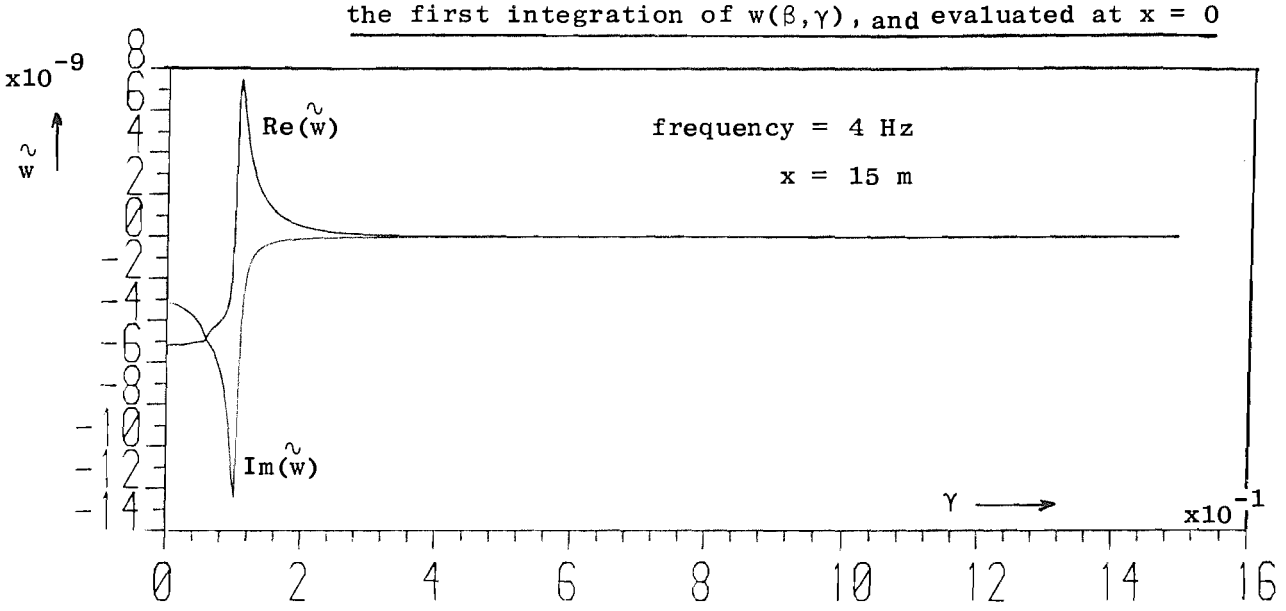

Fig 9.6(b): As for Fig 9.6(a), but evaluated at x = 15 m

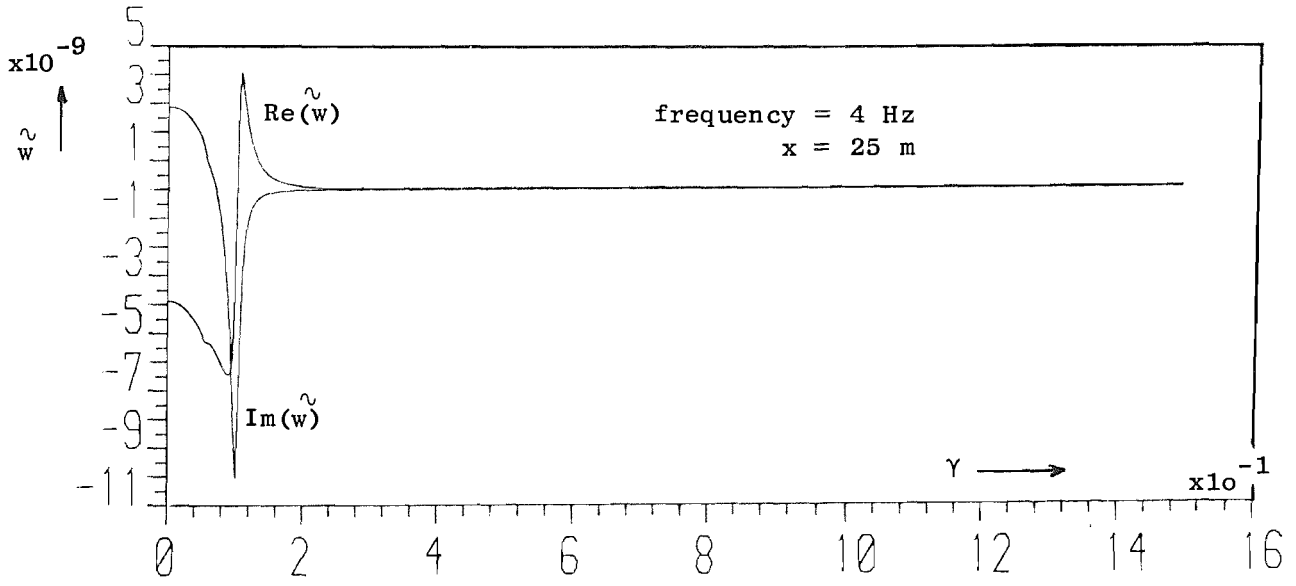

Fig 9.6(c): As for Fig 9.6(a), but evaluated at x = 25 m

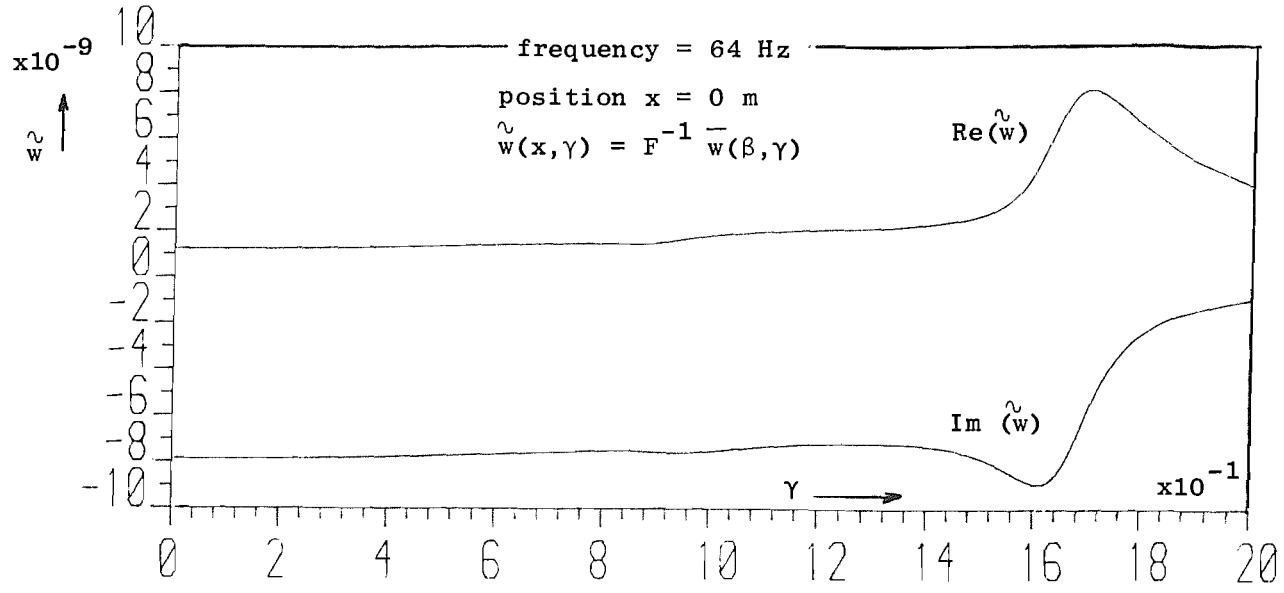

Fig 9.7(a): The function $\tilde{w}$, against wavenumber γ, produced by the first integration of $\bar{w}(\beta,\gamma)$, and evaluated at x = 0

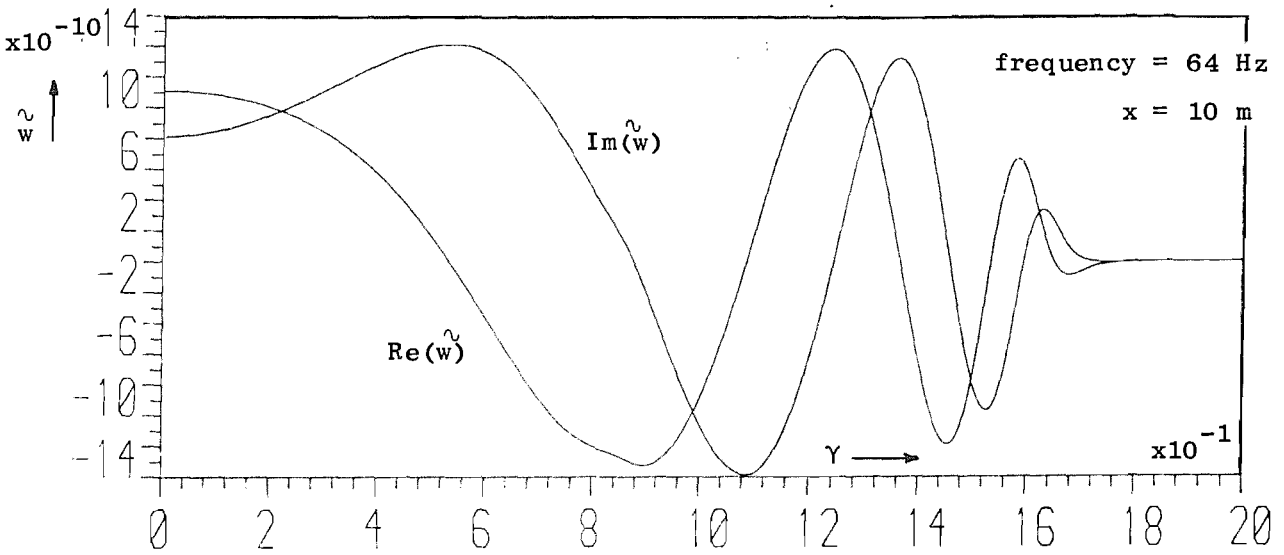

Fig 9.7(b): As for Fig 9.7(a), but evaluated at x = 10 m

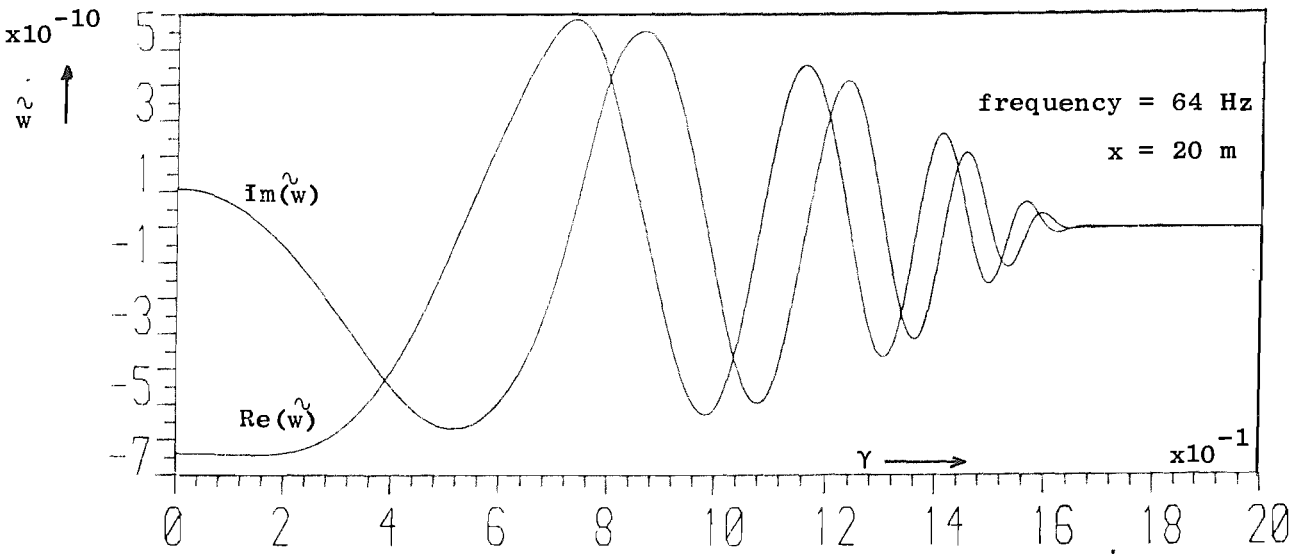

Fig 9.7(c): As for Fig 9.7(a), but evaluated at x = 20 m

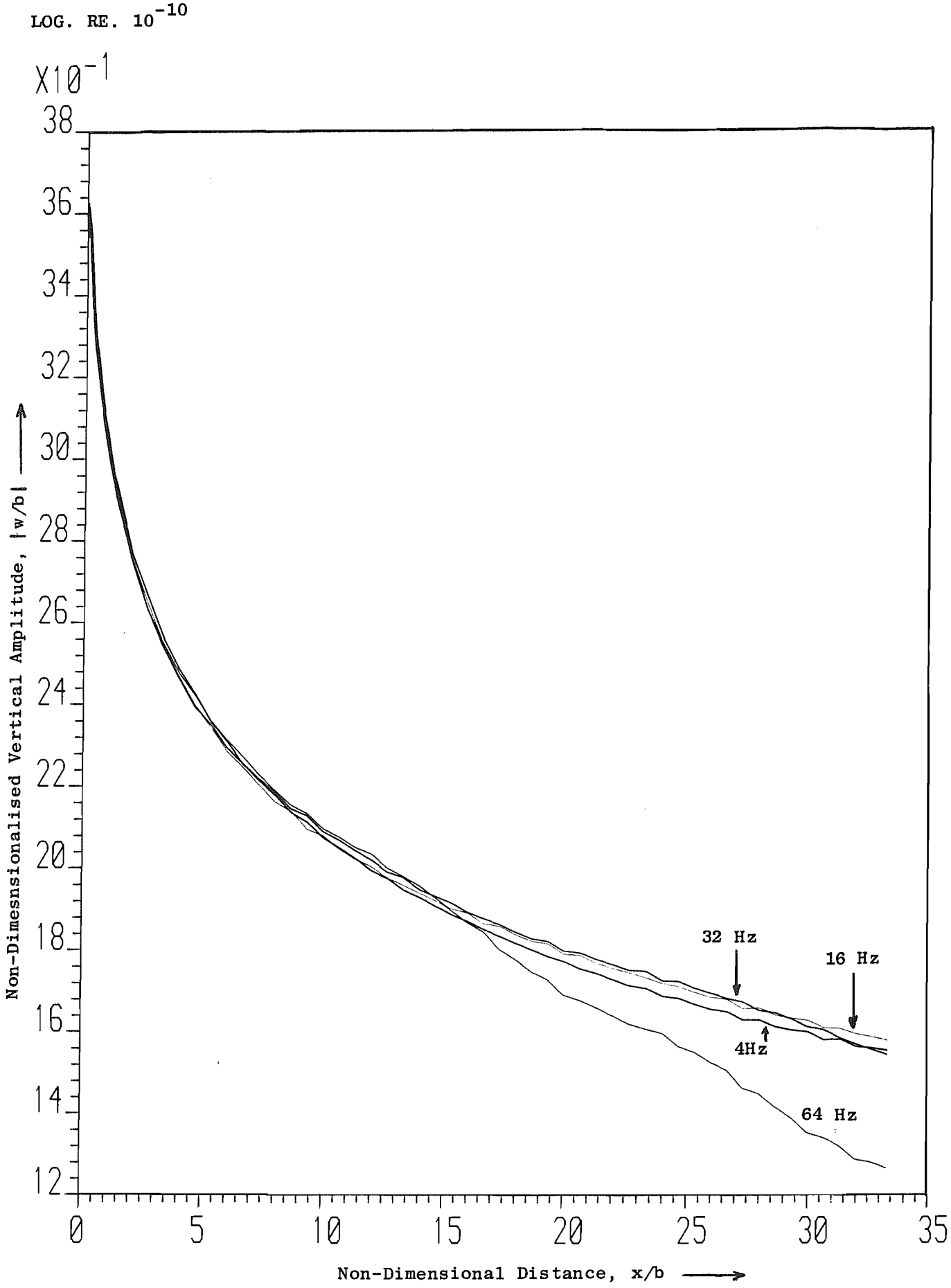

Fig 9.8: Non-Dimensionalised Vertical Amplitude against Distance, For Four Frequencies

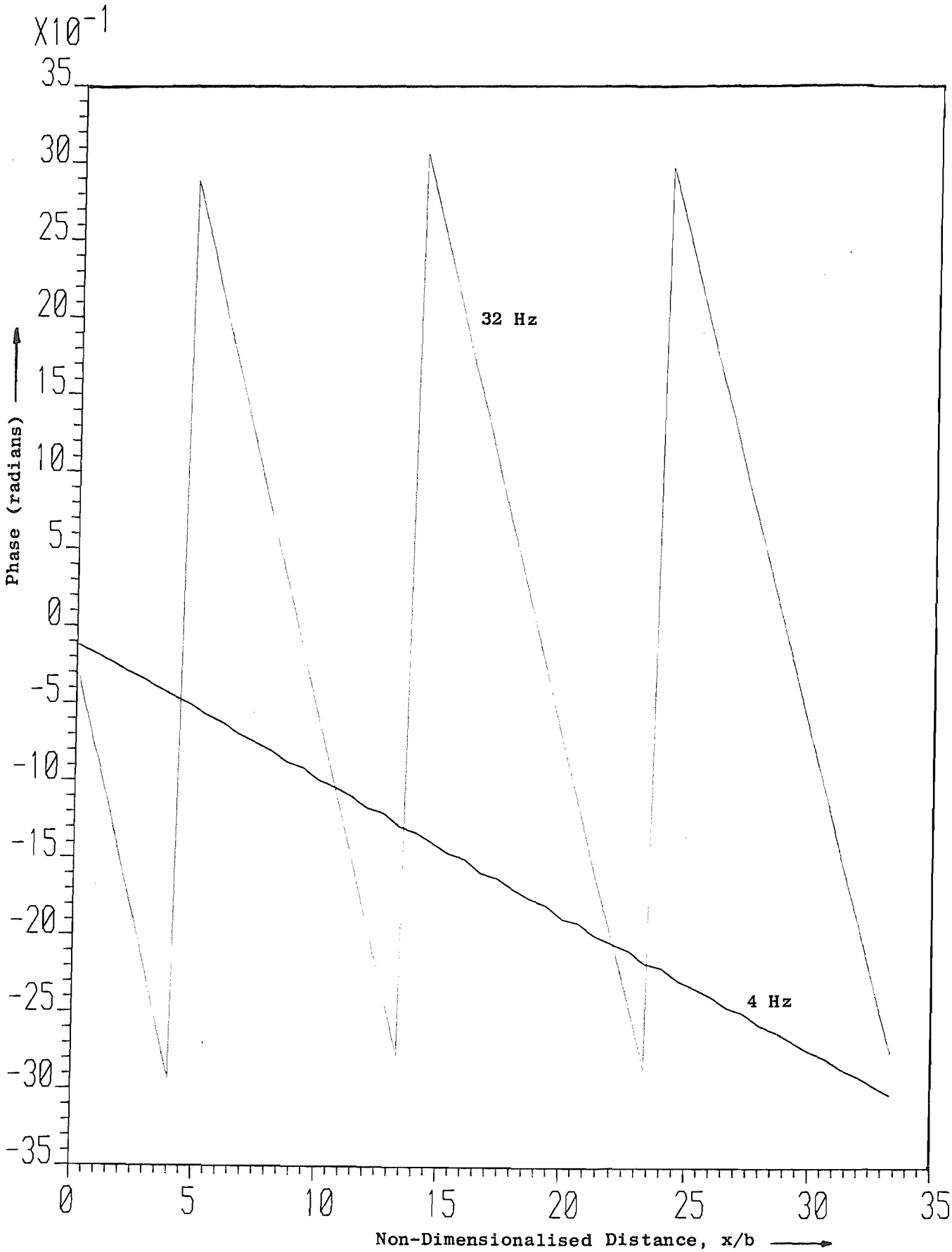

Fig 9.9: Phase Change with distance of vertical motion, frequency = 4 and 32 Hz

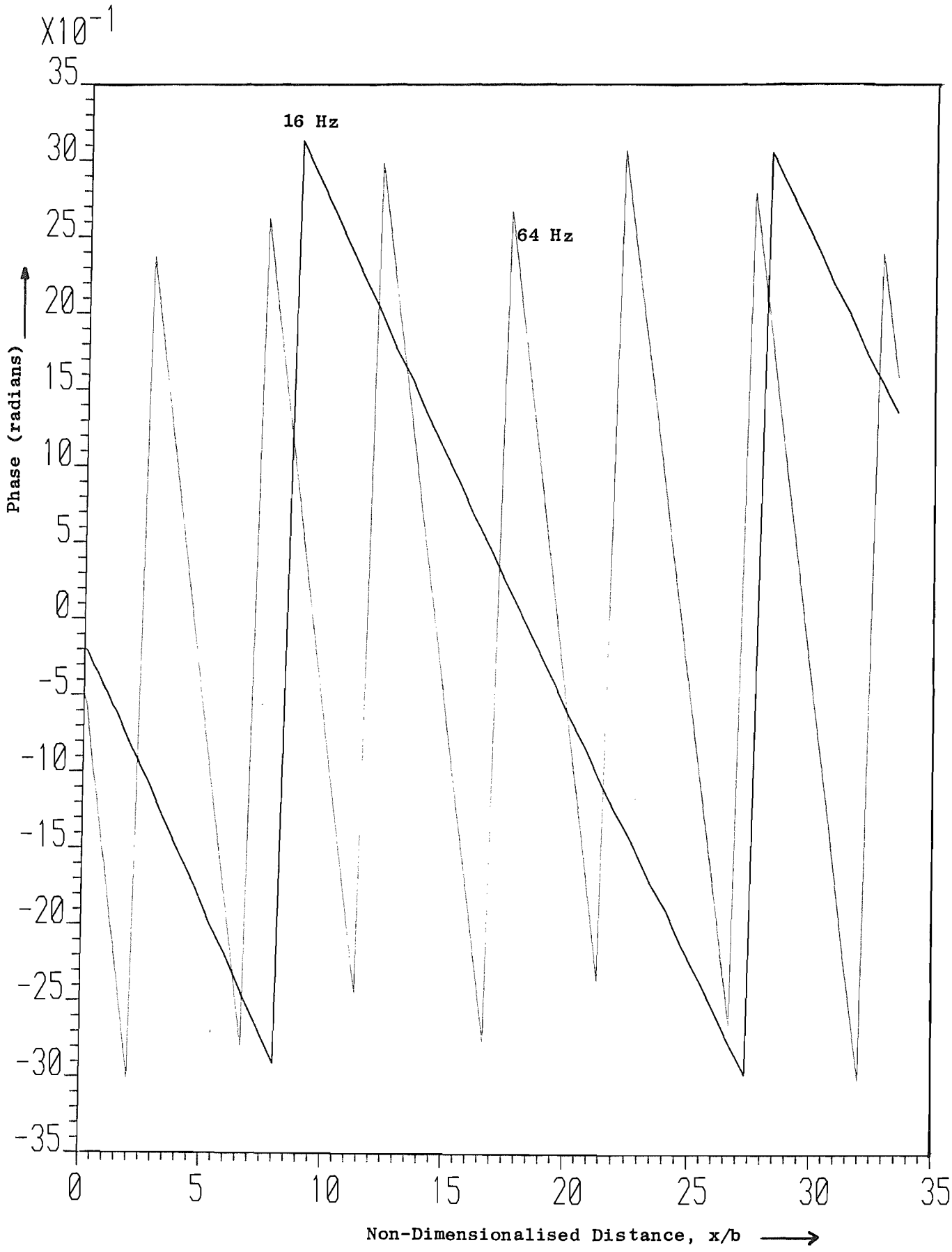

Fig 9.10: Phase Change with distance of vertical motion, frequency = 16 and 64 Hz

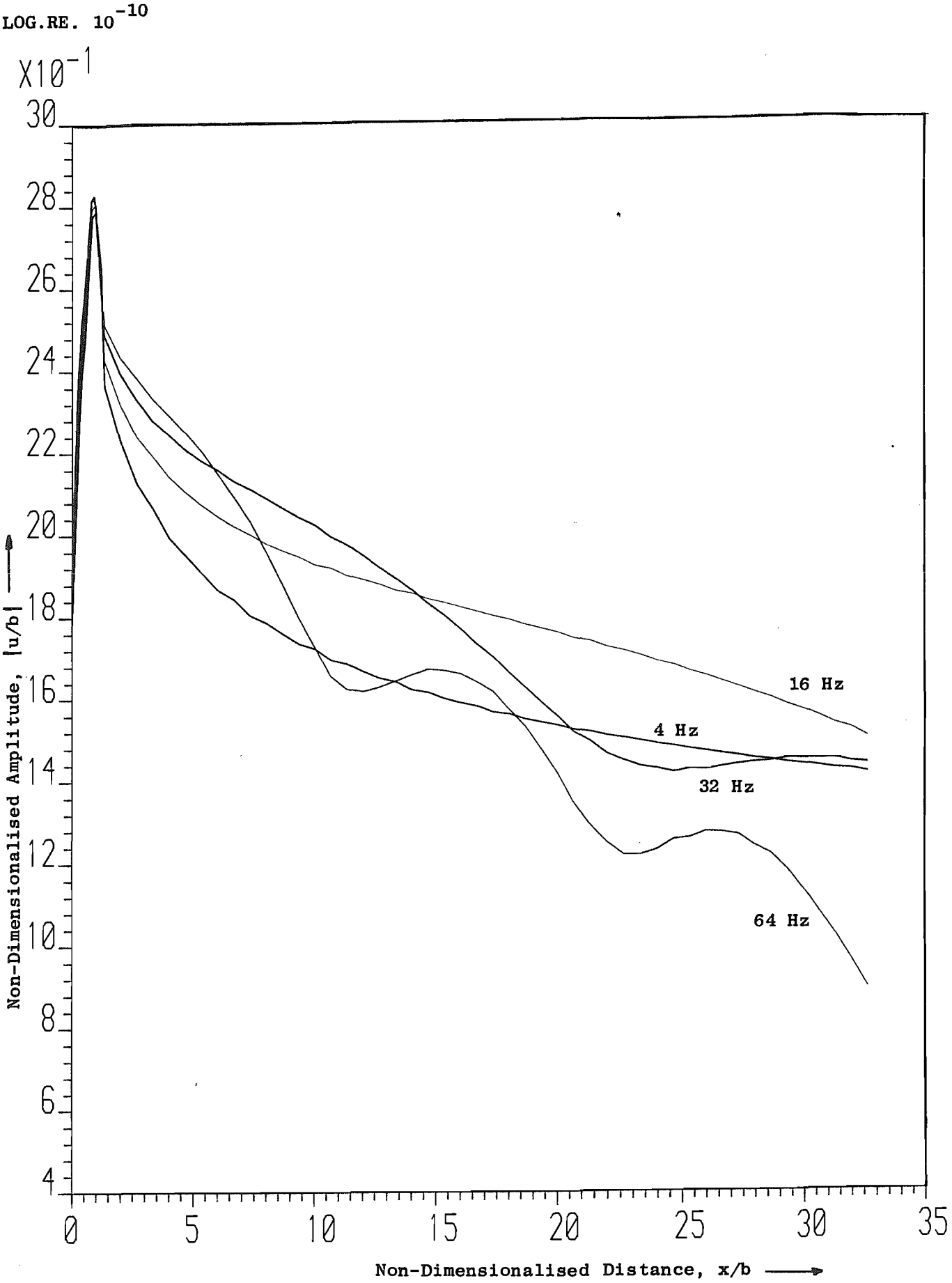

Fig 9.11: Non-Dimensionalised Horizontal Amplitude against Distance, For Four Frequencies

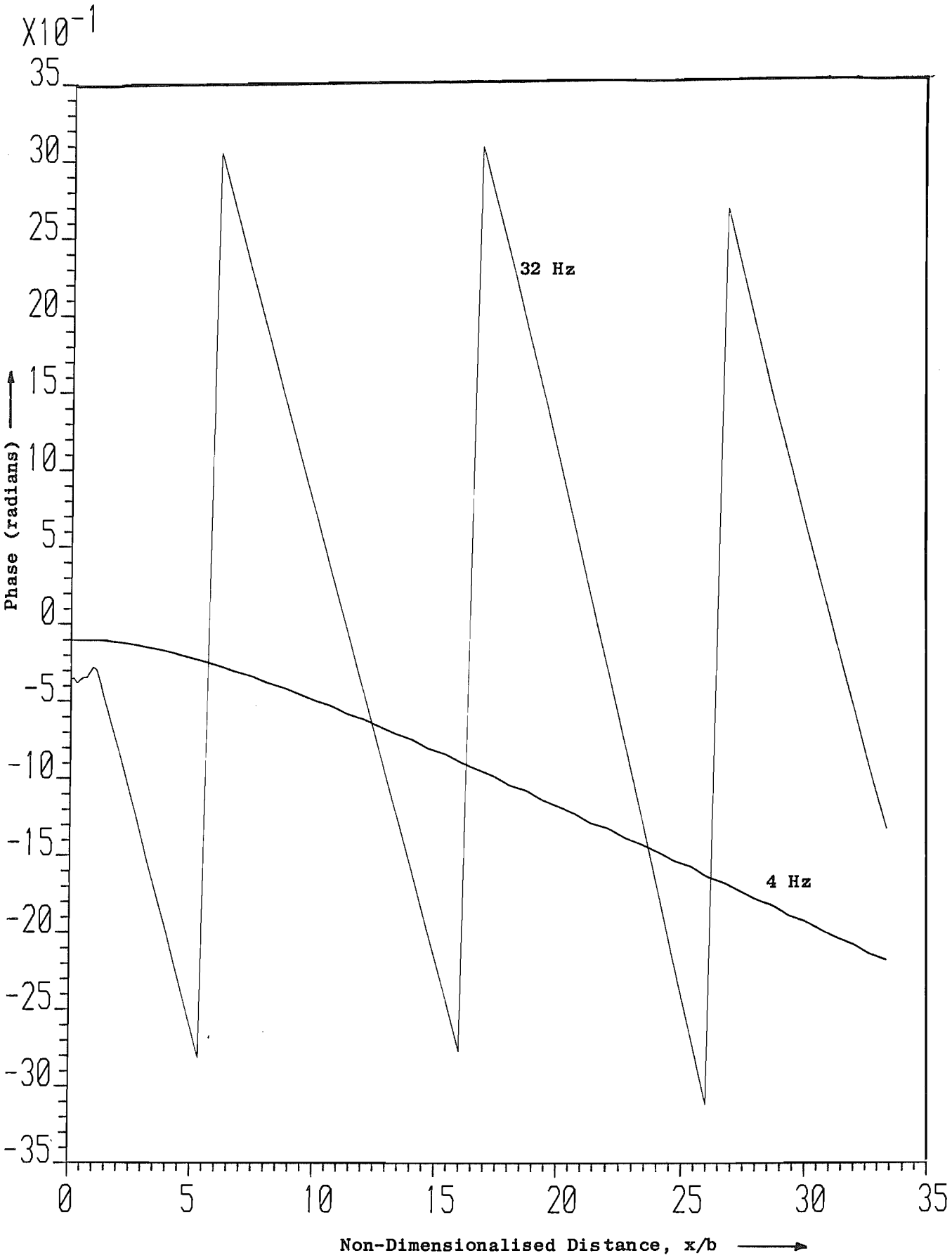

Fig 9.12: Phase Change with Distance of Horizontal Motion, frequency = 4 and 32 Hz

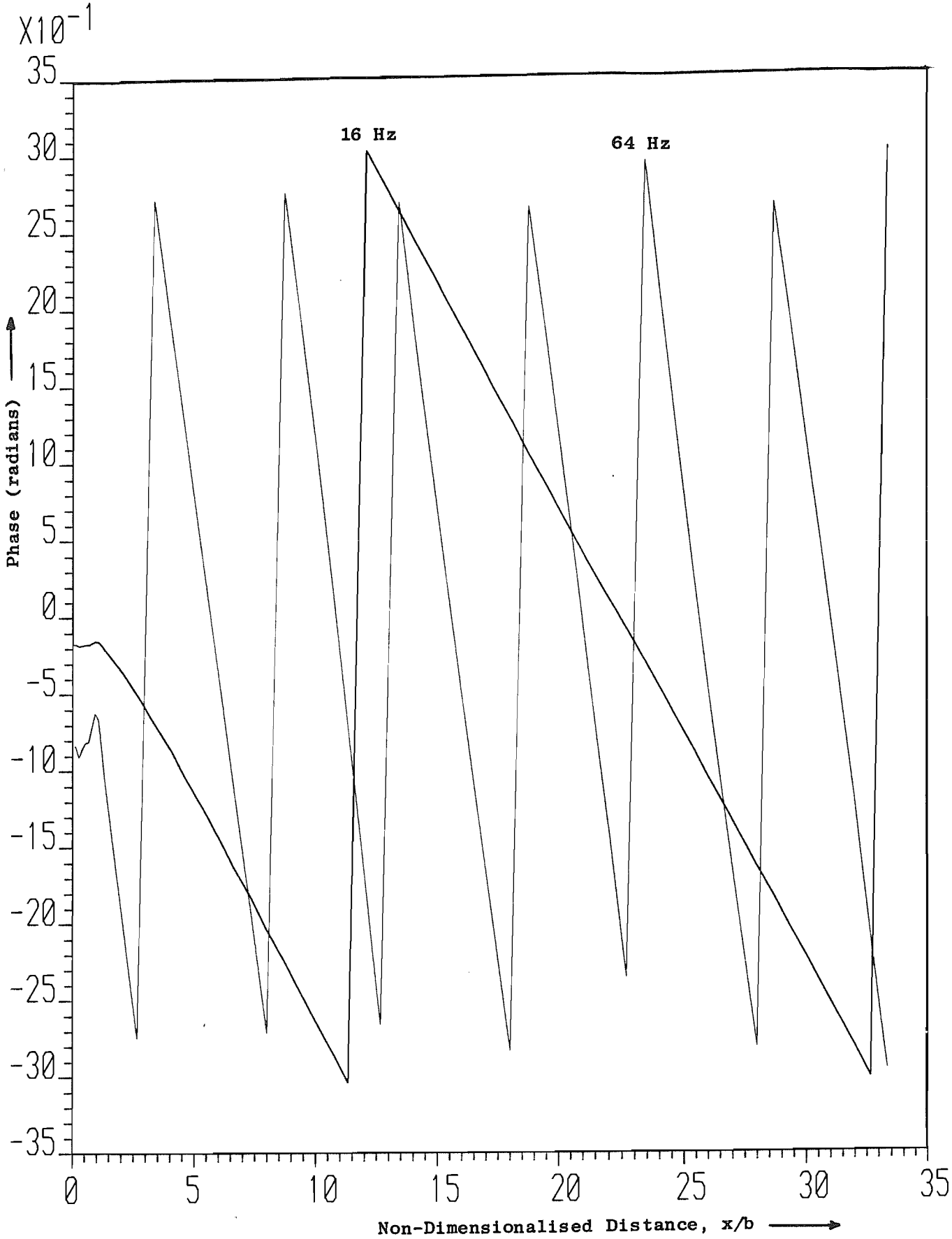

Fig 9.13: Phase Change with Distance of Horizontal Motion, frequency = 16 and 64 Hz

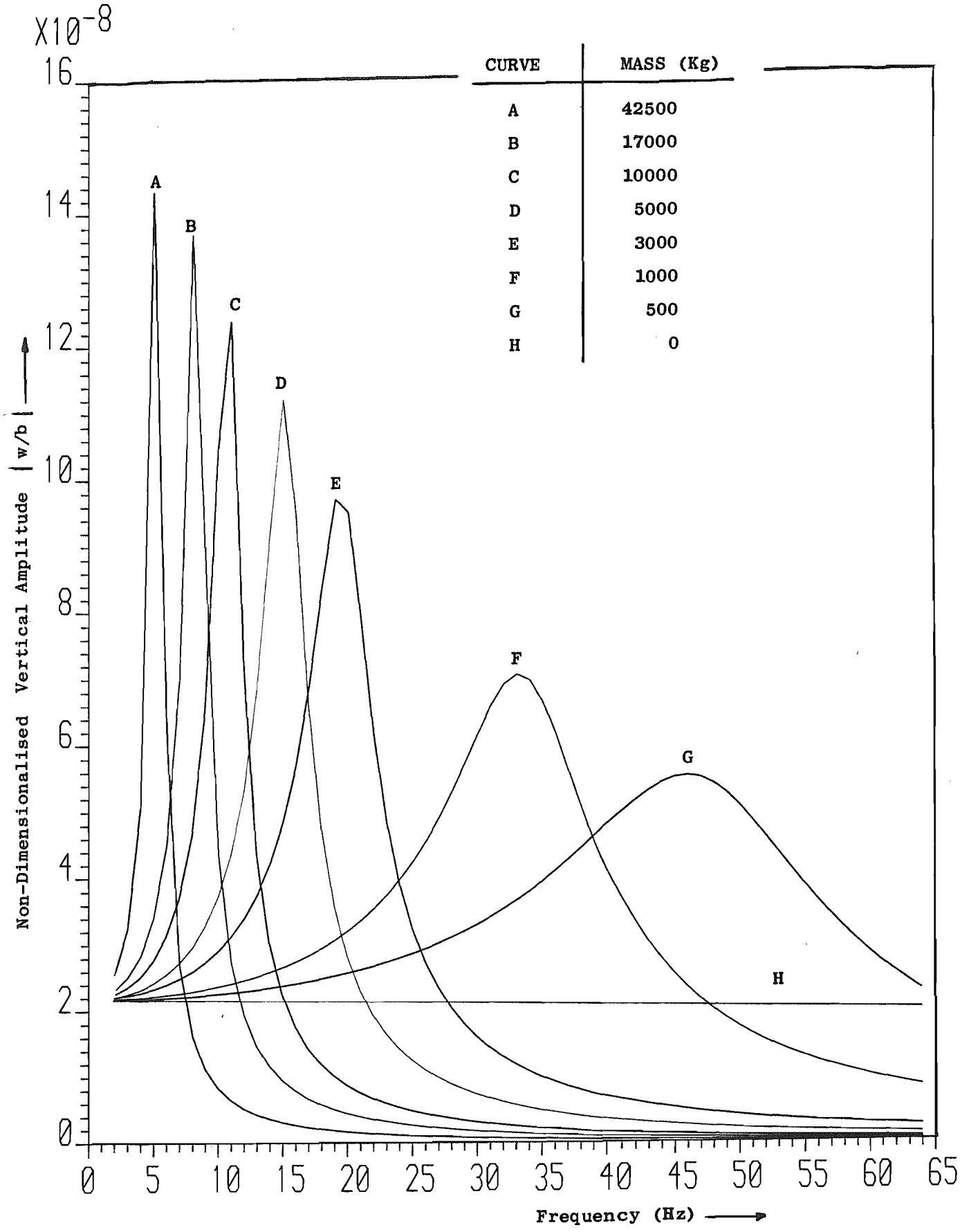

Fig 9.14: Direct Receptance at Centre of Rectangle, with Various Masses

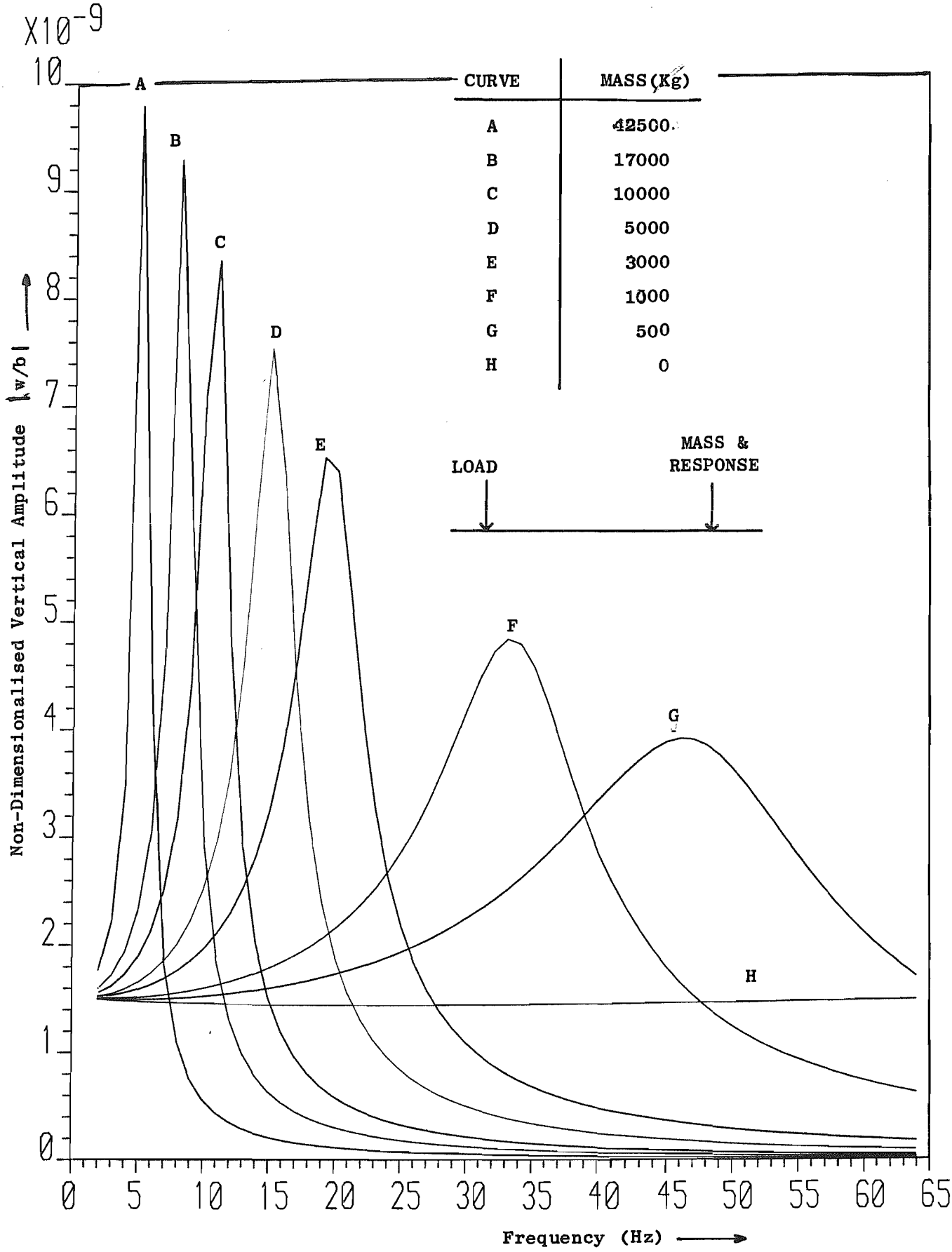

Fig 9.15: Transfer Receptance at x/b = 4, With Various Masses Placed There.

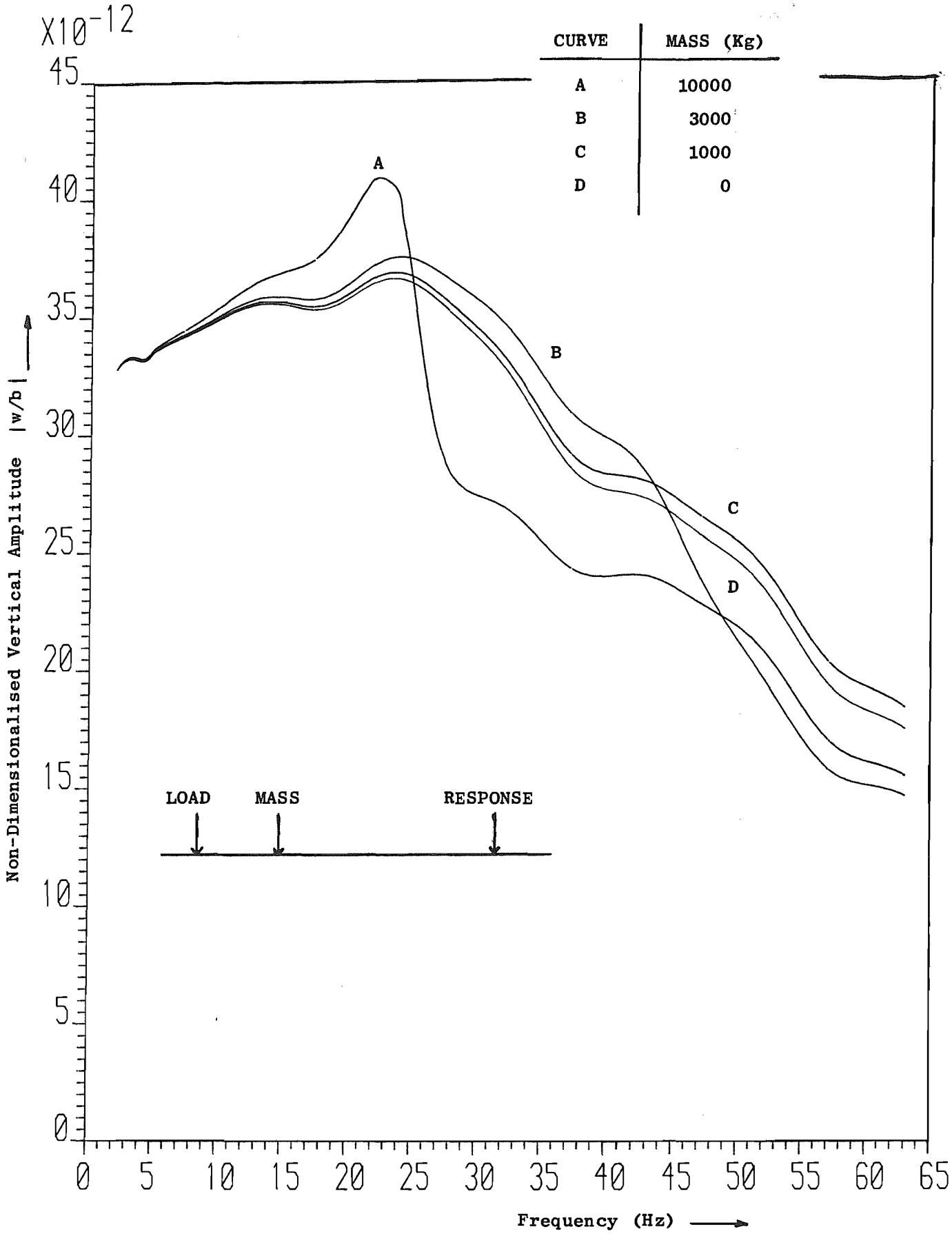

Fig 9.16: Transfer Receptance at x/b = 33.3, with various masses placed at x/b = 4

have calculated the direct receptances of circular bodies, resting on either 'bedrock' or 'elastic foundation' ground structures (the 'elastic foundation' is an elastic layer over an elastic half-space of different material properties), and comparison with the infinite strip load receptances for these ground structures reveals many similarities. It would be of value if a tentative extrapolation could be made from the surface vibration results for an infinite strip, acting on layered ground structures, to predict the effect of a finite strip on the same ground structures.

With the results in this Chapter, a useful comparison can be made beween these two different loads acting on the half-space ground structure. The relevant results for the infinite strip are contained in Chapters 3 and 8. Using Clarborough data, both the infinite and finite strips have a total width of 1.5 m, but the finite strip is only 25 cm long (in the y-direction). Figures 3.3(c) and 3.2(b) show plots of $\bar{u}$ and $\bar{w}$ against wavenumber ζ, for the infinite strip, with a frequency of 32 Hz and a loss factor $\eta = 0.002$. These can be compared with Figs. 9.2(c) and 9.2(a) respectively, which are for the rectangle (or finite strip) with $\eta = 0.02$. They are of exactly the same form, although, of course, this similarity of form does not imply that integration of the different $\bar{u}$ and $\bar{w}$ functions will produce results also of exactly the same form. Figures 9.2(a) and 9.2(c) are sections through a two dimensional surface, chosen to show maximum amplitudes, unlike Figs. 3.3(c) and 3.2(b).

Figures 9.3 to 9.7 in this Chapter have no equivalent in the infinite strip results. They are easy to interpret, and were discussed briefly in Section 9.4.3. Figures 9.8 and 9.11, however, can be compared with the corresponding displacement Figs. 3.4 and 3.5. It is clear, particularly in the high frequency horizontal motion, that a 'wavyness' of the same 'wavelength' exists in the corresponding figures. The probable reason for this is discussed in Section 9.5.2. A comparison of amplitudes under the different loads is possible, but it must be remembered that a total load 2π for Figs. 9.8 and 9.11 compares with a load 2π/unit length in Chapter 3. The displacement at $x = 0$ under the rectangle is approximately frequency independent, at least in the frequency range used here (curve H in Fig. 9.14 shows this). The equivalent variation of

amplitude, with frequency for the infinite strip, can best be seen in Fig. 8.5, curve H. Wei and Petyt [15] have shown that the static displacement of the infinite strip is infinite, and the asymptotic approach to an infinite value at zero frequency is suggested by Fig. 8.5. This is one reason why the response under the infinite strip is much larger than under the rectangle. Another reason is related to the different attenuation of the Rayleigh and body waves in the two models, which also explains why the vibrations from the rectangle are so much more attenuated with distance. The different "spreading" laws for plane and spherical waves are discussed in Section 9.5.2.

Figures 9.9, 9.10, 9.12 and 9.13, which show the change of phase with distance of vertical and horizontal motion, can be compared directly with Figs. 3.6 and 3.7. It is clear, comparing like frequencies, that the wavenumbers are very similar. The only readily noticeable differences are in the high frequency, horizontal phase change under the load, and also the 4 Hz horizontal phase change for the first half of the distance covered. As explained in Section 9.5.2, the lower frequency waves exhibit interference over a greater distance from the load, due to their longer wavelengths.

Figures 9.14 and 9.16 have their counterparts in Figs. 8.5 and 8.8. Because $b = 0.75$ m here, the dimensional distance 25 m used in Chapter 8 corresponds to $x/b = 33\ ^1/_3$. As noted in Chapter 8, by the symmetry of the receptance expressions, a rectangular mass placed at $x/b = 29^1/_3$ from the load, would cause exactly the same response at $x/b = 33^1/_3$ as shown in Fig. 9.16. Figure 9.15 does not have an equivalent figure in Chapter 8. The resonant frequencies in Figs. 9.14 and Fig. 8.5 cannot be expected to match, because in Fig. 8.5 the mass is per unit length, whereas here the mass acts over a strip only 25 cm long.

The difference in amplitude of the peaks is partly due to the difference in mass per unit length, and also because the static deflection of a rectangular load is finite. The curves marked 'H' in each Figure, which are for zero mass, emphasise this point.

Figures 9.16 and 8.8, which show the effect of placing a mass between the load and response point in the two models, have some common

features. In both cases, the largest mass placed at 3 m from the load, is effective in reducing vibrations for much of the frequency range, but also significantly increases the response for lower frequencies. Mass B has a similar effect, although the corresponding positive and negative effects (from the vibration isolation point of view) are both shifted to higher frequencies. All the characteristics of these infinite strip results are shifted to higher frequencies with the rectangular load.

9.5.2 Comparison of near-field displacement results with previous work

A significant feature of the graphs showing displacement amplitude plotted against distance, is a periodic "wavyness". This is most evident in the horizontal components, shown in Fig. 9.11. Exactly the same behaviour was found in the infinite strip results of Chapter 3. Few previous workers give displacement against distance graphs, but a similar periodic wavyness can be found in the results of Kuhlemeyer [43], Waas [79, the relevant results are for an embedded load over an inhomogeneous layer] and Gaul [19]. However, only Kuhlemeyer attempts to explain the phenomenon. He noticed that the wavelength of this apparent interference pattern in his results, equalled the wavelength of an "inhomogenous" wave (see Chapter 6 for a discussion of these waves) corresponding to one of the 'extraneous' roots of the Rayleigh wave equation. Since Rayleigh's original rejection of these 'extraneous' roots, they have been neglected by most subsequent workers. However, Fu and others (see Chapter 6) have shown how inhomogeneous waves could propagate in a half-space.

To test Kuhlemeyer's hypothesis, Rayleigh's equation [67] must be solved for Poisson's ratio $\nu = 0.257$, as at Clarborough. The equation is:

$$k^8 - 8k^6 + 24k^4 - 16k^2 - 16h^2k^2 + 16h^2 = 0 \qquad (9.69)$$

where Rayleigh's notation has been used, and effectively $h = c/c_1$, and $k = c/c_2$. Equation (9.69) can be reduced to a cubic in (k^2), because the ratio k^2/h^2 is known: following Rayleigh's method

$$\frac{k^2}{h^2} = \frac{\lambda + 2\mu}{\mu} \qquad (9.70)$$

Solving the cubic (for λ and μ at Clarborough) gives the roots $k^2 = 3.869$, 3.283 and 0.848, and as $k^2 = (c/c_2)^2$ and $c_2 = 262.7$ ms^{-1} for Clarborough (Table 6.1), it follows that the three solutions have the wavespeeds 516.7, 476.0 and 241.9 ms^{-1}. The third is known to be the Rayleigh wavespeed at Clarborough (Table 6.1). Consulting Fig. 9.11, it is easiest to estimate the 'wavelength' of the 64 Hz curve "wavyness": it is approximately $x/b = 11$, or dimensionalising for Clarborough, a wavelength $\lambda = 8.25$ m. At 64 Hz, the three solution wavespeeds above give wavelengths 8.07 m, 7.44 m and 3.78 m. Considering that the "wavelength" in Fig. 9.11 was estimated by inspection, the first wave has a very similar wavelength to the observed "wavyness". Kuhlemeyer used completely different material properties in his work, and so these results lend weight to his hypothesis.

Holzlöhner [31] has produced results for a rectangular load, acting on a half-space with no internal damping and zero Poisson's ratio. Although no direct comparisons cn be made because of these different material properties, some of his observations are of interest. He found that in the vicinity of the load, the resultant wavespeed was less than the theoretical Rayleigh wavespeed, despite the lack of internal damping in his model. This surprising interference effect is evident in the wavenumber resulting from the 4 Hz load, calculated from Fig. 9.12. Holzlöhner also finds that the near-field attenuation of the total motion is proportional to r^{-1}, but in the far-field it is proportional to $r^{-\frac{1}{2}}$. This has been confirmed experimentally by several workers [58,88]. This shows that the Rayleigh wave only dominates the response in the far-field. Barkan [5] predicts interference effects near the source, from consideration of the asymptotic expressions which describe the body and Rayleigh waves. The O.R.E. Committee [28] analysis is quantitative, and finds that in the range $r/\lambda_p < 0.5$, where λ_p is the compression wavelength, the Rayleigh wave does not contribute more to the total response than the body waves. This is because the body waves' amplitudes are proportional to r^{-2}, whereas the Rayleigh wave amplitude is proportional to $r^{-\frac{1}{2}}$. For Clarborough, and the frequencies 4, 16, 32 and 64 Hz, $(\lambda_p/2b) = 76.5$, 19.12, 9.56 and 4.78 respectively. In Fig. 9.11,

this change at $r = 0.5\lambda_p$ is marked by an inflection in the 16, 32 and 64 Hz curves. This partly explains the behaviour of the 64 Hz curve in Fig. 9.8: the other frequency amplitudes will also drop below the 4 Hz curve, at greater distances from the load (see Table 9.3). The greater effect of the hysteretic damping on the higher frequencies is also important [28], as can be seen clearly in the infinite strip attenuation figures (Chapter 3).

9.5.3 The direct and transfer receptance Figures, and the effect of a mass

The direct receptance graph (Fig. 9.14) is of a form which affords the greatest comparison with previous work. Similar receptance graphs can be found in [4,39,61,69,70,79]. The degree to which the resonant frequency, for a given mass, in this work and these references coincides, depends on the model used. A rigid disc, for example, behaves somewhat differently from the "flexible" rectangle used here. Chae [11] has studied the effect of varying the load shape, and deduced that in comparing disc- and rectangular-shaped loads, an "equivalent radius" based on an equivalent perimeter is superior to one based on equal area. For example, therefore, the "equivalent radius" of the (1.5 m × 0.25 m) rectangle is

$$R_{eq} = \frac{3.5}{2\pi} = 0.557 \qquad (9.71)$$

A radius based on equal area would be

$$R'_{eq} = \left(\frac{1.5 \times 0.25}{\pi}\right)^{1/2} = 0.345 \qquad (9.72)$$

The implication of equations (9.71) and (9.72) is that a rectangular load will cause a bigger displacement than a circular load of the same area.

As an example of the application of this "equivalent radius", consider the expression given by Richardson [69] for the surface static vertical displacement of a rigid disc:

$$w(r,0) = \frac{-P}{8\mu R(1-\gamma^2)} \qquad (9.73)$$

This expression is for $\nu = 0.0$, but Luco and Westmann [51] have shown that for $0 < \nu < 1/3$, the direct receptance does not change greatly. P = the total load, R = the disc radius, and $\gamma = c_2/c_1$. Using the Clarborough data, and with $R = R_{eq} = 0.557$ for the rectangle, gives $w(0,0) = 1.31 \times 10^{-8}$. Figure 9.14 shows this is about 60% less than the static value obtained here, for a "flexible" rectangle. It seems logical that the rigid load should deflect less at its centre than a "flexible" one for a given force. However, using the value $R_{eq}' = 0.345$ gives a value $w'(0,0) = 2.11 \times 10^{-8}$, which is very close to the static value obtained here. Although caution is required when using equation (9.73) with an "equivalent radius", these values suggest that R_{eq} is a better measure than R_{eq}'.

This conviction is supported by application of an expression due to Converse, given by Balakrishna and Nagaraj [66]. This expression predicts the resonant frequencies of a circular load–foundation system, and is

$$f_m = 3.13(840\,\frac{\rho}{\mu}(1.64 - \frac{\sigma_F}{\sigma_W}) + \frac{0.18\mu}{\sigma_W R})^{1/2} \qquad (9.74)$$

where ρ = density in lb/cu.ft.; μ = shear modulus in lb/sq.in.; σ_F and σ_W are, respectively, the unit dynamic force and unit dead load, in lb; and R is the radius of the load in inches. Using Clarborough data, and making the necessary conversions of units, it is found that the second product under the square root sign dominates the first, so that the value of R is important. Using $R_{eq} = 0.557$ m, equation (9.74) becomes:

$$f_m \simeq \frac{1016}{\sqrt{m}} \qquad (9.75)$$

where m is the mass at the load, in kg. For comparison, using $R_{eq}' = 0.345$ gives

$$f_m' \simeq \frac{1292}{\sqrt{m}} \qquad (9.76)$$

For the masses used here, the resonant frequencies predicted by equations (9.75) and (9.76) are tabulated in Table 9.4, with the resonant frequencies measured from Fig. 9.14 (denoted F_m).

Mass (kg)	f_m (Hz) based on R_{eq}	f_m' (Hz) based on R_{eq}'	F_m (Hz) measured in Fig. 9.15
500	45.4	57.8	46
1000	32.1	40.9	33
3000	18.5	23.6	19
5000	14.4	18.3	15
10000	10.2	12.9	11
17000	7.8	9.9	8
42500	4.9	6.3	5

Table 9.4: Resonant frequencies

Clearly, R_{eq} in equation (9.74) gives a better prediction than R_{eq}'.

The order of error beween the f_m' and F_m values is interesting, because it is similar to that between the results in this Chapter and those of rigid discs, as found by Robertson, Awojobi and Grootenhuis, and Waas [70,4,79] respectively. This is consistent with the experimental work of Chae, who found that a mass on a rectangular area has a lower resonant frequency than the same mass on the same area, but circular.

Kobori, Minai and Suzuki [39] are the only workers to consider the effect on static displacement, of changing the ratio c/b which defines the rectangle dimensions. Using Kelvin-Voigt damping, they plot the non-dimensionalised vertical amplitude function:

$$\bar{f}_{sv} = \frac{W_o b_v \mu}{P_v} \qquad (9.77)$$

where W_o = the vertical displacement at the centre of the load in metres, $b_v = (bc)^{1/2}$ (m), and P_v = the total load in N. Hence, for Clarborough and the results shown (Fig. 9.14)

$$\bar{f}_{sv} = \frac{\{(2.2 \times 0.75) \times 10^{-8}\} \times \{0.306\} \times \{1.07 \times 10^{8}\}}{\pi} = 0.17$$

Figure 5(a) in [39] gives the variation of $\bar{f}_{sv}$ with (c/b), and it is clear that 0.17 is close to the value given for c/b = 6, as used here.

Richardson, Warburton and Webster [69] have studied the effect on a circular body of a vibrating load beside it, with $\nu = 0.25$. They have found that the body can be strongly excited, as is found in the results

of Fig. 9.15. It is clear from Fig. 9.16 that, as with the infinite strip load results of Chapter 8, the effect of a mass placed beteen the load and the response point is complicated. Fig. 9.15 suggests that for the 10,000 kg and 3000 kg masses, the amplification of response in Fig. 9.16 (seen by comparison with curve D for zero mass) is for a range of frequencies above the resonant frequency of the mass. Curves C and D indicate that for the frequency range considered, a small mass is of no use as an isolator. If the frequency range around 10 Hz is of most nuisance, these results do not suggest an isolation mass near the load (or, by symmetry, near the response point) will be very effective. However, if higher frequencies are exciting a structure at some distance, a 'large' mass placed near the load might reduce the vibration at the structure.

CHAPTER 10

CONCLUSIONS

10.1 Summary

The aim of this work was to gain some understanding of the propagation of ground vibration produced by trains. No attempt was made to model the train load accurately. The source of vibration was idealised as uniform, harmonically varying vertical pressure, acting over either an infinite strip or a rectangle. The infinite strip load was modelled as acting on either a half-space, a layer over an inflexible half-space, or a layer over a flexible half-space. The rectangular load was modelled as acting on a half-space. In all cases, the ground was idealised as homogeneous, isotropic and elastic, and material damping was included. Computer programs were developed to find numerical approximations to the surface displacements, in the vicinity of the load. To help interpret the results for the two layered ground structures, free vibration analysis was performed to investigate the natural propagating modes. The effect of isolation masses placed at the load, or beween the load and response point, was studied for each model.

10.2 Free Vibration in a Layer

10.2.1 The bedrock model (Chapter 4)

A linearised dynamic stiffness matrix for the bedrock model was used to study the behaviour of the natural propagating modes in the layer. Computer programs were developed which solve this matrix formulation as an eigenvalue problem, resulting in the dispersion curves and modeshapes. It was found that below a certain frequency, no propagation of vibration could occur. The first mode corresponds to the Rayleigh wave at sufficiently high frequency, and the other modes tend to the shear wavespeed with increasing frequency. At discrete frequencies which equal the natural frequencies of a one-dimensional rod, having the same "fixed-free" boundary conditions and height as the layer, pairs of

dispersion curves cross. Additionally, for a small range of frequency, the fourth mode dispersion curve is double-valued. All these frequencies are marked by an increased forced response (Chapter 5), in particular at the frequency where the first two modes' dispersion curves intersect. This important frequency is identical to the fundamental longitudinal frequency of the one-dimensional rod.

10.2.2 The elastic foundation model (Chapter 6)

The exact dynamic stiffness matrix for the elastic foundation model was solved as an eigenvalue problem, using a technique due to Wittrick and Williams [89] which overcame the non-linearity of the matrix. This gave the dispersion curves of the natural propagating modes in the layer, for all real wavenumbers. The period equation for the layer was derived, and used to find the mode shapes. These solutions were found using computer programs developed for this purpose. It was found that for $(\zeta d) > 25$, where ζ is wavenumber and d the layer depth, the dispersion curves are close to those of Newlands [54], as given by an approximate expression valid at large (ζd). As with the bedrock model the first mode corresponds to the Rayleigh wave at sufficiently high frequency, and the other modes approach the shear wavespeed as frequency increases. However, no dispersion curve is double-valued, and no two curves cross. It was found that certain modes contribute most to the forced response (Chapter 7), at frequencies just above the onset of their "leaky" phase. This is particularly true of the fourth mode.

10.3 Forced Response: Plane Problems

10.3.1 The half-space model (Chapter 3)

The theory was developed to analyse an infinite strip load acting on a half-space. The solution for the surface displacements involved the Fourier transformation of equations to the wavenumber domain. The inverse transformation was effected numerically, using a computer program which incorporated a library routine. The results show the behaviour of the transformed displacements, which are dominated by peaks at the Rayleigh, shear and compression wavenumbers, and the amplitude and phase change in the near-field of the actual displacements. The effect on the

displacements of varying the loss factor η has been studied. Although the Rayleigh wave dominates the response, interference patterns due to the effect of the body waves, and also behaviour associated with the extraneous roots of the Rayleigh equation, are evident. This interference means that for low η, the low frequency components will not necessarily dominate near the load.

The effect of varying the strip width, with constant stress per unit width, has been investigated. An attempt has been made to explain the peak response at certain widths, by calculating the "resultant wavelength" of the three propagating waves.

10.3.2 The bedrock model (Chapter 5)

Because a direct extension of the half-space model solution method to the bedrock model would involve computational overflow, an alternative method to find the surface displacements on the layer was used. This involved deriving the exact dynamic stiffness matrix for the layer, in the transform domain. To avoid overflow, the stiffness matrix was assembled for a layer divided into two sub-layers. The inverse transformation of the transformed displacements was achieved using the same method as for the half-space model, incorporated into a different computer program. Graphs of the transformed displacements show peaks at certain wavenumbers, which have been related to the wavenumbers of the natural propagating modes (Chapter 4). A large resonance was found at a frequency which matches the intersection frequency of the first two modes' dispersion curves (Chapter 4). This resonance was compared with a similar resonance described in other work. The near-field amplitude and phase variation of displacements were found, and the effect on attenuation of varying the damping was studied. The amplitude of vibration exhibits maxima and minima, and these peaks and troughs are related to local variations in the wavenumber (or rate of change of phase). Decreasing the damping makes the interference effects more pronounced. As with the half-space model, the effect of varying the strip width was studied, and similar behaviour to the former model was found.

10.3.3 The elastic foundation model (Chapter 7)

The previously derived exact dynamic stiffness matrix for the bedrock model, was combined with the easily derived (2 × 2) stiffness matrix for the half-space, to give the equivalent matrix for the elastic foundation model. A computer program was developed to numerically approximate the surface displacements, using an approach similar to the bedrock model solution. The wavenumber-locations of peaks in the graphs of transformed displacement, were related to the wavenumbers of the natural propagating modes (Chapter 6). The near-field displacements show interference effects of a form similar to the bedrock model results, and decreasing damping again accentuates these effects. As before, low damping can allow the higher frequency components of the vibration to dominate near the load. The receptance graphs show that the fourth propagating wave (which is related to the free vibration fourth mode) causes a pronounced peak in the forced response. This occurs at the frequency for which the fourth wave's speed is just below the shear wavespeed in the under-laying half-space.

Also in Chapter 7, graphs are presented which compare the results of the three ground structure models.

10.4 Forced Response: Rectangular Load on a Half-Space (Chapter 9)

The problem of a rectangular load on a half-space was studied, by solving Navier's elastodynamic equations in three dimensions. The solution method involved a double Fourier transform, and the double inverse transformation was performed numerically using a developed computer program, which incorporates a library routine. The results include sections and surfaces of the transformed displacements in the wavenumber domain, which show most of the information centred on the Rayleigh, shear and compression wavenumbers. Graphs showing the near-field amplitude and phase of displacement were presented. The results were checked by comparison with earlier related work, and close agreement was found. An interference effect due to waves connected with the extraneous roots of the Rayleigh equation was noted. The results were compared with those for the infinite strip on the half-space.

It was found that because of the different "spreading laws" for the body and Rayleigh waves, and also the interference between these waves, the higher frequency components of the propagating waves produce larger displacements near the load, than the low frequency components. For this reason, asymptotic expressions for the far field cannot accurately describe the near-field displacements.

10.5 The Effect of Masses Placed on the Ground's Surface (Chapters 8 and 9)

The effect on surface vibrations of masses placed on the ground's surface was investigated for the infinite strip load acting on all three ground structure models, and for the rectangular load acting on a half-space. The intention was to predict the effectiveness of isolation masses. The theory of receptances was used to generate results showing direct and tranfer receptance. Principally, the effect on the response 25 metres from the load was studied, with one or two masses placed at various locations. A symmetry was found in the results, such that a mass placed at x metres from the load ($x < 25$), produced the same displacement at 25 metres as a mass placed $(25 - x)$ metres from the load. It was found that a small mass is an ineffective isolator, but that a large mass significantly increases the response for part of the frequency range. The effectiveness of the masses as isolators is sensitive to their location, and two masses do not necessarily reduce vibration at 25 m any more than a single mass. The optimal choice of isolation mass, for practical purposes, is probably a single large mass placed near the load. However, this is also a function of the most sensitive frequency range at the response point.

It was found that with increased distance from the load, the receptance peaks for the layered models shifted to slightly higher frequencies. For the bedrock model, this "frequency-shift" was found to be in accordance with an empirical relation. For the rectangular load on a half-space, the location of the direct receptance peaks agree with an expression given by earlier workers.

10.6 Possible Further Work

An extension of this work would be to study the effect of a rectangular load on a layered ground structure. The three- dimensional dynamic stiffness matrix for the bedrock model could be derived, and then combined with the work of Chapter 9 to give the equivalent matrix for the elastic foundation model. These matrices would be formulated in the wavenumber domain, and the required inverse transformation could be achieved as for the half-space model.

The mathematical models of the train vibration problem used here are strongly idealised. Ultimately, a model must be found which incorporates (i) the track design, (ii) the train vehicle characteristics, (iii) the movement of the train, and (iv) the ground properties. This work has incorporated the fourth feature, but the load was modelled as a single, stationary, harmonic area of uniform stress.

It is likely that the Finite Element Method is the best available technique for modelling the track design, which may include embankments, for example.

APPENDIX A

DESCRIPTION OF THE NUMERICAL INTEGRATION SUBROUTINE

A.1 Background

If an integral $I_w[a,b]_f$ is expressed as

$$I_w[a,b]_f = \int_a^b w(x)f(x)dx \qquad (A.1)$$

where $w(x)$ is called the "weighting function" , then its quadrature sum $Q_n[a,b]_f$ can be written

$$Q_n[a,b]_f = \sum_{i=1}^{n} w_i f(x_i) \simeq I_w[a,b]_f \qquad (A.2)$$

where the w_i are termed "weights" and the x_i are the abscissae at which the function $f(x)$ is evaluated. A quadrature sum is of 'degree of precision' d if it is exact for all functions $f(x)$ which are polynomials of degree $\leq d$ (see Ref. [64]). Quadrature sums which use equidistant abscissae for the function evaluations are well-known. An example is Simpson's Rule, which is a special case of the Newton-Cotes formula (see [35], for example), and which is given in Chapter 9. If n abscissae are used, its degree of precision is $d = n - 1$. For the well-behaved functions integrated in Chapter 9, this is adequate.

However, in general, "Gaussian" quadrature offers a much more efficient method of numerical integration. Gaussian quadrature uses abscissae which, rather than being equidistant, are at the zeroes (or "roots") of orthogonal functions. With a correct choice of the weights w_i, $d = 2n - 1$ is possible, by using all $(2n)$ degrees of freedom inherent in n weights and n abscissae. The weights of the Gaussian quadrature formulae, H_{ni}, are given by equation (A.3):

$$H_{ni} = \frac{1}{Q_n'(x_i)} \int_a^b \frac{w(x)Q_n(x)}{(x - x_i)}\, dx \qquad (A.3)$$

The constants H_{ni} are also known as the "Christoffel numbers". $Q_n(x)$ is an orthogonal polynomial of degree n, and $Q_n'(x)$ is its derivative w.r.t. x. The simplest example of these formulae is the Gauss-Legendre formula, for which $w(x) = 1$, and the abscissae are given by the roots of the n'th Legendre polynomial, $P_n(x)$, where

$$P_n(x) = \sum_{k=0}^{N} \frac{(-1)^k(2n - 2k)!}{2^n k!(n - k)!(n - 2k)!} x^{n-2k} \qquad (A.4)$$

$N = n/2$, n even; $N = (n - 1)/2$, n odd.

The orthogonality interval is then $-1 \leq x \leq 1$, and equations (A.2) and (A.3) give

$$\int_{-1}^{1} f(x)dx \simeq \sum_{i=1}^{n} H_{ni} f(x_i) \qquad (A.5)$$

and

$$H_{ni} = \frac{2(1 - x_i^2)}{n^2 P_{n-1}^2(x_i)} \qquad (A.6)$$

Note that the range of integration in equation (A.1) can, if necessary, be changed from $a \leq x \leq b$ to $-1 \leq x \leq 1$, by substituting variables:

$$\int_a^b f(x)dx \equiv \frac{b - a}{2} \int_{-1}^{1} f[x(t)]dt, \qquad t = \frac{2(x - a)}{b - a} - 1 \qquad (A.7)$$

Equation (A.6) is derived using the properties of the Legendre polynomial [6].

In practice, an estimate of the error inherent in a quadrature approximation is required. The usual method is to compute the approximate value of the integral using two separate quadrature formulae of different degree, and then assume that the error is of the

same order as the difference between the two results. Kronrod [42] justifies this method on the basis of experience. This need for an error check reveals a drawback in the Gaussian sequence of formulae. Because the Gaussian formulae do not share common abscissae (except for the mid-point when n is odd), the sequence is said to be "unnested". As a result, many function evaluations are necessary to estimate the error.

However, for each Gaussian formula it is possible to add a specific set of abscissae, to produce a new formula which is "nested" with the original one. If $n = m + 1$ abscissae are added to an m-point rule, then a degree of precision $d = 3m + 1$ can be achieved. The method of finding this "optimal extension" for the Gauss-Legendre formula (equations (A.5) and (A.6)), and the resulting formulae, are given by Kronrod [42], after whom the formulae are named. The Gauss-Legendre and Kronrod formulae together provide an economical way of simultaneously approximating the integral and the error.

A.2 The Problem

The numerical integration performed in this work is of the inverse Fourier transforms, and the integration range is therefore $-\infty < \gamma < \infty$, where γ is the wavenumber. As explained in Section 9.3, the integration can be reduced to the limits $0 \leqslant \gamma \leqslant \gamma_c$, because of the symmetry of the integrand functions, and because most of the information is concentrated at low wavenumber, below γ_c. The problem reduces to solution of integrals of the form:

$$\int_0^{\gamma_c} w(x)G(x)dx, \qquad G(x) = \sin\gamma x \quad \text{or} \quad \cos\gamma x \qquad (A.8)$$

The function $w(x)$ represents either the real or imaginary part of horizontal or vertical transformed motion. $w(x)$ is always well-behaved, as can be seen in the relevant Figures (for example, Figs. 9.2 and 9.3). The numerical integration is therefore only complicated by the oscillation due to $G(x)$. The three-dimensional formulation of the problem involves a double Fourier transform, but

because only the displacements along $y = 0$ are sought, the oscillation is restricted to just the first of the two integrations (see Chapter 9). Three principle methods have been used by previous workers in this field to deal with oscillating integrals. Gazetas [21], for example, uses the Fast Fourier Transform. Although this does not take advantage of the symmetry and generally good behaviour of the integrands, it is still effective because of its great efficiency. Richardson [68], among others, uses techniques due to Longman [47,48], which give approximate solutions to finite and infinite oscillating integrals. These are particularly appropriate if computing time or storage are limited. For an integral of the form

$$I = \int_a^\infty g(x)dx \qquad (A.9)$$

where $g(x)$ oscillates about zero and converges to a finite limit, Longman first expresses the integral as a sum of integrals with the roots of $g(x)$ as the integration limits, so that

$$\int_a^\infty g(x)dx = (\int_a^{x_1} + \int_{x_1}^{x_2} + \int_{x_2}^{x_3} + \ldots)g(x)dx \qquad (A.10)$$

where the x_k are the roots of $g(x)$. By using a transformation due to Euler, Longman transforms this convergent series of integrals into a much faster converging series. A modification of this method also allows the approximate solution of finite integrals.

An alternative approach, used by Luco [52] and others, is Filon's method. Given an integral of the form in equation (A.8), Filon's idea is to approximate the function $w(x)$ by an n'th order polynomial. Substituting this polynomial into equation (A.8), the approximate integral can then be found by direct integration.

The resulting Filon's formula, for $G(x) = \sin\gamma x$, is of the form [17]:

$$\int_a^b w(x)\sin\gamma x dx = h\{\alpha w(a)\cos a\gamma - \alpha w(b)\cos b\gamma + \beta S + \zeta T\} + R_n \qquad (A.11)$$

where h is the quadrature increment, such that

$$2nh = b - a \qquad (A.12)$$

and α, β, ζ, S, T and R_n are functions of a, b, h and γ. The remainder term R_n gives an indication of the error.

The oscillating integrals in this work have been approximately evaluated using a NAG library routine, called D01ANF. It is essentially a refinement of Filon's approach, as its method involves a numerical approximation of $w(x)$, linked with a direct integration. The NAG library has been used as a programming convenience, and an approach based on Filon's method was preferred to the other two approaches mentioned, firstly to take advantage of the integrand's characteristics, and secondly because computer time and storage were not at a premium.

The routine is an adaptation of the subroutine DQAWF, developed by Piessens *et al* [64], who list the program. An earlier, similar program is described and listed by Piessens and Branders [63]. The method of numerically approximating the function $w(x)$ depends on the length of the quadrature sub-intervals. If the exact integral is given by equation (A.8), and the sub-interval is denoted 'L', then define

$$L = \gamma_c 2^{-\ell} \qquad (\gamma_c > 0) \qquad (A.13)$$

Provided $L\gamma_c > 4$ and $\ell \leqslant 20$ (A.14)

the approximation is made with a Chebyshev series of degree 24, with an error estimate obtained with a series of degree 12.

The Chebyshev series can be defined by the following relation:

$$T_n(x) = \cos(n \arccos x) \qquad (A.15)$$

If the conditions given in equation (A.14) are not met, then Kronrod 15-point and Gauss 7-point rules are used, for the numerical integration and error check respectively. This course is most likely near the sharper peaks of the functions $\bar{w}$ and $\bar{u}$ (see, for example, Fig. 9.2).

The routine is "adaptive", i.e., the abscissae can be changed with each subsequent iteration. The user specifies the acceptable error, in both relative and absolute terms, and the subroutine repeats the quadrature with increasingly more abscissae, until the "weaker" accuracy requirement is met.

In those programs in Appendix B which use the routine, the integration range is divided at a point γ_d, and the routine is applied twice, with the limits $0 \leq \gamma \leq \gamma_d$, $\gamma_d < \gamma \leq \gamma_c$. γ_d is chosen so that for $\gamma > \gamma_d$, the integrands are without peaks, so increasing the total efficiency.

A.3 Parameters Required by NAG Routine D01ANF

```
SUBROUTINE D01ANF(G,A,B,OMEGA,KEY,EPSABS,EPSREL,RESULT,
?ABSERR,W,LW,IW,LIW,IFAIL)
EXTERNAL G
```

D01ANF finds a numerical approximation to $\int_A^B G(x)W(x)dx$, where

W(x) is either sinωx or cosωx. In calling the routine, G is a REAL FUNCTION G(X), X also REAL. A and B define the REAL limits of integration. OMEGA ≡ ω. If KEY = 1, then W(x) = cosωx, and if KEY = 2, W(x) = sinωx. EPSABS and EPSREL are the user defined absolute accuracy and relative accuracy, respectively. RESULT will contain the approximation to the integral, and ABSERR will contain an upper bound for the absolute error. W(LW) is a work-space array, where LW/4 is an upper bound for the number of sub-intervals required. IW(LIW) is also a work-space array, with LIW ≥ LW/8 + LW/4 +2. IFAIL takes its usual definition and in each application of D01ANF in this work, IFAIL=0.

APPENDIX B

KEY COMPUTER PROGRAMS

B.1 Introduction

Seven programs are listed in this Appendix, all in the Fortran language. Each is preceded by some brief notes. Some of these can be used to reproduce certain Figures in this work, while others calculate data which can contribute to producing other Figures. Those Figures not included in these two sets can be reproduced with very similar programs, and the necessary alterations are described in each set of notes. The NAG routine D01ANF, which is used in several programs, is described in Appendix A.

The programs require access to either or both of the NAG library of subroutines, and the GINOGRAF graph plotting system. This is mentioned in the notes where appropriate. Those variables which can be changed, to vary the material properties, load frequency, etc. are listed in an Inputs section of each set of Notes. Additional information is included which could be useful for modifying the programs.

The output of each program is also briefly explained.

B.2 Program HSWM4F

This program relates to the half-space model work of Chapter 3, and the variables have dimensions. This version of the program uses 200 points to plot the vertical and horizontal amplitudes of motion, for $x < 25$ m, and a frequency 4 Hz.

In order to produce plots in the wavenumber domain, such as Figs. 3.2 and 3.3, it is necessary to replace the integration loop which begins at line 29, with a loop which calls FUNCTION G(ZETA) directly, and which varies ZETA rather than X. In this way values of first $\bar{w}$ and then $\bar{u}$ (for INDICATOR=1) can be calculated. These values can be stored in arrays, ready to be plotted using SUBROUTINE GRAPH.

To produce the "width-variation" graphs in Fig. 3.10, it is necessary to (i) replace the X variation in the integration loop by a variation of width, also to be stored in an array, say WID(40) - 40 points were used for Fig. 3.10; (ii) replace X(NX) in the calls to DO1ANF by 0.0; (iii) make WIDTH become COMMON to the program and FUNCTION G; (iv) change the definition of PRS at label 168 in G(ZETA) to:

```
PRS = -SIN(ZW)/(ZETA*0.75),
```

where 0.75 is the strip half-width used for Clarborough.

To produce the receptance graphs in Chapter 8, the frequency rather than the distance must be varied in the integration loop. In each call to DO1ANF, X(NX) is replaced by the distance of interest.

Requires GINOGRAF and the NAG library.

Inputs (Variable Parameters)	Comments
FREQ	The frequency of the harmonic load (Hz)
E	Young's modulus, Nm^{-2}
RHO	Density, kgm^{-3}
VNU	Poisson's ratio
DAMP	Half the loss factor, $\eta/2$
In FUNCTION G(ZETA):	
WIDTH	The total strip width, 2a
PRS	The definition at label 168 of this term which is the transformed stress at the load, implies the scaling $P/2\pi = 1$.

Additionally, the range of κ covered can be changed at lines 31 and 50, where the range is defined as 25.0. If the frequency FREQ is increased, then in each call to DO1ANF (there are four in total), the number '1.5' should be increased accordingly, in order that it should be several times greater than the Rayleigh wavenumber at the new frequency.

Output

For each value of X(NX), and for each of the vertical and horizontal components of motion, the four estimates of the maximum error inherent in the applications of D01ANF are printed. A graph is produced, showing the variation with distance of the vertical and horizontal amplitudes of motion, using a different colour for each component.

PROGRAM HSWM4F

```
C  HSWM PLOTS THE MODULI OF VERTICAL AND HORIZONTAL MOTION AGAINST X.
      COMPLEX MU,LAMBDA,C1,C2,K1,K2
      DIMENSION WM(200),WP(200),X(200),WR(200),WI(200)
     ?,TW(6000),IW(2500)
      COMMON K1,K2,MU,LAMBDA,INDICATOR,KEY1
      EXTERNAL G
      CALL CC036N
      FREQ=4.0
      E=2.69E08
      RHO=1550.0
      VNU=0.257
      ALAM=(VNU*E)/((1.0+VNU)*(1.0-2.0*VNU))
      AMU=E/(2.0*(1.0+VNU))
      AC1=SQRT((2.0*AMU+ALAM)/RHO)
      AC2=SQRT(AMU/RHO)
      DAMP=0.05
      AA=SQRT(0.5*(1.0+SQRT(1.0+4.0*DAMP*DAMP)))
      MU=CMPLX(AMU,0.0)*CMPLX(1.0,(2.0*DAMP))
      LAMBDA=CMPLX(ALAM,0.0)*CMPLX(1.0,(2.0*DAMP))
      C1=CMPLX(AC1,0.0)*CMPLX(AA,(DAMP/AA))
      C2=CMPLX(AC2,0.0)*CMPLX(AA,(DAMP/AA))
      OMEGA=6.283185308*FREQ
      K1=OMEGA/C1
      K2=OMEGA/C2
      WMAX=0.0
      DO 100 NKEY=1,2
      KEY1=NKEY
      KEY=NKEY
      DO 75 NX=1,200
      XN=FLOAT(NX)
      X(NX)=(XN-1.0)*25.0/199.0
      INDICATOR=0
      CALL D01ANF(G,0.0,1.5,X(NX),KEY,10E-18,10E-6,BWRCOS1,ABSERR1,
     ?TW,6000,IW,2500,0)
      CALL D01ANF(G,1.5,20.0,X(NX),KEY,10E-18,10E-6,BWRCOS2,ABSERR2,
     ?TW,6000,IW,2500,0)
      INDICATOR=1
      CALL D01ANF(G,0.0,1.5,X(NX),KEY,10E-18,10E-6,BWICOS1,ABSERR3,
     ?TW,6000,IW,2500,0)
      CALL D01ANF(G,1.5,20.0,X(NX),KEY,10E-18,10E-6,BWICOS2,ABSERR4,
     ?TW,6000,IW,2500,0)
      WR(NX)=2.0*(BWRCOS1+BWRCOS2)
      WI(NX)=2.0*(BWICOS1+BWICOS2)
      WM(NX)=SQRT(WR(NX)**2+WI(NX)**2)
      IF(WM(NX).GT.WMAX)WMAX=WM(NX)
      WRITE(6,90)ABSERR1,ABSERR2,ABSERR3,ABSERR4
90    FORMAT(//,1X,4(E11.5,1X),/,1X,4(E11.5,1X))
75    CONTINUE
      IF(NKEY.EQ.2)GOTO 105
      CALL GRAPH(250.,125.,0.0,25.0,0.0,WMAX,26)
105   IF(NKEY.EQ.2)CALL PENSEL(2,0.1,2)
      CALL GRACUR(X,WM,200)
100   CONTINUE
      CALL DEVEND
      STOP
      END
      SUBROUTINE GRAPH(A,B,C,D,E,F,I)
      CALL AXIPOS(1,30.,30.,A,1)
      CALL AXIPOS(1,30.,30.,B,2)
      CALL AXISCA(1,I,C,D,1)
      CALL AXISCA(1,I,E,F,2)
```

```
      CALL AXIDRA(2,1,1)
      CALL AXIDRA(-2,-1,2)
      RETURN
      END
      FUNCTION G(ZETA)
      COMPLEX K1,K2,ALPHA,BETA,T(2,2),MU,LAMBDA,Y1,Y2,Y3,Y4,
     ?TMZ,B(2,2),TINV(2,2),RD,R(2,2),ZK1,ZK2,BARW
      COMMON K1,K2,MU,LAMBDA,INDICATOR,KEY1
      WIDTH=1.5
      ZK1=ZETA*ZETA-K1*K1
      ZK2=ZETA*ZETA-K2*K2
      ALPHA=CSQRT(ZK1)
      BETA=CSQRT(ZK2)
      TMZ=2.0*MU*ZETA
      Y1=TMZ*ZETA-(LAMBDA+2.0*MU)*K1*K1
      Y2=-TMZ*ALPHA
      Y3=-TMZ*BETA
      Y4=-TMZ*ZETA+MU*K2*K2
      A=REAL(Y2)
      BB=REAL(Y3)
      C=IMAG(Y2)
      D=IMAG(Y3)
      T(1,1)=Y1
      T(2,1)=CMPLX(-C,A)
      T(1,2)=CMPLX(-D,BB)
      T(2,2)=Y4
      B(1,1)=CMPLX(0.0,ZETA)
      B(2,1)=-ALPHA
      B(1,2)=BETA
      B(2,2)=CMPLX(0.0,ZETA)
      RD=T(1,1)*T(2,2)-T(1,2)*T(2,1)
      TINV(1,1)=T(2,2)/RD
      TINV(2,2)=T(1,1)/RD
      TINV(1,2)=-T(1,2)/RD
      TINV(2,1)=-T(2,1)/RD
      DO 9995 I=1,2
      DO 9995 J=1,2
      R(I,J)=CMPLX(0.0,0.0)
      DO 9995 K=1,2
9995  R(I,J)=R(I,J)+B(I,K)*TINV(K,J)
      ZW=ZETA*WIDTH*0.5
      IF(ZETA.LT.10E-7)GOTO 167
      GOTO 168
167   PRS=-1.0
      GOTO 169
168   PRS=-SIN(ZW)/ZW
169   IF(KEY1.EQ.1)BARW=R(2,1)*PRS
      IF(KEY1.EQ.2)BARW=R(1,1)*PRS
      IF(INDICATOR.EQ.0)G=REAL(BARW)
      IF(INDICATOR.EQ.1)G=IMAG(BARW)
      RETURN
      END

END OF LISTING OF FILE :ISR008.HSWM4F(1,*,1) FOR USER :ISR008 AT 1936/04

**********************************************************************
```

B.3 Program ZFINDW

This program produces the bedrock free propagation modeshapes shown in Figs. 4.3 and 4.4. The program logic is directly related to the analysis of Section 4.2, for the "Quadratic Eigenvalue Problem". Although the version shown will plot the vertical amplitude components of the modeshapes, for the frequencies 16, 32, 48 and 64 Hz, the program can easily be changed to give the horizontal components. This is achieved by changing the definition of VRR(NQ), just above label 52, to

VRR(NQ) = VR((2*NQ - 1),NK).

Two NAG library routines are used; these are F04ACF, which inverts a real, square, symmetric, banded matrix, and F02AGF, which finds the eigenvalues and eigenvectors of a matrix.

Although a different program was used to plot the dispersion curves in Figs. 4.1 and 4.2, which was based on the "Linear Eigenvalue Problem" of Section 4.2, this program has not been listed here. This is because Figs. 4.1 and 4.2 could also have been produced by a slightly modified version of program ZFINDW, which gives the propagating (real wavenumber) modes as a subset of the complete set of (complex wavenumber) excited modes.

Requires GINOGRAF and the NAG library.

Inputs (Variable Parameters)	Comments
N	The number of sub-layers used: large enough to lend accuracy to the linearised dynamic stiffness matrix, and to give smooth graphs of the modeshapes.
H	The height of each sub-layer - hence 7.0 (see program) defines the total layer height (in m)
E	Young's modulus (Nm^{-2})
RHO	Density ($kg\ m^{-3}$)
VNU	Poisson's ratio

Inputs (cont.)

FREQ	As listed, 16 Hz,32 Hz, 48 Hz and 64 Hz are used; the number of frequencies, and the lowest frequency can be changed at lines 18 and 21.

Output

Four graphs, showing the modeshapes in different colours for each frequency, are produced. Much written data is also produced:

(i) N, the number of layers;

(ii) FREQ, the frequency (the data are listed for each frequency);

(iii) the real and imaginary parts of each eigenvalue;

(iv) the eigenvectors corresponding to each real eigenvalue.

PROGRAM ZFINDW

```
      DIMENSION A(50,50),B(50,50),RL(50,3),C(100,100),RR(100),RI(100),
     *INTGER(100),VR(100,100),VI(100,100),KOUNT(100),VRR(26),Z(26)
      REAL LAM,MU
      CALL CC036N
      N=25
      N2=2*N
      IRL=N2
      N4=2*N2
      IFAIL=0
      H=7.0/N
      E=2.69E08
      RHO=1550.0
      VNU=0.257
      LAM=(VNU*E)/((1.0+VNU)*(1.0-2.0*VNU))
      MU=E/(2.0*(1.0+VNU))
      DO 53 IA=1,26
53    Z(IA)=-FLOAT(IA-1)*7.0/25.0
      DO 50 IF=1,4
      CALL GRAPH(100.,140.,-0.25,0.25,-7.0,0.0,8)
      FI=FLOAT(IF)
      FREQ=FI*16.0
      OM=6.283185308*FREQ
      A(1,3)=H*(LAM+2.0*MU)/3.0
      A(2,2)=0.0
      A(2,3)=H*MU/3.0
      DO 1 I=3,(2*N-1),2
      A(I,1)=A(1,3)/2.0
      A(I,2)=0.0
1     A(I,3)=4.0*A(I,1)
      DO 2 J=4,(2*N),2
      A(J,1)=H*MU/6.0
      A(J,2)=0.0
2     A(J,3)=4.0*A(J,1)
      DO 3 K=1,N2
      DO 3 L=1,N2
3     B(K,L)=0.0
      DO 4 M=1,N2
4     B(M,M)=1.0
      CALL F04ACF(A,N2,B,N2,N2,2,N2,B,N2,RL,IRL,3,IFAIL)
      DO 10 I1=1,N4
      DO 10 I2=1,N4
10    C(I1,I2)=0.0
      DO 11 I3=1,N2
11    C(I3,(I3+N2))=1.0
      C1=(LAM-MU)*0.5
      C2=(LAM+MU)*0.5
      C3=MU/H-OM*OM*RHO*H/3.0
      C4=-MU/H-OM*OM*RHO*H/6.0
      C5=(LAM+2.0*MU)/H-OM*OM*RHO*H/3.0
      C6=-(LAM+2.0*MU)/H-OM*OM*RHO*H/6.0
      DO 5 M=1,(N2-1),2
      C((M+N2),(N2+2))=-B(M,1)*C1-B(M,3)*C2
      C((M+N2+1),(N2+1))=-B((M+1),2)*C1+B((M+1),4)*C2
      C((M+N2),N4)=C2*B(M,(N2-3))
      C((M+N2+1),(N4-1))=-C2*B((M+1),(N2-2))
      DO 5 I=3,(N2-3),2
      C((N2+M),(N2+I+1))=-C2*(B(M,(I+2))-B(M,(I-2)))
5     C((N2+M+1),(N2+I))=-C2*(B((M+1),(I-1))-B((M+1),(I+3)))
      DO 6 J=1,(N2-1),2
      C((N2+J),1)=-C3*B(J,1)-C4*B(J,3)
      C((N2+1+J),2)=-C5*B((J+1),2)-C6*B((J+1),4)
```

```
      C((N2+J+1),N2)=-C6*B((J+1),(N2-2))-2.0*C5*B((J+1),N2)
      C((N2+J),(N2-1))=-C4*B(J,(N2-3))-2.0*C3*B(J,(N2-1))
      DO 6 L=3,(N2-3),2
      C((J+N2),L)=-C4*(B(J,(L-2))+B(J,(L+2)))-2.0*C3*B(J,L)
      C((J+N2+1),(L+1))=-C6*(B((J+1),(L-1))+B((J+1),(L+3)))-2.0*C5*
     ?B((J+1),(L+1))
6     CONTINUE
      CALL F02AGF(C,N4,N4,RR,RI,VR,N4,VI,N4,INTGER,IFAIL)
      IF(IFAIL.NE.0)WRITE(6,30)IFAIL
      IF(IFAIL.NE.0)STOP
30    FORMAT(/,' IFAIL=',I2)
      WRITE(6,29)N
29    FORMAT(/,' NO. OF LAYERS=',I3)
      WRITE(6,31)FREQ
31    FORMAT(/,' FREQ=',F7.3)
      WRITE(6,32)
32    FORMAT(//,'       E.V. REAL PART     IMAG. PART')
      K=1
      DO 33 NH=1,N4
      KOUNT(NH)=0
      IF(ABS(RI(NH)).GT.10E-30)GOTO 45
      KOUNT(K)=NH
      K=K+1
45    CONTINUE
33    WRITE(6,34)RR(NH),RI(NH)
34    FORMAT(4X,F14.10,2X,F14.10)
      KM1=K-1
      DO 40 NN=1,KM1
      NK=KOUNT(NN)
      WRITE(6,41)NK
      DO 42 NP=1,N2
42    WRITE(6,36)VR(NP,NK),VI(NP,NK)
40    CONTINUE
      VRRMAX=0.0
      KK=0
      DO 51 NO=2,KM1,2
      NK=KOUNT(NO)
      DO 52 NQ=1,25
      VRR(NQ)=VR((2*NQ),NK)
52    IF(ABS(VRR(NQ)).GT.VRRMAX)VRRMAX=ABS(VRR(NQ))
      VRR(26)=0.0
      KK=KK+1
      IF(KK.GT.4)KK=(KK-4)
      CALL PENSEL(KK,0.1,2)
      CALL GRACUR(VRR,Z,26)
51    CONTINUE
      CALL PICCLE
41    FORMAT(//,' EIGENVECTORS FOR EIGENVALUE NO:',I3)
36    FORMAT(4X,F14.9,2X,F14.9)
50    CONTINUE
      CALL DEVEND
      STOP
      END
      SUBROUTINE GRAPH(A,B,C,D,E,F,I)
      CALL AXIPOS(1,30.,30.,A,1)
      CALL AXIPOS(1,30.,30.,B,2)
      CALL AXISCA(1,I,C,D,1)
      CALL AXISCA(1,I,E,F,2)
      CALL AXIDRA(2,1,1)
      CALL AXIDRA(-2,-1,2)
      RETURN
      END
```

B.4 Program MODE2

The program plots graphs of the form shown in Figs. 6.4 to 6.7. A particular wavenumber/"eigenfrequency" pair, found very accurately with program EIGFREQ (see Section B.6) is used to solve equation (6.50), to give matrix [A] to within an arbitrary multiplicative constant. This allows solution of equations (6.24) and (6.25) for C_1 and D_1, which in turn gives u, w, u' and w' from equations (6.18) to (6.21). The parameters are non-dimensional, and the program plots the horizontal and vertical components of the modeshapes, using 200 points for each curve.

Requires GINOGRAF

Inputs (Variable Parameters)	Comments
ZETA	Defined as (ζa); as shown, ZETA = 0.55*0.75
FREQ	Frequency f in Hz, corresponding to chosen wavenumbers
DEPTH	Non-dimensional depth of layer, (h/a)
VNU	ν in layer
OMSQ	Ω^2, defined here as $[(2\pi)^2 a^2 \rho/E]f^2$
OMSQ2	Ω^2 for the half-space, defined here as for OMSQ
VNU2	ν in half-space

Additionally, the value 9.333 appears at several places in the program and represents DEPTH; this could be changed by a global editing command. In the call to AXISCA near the end of the program, 18.666 represnts (2 × DEPTH).

Output

The program prints X3 and X3CHECK as a check on the accuracy of the solution eigenfrequency; the two values should be the same. A graph of the form shown in Figs. 6.4 to 6.7 is produced.

```
      COMPLEX ALPHA,BETA,ALPHA1,BETA1,MZ,MZ1,A1,A2,A3,A4,A5,EYE,B1,B2,
     ?D1,D2,D3,D4,E1,E2,E3,E4,AZ,AZ1,F1,F2,F3,F4,F5,S11,S12,S13,
     ?S14,S21,S22,S23,S24,S31,S33,S41,S43,H,EZ,Y1,Y2,Y3,X3CHECK,
     ?X1,X2,X3,X5,X6,U(100),W(100),U1(100),W1(100),A2I,BZ,BZ1,O
     ?,UA,WA,U1A,W1A,ONE
      DIMENSION Z(100),UTOT(200),WTOT(200),ZTOT(200)
      REAL K1,K2,K11,K21,MU,MU1,LAPMU,LAPMU1
      CALL CC036N
      ZETA=0.55*0.75
      FREQ=62.5359477427122
      DEPTH=9.333
      VNU=0.257
      OMSQ=1.2796E-04*FREQ*FREQ
      OMSQ2=2.666E-06*FREQ*FREQ
      C1=SQRT((1.-VNU)/((1.+VNU)*(1.-2.*VNU)*OMSQ))
      C2=1.0/SQRT(2.0*(1.0+VNU)*OMSQ)
      K1=1.0/C1
      K2=1.0/C2
      VNU2=0.179
      C11=SQRT((1.0-VNU2)/((1.+VNU2)*(1.-2.*VNU2)*OMSQ2))
      C21=1.0/SQRT(2.0*(1.0+VNU2)*OMSQ2)
      K11=1.0/C11
      K21=1.0/C21
      MU=OMSQ*C2*C2
      MU1=OMSQ2*C21*C21
      LAPMU=OMSQ*C1*C1
      LAPMU1=OMSQ2*C11*C11
      EYE=CMPLX(0.0,1.0)
      ZZ=ZETA*ZETA
      SIGN1=ZZ-K1*K1
      SIGN2=ZZ-K2*K2
      ONE=CMPLX(1.0,0.0)
      IF(SIGN1.GT.0.0)ALPHA=SQRT(ZZ-K1*K1)*ONE
      IF(SIGN1.LT.0.0)ALPHA=SQRT(K1*K1-ZZ)*EYE
      IF(SIGN2.GT.0.0)BETA=SQRT(ZZ-K2*K2)*ONE
      IF(SIGN2.LT.0.0)BETA=SQRT(K2*K2-ZZ)*EYE
      ALPHA1=SQRT(ZZ-K11*K11)*ONE
      BETA1=SQRT(ZZ-K21*K21)*ONE
      MZ=2.0*MU*ALPHA*ZETA*EYE
      MZ1=2.0*MU1*ALPHA1*ZETA*EYE
      A1=ZZ-ALPHA*BETA1
      A2=ZZ-ALPHA1*BETA1
      A3=ZZ+ALPHA*BETA1
      A4=ZZ-ALPHA1*BETA
      A5=ZZ+ALPHA1*BETA
      B1=BETA1*BETA1+ZZ
      B2=BETA*BETA+ZZ
      D1=ALPHA1-ALPHA
      D2=ALPHA1+ALPHA
      D3=BETA-BETA1
      D4=BETA+BETA1
      E1=EXP(-ALPHA*DEPTH)
      E2=EXP(ALPHA*DEPTH)
      E3=EXP(-BETA*DEPTH)
      E4=EXP(BETA*DEPTH)
      F1=(2.0*MU*ZZ-LAPMU*K1*K1)*CMPLX(1.0,0.0)
      F2=(2.0*MU1*ZZ-LAPMU1*K11*K11)*CMPLX(1.0,0.0)
      F3=2.0*MU1*ZZ*BETA1
      F4=2.0*MU*EYE*ZETA*BETA
      F5=2.0*MU1*EYE*ZETA*BETA1
      H=MU1*EYE*ZETA
```

```
      O=2.0*MU1*ALPHA1*ZZ
      EZ=EYE*ZETA
      S11=(MZ-MZ1*A1/A2+H*B1*D1/A2)*E1
      S12=(-MZ-MZ1*A3/A2+H*B1*D2/A2)*E2
      S13=(-MU*B2+0*D3/A2+MU1*B1*A4/A2)*E3
      S14=(-MU*B2-0*D4/A2+MU1*B1*A5/A2)*E4
      S21=(F1+F3*D1/A2-F2*A1/A2)*E1
      S22=(F1+F3*D2/A2-F2*A3/A2)*E2
      S23=(F4-(H/MU1)*D3*F2/A2-F5*A4/A2)*E3
      S24=(-F4+EZ*D4*F2/A2-F5*A5/A2)*E4
      S31=F1
      S33=F4
      S41=MZ
      S43=-B2*MU
      X4=CMPLX(1.0,0.0)
      Y1=S43*S31
      Y2=S33*S41
      Y3=S31*S41
      A2I=1.0/A2
      X3=X4*(S11*(Y1-Y2)-S12*(Y1+Y2)-2.0*S14*Y3)/(-S11*(Y1+Y2)+S12*(Y1
     ?Y2)+2.0*S13*Y3)
      X3CHECK=X4*(S21*(Y1-Y2)-S22*(Y1+Y2)-2.0*S24*Y3)/(-S21*(Y2+Y1)+
     ?S22*(Y1-Y2)+2.0*S23*Y3)
      X2=0.5*(X3*(Y1-Y2)+X4*(Y1+Y2))/Y3
      X1=(S33/S31)*(X4-X3)-X2
      X5=A2I*(X1*E1*A1+X2*E2*A3+EZ*(X3*E3*D3-X4*E4*D4))
      X6=A2I*(X1*EZ*E1*D1+X2*E2*EZ*D2-(X3*E3*A4+X4*E4*A5))
      WRITE(6,700)X3,X3CHECK
      UMAX=0.0
      AZ=ALPHA*9.333
      BZ=BETA*9.333
      UA=-EZ*(X1*EXP(-AZ)+X2*EXP(AZ))+BETA*(X3*EXP(-BZ)-X4*EXP(BZ))
      WA=-ALPHA*(X1*EXP(-AZ)-X2*EXP(AZ))-EZ*(X3*EXP(-BZ)+X4*EXP(BZ))
      U1A=-EZ*X5+X6*BETA1
      W1A=-ALPHA1*X5-EZ*X6
      CO1=IMAG(UA)/REAL(UA)
      CO2=REAL(U1A)/REAL(UA)
      CO3=IMAG(W1A)/IMAG(WA)
      DO 500 I=1,100
      Z(I)=FLOAT(I-1)*(9.333/99.0)
      AZ=ALPHA*Z(I)
      AZ1=ALPHA1*Z(I)
      BZ=BETA*Z(I)
      BZ1=BETA1*Z(I)
      UA=(-EZ*(X1*EXP(-AZ)+X2*EXP(AZ))+BETA*(X3*EXP(-BZ)-X4*EXP(BZ)))
     ?*CMPLX(1.0,CO1)
      WA=(-ALPHA*(X1*EXP(-AZ)-X2*EXP(AZ))-EZ*(X3*EXP(-BZ)+X4*EXP(BZ)))
     ?*CMPLX(1.0,CO1)
      U1A=(-EZ*X5*EXP(-AZ1)+X6*BETA1*EXP(-BZ1))*CMPLX(1.0,CO1)
     ?/CO2
      W1A=(-ALPHA1*X5*EXP(-AZ1)-EZ*X6*EXP(-BZ1))*CMPLX(1.0,CO1)
     ?/CO3
      U(I)=REAL(UA)
      W(I)=IMAG(WA)
      U1(I)=REAL(U1A)
      W1(I)=IMAG(W1A)
      IF(ABS(U(I)).GT.UMAX)UMAX=ABS(U(I))
      IF(ABS(W(I)).GT.UMAX)UMAX=ABS(W(I))
      IF(ABS(U1(I)).GT.UMAX)UMAX=ABS(U1(I))
      IF(ABS(W1(I)).GT.UMAX)UMAX=ABS(W1(I))
500   CONTINUE
      DO 800 J=1,100
```

```
 800    UTOT(J)=U(J)
        DO 850 J=101,200
 850    UTOT(J)=U1(J-100)
        DO 900 K=1,100
        ZTOT(K)=-Z(K)
 900    WTOT(K)=W(K)
        DO 950 K=101,200
        ZTOT(K)=-Z(K-100)-9.333
 950    WTOT(K)=W1(K-100)
        CALL AXIPOS(1,50.,50.,70.,1)
        CALL AXIPOS(1,50.,50.,100.,2)
        CALL AXISCA(1,10,-UMAX,UMAX,1)
        CALL AXISCA(1,10,-18.666,0.0,2)
        CALL AXIDRA(2,1,1)
        CALL AXIDRA(-2,-1,2)
        CALL GRACUR(WTOT,ZTOT,200)
        CALL PENSEL(2,0.1,2)
        CALL GRACUR(UTOT,ZTOT,200)
        CALL PENSEL(3,0.1,2)
        CALL GRAMOV(-UMAX,-9.333)
        CALL GRALIN(UMAX,-9.333)
        CALL DEVEND
 700    FORMAT(1X,'X3=',F8.4,1X,F8.4,' X3CHECK= ',F8.4,1X,F8.4)
        STOP
        END
```

END OF LISTING OF FILE :ISR008.MODE2(68,*,1) FOR USER :ISR008 AT

****

B.5 Program EFEIG

This program finds the lowest fundamental frequency in a layer with fixed-fixed boundary conditions. The problem is dimensionalised with Clarborough parameters, and the solution follows the work of Section 4.2. The eigenvalue problem is formulated as in equation (4.11), which for convenience is re-stated here:

$$Ax = \lambda' Bx \qquad (4.11)$$

λ' represents ω^2 here, and the matrices [A] and [B], which have the same names in the program, are given by matrices [G] and [M] in equations (4.5) and (4.6). The matrices given by equations (4.3) and (4.4) do not contribute to the stiffness matrix, because a solution is sought for $\zeta = 0$, which will give the lowest fundamental frequency. The problem is solved for a range of 10 layer depths, and the program prints each lowest frequency/depth pair. The NAG routine F02ADF which solves the eigenvalue problem is mentioned in Section 4.3.

Requires The NAG library.

Inputs (Variable Parameters)	Comments
N	Number of sub-layers to be used.
E	Young's modulus (dimensional)
RHO	Density (dimensional)
VNU	Poisson's ratio in layer
H	The dimensional depth, which is 7 m for Clarborough, is defined in the expression for H.

Output

Ten layer depth/eigenfrequency pairs are printed.

```
      DIMENSION A(46,46),B(46,46),R(46),DE(48)
      N=24
      M=2*N-2
      DO 25 MZ=1,M
      DO 25 MY=MZ,M
25    A((MY+1-MZ),MY)=0.0
      E=2.69E08
      RHO=1550.0
      VNU=0.257
      ALAM=(VNU*E)/((1.0+VNU)*(1.0-2.0*VNU))
      AMU=E/(2.0*(1.0+VNU))
      ALAMU=ALAM+2.0*AMU
      IFAIL=0
      DO 1 I=1,10
      H=(7.0/FLOAT(I))/N
      HEIGHT=H*N
      CON=RHO*H/6.0
      DO 15 MA=1,M
15    B(MA,MA)=4.0*CON
      DO 16 MB=2,M
16    B((MB-1),MB)=0.0
      DO 17 MC=3,M
17    B((MC-2),MC)=CON
      DO 18 ME=4,M
      DO 18 MD=ME,M
18    B((MD+1-ME),MD)=0.0
      DO 19 L=1,(N-2)
      A((2*L-1),(2*L+1))=-ALAMU/H
      A((2*L-1),(2*L+2))=0.0
      A((2*L),(2*L+1))=0.0
      A((2*L),(2*L+2))=-AMU/H
      A((2*L-1),(2*L-1))=2.0*ALAMU/H
19    A((2*L),(2*L))=2.0*AMU/H
      A(M-1,M-1)=2.0*ALAMU/H
      A(M,M)=2.0*AMU/H
      CALL F02ADF(A,M,B,M,M,R,DE,IFAIL)
      IF(IFAIL.NE.0)WRITE(6,4)IFAIL
      IF(IFAIL.NE.0)STOP
      R(1)=SQRT(ABS(R(1)))/6.283185308
      WRITE(6,5)R(1),HEIGHT
1     CONTINUE
4      FORMAT(1X,'IFAIL=',I2)
5     FORMAT(1X,'FREQ.=',F9.4,' FOR H=',F9.4)
      STOP
      END
```

END OF LISTING OF FILE :ISR008.EFEIG(14,*,1) FOR USER :ISR008 AT

****

B.6 Program EFIND

This program plots the dispersion curves shown in Figs. 6.2 and 6.3. The program uses the method of solution described in Section 6.3. All parameters are non-dimensionalised, except the frequency in the main part of the program, which is in Hz. However, the graph-plotting logic redimensionalises the information for Clarborough. For a given wavenumber, the frequency of each mode is calculated to within 0.01 Hz. Six dispersion curves are found, in the range $0 \leqslant \zeta \leqslant 1.67$, and $0 <$ frequency $\leqslant 64$ Hz. The Subroutine G is very similar to its counterpart in program EF64H2, with the difference that instead of solving the dynamic stiffness matrix for $\bar{w}$ and $\bar{u}$, here this matrix is changed to upper triangular form to find the sign count of the matrix (see Section 6.3). Also, a larger matrix is defined here, in accordance with the number of layers necessary to make the lowest fundamental frequency in each sub-layer (with fixed-fixed boundary conditions) greater than 64 Hz. This number of sub-layers is found with program EFEIG.

Note that program EIGFREQ can be easily derived from program EFIND, by introducing quadruple precision, and changing the logic to calculate just one frequency to fourteen decimal places.

Requires GINOGRAF

Inputs (Variable Parameters)	Comments
NNN	Maximum number of plotting points per dispersion curve (in practice fewer are used to avoid leaky behaviour, i.e., for wavespeed $< c_2'$)
MMM	Defines how many dispersion curves are to be plotted
A	Arbitrary number, which must be set much larger than FREQN
FREQN	Maximum frequency of interest
ZETA	Defined here as ZETA = 1.25*FLOAT(IO)/NNN The '1.25' gives the largest value of (ζa) to be considered.

The following parameters are in FUNCTION (ZETA,FREQ,CV):

N	The number of layers to be used (found using program EFEIG)
H	Non-dimensionalised sub-layer depth, defined by (h/a)/N
VNU	Poisson's ratio in the layer
OMSQ, OMSQ2	Ω^2 in the layer and half-space, defined as a function of frequency as in program MODE2
VNU2	Poisson's ratio in the half-space

Additionally, certain numbers appearing in the program must be changed, for different material properties. These numbers, with the quantity they represent, are:

Number	Quantity Represented
0.75	a, the strip half-width
64.0	maximum frequency
1.7	maximum dimensional wavenumber
1880.3	shear wavespeed in the half-space
1.531	k_2 at 64 Hz
0.875	k_1 at 64 Hz
0.214	k_2' at 64 Hz
459.4	layer compression wavespeed
262.7	layer shear wavespeed
241.7	layer Rayleigh wavespeed

These numbers could be changed using a global edit.

Output

If the program is unable to find an eigenfrequency, it stops and writes an appropriate message. Otherwise, two graphs are produced giving dispersion curves of the form shown in Figs. 6.2 and 6.3.

```
      DIMENSION FREQ(1000,10),ZETAG(1000),C(1000,10),FREQG(1000),
     ?CG(1000),ZETAA(1000)
      COMMON INDICATOR
      NNN=1000
      MMM=6
      CMAX=0.0
      DO 50 IZ=1,NNN
      DO 50 IY=1,MMM
      FREQ(IZ,IY)=0.0
50    C(IZ,IY)=0.0
      CALL CC036N
      A=1000.0
      FREQN=64.0
      DO 39 IO=1,NNN
      INDICATOR=0
      ZETA=1.25*FLOAT(IO)/NNN
      ZETAA(IO)=ZETA/0.75
      CALL G(ZETA,FREQN,CN)
      CD=CN
      IF(CN.GT.10)CD=10
      DO 39 K=1,CD
      INDICATOR=(K-1)
      DO 30 I=1,1000
      FREQK=FREQN/FLOAT(2*I)
      IF(K.GT.1)FREQK=FREQM
      CALL G(ZETA,FREQK,CK)
      IF(CK.EQ.0.0)FREQM=FREQK
      IF(CK.EQ.0.0)GOTO 31
      IF(I.EQ.1000)WRITE(6,32)FREQK,ZETA
      IF(I.EQ.1000)GOTO 39
30    CONTINUE
31    FREQNL=FREQN
      NC=1
33    FREQK=(FREQNL-FREQM)/2.0+FREQM
      NC=NC*2
      CALL G(ZETA,FREQK,CK)
      IF(ABS(A-FREQK).LT.0.01)FREQ(IO,K)=FREQK
      IF(ABS(A-FREQK).LT.0.01)C(IO,K)=6.2832*FREQK/(ZETA*1.3333333
      IF(ABS(A-FREQK).LT.0.01)GOTO 38
      A=FREQK
      IF(CK.EQ.0.0)FREQM=FREQK
      IF(CK.EQ.0.0)GOTO 33
      IF(FLOAT(NC).GT.1.0E10)WRITE(6,34)FREQK,ZETA
      IF(CK.NE.0.0)FREQNL=FREQK
      GOTO 33
38    FREQM=FREQK-1.0
39    CONTINUE
32    FORMAT(1X,'I.EQ.1000 AND FREQK=',F10.5,' FOR ZETA=',F7.4)
34    FORMAT(1X,'NC.GT.1.0E10 AND FREQK=',F10.5,' FOR ZETA=',F7.4)
      CALL GRAPH(150.,200.,0.0,64.0,0.0,1.7,10,1)
      DO 70 J=1,MMM
      NG=0
      DO 60 I=1,NNN
      IF(FREQ(I,J).EQ.0.0)GOTO 65
      WK=6.2832*FREQ(I,J)/1880.3
      IF(ZETAA(I).LT.WK)GOTO 60
      NG=NG+1
      ZETAG(NG)=ZETAA(I)
      FREQG(NG)=FREQ(I,J)
60    CONTINUE
65    CONTINUE
```

```
70      CALL GRACUR(FREQG,ZETAG,NG)
        CALL WLINE(2,64.0,1.531)
        CALL WLINE(3,64.0,0.875)
        CALL WLINE(4,64.0,0.214)
        CALL PICCLE
        CALL PENSEL(1,0.1,2)
        CALL GRAPH(150.,200.,0.0,64.0,150.0,2000.0,10,4)
        DO 90 J=1,MMM
        NG=0
        DO 80 I=1,NNN
        IF(C(I,J).EQ.0.0)GOTO 85
        IF(C(I,J).GT.1880.3)GOTO 80
        IF(C(I,J).GT.CMAX)CMAX=C(I,J)
        NG=NG+1
        CG(NG)=C(I,J)
        FREQG(NG)=FREQ(I,J)
80      CONTINUE
85      CONTINUE
90      CALL GRACUR(FREQG,CG,NG)
        CALL WLINE2(2,1880.3,64.0,1880.3)
        CALL WLINE2(3,459.4,4.0,459.4)
        CALL WLINE2(4,262.7,4.0,262.7)
        CALL WLINE2(2,241.7,4.0,241.7)
        CALL DEVEND
        STOP
        END
        SUBROUTINE WLINE(I,A,B)
        CALL PENSEL(I,0.1,2)
        CALL GRAMOV(0.0,0.0)
        CALL GRALIN(A,B)
        RETURN
        END
        SUBROUTINE WLINE2(I,A,B,C)
        CALL PENSEL(I,0.1,2)
        CALL GRAMOV(0.0,A)
        CALL GRALIN(B,C)
        RETURN
        END
        SUBROUTINE GRAPH(A,B,C,D,E,F,I,J)
        CALL AXIPOS(1,50.,50.,A,1)
        CALL AXIPOS(1,50.,50.,B,2)
        CALL AXISCA(1,I,C,D,1)
        CALL AXISCA(J,I,E,F,2)
        CALL AXIDRA(2,1,1)
        CALL AXIDRA(-2,-1,2)
        RETURN
        END
        SUBROUTINE G(ZETA,FREQ,CV)
        COMPLEX U,V,W,X,Y,Z,MU,C1,C2,K1,K2,ALPHA,BETA,DEN,
      ?ALPHAI,BETAI,LAPMU,SHA,SHB,CHA,CHB,AH,BH,ZETAI,A(10,10)
      ?,AL,ETA,COEFF,PHI,D,B,C,DD,E,C12,C22,K12,K22,R11,R12,R22

        COMMON INDICATOR
        REAL ZETA,H
        INTEGER N
        N=4
        M=2*N+2
        H=9.333/N
        VNU=0.257
        OMSQ=1.2796E-04*FREQ*FREQ
        OMSQ2=2.666E-06*FREQ*FREQ
        AC1=SQRT((1.-VNU)/((1.+VNU)*(1.-2.*VNU)*OMSQ))
```

```
      AC2=1.0/SQRT(2.0*(1.0+VNU)*OMSQ)
      DAMP=0.0
      AA=SQRT(0.5*(1.0+SQRT(1.0+4.0*DAMP*DAMP)))
      C1=CMPLX(AC1,0.0)*CMPLX(AA,(DAMP/AA))
      C2=CMPLX(AC2,0.0)*CMPLX(AA,(DAMP/AA))
      K1=1.0/C1
      K2=1.0/C2
      VNU2=0.179
      DAMP2=0.0
      AC12=SQRT((1.0-VNU2)/((1.+VNU2)*(1.-2.*VNU2)*OMSQ2))
      AC22=1.0/SQRT(2.0*(1.0+VNU2)*OMSQ2)
      AA2=SQRT(0.5*(1.0+SQRT(1.0+4.0*DAMP2*DAMP2)))
      C12=CMPLX(AC12,0.0)*CMPLX(AA2,(DAMP2/AA2))
      C22=CMPLX(AC22,0.0)*CMPLX(AA2,(DAMP2/AA2))
      K12=1.0/C12
      K22=1.0/C22
      ALPHA=CSQRT(ZETA*ZETA-K12*K12)
      BETA=CSQRT(ZETA*ZETA-K22*K22)
      DEN=1.0/(ALPHA*BETA-ZETA*ZETA)
      LAPMU=OMSQ2*C12*C12
      MU=OMSQ2*C22*C22
      R11=LAPMU*BETA*K12*K12*DEN
      R22=R11*ALPHA/BETA
      R12=(2.0*MU*ALPHA*BETA*ZETA-2.0*MU*ZETA**3+LAPMU*ZETA*K12*K12)*
      DO 1 I=1,M
      DO 1 J=1,M
1     A(I,J)=CMPLX(0.0,0.0)
      IF(ZETA.GT.10E-12)GOTO 3
      ETA=H/C2
      AL=C2/C1
      COEFF=OMSQ*C2
      PHI=AL*ETA
      A(1,1)=COEFF/(AL*CSIN(PHI)/CCOS(PHI))
      A(2,2)=COEFF*CCOS(ETA)/CSIN(ETA)
      DO 4 L=1,N
      A((2*L-1),(2*L+1))=-COEFF/(AL*CSIN(PHI))
      A((2*L),(2*L+2))=-COEFF/CSIN(ETA)
      A((2*L+1),(2*L-1))=A((2*L-1),(2*L+1))
      A((2*L+2),(2*L))=A((2*L),(2*L+2))
      A((2*L+1),(2*L+1))=2.0*A(1,1)
      A((2*L+2),(L*2+2))=2.0*A(2,2)
4     CONTINUE
      A(M-1,M-1)=A(M-1,M-1)/2.0-R11
      A(M-1,M)=-R12
      A(M,M-1)=-R12
      A(M,M)=A(M,M)/2.0-R22
      GOTO 6
3     ALPHA=CSQRT(ZETA*ZETA-K1*K1)
      BETA=CSQRT(ZETA*ZETA-K2*K2)
      ALPHAR=REAL(ALPHA)
      ALPHAIM=IMAG(ALPHA)
      ALPHAI=CMPLX(-ALPHAIM,ALPHAR)
      BETAR=REAL(BETA)
      BETAIM=IMAG(BETA)
      BETAI=CMPLX(-BETAIM,BETAR)
      ZETAI=CMPLX(0.0,ZETA)
      LAPMU=OMSQ*C1*C1
      MU=OMSQ*C2*C2
      AH=ALPHA*H
      BH=BETA*H
      SHA=0.5*(CEXP(AH)-CEXP(-AH))
      SHB=0.5*(CEXP(BH)-CEXP(-BH))
```

```
      CHA=0.5*(CEXP(AH)+CEXP(-AH))
      CHB=0.5*(CEXP(BH)+CEXP(-BH))
      U=2.0*BETAI*LAPMU*K1*K1*(ZETA*ZETA*SHA*CHB-ALPHA*BETA*SHB
     ?*CHA)/(ALPHA*ZETA)
      V=2.0*BETAI*(1.0-CHA*CHB)*(LAPMU*K1*K1-4.0*MU*ZETA*ZETA)+
     ?2.0*ZETAI*SHA*SHB*((LAPMU*K1*K1*ZETA/ALPHA)-2.0*MU*((ALPHA*
     ?BETA*BETA/ZETA)+(ZETA**3/ALPHA)))
      W=2.0*MU*K2*K2*(ZETA*ZETAI*CHA*SHB-ALPHA*BETAI*SHA*CHB)/
     ?ZETA
      X=2.0*BETAI*LAPMU*K1*K1*(ALPHA*BETA*SHB-ZETA*ZETA*SHA)/
     ?(ALPHA*ZETA)
      Y=2.0*MU*BETAI*K2*K2*(CHA-CHB)
      Z=2.0*MU*K2*K2*(ALPHA*BETAI*SHA-ZETA*ZETAI*SHB)/ZETA
      D=4.0*BETAI*ZETA*(1.0-CHA*CHB)+2.0*(ALPHA*BETA*BETAI/ZETA-
     ?(ZETA**3)/ALPHAI)*SHA*SHB
      A(1,1)=U/D
      A(1,2)=V/D
      A(2,1)=V/D
      A(2,2)=W/D
      DO 5 K=1,N
      A((2*K-1),(2*K+1))=X/D
      A((2*K-1),(2*K+2))=Y/D
      A((2*K),(2*K+1))=-Y/D
      A((2*K),(2*K+2))=Z/D
      A((2*K+1),(2*K-1))=A((2*K-1),(2*K+1))
      A((2*K+1),(2*K))=A((2*K),(2*K+1))
      A((2*K+2),(2*K-1))=A((2*K-1),(2*K+2))
      A((2*K+2),(2*K))=A((2*K),(2*K+2))
      A((2*K+1),(2*K+1))=2.0*A(1,1)
      A((2*K+2),(2*K+2))=2.0*A(2,2)
5     CONTINUE
      A(M-1,M-1)=A(M-1,M-1)/2.0-R11
      A(M-1,M)=-R12-V/D
      A(M,M-1)=-R12-V/D
      A(M,M)=A(M,M)/2.0-R22
6     B=A(2,1)/A(1,1)
      A(2,2)=A(2,2)-A(1,2)*B
      A(2,3)=A(2,3)-A(1,3)*B
      A(2,4)=A(2,4)-A(1,4)*B
      DO 25 I=1,(M-3),2
      C=A(I+2,I)/A(I,I)
      DD=(A(I+2,I+1)-C*A(I,I+1))/A(I+1,I+1)
      A(I+2,I+2)=A(I+2,I+2)-A(I,I+2)*C-A(I+1,I+2)*DD
      A(I+2,I+3)=A(I+2,I+3)-A(I,I+3)*C-A(I+1,I+3)*DD
      C=A(I+3,I)/A(I,I)
      DD=(A(I+3,I+1)-C*A(I,I+1))/A(I+1,I+1)
      E=(A(I+3,I+2)-C*A(I,I+2)-DD*A(I+1,I+2))/A(I+2,I+2)
      A(I+3,I+3)=A(I+3,I+3)-A(I,I+3)*C-A(I+1,I+3)*DD-A(I+2,I+3)*E
      IF(I.EQ.(M-3))GOTO 25
      A(I+3,I+4)=A(I+3,I+4)-A(I+2,I+4)*E
      A(I+3,I+5)=A(I+3,I+5)-A(I+2,I+5)*E
25    CONTINUE
      CV=0.0
      DO 26 JJ=1,10
26    IF(REAL(A(JJ,JJ)).LT.0.0)CV=CV+1.0
      CV=CV-INDICATOR
      IF(CV.LT.0.0)CV=0.0
      RETURN
      END

END OF LISTING OF FILE :ISR008.EFIND(79,*,1) FOR USER :ISR008 AT 19:
```

B.7 Program EF64H2

This program calculates data for plotting the elastic foundation model results. It contains all the logic required for the bedrock model computations, and therefore a bedrock program has not been included. To generate such a bedrock program, the (6 × 6) dynamic stiffness matrix defined by FUNCTION G(ZETA) here, should be reduced to a (4 × 4) matrix composed of its top left corner elements. All variables are non-dimensional, and this version of the program calculates the horizontal motion amplitude and phase, at 41 points in the range $16^{2}/_{3} < x/a \leq 33^{1}/_{3}$. The program can be modified to produce wavenumber domain graphs (e.g., Fig. 7.2), "width variation" graphs (Fig. 7.11) or receptance graphs (Figs. 8.20 to 8.25) in exactly the same way as described for the program HSWM4F in Section B.2.

Two NAG routines are used in FUNCTION G(ZETA). (The routine D01ANF is explained in Appendix A). Routine F03AHF decomposes the complex dynamic stiffness matrix [A] into triangular matrices, in preparation for solution of the problem, by forward and backward substitution, by routine F04AKF.

Clearly a second application of the program is necessary, to obtain sufficient data to plot a graph of the variation of horizontal motion amplitude and phase over the range $x/a < 33^{1}/_{3}$.

To calculate the vertical motion variation, the only change necessary in the main part of the program is to the phase definition at line 38, which should become

```
WP(NX) = ATAN2(WI,WR)
```

In addition, the definition of BARW at the end of FUNCTION G(ZETA) should become

```
BARW = CMPLX(0.0,-1.0)*B(1,1)
```

Requires: The NAG library.

Inputs (Variable Parameters)	Comments
N	Number of sub-layers composing dynamic stiffness matrix
H	Non-dimensional sub-layer height; therefore 9.333 = h/a
OMSQ	Non-dimensional (frequency)^2, Ω^2
VNU	Poisson's ratio
DAMP	Half the loss factor, $\eta/2$
In FUNCTION G(ZETA):	
OMSQ2	Non-dimensional (frequency)^2, Ω^2 in the half-space
VNU2	Poisson's ratio in the half-space
DAMP2	Half the loss factor, $\eta/2$, in the half-space
BBIT (defined twice)	Non-dimensional, transformed stress on the strip; if the value 4.96×10^{-9} is used, this is equivalent to $P = 2\pi$ at Clarborough.

Additionally, to calculate information for $0 \leq x/a < 16^2/_3$, it is necessary to replace the first (16.667) at line 24 by 0.0. If the frequency is changed, the same logic applies to the value '1.4' in each call to DO1ANF, as for the program HSWM4F; the only difference here is that now this value of wavenumber is non-dimensional.

Outputs

Sets of X position, horizontal (or vertical) amplitude and phase are written to a data file. For one value of the loop variable NX, the upper bounds for each error inherent in the applications of DO1ANF are written.

PROGRAM EF64H2

```
C     EF6 USES THE MANUALLY INVERTED STIFFNESS MATRIX,T,AND QUADRATURE
      COMPLEX C1,C2,K1,K2
      DIMENSION WM(120),WP(120),X(120)
     ?,TW(6000),IW(2500)
      COMMON H,N,OMSQ,C1,C2,K1,K2,M,INDICATOR
      EXTERNAL G
      N=2
      M=2*N+2
      H=0.333/N
      OMSQ=0.524
      WRITE(6,49)N
49    FORMAT(///,'NO. OF LAYERS=',I2)
      VNU=0.257
      AC1=SQRT((1.-VNU)/((1.+VNU)*(1.-2.*VNU)*OMSQ))
      AC2=1.0/SQRT(2.0*(1.0+VNU)*OMSQ)
      DAMP=0.05
      AA=SQRT(0.5*(1.0+SQRT(1.0+4.0*DAMP*DAMP)))
      C1=CMPLX(AC1,0.0)*CMPLX(AA,(DAMP/AA))
      C2=CMPLX(AC2,0.0)*CMPLX(AA,(DAMP/AA))
      K1=1.0/C1
      K2=1.0/C2
      DO 75 NX=1,41
      XN=FLOAT(NX)
      X(NX)=16.667+(XN)*16.667/40.0
      INDICATOR=0
      CALL D01ANF(G,0.0,1.4,X(NX),2,10E-18,10E-6,BWRCOS1,ABSERR1,
     ?TW,6000,IW,2500,0)
      CALL D01ANF(G,1.4,9.0,X(NX),2,10E-18,10E-6,BWRCOS2,ABSERR2,
     ?TW,6000,IW,2500,0)
      INDICATOR=1
      CALL D01ANF(G,0.0,1.4,X(NX),2,10E-18,10E-6,BWICOS1,ABSERR3,
     ?TW,6000,IW,2500,0)
      CALL D01ANF(G,1.4,9.0,X(NX),2,10E-18,10E-6,BWICOS2,ABSERR4,
     ?TW,6000,IW,2500,0)
      WR=2.0*(BWRCOS1+BWRCOS2)
      WI=2.0*(BWICOS1+BWICOS2)
      WM(NX)=SQRT(WR**2+WI**2)
      WP(NX)=ATAN2(-WR,WI)
      IF(WM(NX).GT.WMAX)WMAX=WM(NX)
      WRITE(4,55)X(NX),WM(NX),WP(NX)
      IF(NX.EQ.59)WRITE(6,90)ABSERR1,ABSERR2,ABSERR3,ABSERR4
90    FORMAT(//,1X,4(E11.5,1X),/,1X,4(E11.5,1X))
75    CONTINUE
55    FORMAT(1X,F7.3,2X,F15.11,2X,F7.3)
      STOP
      END
      FUNCTION G(ZETA)
      COMPLEX U,V,W,X,Y,Z,MU,C1,C2,K1,K2,ALPHA,BETA,DEN,
     ?ALPHAI,BETAI,LAPMU,SHA,SHB,CHA,CHB,AH,BH,ZETAI,A(6,6)
     ?,AL,ETA,COEFF,PHI,D,B(6,1),BARW,C12,C22,K12,K22,R11,R12,R22
      DIMENSION RINT(6)
      COMMON H,N,OMSQ,C1,C2,K1,K2,M,INDICATOR
      REAL ZETA,H,BBIT
      INTEGER N
      OMSQ2=0.0109
      VNU2=0.179
      DAMP2=0.05
      AC12=SQRT((1.0-VNU2)/((1.+VNU2)*(1.-2.*VNU2)*OMSQ2))
      AC22=1.0/SQRT(2.0*(1.0+VNU2)*OMSQ2)
      AA2=SQRT(0.5*(1.0+SQRT(1.0+4.0*DAMP2*DAMP2)))
      C12=CMPLX(AC12,0.0)*CMPLX(AA2,(DAMP2/AA2))
```

```
      C22=CMPLX(AC22,0.0)*CMPLX(AA2,(DAMP2/AA2))
      K12=1.0/C12
      K22=1.0/C22
      ALPHA=CSQRT(ZETA*ZETA-K12*K12)
      BETA=CSQRT(ZETA*ZETA-K22*K22)
      DEN=1.0/(ALPHA*BETA-ZETA*ZETA)
      LAPMU=OMSQ2*C12*C12
      MU=OMSQ2*C22*C22
      R11=LAPMU*BETA*K12*K12*DEN
      R22=R11*ALPHA/BETA
      R12=(2.0*MU*ALPHA*BETA*ZETA-2.0*MU*ZETA**3+LAPMU*ZETA*K12*K12)*D
      DO 1 I=1,M
      B(I,1)=CMPLX(0.0,0.0)
      DO 1 J=1,M
1     A(I,J)=CMPLX(0.0,0.0)
      IF(ZETA.GT.10E-12)GOTO 3
      ETA=H/C2
      AL=C2/C1
      COEFF=OMSQ*C2
      PHI=AL*ETA
      A(1,1)=COEFF/(AL*CSIN(PHI)/CCOS(PHI))
      A(2,2)=COEFF*CCOS(ETA)/CSIN(ETA)
      DO 4 L=1,N
      A((2*L-1),(2*L+1))=-COEFF/(AL*CSIN(PHI))
      A((2*L),(2*L+2))=-COEFF/CSIN(ETA)
      A((2*L+1),(2*L-1))=A((2*L-1),(2*L+1))
      A((2*L+2),(2*L))=A((2*L),(2*L+2))
      A((2*L+1),(2*L+1))=2.0*A(1,1)
      A((2*L+2),(L*2+2))=2.0*A(2,2)
4     CONTINUE
      BBIT=4.96E-09
      A(M-1,M-1)=A(M-1,M-1)/2.0-R11
      A(M-1,M)=-R12
      A(M,M-1)=-R12
      A(M,M)=A(M,M)/2.0-R22
      GOTO 6
3     ALPHA=CSQRT(ZETA*ZETA-K1*K1)
      BETA=CSQRT(ZETA*ZETA-K2*K2)
      ALPHAR=REAL(ALPHA)
      ALPHAIM=IMAG(ALPHA)
      ALPHAI=CMPLX(-ALPHAIM,ALPHAR)
      BETAR=REAL(BETA)
      BETAIM=IMAG(BETA)
      BETAI=CMPLX(-BETAIM,BETAR)
      ZETAI=CMPLX(0.0,ZETA)
      LAPMU=OMSQ*C1*C1
      MU=OMSQ*C2*C2
      AH=ALPHA*H
      BH=BETA*H
      SHA=0.5*(CEXP(AH)-CEXP(-AH))
      SHB=0.5*(CEXP(BH)-CEXP(-BH))
      CHA=0.5*(CEXP(AH)+CEXP(-AH))
      CHB=0.5*(CEXP(BH)+CEXP(-BH))
      U=2.0*BETAI*LAPMU*K1*K1*(ZETA*ZETA*SHA*CHB-ALPHA*BETA*SHB
     ?*CHA)/(ALPHA*ZETA)
      V=2.0*BETAI*(1.0-CHA*CHB)*(LAPMU*K1*K1-4.0*MU*ZETA*ZETA)+
     ?2.0*ZETAI*SHA*SHB*((LAPMU*K1*K1*ZETA/ALPHA)-2.0*MU*((ALPHA*
     ?BETA*BETA/ZETA)+(ZETA**3/ALPHA)))
      W=2.0*MU*K2*K2*(ZETA*ZETAI*CHA*SHB-ALPHA*BETAI*SHA*CHB)/
     ?ZETA
      X=2.0*BETAI*LAPMU*K1*K1*(ALPHA*BETA*SHB-ZETA*ZETA*SHA)/
     ?(ALPHA*ZETA)
```

```
      Y=2.0*MU*BETAI*K2*K2*(CHA-CHB)
      Z=2.0*MU*K2*K2*(ALPHA*BETAI*SHA-ZETA*ZETAI*SHB)/ZETA
      D=4.0*BETAI*ZETA*(1.0-CHA*CHB)+2.0*(ALPHA*BETA*BETAI/ZETA-
     ?(ZETA**3)/ALPHAI)*SHA*SHB
      BBIT=4.96E-09*SIN(ZETA)/ZETA
      A(1,1)=U/D
      A(1,2)=V/D
      A(2,1)=V/D
      A(2,2)=W/D
      DO 5 K=1,N
      A((2*K-1),(2*K+1))=X/D
      A((2*K-1),(2*K+2))=Y/D
      A((2*K),(2*K+1))=-Y/D
      A((2*K),(2*K+2))=Z/D
      A((2*K+1),(2*K-1))=A((2*K-1),(2*K+1))
      A((2*K+1),(2*K))=A((2*K),(2*K+1))
      A((2*K+2),(2*K-1))=A((2*K-1),(2*K+2))
      A((2*K+2),(2*K))=A((2*K),(2*K+2))
      A((2*K+1),(2*K+1))=2.0*A(1,1)
      A((2*K+2),(2*K+2))=2.0*A(2,2)
5     CONTINUE
      A(M-1,M-1)=A(M-1,M-1)/2.0-R11
      A(M-1,M)=-R12-V/D
      A(M,M-1)=-R12-V/D
      A(M,M)=A(M,M)/2.0-R22
6     B(1,1)=CMPLX(0.0,BBIT)
      IFAIL=0
      CALL F03AHF(M,A,M,DETR,DETI,ID,RINT,IFAIL)
      IF(IFAIL.EQ.0)GOTO 10
      WRITE(6,7)IFAIL
7     FORMAT(/,'IFAIL=',I2)
      STOP
10    CALL F04AKF(M,1,A,M,RINT,B,M)
      BARW=B(2,1)
      IF(INDICATOR.EQ.0)G=REAL(BARW)
      IF(INDICATOR.EQ.1)G=IMAG(BARW)
      RETURN
      END

END OF LISTING OF FILE :ISR008.EF64H2(2,*,1) FOR USER :ISR008 AT 198
```

B.8 Program W

This program was used to produce the results of Chapter 9, which are for a rectangular load. The program writes the real and imaginary parts of vertical motion (WR and WI, respectively) to a data file, for six values of distance X from the centre of the rectangle. Several applications of program W are required, to produce enough information for a graph of the range of Figs. 9.8 to 9.13. Alternatively, if running time for the program is not limited, all the data could be collected with one run.

To obtain horizontal motion data, the definition of WB in FUNCTION G(GAMA) must be changed to the correct expression (given by equations (9.37), (9.54) and (9.56) - all the program names are the same as in the analysis, except for H and K, which represent k_1 and k_2 respectively in the analysis; clearly WB represents $\bar{w}$). To produce the receptance graphs, FREQ must be varied instead of X; this involves changing lines 4 and 25. To produce the wavenumber domain graphs (Figs. 9.2 to 9.7), the functions in the (β, γ) plane are generated using FUNCTION G, with BETA varied in COMMON. SUBROUTINES INTEG and SIMPSON are then irrelevant. If plots of $\tilde{w}$ are required, INTEG should be used, but without the call to SIMPSON. In each case, the data produced can be converted into a graph using a simple plotting routine.

Requires: the NAG library.

Inputs (Variable Parameters)	Comments
FREQ	Frequency of harmonic load in Hz
BEE, CEE	Dimensions of rectangle, in metres
E, RHO, VNU	Young's modulus (Nm^{-2}), Density (kgm^{-3}), Poisson's ratio
DAMP	Half the loss factor, $\eta/2$

Additionally, the '6' at line 22 defines how many X positions are to be considered. The four calls to SUBROUTINE INTEG(M,BINC,ANSW,BETA1,X) break the integration into convenient sections; the values of BETA1 must be increased with increased frequency, to ensure the relevant features of $\tilde{w}$ (see Figs. 9.6 and 9.7) are within the correct sections. M is the total number of points per section integration, for the Simpson's Rule

calculation - the NAG routine D01ANF uses as many points as required for the desired accuracy. BINC = (Section Length)/(M - 1).

Output

The program prints six sets of values of X, WR and WI, i.e., corresponding values of x, Re(w) and Im(w), where the horizontal motion u can be substituted for w.

PROGRAM W

```
      COMPLEX MU,C1,C2,H,K
      COMMON BETA,BEE,CEE,INDIC,H,K,MU
      EXTERNAL G
      FREQ=16.0
      BEE=0.75
      CEE=0.125
      E=2.69E08
      RHO=1550.0
      VNU=0.257
      ALAM=(VNU*E)/((1.0+VNU)*(1.0-2.0*VNU))
      AMU=E/(2.0*(1.0+VNU))
      AC1=SQRT((2.0*AMU+ALAM)/RHO)
      AC2=SQRT(AMU/RHO)
      DAMP=0.05
      AA=SQRT(0.5*(1.0+SQRT(1.0+4.0*DAMP*DAMP)))
      MU=CMPLX(AMU,0.0)*CMPLX(1.0,(2.0*DAMP))
      C1=CMPLX(AC1,0.0)*CMPLX(AA,(DAMP/AA))
      C2=CMPLX(AC2,0.0)*CMPLX(AA,(DAMP/AA))
      OMEGA=6.28318508*FREQ
      H=OMEGA/C1
      K=OMEGA/C2
      DO 5 I=1,6
      DO 6 J=1,2
      INDIC=J
      X=FLOAT(I-1)*0.1
      CALL INTEG(19,(0.2/18.),ANS1,0.0,X)
      WRITE(6,65)ANS1
      CALL INTEG(35,(0.4/34.),ANS2,0.2,X)
      WRITE(6,65)ANS2
      CALL INTEG(33,(0.4/32.),ANS3,0.6,X)
      WRITE(6,65)ANS3
      CALL INTEG(75,(19.0/74.),ANS4,1.0,X)
      WRITE(6,65)ANS4
65    FORMAT(1X,'ANS= ',F18.14)
      ANSW=ANS1+ANS2+ANS3+ANS4
      IF(J.EQ.1)WR=ANSW
      IF(J.EQ.2)WI=ANSW
6     CONTINUE
5     WRITE(4,60)X,WR,WI
60    FORMAT(1X,' X=',F6.3,' WR=',F18.14,' WI=',F18.14)
      STOP
      END
      SUBROUTINE INTEG(M,BINC,ANSW,BETA1,X)
      DIMENSION TW(6000),IW(2500),B(100)
      EXTERNAL G
      COMMON BETA,BEE,CEE,INDIC,H,K,MU
      IFAIL=0
      DO 1 I=1,M
      BETA=BETA1+(I-1)*BINC
      CALL D01ANF(G,0.0,20.0,X,1,10D-18,10D-6,BB,ABSERR,TW,6000,
     ?IW,2500,IFAIL)
      IF(IFAIL.NE.0)WRITE(6,67)IFAIL
      IF(IFAIL.NE.0)STOP
1     B(I)=BB
67    FORMAT(1X,'IFAIL= ',I3)
      CALL SIMPSON(B,M,BINC,ANSW)
      RETURN
      END
      FUNCTION G(GAMA)
      COMPLEX MU,H,K,A1,A2,FR,A,B,C,A12,BCM,EYE,WB
      COMMON BETA,BEE,CEE,INDIC,H,K,MU
```

```
      BG=BETA*BETA+GAMA*GAMA
      A1=CSQRT(BG-H*H)
      A2=CSQRT(BG-K*K)
      A12=A1*A2
      IF(ABS(BETA).GT.10E-30.AND.ABS(GAMA).GT.10E-30)
     ?STERM=SIN(BETA*BEE)*SIN(GAMA*CEE)/(BETA*GAMA)
      IF(ABS(BETA).LT.10E-30.AND.ABS(GAMA).GT.10E-30)STERM=(SIN(GAMA*
     ?CEE))/GAMA
      IF(ABS(BETA).GT.10E-30.AND.ABS(GAMA).LT.10E-30)STERM=(SIN(BETA)*
     ?BEE)/BETA
      IF(ABS(BETA).LT.10E-30.AND.ABS(GAMA).LT.10E-30)STERM=1.0
      FR=(2.0*BG-K*K)**2-4.0*A12*BG
      BCM=(1.0/(BEE*CEE*MU))
      A=BCM*STERM*H*H*(2.0*BG-K*K)/FR
      EYE=CMPLX(0.0,1.0)
      B=-EYE*BCM*STERM*2.0*A12*BETA/FR
      C=-EYE*BCM*STERM*2.0*A12*GAMA/FR
      WB=A1*A/(H*H)-(EYE/A2)*(BETA*B+GAMA*C)
      IF(INDIC.EQ.1)G=REAL(WB)
      IF(INDIC.EQ.2)G=IMAG(WB)
      RETURN
      END
      SUBROUTINE SIMPSON(A,N,AINC,ANSW)
      DIMENSION A(N)
      ANS1=A(1)+A(N)
      ANS2=0.0
      ANS3=0.0
      DO 1 I=2,(N-1),2
1     ANS2=ANS2+A(I)
      DO 2 J=3,(N-2),2
2     ANS3=ANS3+A(J)
      ANSW=(AINC/3.0)*(ANS1+4.0*ANS2+2.0*ANS3)
      RETURN
      END

END OF LISTING OF FILE :ISR008.W(5,*,1) FOR USER :ISR008 AT 1986/09/18

**********************************************************************
```

REFERENCES

[1] Abramowitz, M. Stegun, I. "Handbook Of Mathematical Functions", Dover Publications, New York, 1965.

[2] Alabi, B. "Harmonic Vertical Motion Of A Rigid Strip - A Mapping Finite Difference Model For The Elastic Half-Space" ANSTI, African Journal Of Science Technology 4 (1), June 1985.

[3] Awojobi, A.O. "Vertical Vibrations Of A Rigid Circular Foundation On Gibson Soil", Geotechnique 22 (2) 333-343, 1972.

[4] Awojobi, A.O. Grootenhuis, P. "Vibration Of Rigid Bodies On Semi-Infinite Elastic Media", Proc. Roy. Soc. A 287, 27-63, 1965.

[5] Barkan, D.D. "Dynamics Of Bases And Foundations", McGraw Hill Book Co. 1962.

[6] Beckmann, P. "Orthogonal Polynomials For Engineers And Physicists", The Golem Press, 1973.

[7] Woods, R.D. "Screening Of Surface Waves In Soils", J. Soil Mech. Found. Div. Trans. ASCE 94 (SM4) 951-979, 1968.

[8] Bucher, H.P. "Sound Propagation In A Channel With Lossy Boundaries", JASA 18 1187-1194, 1970.

[9] Bycroft, G.N. "Forced Vibrations Of A Rigid Circular Plate On A Semi-Infinite Elastic Space And On An Elastic Structure", Phil. Trans. Roy. Soc. Lon. 248, 1956.

[10] Scholte, J.G. "The Range Of Existence Of Rayleigh And Stoneley Waves", Mon. Not. Roy. Astrom. Geophys. Suppl. 5 120-127, 1947.

[11] Chae, Y.S. "Vibrations Of Non-Circular Foundations", Jnl. Of. Soil mech. & Foundations Div. Proc. ASCE 1411-1430, Nov 1969

[12] Chapman, C.H. "Lamb's Problem And Comments On The Paper "On Leaking Modes" By Usha Gupta", Pure & Applied Geophysics 94 233-247, 1972.

[13] Dawn, T.M. Stanworth, C.G. "Ground Vibration From Passing Trains", J.S.V. 66 (3) 355-362, 1979

[14] E.C.O.M. (US Army Electronics Command, R & D) "Continuous Seismic Wave Communications Experiments At 80Hz In Diverse Terrains", Tech. Report ECOM 2921, Jan 1968,

[15] Wei, J. Petyt, M. "Two Dimensional Analysis Of Ground Deformation Due To Static Loads", ISVR, Univ. Of Southampton, Memo No. 672, Sept 1986.

[16] Zeng, X. Cakmak, A.S. "Dynamic Structure - Soil Interaction Under The Action Of Vertical Ground Motion: Axisymmetric And Plane Problems", Soil Dynamics And Earthquake Engineering 3 (4) 200-219, Oct 1984.

[17] Fröberg, C-E. "Introduction To Numerical Analysis", Addison Wesley Publ. Co., 1957.

[18] Fu, C.Y. "Studies On Seismic Waves, II", Geophysics 2 10-20, 1946.

[19] Gaul, L. "Zur Dynamik Der Wechselwirkung Von Strukturen Mit Dem Baugrund", Univ. Of Hannover Inst. Of Mechanics, internal publication, 1979.

[20] Bishop, R.E.D. Johnson, D.C. "The Mechanics Of Vibration", C.U.P. 1960.

[21] Gazetas, G.C. "Dynamic Stiffness Functions Of Strip And Rectangular Footings On Layered Media", M.Sc. Thesis, M.I.T., 1975.

[22] Gazetas, G.C. Roesset, J.M. "Forced Vibrations Of Strip Footings On Layered Soils", Meth. Struct. And ASCE (1) 115, 1975.

[23] Gazetas, G. Roesset, J.M. "Vertical Vibration Of Machine Foundations", Jnl. Of The Geotechnical Eng. Div, Vol GT12, Dec 1979.

[24] Girardi, L. "Propagation Des Vibrations Dans Les Sols Homogènes On Stratifiés", Sols et Fondations, No 397, 31-66, Sept 1981.

[25] Gopalacharyulu, S. Rebbeck, R.G. "Ground Borne Vibrations 1: Rayleigh Waves In Semi-Infinite Soil", B.R.B. R&D Div. Track and Structures Group, I.M. TS 81, April 1977.

[26] Graff, K.F. "Wave Motion In Elastic Solids", Clarendon Press, Oxford, 1975.

[27] Grootenhuis, P. Awojobi, A. "The In-Situ Determination Of The Dynamic Properties Of Soil", (Proc. Intl. Conf. On Earthquake Eng., Imperial Coll. Lon., April 1965) Vibrations in Civil Engineering, Butterworth, London, p181, 1965.

[28] Office For Research And Experiments Of The International Union Of Railways, Utrecht, "Theoretical Prediction Of Ground Vibrations And Comparison With Experimental Results", Committee D151, Report No. 3, 1983.

[29] Gutowski, T.G. Dyne, C.L. "Propagation Of Ground Vibration: A Review", JSV 2 (49) 179-193, 1963.

[30] O.R.E., Utrecht, Personal Communication, Feb 1986.

[31] Holzlöhner, U. "Vibrations Of The Elastic Half-Space Due To Vertical Surface Loads", Earthquake Engineering & Structural Dynamics 8 405-414, 1980.

[32] Dawn, T.M. British Rail Technical Centre, Derby, Personal Communication, Feb 1986.

[33] Hushmand, B. "Experimental Studies Of Dynamic Response Of Foundations", Calif. Inst. Of Techn., Ph.D. Thesis, 1983.

[34] Sezawa, K. Kanai, K. "The Range Of Possible Existence Of Stoneley Waves And Some Related Problems", Bull. Earthq. Res. Inst. 17 p3, 1939.

[35] Spencer, A.J.M et al "Engineering Mathematics", Van Nostrand Rheinhold Co. Ltd., 1980.

[36] Kausel, E. Roesset, J.M. "Stiffness Matrices For Layered Soils", Bull. Seism. Soc. Am. 71 (6) 1743-1761, Dec 1981.

[37] Kausel, E. Roesset, J.M. Waas, G. "Dynamic Analysis Of Footings On Layered Media", Jnl. Of. The Eng. Mech. Div. Proc. ASCE 101 (EMS) p679, Oct 1975.

[38] Kausel, E. Peek, R. "Dynamic Loads In The Interior Of A Layered Stratum: An Explicit Solution", Bull. Of Seism. Soc. Of Am. 72 (5) 1459-1481, Oct 1982.

[39] Kobori, T. Minai, R. Suzuki, T. "The Dynamical Ground Compliance Of A Rectangular Foundation On A Viscoelastic Stratum", Bull. Of The Disaster Prevention Res. Inst., Kyoto Univ. 20 289-329, March 1981.

[40] Kobori, T. Thompson, W.T. "Dynamical Compliance Of Rectangular Foundations On An Elastic Half-Space", Jnl. Of Applied Mechanics, Trans. ASME 579-584, Dec 1963.

[41] Kolsky, H. "Stress Waves In Solids", Dover Publ., 1963.

[42] Kronrod, A.S. "Nodes And Weights Of Quadrature Formulas", Consultants Bureau, New York, 1965.

[43] Kulhemeyer, R. "Vertical Vibrations Of Footings Embedded In Layered Media", Univ. Of Calif., Berkeley, Ph.D. Thesis, 1969.

[44] Lamb, H. "On Boussinesq's Problem", Proc. Lon. Math. Soc. 34 276-284, 1902.

[45] Lamb, H. "On The Propagation Of Tremors Over The Surface Of An Elastic Solid", Phil. Trans. A 203 1-42, 1904.

[46] Lin, Y.J. "Dynamic Response Of Circular Plates On Viscoelastic Half-Space", J. Of Appl. Mech., Trans. ASME 45 (E379), 1978.

[47] Longman, I.M. "Note On A Method Of Computing Integrals Of Oscillating Functions", Proc. Camb. Phil. Soc. 52 764-768, 1956.

[48] Longman, I.M. "A Method For The Numerical Evaluation Of Finite Integrals Of Oscillating Functions", Math. Tables and other aids to computation, 14 53-59, 1960.

[49] Love, A.E.H. "The Stress Produced In A Semi-Infinite Solid By Pressure On Part Of The Boundary", Phil. Trans. Roy. Soc. Lon. A 228 377-420, 1929.

[50] Luco, J.E. Westmann, R.A. "Dynamic Response Of Circular Footings", Jnl. Of Eng. Mech. Div. ASCE 97 (EMS) 1381-1395, 1971.

[51] Luco, J.E. Westmann, R.A. "Dynamic Response Of a Rigid Footing Bonded To An Elastic Half-Space", J. App. Mechs. Trans. ASME, 39 E(2) 527-534, 1972.

[52] Luco, J.E. "Vibration Of A Rigid Disc On A Layered Viscoelastic Medium", Nucl. Eng. & Des. 36 325-340, 1976.

[53] Timoshenko, S.P. Goodier, J.N. "Theory Of Elasticity", 3rd Edition, McGraw Hill, 1984.

[54] Newlands, M. "The Disturbance Due To A Line Source In A Semi-Infinte Elastic Medium With A Single Surface Layer", Phil. Trans. A 245 p896, Dec 1952.

[55] Thomson, W.T. "Theory Of Vibrations With Applications", Prentice-Hall, 1972.

[56] Miller, G.F. Pursey, H. "The Field And Radiation Impedance Of Mechanical Radiations On The Free Surface Of A Semi-Infinite Isotropic Solid", Proc. Roy. Soc. Lon. A 233 521-541, 1955.

[57] Miller, G.F. Pursey, H. "On The Partition Between Elastic Waves In A Semi-Infinite Solid", Proc. Roy. Soc. Lon. A 233, 1955.

[58] North Carolina Coastal Energy Impact Program, Rayleigh, "Railroad Induced Vibrations, New Bern, North Carolina, Aug 10 & 11, 1983 (Final Report)", March 1983.

[59] Novak, M. Beredugo, Y.O. "The Effect Of Embedment On Footing Vibrations", Proc. 1st Can. Conf. Earthq. Eng. Res., Vancouver, B.C., 1-14, May 1971.

[60] Oien, M.A. "Steady Motion Of A Rigid Strip Bonded To An Elastic Half-Space", J. Applied Mechanics Trans. ASME 38 (Ser E No.2) 328-334, 1971.

[61] Ottenstreuer, M. "Frequency Dependent Dynamic Response Of Footings", Proc. Soil Dynamics & Earthquake Eng. Conf., Southampton, 799-809, July 1982.

[62] Pekeris, C.L. "Theory Of Propagation Of Explosive Sound In Shallow Water", Geol. Soc. Am. Men 27, 1948.

[63] Piessens, R. Branders, M. "Computation Of Oscillating Integrals", Jnl. Of. Computational & Applied Mechanics, 1 (3), 1975.

[64] Piessens, R. De Doncker, E. Uberhuber, C. Kahaner, D. "QUADPACK A Quadrature Subroutine Package", 1980.

[65] Phynney, R.A. "Propagation Of Leaking Interface Waves", Bull. Seismol. Soc. Am. 51 p527, 1961.

[66] Balakrishna, H.A.B. Nagaraj, C.N. "A New Method For Predicting The Natural Frequency Of Foundation-Soil Systems", Structural Engineer 38 p310, Oct 1960.

[67] Lord Rayleigh "On Waves Propagated Along The Surface Of An Elastic Solid", Proc. Lon. Math. Soc. 17 4-11, 1885.

[68] Richardson, J.D. "Forced Vibrations Of Rigid Bodies On A Semi-Infinite Elastic Medium", Univ. of Nottingham, Ph.D. Thesis, May 1969.

[69] Richardson, J.D. Webster, J.J. Warburton, G.B. "The Response On The Surface Of An Elastic Half-Space Near To An Harmonically Excited Mass", JSV 14 307-316, 1971.

[70] Robertson, I.A. "Forced Vertical Vibrations Of A Rigid Circular Disc On A Semi-Infinite Elastic Solid", Proc. Camb. Phil. Soc. Maths. Phys. Sci. 62 p547, 1962.

[71] Seed, H.B. Idriss. I.M. "Soil Moduli And Damping Factors For Dynamic Response Analysis", Report No. EERC 70-100 Earthquake Engineering Research Center, Univ. of California, Berkeley, 1970.

[72] Small, J.C. Booker, J.R. "Finite Layer Analysis Of Layered Elastic Material Using A Flexibility Approach. Part 1 - Strip Loading", Inter. J. For Numerical Methods in Eng. 20 1025-1037, 1984.

[73] Stoneley, R. Proc. Roy. Soc. A 106 416-428, 1924.

[74] Stump, B. "Stress Waves In An Elastic Half-Space: Single And Multiple Surface Sources", JSV 92 (2) 181-202, Jan 1984.

[75] Sutherland, L.C. "A Brief Review Of The Impedance Of The Soil Presented To The Reaction Mass", Wyle Labs. - Research Staff Report WR 65-39, (date unknown).

[76] Grassie, S.L. Cox, S.J. "The Dynamic Response Of Railway Track With Unsupported Sleepers", Proc. Inst. Mech. Engrs. 199 (2) 123-135, 1985.

[77] Tolstoy, I. Usdin, E. "Dispersive Properties Of Stratified Elastic And Liquid Media: A Ray Theory", Geophysics 18 (4) 844-870, Oct 1953.

[78] Alvarez, Clement "Propagation Des Vibrations Dans Le Sol", Memoire de DEA - Département Des Etudes Générales Et Projets De La SNCF, 1981

[79] Waas, G. "Linear Two Dimensional Analysis Of Soil Dynamics Problems In Semi-Infinite Layered Media", Univ. Of Calif., Berkeley, Ph.D. Thesis, 1972.

[80] Warburton, G.B. "Forced Vibrations Of A Body On An Elastic Stratum", Trans. ASME. J. Appl. Mech. 24 55-58, 1957.

[81] Reissner, E. Inger. Arch. 7 p838, 1986.

[82] Richart, F.E. Whitman, P.V. Jnl. Of Soil Mechs. & Fndtns. Div. Proc. ASCE 143-168, Nov 1967.

[83] Gilbert, F. Laster, S.F. "Excitation And Propagation Of Pulses On An Interface", Bull. Seism. Soc. Am. 52 299-319, 1962.

[84] Pack, P. "The Finite Element Method In Underwater Acoustics", ISVR, Univ. Of Southampton, Ph.D. Thesis, 1986.

[85] Wilkinson, J.H. Reinsch, C. "Handbook For Automatic Computation", Vol II Linear Algebra, 93-110 & 339-358 & 359-371, Berlin, Springer, 1971.

[86] Williams, A.O. "Some Effects Of Velocity Structure On Low-Frequency Propagation In Shallow Water", JASA 32 363-371, 1960.

[87] Fu, C.Y. "Some Problems Of The Propagation Of Elastic Waves In A Horizontally Stratified Medium", Jnl. Of The Chinese Geophysical Soc. 2 (1) 40-59, June 1950.

[88] Willis, D.E. Wilson, J.T. "Maximum Vertical Ground Displacement Of Seismic Waves Generated By Explosive Blasts", Bull. Seism. Soc. Am. 50 (3) 455-459, July 1960.

[89] Wittrick, W.H. Williams, F.W. "A General Algorithm For Computing Natural Frequencies Of Elastic Structures", Quarterly Jnl. Of Mechanics & Applied Matematics 24 (3), Aug 1971